ISSN 0916-7501
CODEN: TTEREB

TOYOTA Technical Review

2005/ 11
220

Hybrid

Vol. 54 No. 1

Contents

The 21st Century: The Age of the Hybrid

Masatami Takimoto,
Executive Vice President, Member of the Board

1. Today for Tomorrow—What We Must Do Now for Future Generations

Since the Industrial Revolution, human beings have consumed enormous quantities of coal, petroleum, and other fossil fuels in their pursuit of comfort and convenience. But as a consequence, enormous quantities of carbon dioxide and other greenhouse gases have been generated, bringing with them the problems of global warming and large-scale climate change. The Kyoto Protocol came into effect on February 16 of this year, and it will require more truly effective action than ever before to put a halt to global warming, mainly through the reduction of CO_2 emissions.

It must also be noted that the production of petroleum, on which today's affluent society was built, is expected to peak in the next few decades. Not only must we manage this limited resource carefully, but we must also convert to alternative energy sources that are easy to use and have lower environmental impact.

In essence, it is vital that our generation stops the increase in atmospheric CO_2 concentrations right now, for the sake of future generations in the decades to come. We must build a society capable of sustainable development by constructing infrastructure systems to use new energy resources that are clean and safe, alongside the limited amounts of petroleum available.

2. The Age of the Hybrid Powertrain

Shifting our focus to the automotive realm, petroleum is still essential for automobiles, and CO_2 emissions are therefore hard to avoid. But that is exactly the reason why, while we must develop cars that consume less fuel and make every effort to reduce CO_2 emissions, we must also prepare for an age of energy alternatives to petroleum.

It is therefore time for hybrid powertrain technology to assume a leading role. The Toyota Hybrid System (THS) realizes low fuel consumption and low CO_2 emissions by reducing energy loss as far as possible. This is achieved by recovering the energy that would otherwise be wasted during deceleration, and by stopping needless engine idling when the vehicle is stopped. Moreover, by reutilizing the recovered energy for acceleration, the system realizes a synergy effect. In other words, the system simultaneously achieves exemplary environmental performance (low NOx and particulate matter levels) and excellent acceleration performance superior to a conventional car. The THS is truly the ultimate high-efficiency powertrain system.

We believe the hybrid system is a core technology for the future. It can be applied not only to gasoline engines, but also to diesel engines, natural gas engines, and synthetic liquid fuel engines. It can also be used with fuel cell vehicles, which are expected to become the cars of the future. This is why we want to improve and develop the system further, and promote its wider use throughout the world as a gift to future generations.

3. The Age of Hybrid Energy

It is believed that the exploitation period of petroleum can be extended through further evolution of extraction technology, but sooner or later, the supply of low-cost, high-quality petroleum will be exhausted. The world will then enter the so-called hybrid energy age, when primary energy resources such as oil shale, natural gas, coal, biomass, sunlight, water power, wind power, and nuclear power will be used to make a variety of secondary energy resources, such as ethanol, hydrogen, and electricity, as well as synthetic fuels like gas-to-liquid (GTL) and biomass-to-liquid (BTL). The optimum combination of these secondary resources will then be used in industry, homes and transportation.

A number of issues in the sequence from primary energy to secondary energy to industry, homes, and transportation must be addressed in a thoroughgoing and comprehensive manner if the optimum system is to be established. As well as straightforward economic considerations, these include reducing CO_2 generated by the manufacture and consumption of secondary energy, ensuring global supply capacity and energy security, and prioritizing the use of resources according to their energy density and the ease of establishing a refueling infrastructure. Therefore, research into hybrid energy is needed now more than ever before. The key element for this research will be collaborative thinking, not just between the automobile and energy industries, but also from the combined perspectives of government, academia, and industry at large.

The effort to realize our dream of making safe, enjoyable cars that do not emit exhaust gas and CO_2 will open the way to the optimum energy solution. Let us approach this task from a variety of perspectives, so that we can build a society capable of sustainable development for future generations.

The Present and Future of Hybrid Technology

Takehisa Yaegashi
Power Train Development Group

1. Introduction

Almost eight years have passed since the launch of the Prius, the world's first production hybrid vehicle and the first step toward realization of sustainable mobility, which is a concept that aims to address the issues of global warming, dwindling petroleum resources, and air pollution. At Toyota Motor Corporation, we view these environmental issues as the most important business challenges for a car manufacturer, and we have been quick to initiate efforts to mass produce hybrids as practical yet environmentally friendly vehicles. Starting with the Prius, Toyota has applied hybrid technology to various categories of vehicles including minivans, and is striving to further develop the technology. In September 2003, Toyota succeeded in developing a next-generation hybrid system under the Hybrid Synergy Drive concept, which aims to create vehicles that have a high level of environmental performance as well as being fun to drive. This new technology was installed in the Prius, which was subsequently released onto the market. 2005 has seen the launch of the RX400h, powered by a version of this next-generation hybrid technology updated for use in a luxury V6-engined SUV. As for other car makers, last year Honda added the Accord V6 Hybrid to the Insight and Civic Hybrid, and Ford introduced the Escape SUV hybrid. This spate of releases indicates that the hybrid system has entered the popularization stage as an environmentally sound power train.

This article describes present and future trends for environmental and resource related issues that are relevant to vehicles. It also presents an overview of Toyota's past efforts and future perspectives on hybrid technology, which is positioned as a core technology for future vehicles.

2. Vehicles and Issues Related to the Environment and Resources

Emissions of CO_2 and other greenhouse gases that are generated by human activities are having a profound impact on global warming and associated global climate change. In the same year as the launch of the first Prius, the Third Conference of the Parties to the United Nations Framework Convention on Climate Change (COP3) was held in Kyoto to discuss global efforts to counter climate change. As a result, a medium-term action plan called the Kyoto Protocol was drafted. Although the US refusal to ratify the protocol cast dark clouds over its future, the protocol finally came into effect after being ratified by Russia this year. **Fig. 1** shows data presented in the third assessment report of the Intergovernmental Panel on Climate Change (IPCC) published in June 2001. [1] It shows the changes that have been observed in mean atmospheric CO_2 concentration and average global temperature up to the current point in time, and the predictions for CO_2 concentration and temperature increase based on various scenarios for curbing global warming.

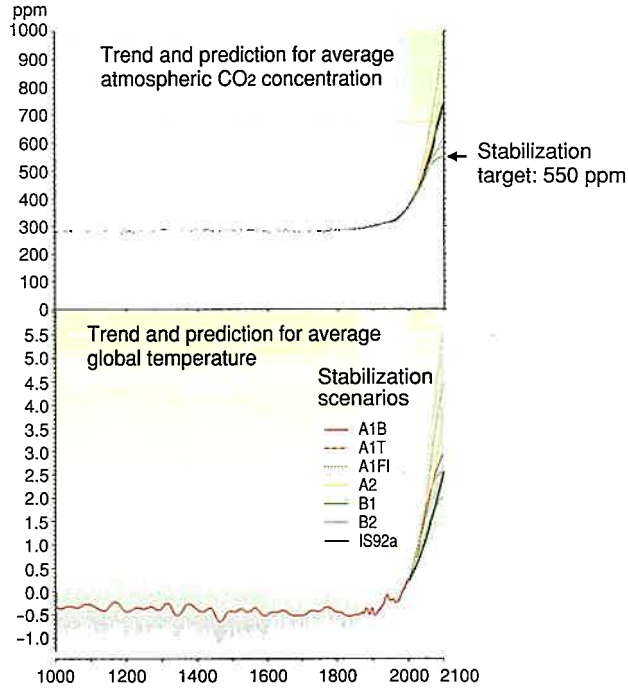

Source: IPCC Third Assessment Report

Fig. 1 Trends for Atmospheric CO_2 Concentration and Average Ground Temperature

Atmospheric CO_2 concentration has increased from around 280 ppm in the pre-Industrial Revolution era to around 380 ppm at present. If energy consumption continues as it is, CO_2 concentration will approach 1,000 ppm in the year 2100, increasing concern that climate change will become more serious. Internationally, various scenarios for reducing CO_2 emissions in transportation and other sectors are being studied with the aim of stabilizing CO_2 concentration at 550 ppm. The

burning of coal, petroleum, and other fossil fuels accounts for most CO_2 emissions. In particular, the CO_2 emissions from transportation that mainly uses oil for fuel accounts for at least 20% of the total. In the future, increased motorization in countries like China, India, and Russia will rapidly increase the total number of vehicles owned in the world, and further boost CO_2 emissions. It has been predicted that extraction of the world's petroleum reserves will peak around the year 2040, which means that the problems surrounding exhaustion of this resource are fast approaching. Therefore, popularization of vehicles that emit less CO_2 and consume less fuel is becoming an urgent issue. At the same time, it is also important to clean exhaust emissions to prevent air pollution.

It is clear that the impending challenges cannot be met by mere extension of conventional technologies. Greater expectations are being placed on the shoulders of hybrid and fuel cell vehicles.

3. Hybrid Synergy Drive

No matter how low the CO_2 emissions or how clean the exhaust gas of a vehicle, it cannot expect to gain popularity among drivers if it is inferior to conventional vehicles in terms of running performance, driving range, user-friendliness, and price. After the Prius, Toyota introduced a variety of hybrid vehicles, including the Crown Mild Hybrid, and the Estima Hybrid. Subsequent developmental efforts have produced a synergy between the engine and the electric power train. This has enabled improvements in both the environmental performance of hybrid vehicles and so-called "fun to drive" performance aspects such as running performance. Consequently, the idea of simultaneously achieving high levels of both environmental and fun to drive performance aspects was adopted as the direction for the next generation of hybrid vehicles. This was encapsulated by the Hybrid Synergy Drive concept, which became the catalyst for a further acceleration in development efforts (**Fig. 2**).

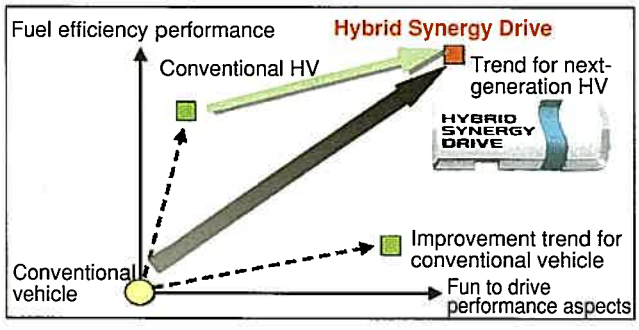

Simultaneous achievement of environmental performance and exciting driving experience

Fig. 2 Hybrid Synergy Drive

4. Hybrid Systems and Improvements in Environmental Performance

This section discusses how the functions and configuration of a hybrid system contribute to reducing CO_2 emissions and fuel consumption.

A hybrid system is defined as a system in which two or more types of power units with different working principles are operated in combination. Configurations of power units where the internal combustion engine is used with either an electric or a hydraulic motor have been implemented commercially. The currently mainstream configuration is the electric system, thanks to dramatic advances in electric motor, battery, and control technology as a result of the development of electric vehicles. The most significant feature of the hybrid system is the installation of high-power and high-capacity batteries as a rechargeable energy buffer in the driving force transmission path to create a circulation route for efficient use of energy. This enables part of the energy to run the vehicle to be temporarily stored in the battery for later use (**Fig. 3**).

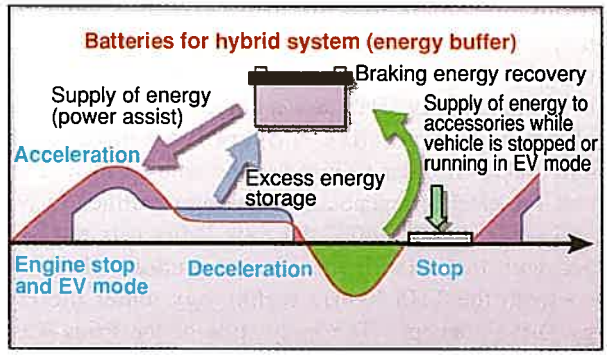

Fig. 3 Features of Hybrid System (Energy Storage)

4.1 Hybrid systems and improvements in fuel efficiency

This section describes how the introduction of the hybrid system has improved fuel efficiency. The key ways in which this has been accomplished include optimizing and increasing the efficiency of the engine, motor, and other individual components, in addition to combinations of the following four factors.

(1) Engine operation is stopped and the vehicle is put into EV mode when parked or running at low speeds where engine efficiency is low.

(2) The use of a continuously variable transmission (CVT) function enables the engine to be operated at optimum efficiency.

(3) High efficiency engines, such as high expansion ratio engines, are used. These engines have been designed to operate at maximum efficiency in the hybrid use region, on the assumption that battery power assist can be obtained for acceleration during high-speed driving where considerable driving power is necessary.

(4) The electric motor is operated as a generator, and the kinetic energy of the vehicle, which would otherwise be released into the air during deceleration, is converted into electricity and stored in the battery. The energy is reused as the driving energy described in points 1 and 3 (electric regenerative braking).

The rate of improvement depends on the mechanism of the hybrid system and to what degree the functions described above are performed. Particularly, a hybrid system that is able to stop engine operation and run the vehicle under EV mode during driving is often called a "strong hybrid" or a "full hybrid" to distinguish it from other simplified hybrid systems.

The Prius was positioned to be the leading environmentally friendly car. When its hybrid system was selected, a basic goal was set to achieve the ultimate in fuel efficiency performance while maintaining the equivalent running performance and utility space of a conventional vehicle. Naturally, this meant that a lightweight and compact system that could be installed in a small passenger car was required for commercial implementation. A system was subsequently selected from nearly 100 different types of hybrid systems, but this system did not fit the available definitions of conventional hybrid systems. Thus, a new definition was created, called the "series/parallel hybrid." This is the strong hybrid type in the various Toyota Hybrid Systems (THS). In addition, the THS uses a brake system that is capable of performing regenerative cooperative control with the hydraulic brakes in order to increase the amount of regenerated energy of the electric regenerative braking described in point 4 above. In September 2003, the new Prius was put on sale equipped with the THS II, the next-generation hybrid system evolved from the THS hybrid technology under the Hybrid Synergy Drive concept. The body style of the Prius was also totally renewed to expand the interior capacity of the vehicle. As a result, the Prius was classed as a mid-size vehicle instead of as a compact. In March of this year, the RX400h was launched with a high-power version of the THS II that incorporates further improved technologies to meet the needs of V6-engined SUVs. The technical details of the high-power version of the THS II are described elsewhere in this Toyota Technological Review. The optimization of fuel efficiency by the hybrid system has already been described above. In addition, the system in the Prius and the RX400h that performs regenerative cooperative control with the hydraulic brakes includes the Electronically Controlled Brake System (ECB) that was previously adopted in the Estima Hybrid. ECB has a high degree of controllability and less brake drag, thereby enabling an increase in regeneration efficiency and making a significant contribution to improving fuel efficiency. Furthermore, the secondary battery in hybrid vehicles is used as an energy buffer to optimize running efficiency, and to supply power to the heater, air conditioner, and other accessories via a DC-DC converter. Energy optimization from the perspective of total vehicle energy consumption (i.e., the sum of the energy required for running both the vehicle and accessories) is also a key point for the improvement in fuel efficiency. The regeneration and fuel efficiency of the new Prius was also improved by the adoption of an aerodynamic body with a coefficient of drag (CD) of 0.26, and by reducing losses in the drive system. Taking these steps to optimize the energy efficiency and specifications of the entire vehicle enables hybrids to realize a considerable improvement in fuel efficiency performance over conventional vehicles. **Fig. 4** shows the fuel efficiency improvement effect achieved by the hybrid functions described in points 1 to 4, in terms of engine efficiency and operating characteristics.

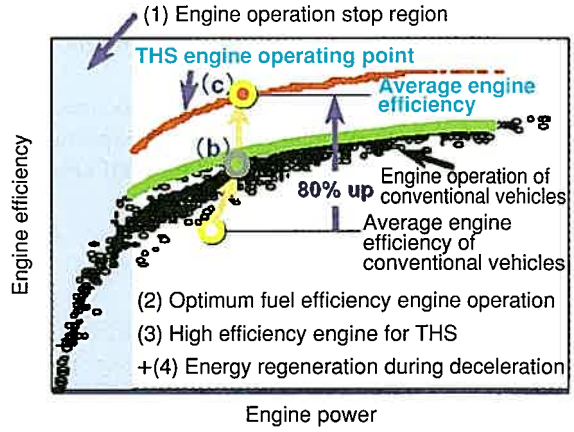

Fig. 4 Improvement in Fuel Efficiency by Introduction of Hybrid System

4.2 Fuel efficiency performance of hybrid vehicles

(1) Official fuel efficiency

The fuel efficiency performance of a vehicle varies according to specifications such as weight, and various driving patterns such as city driving in congestion, suburban driving, highway driving, uphill/downhill driving, and at various levels of acceleration. The operations of the driver and the ambient temperature can also affect fuel efficiency. From the perspective of reducing levels of CO_2 emissions and fuel consumption, it is important to enhance the actual fuel consumption reduction effect across all driving patterns, operations and environmental conditions. The official fuel efficiency indicated in catalogs and the like is determined according to test methods and notations that differ from location to location. Examples include 10-15 mode (Japan), city mode and highway mode (US), and EU mode (Europe). In all cases, the purpose of these test methods and notations is to compare the fuel efficiency potential of vehicles under set conditions that exclude impacts from the differences in driving pattern, operation and the environment as described above.

Fig. 5 [2] compares the Japan-certified fuel efficiency (10-15 mode) of hybrid vehicles and conventional vehicles. Hybrid vehicles have achieved a dramatic fuel efficiency improvement in comparison with conventional vehicles. The improvement rates of strong hybrids such as the Prius and RX400h are particularly high. Furthermore, hybrid vehicles equipped with the THS II have achieved a considerable improvement in fuel

efficiency over conventional vehicles in each of the different official fuel efficiency test driving modes in Japan, the US, and Europe. These vehicles have among the best fuel efficiency performance of any vehicles in the world.

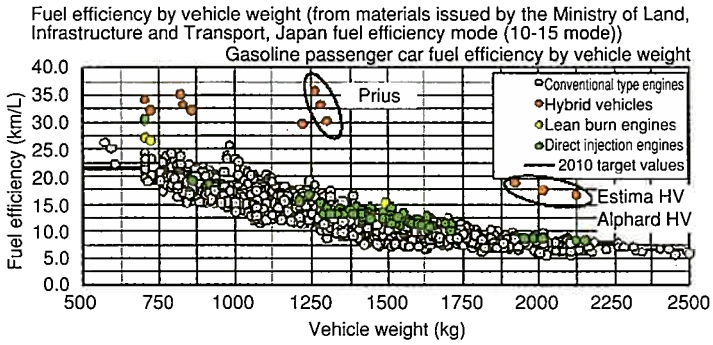

Fig. 5 Official Fuel Efficiency Performance of Hybrid Vehicles

(2) On-road fuel efficiency

In order to reduce fuel consumption and CO_2 emissions in the on-road environment, it is important to understand and improve the vehicle's fuel efficiency performance in various driving patterns, operations, and atmospheric environments. One of the aims of the THS II was to improve fuel efficiency in various driving environments that are not evaluated in the official tests, as well as those in the official tests. As shown in Section **4.1**, functions such as engine stop, EV mode operation and energy regeneration during deceleration are some of the factors that have enabled hybrid systems to improve fuel efficiency considerably in city driving where there are many intersections and traffic lights, frequent stops and longer periods of low-speed driving. In highway driving where engine-stop operation and deceleration occur less frequently, improved fuel efficiency performance is achieved by capitalizing on the functions of strong hybrid vehicles. These include the adoption of high efficiency engines in combination with the electric power assist function during acceleration, optimum engine efficiency operation using CVT functionality, and precise power control for accessories. Fuel consumption during air conditioner operation is a factor not evaluated in official tests, but it has a significant impact on actual on-road fuel efficiency. Starting with the new Prius, hybrids have used an electric air conditioner driven by a high efficiency inverter to make use of the high voltage of the hybrid system, instead of a conventional engine-driven air conditioner. The new air conditioner does not just improve air conditioning capacity while the engine is stopped. It also enables a dramatic improvement in fuel efficiency while in use by operating under precise optimum efficiency conditions according to various cooling demands (**Fig. 6**).

Fig. 7 [3] shows a comparison of the monthly average fuel efficiency trends for old and new models of the Prius, as reported by users in Japan. The user fuel efficiency report shows that the new Prius achieves the same improvement in fuel efficiency over the previous models as seen in the official fuel efficiency tests.

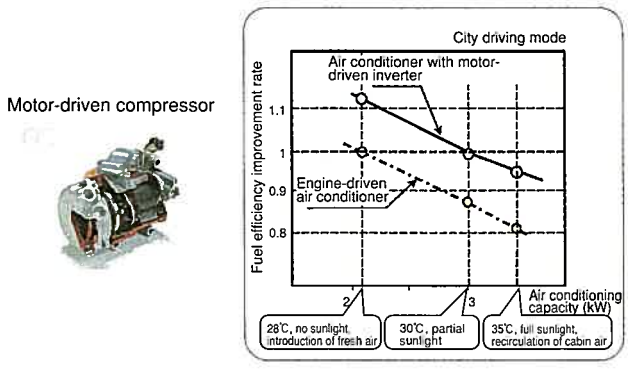

Fig. 6 Air Conditioner Fuel Efficiency

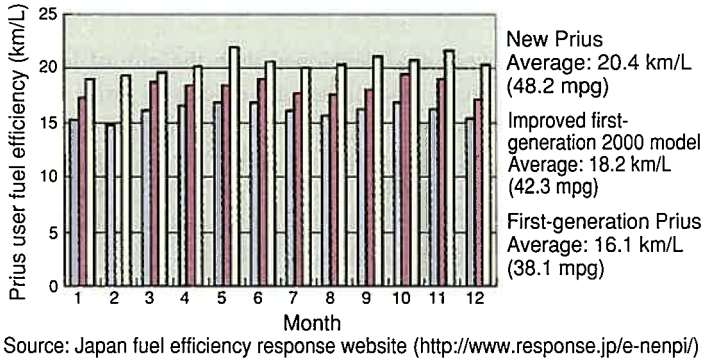

Source: Japan fuel efficiency response website (http://www.response.jp/e-nenpi/)

Fig. 7 Prius Fuel Efficiency as Reported by Users

(3) Life Cycle Assessment (LCA) CO_2 evaluation

Reduction of emissions and fuel consumption during driving as described above is not the only important factor in improving the environmental performance of a vehicle. It is also important to evaluate and reduce the potential emissions of a vehicle during its entire life, from the production stages of the vehicle, parts and component materials, to the extraction and refining of fuel, the maintenance of the vehicle, and the final stage where the vehicle is scrapped. **Fig. 8** shows an example of LCA analysis with the new Prius. The fuel efficiency value used here is the European official fuel efficiency value that is close to the average fuel efficiency value reported by the Japanese users shown in **Fig. 7**.

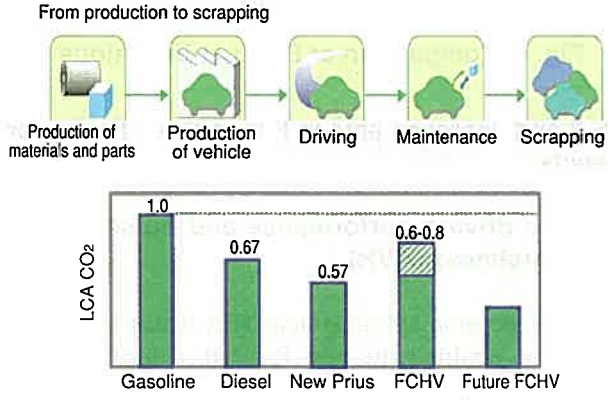

Calculation conditions: European official fuel efficiency/mileage: 150,000 km

Fig. 8 Example of LCA Analysis for New Prius

When compared with conventional vehicles, the ratio of CO_2 emissions during the driving process decreases due to the increase in efficiency. The LCA shows a CO_2 reduction effect of over 40%. Fuel cell hybrid vehicles (FCHV) show zero CO_2 emissions in the use process but generate high levels of CO_2 in the fuel and vehicle production processes. This means that the CO_2 emissions of these vehicles may exceed those of the newest gasoline HVs. As a result, technological breakthroughs to radically reduce CO_2 emissions during the production processes of FC parts and hydrogen fuel, and improvements in running efficiency are required before FC vehicles can be commercially implemented.

4.3 Cleanliness of exhaust emissions

Hybrid vehicles were also developed with the aim of leading the market for advanced environmental vehicles in terms of the cleanliness of exhaust emissions. All strong hybrid vehicles have attained the highest category of cleanliness regulations specified around the world, such as the Super Ultra Low Emission Vehicle (SULEV) category in the United States. This has been accomplished with engines that make use of electric power assist, which is one of the typical hybrid functions, in combination with exhaust treatment systems found on conventional vehicles. In addition, emissions during start-up have been reduced by enabling quick warm-up of the exhaust emission control catalysts, and by using a powerful generator as the engine starter. **Fig. 9** compares the cleanliness of the new Prius with the European diesel regulations (Euro4).

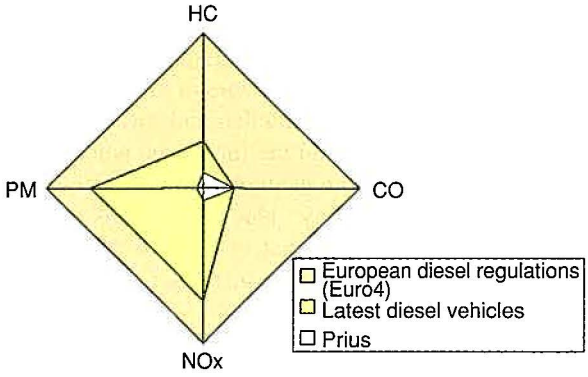

Fig. 9 Comparison of Exhaust Emissions

5. THS II and Improvements in Fun to Drive Performance Aspects

5.1 Vehicle driving performance and noise, vibration and harshness (NVH)

The next-generation hybrid system THS II that evolved from the THS, has enabled the new Prius to achieve a driving performance superior to conventional vehicles equipped with a 2.0 L engine. **Fig. 10** shows the driving force characteristics of the new Prius.

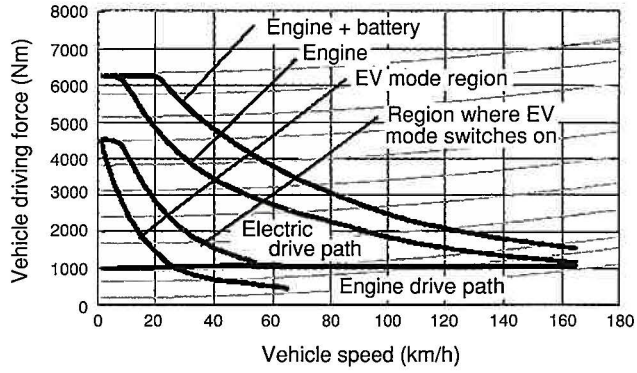

Fig. 10 Driving Force Characteristics of Prius

The details of the working principles of the THS II system are not described in this article. However, in the THS II, a considerable portion of the engine output is converted into electricity, and battery output is added in driving where a large driving force is required. The THS II does not use a mechanical transmission, but allows continuous use of the highest hybrid system outputs (engine output + battery output) in a wide region from medium to high vehicle speeds. The system has achieved a considerable improvement in passing acceleration performance, which is frequently used in the on-road environment. **Fig. 11** shows trends for passing acceleration in comparison with a conventional vehicle.

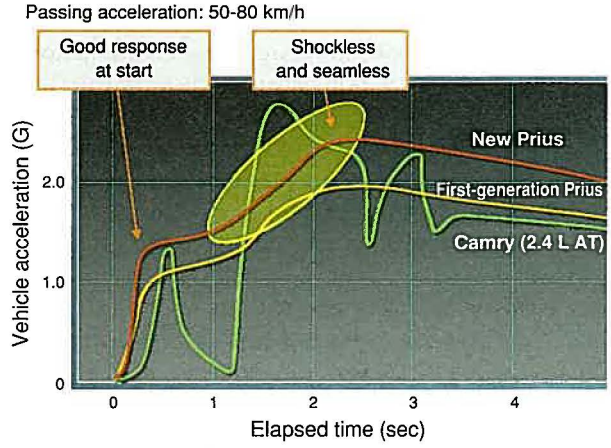

Fig. 11 Passing Acceleration Performance

Shockless and seamless acceleration is achieved by making use of stepless continuous system output where battery output assists a fast response electric motor. In the RX400h, the power of the electric drive system has been radically increased to cope with the 3.3 L V6 engine. This increase in power alongside the adoption of newly developed high-output batteries enables the RX400h to achieve a shockless and seamless acceleration performance superior to V8-engined SUVs in the same class up to the super fast region. Moreover, the quiet cabin during EV mode with the engine stopped and during cruising at optimum engine efficiency operation is an appeal point unique to a strong hybrid vehicle.

5.2 New functions of hybrid system

e-Four

In 2001, "e-Four," the world's first four-wheel drive system where the rear wheels are driven by an electric motor was adopted in the Estima Hybrid. e-Four is also an example of hybrid technology application. The dramatic improvement in electric driving power in the THS II described below has radically increased the driving power of the rear motor, improving the 4WD performance of the RX400h.

Hybrid VDIM

The RX400h uses the newly developed Vehicle Dynamic Integrated Management (VDIM). This system detects the behavior of the vehicle through a combination of the high-controllability ECB, the high-output front wheel driving motor with the brake function capable of performing regenerative cooperative control, the e-Four system that uses a high-output motor, and electric power steering (EPS) driven by a newly developed 42 V motor that receives power from the hybrid battery. VDIM controls these functions together with the Anti-Lock Brake System (ABS), Traction Control (TRC), and Vehicle Stability Control (VSC) in an integrated and seamless fashion to dramatically improve driving safety on slippery road surfaces.

External power supply function

In strong hybrids that have a high-output generator, such as those that use the THS II, external power supply is a versatile function that increases vehicle functionality and marketability. The motor-driven air conditioner mentioned in Section **4.2** contributes not only to improving fuel efficiency, but also to improving actual air conditioning performance aspects such as cooling down performance. In addition, the Estima Hybrid uses a high-power 100 V power supply system. This system, which is capable of supplying power outdoors, for a mobile office and even in disasters, is a function unique to hybrid vehicles.

6. Future Issues and Perspectives on Hybrid Technology

As pointed out in this article, hybrid vehicles cannot expect to gain popularity unless their product appeal, including fun to drive performance aspects, safety, and comfort are upgraded to complement revolutionary environmental performance. The vehicles must also carry a price tag appropriate to their appeal. **Fig. 12** shows that Toyota is positioning hybrid technology not as a separate category that competes with conventional internal combustion engine (ICE) and fuel-cell vehicles, but as a core technology to achieve dramatic improvement in the efficiency of vehicles themselves.

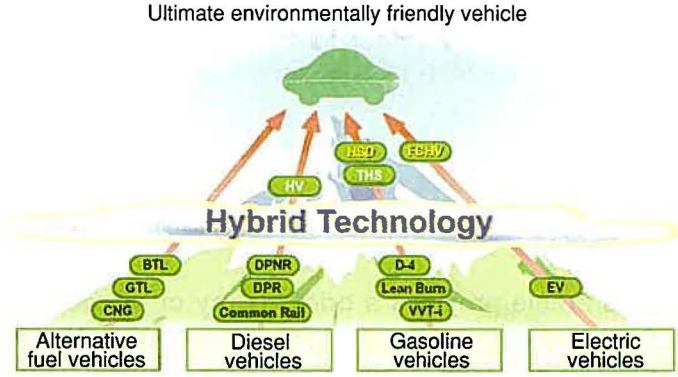

Fig. 12 Approaches to Accomplishing the Ultimate Environmentally Friendly Vehicle

Initially, some people considered hybrid vehicles as a temporary means to facilitate the transition from ICE vehicles to FCHVs. However, it is now realized that hybrid technology is indispensable for improving the efficiency of vehicles driven not only by gasoline engines, but also by diesel and alternative fuel engines, as well as in fuel-cell vehicles. As described in this article, the role of hybrid technology is not simply to enhance environmental performance. Hybrid technology is also expected to develop in the future as a technology that will increase the appeal of vehicles. Hybrid technology enables this by enhancing the driving performance, quietness and running feel of a vehicle by effectively using high-output, high-capacity batteries as an energy buffer, and by radically improving running stability with high-response electric motors. Toyota took on the challenge of implementing hybrid vehicles on a commercial basis as the first step toward sustainable mobility and in the spirit of the slogan "Today for Tomorrow." Since then, the company has exerted great efforts to advance the technology. We are hoping to continue playing a leading role in the approach to the ultimate environmentally friendly vehicle. This will entail, for example, furthering the evolution of vehicle and engine technology, combining bio-fuels and synthetic fuels, and applying hybrid technology to the fuel cell. Hybrid technology will be at the core of all these developments.

References

(1) Intergovernmental Panel on Climate Change (IPCC). "Third Assessment Report" (2001).
(2) Ministry of Land, Infrastructure and Transport. "2004 Fuel Efficiency by Vehicle Weight."
(3) Prius user fuel consumption figures on Japan fuel efficiency response website. Available at: http://www.response.jp/e-nenpi/.

The History of Hybrid Technology in Toyota

Shoichi Sasaki*

Abstract

This article provides a brief history of the development of hybrid technology in Toyota. In the 1970s, Toyota began development on a gas turbine hybrid vehicle. Subsequent in-house development followed on a motor, inverter and battery for electric and hybrid vehicles. Such effort led to the launch of the Coaster Hybrid, a small bus, in 1997, as well as the Toyota Hybrid System (THS) that powers the Prius, the world's first mass-produced hybrid car. New developments followed in the wake of the Prius with the THS-C mounted in the Estima minivan, and the THS-M in the Crown luxury sedan. In 2003, the second-generation Prius was equipped with the THS II boasting significantly improved power output. Hybrid technology is also utilized in diesel engine and fuel cell vehicles, which are sold as the Dyna HV and Toyota FCHVs on the market.

Keywords: *hybrid system, hybrid vehicle, history, engine, motor, inverter, battery*

1. Introduction

Toyota Motor Corporation is currently developing its hybrid systems as promising power trains for the future. This edition of the Toyota Technical Review introduces the latest accomplishments and the outlook for the future, but this article will first review the history of hybrid development at Toyota.

2. History of Hybrid Vehicle Development

The development of hybrid vehicles at Toyota began in the 1970s with a gas turbine hybrid vehicle.[1] The man chosen to lead the gas turbine development was the late Kenya Nakamura, Toyota's first chief engineer for the Crown and one of our great predecessors. At almost the same time, the company also participated in the planning of an Electric Vehicle Development Project under what was then the Ministry of International Trade and Industry.

Current hybrid vehicles combine a gasoline engine with an electric motor and battery, but the history of motor and battery development goes all the way back to those early days. Thereafter, development was suspended for a time, but motor and battery development continued at the Higashifuji Technical Center.

Meanwhile, research and development on motors was underway in the Machinery Group, where production equipment was developed, and those achievements were reflected in the RAV4 electric vehicle.

Early in the 1990s, measures to improve fuel economy in the future were being studied within Toyota. Recognizing that the serious limitations of electric vehicle batteries would make it difficult for a fully electric system to become the power train of the future, the company turned its attention to the feasibility of hybrid systems that combine a motor with a liquid-fuel engine. A variety of hybrid configurations were studied.

The Toyota Prius, the world's first mass-produced hybrid car, was developed on the basis of these studies, and in turn, it has ignited the development of a wide variety of hybrid systems. The two main focuses of the studies were whether to transmit motive power electrically or by conventional mechanical means and how to simplify the functioning of the brakes, air conditioning, and other systems that are affected when the engine is turned off to save fuel.

Special mention should also be made of the fact that development efforts since the Prius made its debut have reached the level where it is possible to mass produce what were once relatively expensive batteries, motors, and inverters.

Fig. 1 shows the history of hybrid vehicle development over the years. The main hybrid vehicles are described in the sections that follow.

2.1 Gas turbine hybrid [1]

The gas turbine hybrid vehicle shown in **Fig. 2** was exhibited at the Tokyo Motor Show in 1977. It was a configuration that took advantage of the compactness that is characteristic of a gas turbine engine.

The extremely compact configuration was achieved by increasing the revolution speed of the generator to match that of the gas turbine engine.

* Hybrid Vehicle System Engineering Div.

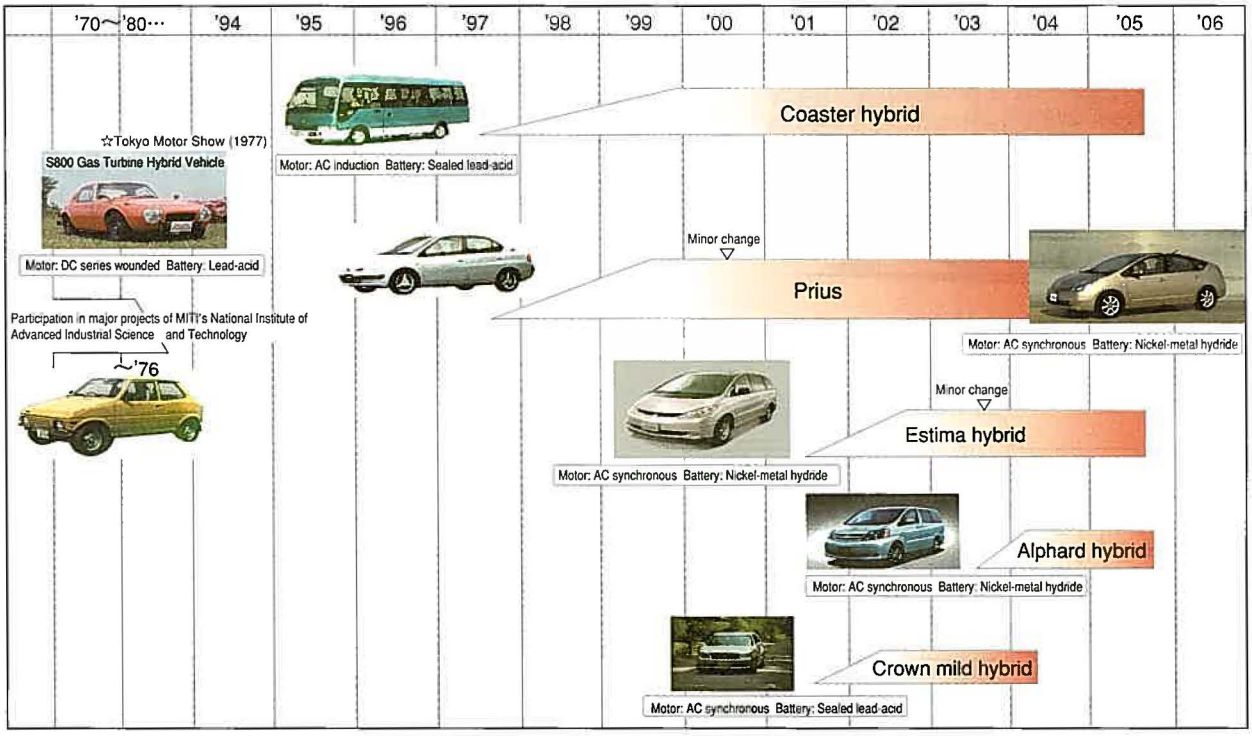

Fig. 1 History of Hybrid Vehicle Development at Toyota

Fig. 2 S800 Gas Turbine Hybrid Vehicle

Figs. 3 and **4** show the equipment layout and the system configuration. This was a series hybrid vehicle. (See Appended **Fig. 1** at the end of this article.) It featured a two-speed manual transmission and a compact motor.

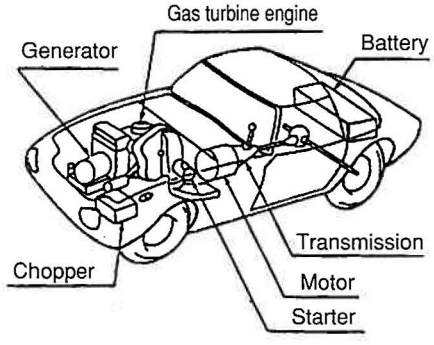

Fig. 3 Equipment Layout

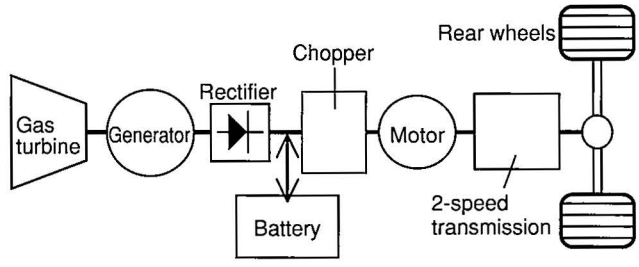

Fig. 4 Gas Turbine Hybrid System Configuration

2.2 Coaster hybrid

In 1997, Toyota developed and put on sale a compact hybrid bus based on the Coaster. It is intended for use by preschools, tourist attractions, hotels, and the like in transporting students and guests. It features a series hybrid layout that combines a 1.5-liter gasoline engine with an AC generator and AC induction motor to reduce exhaust gas emissions of hydrocarbons and NOx. **Figs. 5** and **6** show the vehicle and its system configuration.

The operating principle of the series hybrid requires that the engine power be converted into electricity, and that requires a generator and motor that are equivalent in power to the engine. But while the generator, motor, and control unit can be made bigger to give the hybrid superior power performance, there is a limit to how much the performance can be improved.

Fig. 5 Coaster Hybrid

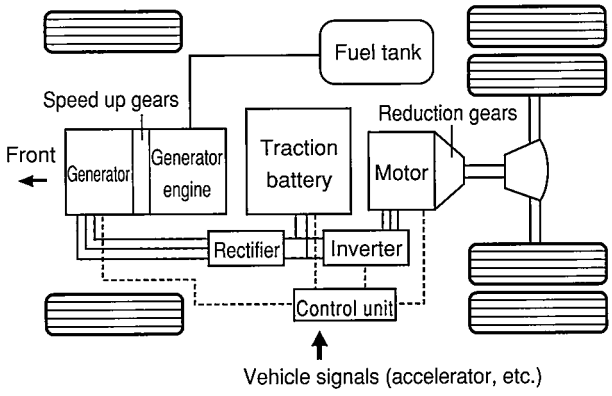

Fig. 6 Coaster Hybrid System Configuration

2.3 Prius [1][3]

Sales of the Prius, the world's first mass-produced hybrid car, began in December 1997. In keeping with the meaning of its name, "leading the way," the Prius, shown in **Fig. 7**, became the pioneer in mass production hybrid vehicle development.

Fig. 7 First-Generation Prius

It is worth reviewing the points that were the focus of system configuration studies for the Prius.

Four functions were identified as the focuses for achieving the main objective of better fuel economy: (1) engine starting and stopping, (2) regeneration, (3) running as an electric vehicle, and (4) the continuously variable transmission (CVT) function. Systems that combined these functions in various configurations were studied and compared to select the optimum configuration for a compact passenger car.

It should be noted that one of the factors in this selection process was that a similar study using an oil hydraulic motor was already studied within the company.

The basis for the hydraulic motor configuration was a 1971 SAE paper [2] by an engineer for TRW Automotive. It described a combination of a 1.6-liter gasoline engine, a 10-kilowatt alternator, a 22.5-kilowatt DC motor, and a thyristor chopper.

Due to physical limitations at the time, the paper described only bench tests, but the integration of technologies developed thereafter ultimately made the Prius hybrid system feasible for a passenger car. Of particular importance were the development of rechargeable batteries, the development of high-performance magnets typified by the neodymium magnet, improvements in power semiconductors, AC motor torque control technologies such as field-oriented control, the use of microcomputers to make on-board control devices more compact, and system simulation technologies.

The Prius underwent a minor change in 2000 before being put on the market in the United States and Europe. The vehicle was modified to meet the US emission regulation for a super ultra-low emission vehicle (SULEV) while also satisfying European performance requirements, thus proving its high potential in terms of both fuel economy and emissions performance.

Fig. 8 shows the configuration of the Prius hybrid system. The engine power is split by a planetary gear train, with one part going to the generator and the other being combined with the motor power and transmitted to the drive shaft. The power is distributed by controlling the speed of the generator. Because the driving force is the total of the motor power combined with a portion of the engine power, the system is designed so that the engine torque can be set to a relatively low value. This allows the engine to be turned off while the vehicle is in motion, so that it operates as an electric vehicle. The system is a series/parallel hybrid layout. (See Appended **Fig. 1**.)

The main components for the system were basically designed and manufactured internally, albeit with some cooperation from suppliers.

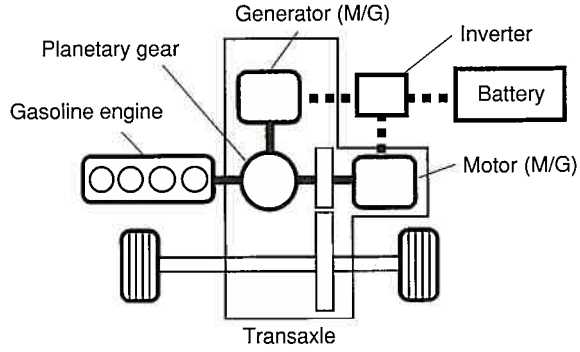

Fig. 8 Prius System Configuration (THS)

2.4 Estima hybrid [4]

The THS-C is a hybrid system that was developed for medium-to-large vehicles like minivans and uses a CVT. The system was installed in the Estima and went on sale in Japan in 2001. The vehicle is shown in **Fig. 9**, and the system configuration in **Fig. 10**. The system is a series/parallel hybrid layout (see Appended **Fig. 1**) comprising (1) a series system that uses the starter motor to generate electricity and the drive motor to propel the vehicle, and (2) a parallel hybrid layout made up of the engine and a power switching mechanism composed of the motor, CVT, and planetary gear train.

The use of the CVT allowed the electrical units to be made relatively small, which in turn made it possible to mount the hybrid system in an already heavy Estima-class vehicle. Another distinctive feature is the electric four-wheel drive system, which uses a dedicated motor to drive the rear wheels, enabling the vehicle to maneuver in a stable manner even on slippery roads. Just like the Prius, the Estima hybrid can turn its engine off while in motion and operate as an electric vehicle to improve its fuel economy to roughly twice that of a conventional car. The hybrid system's generator function also drives a 1,500-watt, 100-volt AC power supply, which can be used in emergencies or for powering a mobile office.

Fig. 9 Estima Hybrid

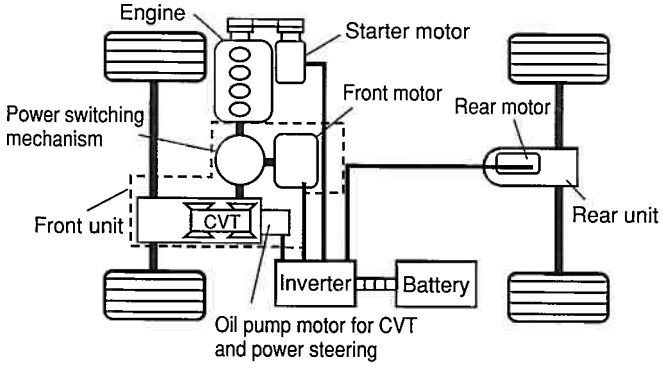

Fig. 10 Estima Hybrid System Configuration (THS-C)

The THS-C system was also used in the Alphard hybrid in 2003.

2.5 Crown mild hybrid [5]

The mild hybrid system (THS-M) uses a 42-volt power system and was developed as a system that could be applied to a wide range of models with only minimal changes to the vehicles themselves. It was put on the market in August 2001, in the Crown, shown in **Fig. 11**.

Fig. 12 shows the mild hybrid system configuration. It is a parallel hybrid layout. (See Appended **Fig. 1**.)

In this configuration, a motor-generator that is linked to the engine crankshaft by a belt replaces the alternator that is used in a conventional vehicle. Because the motor-generator is controlled electronically, the environmentally friendly, yet comfortable vehicle can make a smooth transition from a full stop into motor-driven take-off, regenerate the energy of braking, and ensure air conditioning function even when it is stopped, while reducing fuel consumption and emissions.

Fig. 11 Crown Mild Hybrid

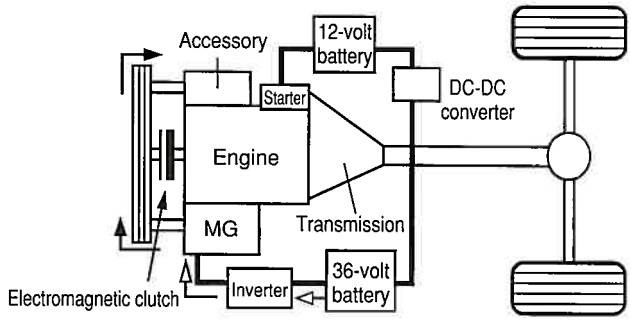

Fig. 12 Crown Mild Hybrid System Configuration (THS-M)

2.6 New Prius [1]

The new Prius that resulted from a full model change in 2003 features even better fuel economy and a remarkable improvement in power performance. The vehicle's weight has been reduced by using aluminum for some body parts, and the

power performance has been enhanced by increasing the power of the engine, generator, and motor. The vehicle is shown in **Fig. 13**.

The power of the generator, motor, and inverter was increased without making the units larger, allowing the system voltage to be increased from 288 volts to 500 volts.

Increasing the voltage of a motor or inverter generally allows the unit to be made smaller, but by contrast, a battery tends to increase in size. This problem was solved by using a booster system that allows the battery to be made more compact even as the motor power is increased by using a higher voltage.

The booster system configuration is shown in **Fig. 14**.

Fig. 13 New Prius

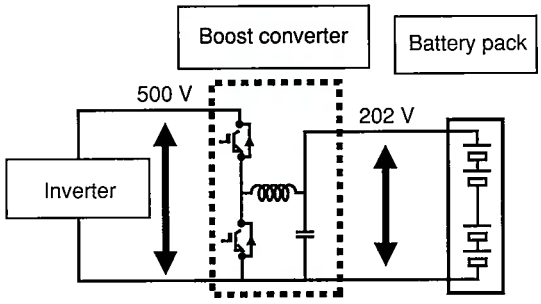

Fig. 14 Booster System Configuration

The boost converter is housed in the same unit with the inverter for the generator and motor. Nonetheless, the unit's size is equivalent to that of the unit used in the original Prius, despite the increase in power.

2.7 Diesel hybrid [1]

Toyota also developed a diesel hybrid system for small trucks and installed it in the Dyna in November 2003, as shown in **Fig. 15**. It is a parallel hybrid layout (see Appended **Fig. 1**) that combines a motor-generator with a 4-liter common-rail diesel engine. The system achieved a 25% CO_2 reduction as compared to a conventional vehicle in the domestic mode. The combination of hybrid technology and engine exhaust technology also dramatically reduces NOx and particulate emissions.

Fig. 15 Dyna Hybrid

2.8 Fuel cell hybrid

Limited sales of the Toyota FCHV, a fuel cell hybrid vehicle that uses hydrogen fuel, began in Japan and the U.S. in December of 2002. The current focus in Japan is on lease sales to government-related bodies, local governments, and companies concerned with energy. The vehicle is shown in **Fig. 16**.

This hybrid system combines fuel cell stacks and rechargeable batteries to achieve the conceptual counterpart of a gasoline vehicle.

The vehicle's performance is demonstrated by a fuel cell stack output of 90 kilowatts, a maximum speed of 155 km/h, and a cruising range of 300 kilometers.

Fig. 16 Kluger Fuel Cell Hybrid Vehicle

This hybrid technology has also been applied to a fuel cell bus.

The fuel cell hybrid bus, or FCHV-BUS2, was operated as a city bus on regular routes in Tokyo from August 2003, until December 2004, as shown in **Fig. 17**. In 2005, it is being used to ferry visitors between attractions at the Aichi Expo.

Fig. 17 Fuel Cell Hybrid Bus in Operation (at Tokyo Station, Yaesu Exit)

3. Conclusion

This article has reviewed the history of hybrid technology development at Toyota. That history can be divided into two periods, as described below.

(1) Before the Prius

Development was focused on the series hybrid systems seen in the gas turbine hybrid and Coaster hybrid. These systems just added a generator and motor to the gasoline engine, essentially borrowing electric vehicle technology to make the conversion to hybrid comparatively simple. But the physical form of the components and the improvement of power performance were issues that still had to be addressed.

Research and development work on the elements of a hybrid system, such as the battery, the motor, and the control unit, continued at the Higashifuji Technical Center and in the Machinery Group. The basic technologies for the current generation of hybrids were developed during this period.

(2) From the Prius to the present

Starting with the Prius, Toyota has gone on to develop a variety of hybrid vehicles. The original Prius system, the THS, was developed for passenger cars. The Estima system (THS-C) incorporates a CVT for medium-to-large vehicles like minivans. The Crown system (THS-M) is a hybrid configuration designed to minimize the changes to existing vehicles. Research and development into the optimum hybrid system is still being promoted, and a system has been established to develop and manufacture the main components internally at Toyota.

The development of the fuel cell hybrid vehicle as the power train of the future is also being promoted.

References

(1) T. Yaegashi. "The History of Hybrid Technology." *Auto Technology*. FISITA (2005).

(2) G. H. Gelb et al. "An Electromechanical Transmission for Hybrid Vehicle Power Trains—Design and Dynamometer Testing." *SAE Paper* 710235 (1971).

(3) S. Sasaki et al. "Toyota's Newly Developed Electric-Gasoline Engine Hybrid Powertrain System." *EVS14 Proceedings* (1997).

(4) H. Oba et al. "Development of Minivan Hybrid System with Continuously Variable Transmission." *JSAE Autumn Convention Proceedings* (2001).

(5) T. Teratani et al. "Development of Toyota Mild-Hybrid System." *Toyota Technical Review* Vol. 52 No. 1 (2002) pp. 48-53.

Author

S. SASAKI

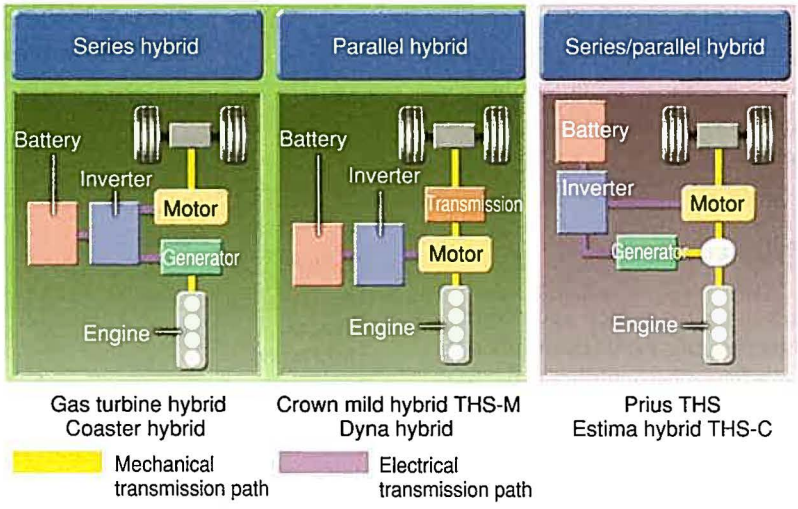

Appended Fig. 1 Classification of Hybrid Systems

Introducing the Lexus RX400h

Osamu Sadakata*
Yasuhiro Ikuta**

Abstract

This article introduces the new RX400h, the Lexus brand's first hybrid vehicle, launched by Toyota Motor Corporation in the spring of 2005. Developed under the Hybrid Synergy Drive (HSD) concept, the second-generation Toyota Hybrid System that powers the new RX400h model is a more powerful version of the hybrid system adopted on the second-generation Prius. More specifically, improvements include motors with higher power and speed, a higher voltage power supply to drive the motors, and greater motor torque realized by incorporating a planetary type reduction gear on the motor rotational shaft. The nickel-metal hydride batteries essential to hybrid vehicles have also been newly developed and made more compact. Furthermore, Vehicle Dynamic Integrated Management (VDIM) has been employed for the first time in an all-wheel drive (AWD) system, and a motor with increased power output is used for driving the rear wheels. The RX400h is therefore a luxury hybrid SUV for the 21st century that simultaneously offers superb environmental and dynamic performance.

Keywords: *HSD, THS, reduction, RX400h, E-Four, AWD, VDIM, nickel-metal hydride battery*

1. Introduction

A hybrid vehicle is defined as a vehicle that is driven by two or more types of power sources. Its history goes back one hundred years to September 23, 1905, when an engineer by the name of H. Piper filed for a patent on a hybrid vehicle in the United States. Some 90 years later, Toyota Motor Corporation led the world by developing the Toyota Hybrid System (THS). Subsequently, the THS was installed in a dedicated hybrid vehicle called the Prius, which was launched in December 1997. The dream hybrid vehicle that was thought to be unfeasible for mass production thus became an everyday item for anyone to own even before the turn of the century.

2. Evolution of the Toyota Hybrid System

Developed with environmental performance (ecological cleanliness) in mind, the aim when creating the THS installed in the first-generation Prius was to produce a car with twice the fuel economy of conventional vehicles. The resulting fuel economy of 28 km/L astonished the world by exceeding what was considered to be feasible.

Later, Toyota developed the THS-C hybrid system that uses a mechanical continuously variable transmission (CVT), and an electric four-wheel drive (E-Four) system that uses an electric motor to drive the rear wheels. These systems were installed in the Estima Hybrid and Alphard Hybrid sold in Japan.

Furthermore, THS-M, which is a THS-based mild hybrid system that features an idle stop function, was developed to power the Japanese market Crown. Thus, the reputation of Toyota hybrids as vehicles with excellent fuel economy was established (**Table 1**).

Table 1 First-Generation THS: Innovations in Environmental Performance

	Vehicle application	Features
THS	First-generation Prius	Environmental performance (ecological cleanliness)
THS-C + E-Four	Estima Alphard	2.4 L engine combined with CVT hybrid. Driving performance improved by use of E-Four system.
THS-M Mild hybrid	Crown	Mild type THS Includes idle stop function, motor assist during vehicle start, and energy recovery function during deceleration.

Toyota launched the HSD concept in 2003, six years after the introduction of the first-generation Prius. The second-generation hybrid system was developed under this concept and installed in the new Prius model.

* Lexus Development Center
** Hybrid Vehicle System Engineering Div.

The epoch-making second-generation hybrid system developed under the HSD concept simultaneously realizes both the greatest merit of the THS (i.e., ecological cleanliness) as well as power, features that are generally thought to be contradictory.

Then, in the spring of 2005, Toyota developed a new, high-power hybrid system for sport utility vehicles (SUVs) under the HSD concept, and installed it in the RX400h (**Table 2**). This system meets the requirements of SUVs, which demand power and agility in spite of having a large body size and weight.

Table 2 Second-Generation THS: HSD that Realizes Both Environmental Performance and Power

	Vehicle application	Features
HSD (THS II)	Second-generation Prius	A booster circuit increases the battery voltage to 500 V to drive the vehicle, while realizing high levels of both environmental performance and power.
HSD (THS II + AWD)	RX400h	A reduction gear amplifies the torque of the high-speed motor. Voltage is 650 V to produce high power, and AWD is combined with VDIM to improve driving performance.

3. Central Concepts of Development

3.1 Basic policies

Toyota makes cars based on the concept of "Today for Tomorrow." Literally, this means to make cars not only for today, but also with tomorrow in mind. In other words, Toyota aims to build cars by taking a hard look at the requirements of the future. These cars should not damage or pollute nature (i.e., they should "zero-nize" negative impacts) but they should also possess performance levels that enhance the spiritual happiness of the customer (i.e., they should "maxi-mize" the enjoyment of driving).

Lexus makes cars based on the concepts "The Pursuit of Perfection" and "Make the Most of Every Moment." This means to constantly strive to make cars by pursuing the essence of high quality while making a profound impact on the customer through their contact with Lexus. Specifically, Lexus emphasizes various performance features using the keyword IDEAL (I: impressive, D: dynamic, E: elegant, A: advanced, and L: lasting). The purpose is to create ideal products with the highest level of performance that exceeds the expectations of Lexus users.

The RX400h is Toyota's first hybrid SUV. At the same time, it is the first Lexus hybrid vehicle sold in the United States and Europe. In other words, this model incorporates development activities and car-making processes in accordance with the basic development policies of both Toyota and Lexus.

Photo 1 New Model RX400h

3.2 How the RX400h integrates the Maxi-mize, IDEAL, and Zero-nize concepts

Maxi-mize and IDEAL: The basic functions of an automobile are running, turning, and stopping. The developmental aims for the RX400h were to create a vehicle capable of running more comfortably than other SUVs, turning confidently on any type of road surface, and stopping with plenty of room to spare. At each stage, the developers themselves checked whether the performance features were IDEAL. Third-party evaluations were also conducted to enable the development to constantly pursue the essence of quality without becoming self-complacent.

Zero-nize: The world's best exhaust emission control technology was applied to clean environmentally damaging exhaust gases. The RX400h aims to meet the most stringent regulations in any country or region around the world. In terms of fuel economy, the target was to approximately double the fuel economy of the best SUV in the same class.

4. Features of the RX400h

4.1 Realizing the Maxi-mize concept

Outstanding acceleration performance and fuel economy based on new sensibilities

The RX400h is powered by a combination of a hybrid system that has been newly developed for the RX400h under the HSD concept, and an electric AWD system that has a dramatically increased power output. This combination clearly distinguishes the RX400h from conventional gasoline engine vehicles. As a result, the RX400h achieves a shiftless, outstanding performance to accelerate smoothly and steadily up to maximum speed, while maintaining the fuel economy of a compact car.

In terms of acceleration, the 0 to 100 km/h performance of the RX400h is the fastest in its category of mass production SUVs (excluding turbocharged vehicles) (**Fig. 1**).

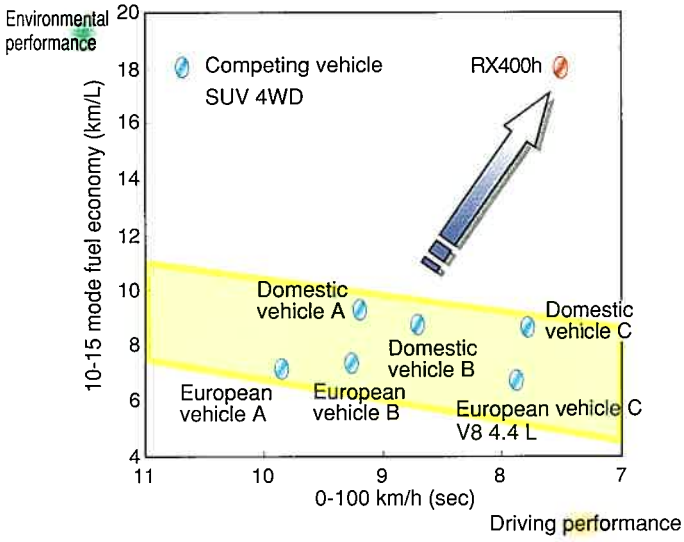

Fig. 1 Fuel Economy (Japan) and Acceleration Performance

Drivability and driving stability to bring out the fun of driving

To support the power train that delivers outstanding dynamic performance, the underbody rigidity and the suspension specifications of the vehicle have been completely revised. Using the structure of the base gasoline model as a reference, body rigidity has been optimized through the use of the latest computer simulation technology. The basic design of the suspension was created on test courses and then optimally tuned to suit the road and traffic conditions of various countries. To do so, permits were obtained in the target countries so that the vehicle could be driven on autobahns and country roads in Europe, and on freeways and city streets in the United States.

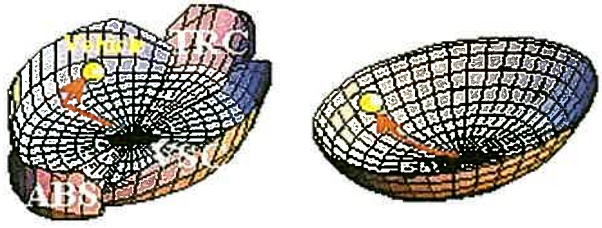

Conventional control VDIM control

Fig. 2 Representative Diagram of Vehicle Control

In addition to these accomplishments, Toyota has applied Vehicle Dynamic Integrated Management (VDIM) for the first time in a four-wheel drive (4WD) system, to stabilize the vehicle before critical behavior is reached (**Fig. 2**). Consequently, the system is able to bring the best out of the high level of dynamic performance that the RX400h provides. Together with shiftless, torqueful acceleration that rises instantly, the RX400h embodies the fun of driving through seamless control, and an astonishing level of drivability and driving stability that the user can enjoy.

During a test drive meet for the media, an automobile journalist was asked about his impressions. He blurted out, "Quick, wow, and impressive!" This exclamatory phrase suggests that the vehicle not only offers quick acceleration, but has also achieved the highest level of product quality that exceeds the expectations of our customers. In other words, the RX400h achieves the features summarized by IDEAL.

4.2 Realizing the Zero-nize concept

High fuel economy and clean exhaust gas

With the reduction of CO_2 emissions in mind, the RX400h has achieved the world's highest level of fuel economy[*1] in its class, equivalent to a compact vehicle. The RX400h has surpassed the "2010 Fuel Economy Standards + 5%" (**Photo 2**) established by the Ministry of Land, Infrastructure and Transport in Japan by a wide margin.

In terms of exhaust gases, the RX400h has drastically reduced nitrogen oxides (NOx) and non-methane hydrocarbons (NMHC) to meet the most stringent regulations[*2] in any country or region around the world. In Japan, this vehicle has earned four stars (**Photo 2**).

Photo 2 Certificates of Compliance

[*1] Japan: 17.8 km/L (10-15 mode value as inspected by the Ministry of Land, Infrastructure and Transport)
US: 29 mpg/AWD (combination label value as inspected by the EPA)
Europe: 8.1 L/100 km combination fuel economy

[*2] Japan: 2005 standard exhaust gas 75% reduction level
US: California Super Ultra Low Emission Vehicle (SULEV)
Europe: Step IV

4.3 Uncanny levels of quietness

Normally, the engine of the RX400h stops when the vehicle itself stops. Depending on the road conditions and accelerator effort, the engine may also stop when the vehicle is in motion, allowing the vehicle to continue running using the electric motor alone. The state in which this happens is called the "EV driving mode." Because the engine does not produce any sound or vibration in this mode, a driver operating a hybrid vehicle for the first time experiences a soundless and vibrationless world. Initially, this may be a somewhat uncanny experience, but this feeling is soon replaced by one of delight. It is truly a quiet world that enables the users of the vehicle to enjoy an incredible sensation unmatched in other cars.

4.4 Appearance and style

The appearance of the RX400h body has not been differentiated from the base RX330 (RX300) model that is already on sale. Instead, the basic completed interior and exterior design of the vehicle was created to be suitable for a new-generation hybrid SUV, under the concept of harmonizing the innovation and power inherent to hybrids (**Photo 3**).

Photo 3 RX400h

5. Hybrid System

The individual systems (**Photo 4**) that comprise the new hybrid system developed under the HSD concept for the RX400h are described in detail elsewhere. This section presents an overview of the system from the perspective of the vehicle.

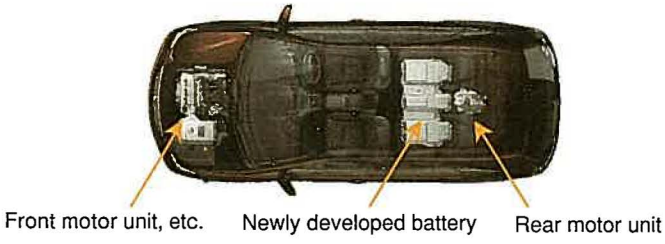

Photo 4 Unit Installation Diagram

5.1 HSD and AWD

The new hybrid system developed under the HSD concept for the RX400h is based on the second-generation hybrid system adopted on the current Prius. The basic system has been combined with a large displacement, 3.3 L engine to create a system configuration that provides the high power and torque required by an SUV (**Photo 5**).

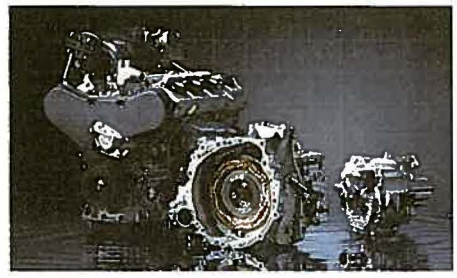

Photo 5 3MZ Engine and Hybrid System Newly Developed Under HSD Concept

Generally, motor size increases in accordance with the amount the power and torque produced. However, because the engine compartment in which the motor is installed has a fixed capacity, there is a limit to how far the size of the motor can be increased.

Therefore, on the RX400h, the motor drive voltage has been raised to a maximum of 650 V, to achieve a power output of 123 kW. The speed of the motor itself has been increased to 12,400 rpm, and the 333 Nm of motor torque is amplified 2.478 times by a newly developed, planetary type reduction gear that is built into the transaxle. As a result, a compact and high power output hybrid system has been developed under the HSD concept to deliver ample power and torque in a large SUV (**Photo 6**).

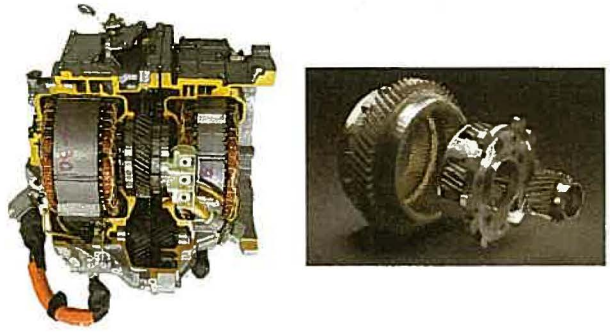

Photo 6 Drive Motor (Left) and Reduction Gear (Right)

Furthermore, a high power output and high torque (50 kW/130 Nm) rear motor (**Photo 7**) is used to drive the rear wheels of the RX400h. This motor coordinates with the front drive motor in order to optimize the rear drive force in accordance with driving conditions, such as at start, during acceleration, or when driving uphill. Furthermore, AWD is incorporated in the VDIM system to stabilize the vehicle behavior, while allowing the driving performance of the RX400h to make a quantum leap forward.

Photo 7 Appearance of Unit with Built-In Rear Motor and Differential Gear

5.2 New nickel-metal hydride batteries

To realize a spacious and flat luggage floor, which is an important part of the product appeal of SUVs, and a variety of seat arrangements, newly developed nickel-metal hydride batteries have been installed in the space between the rear seat cushion and the fuel tank located under the floor (**Photo 8**).

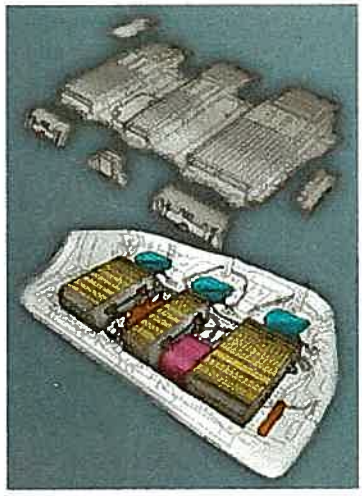

Photo 8 Installed View of Newly Developed Nickel-Metal Hydride Batteries

Based on the prismatically shaped nickel-metal hydride batteries housed in a plastic battery case and used on the Prius, the newly developed nickel-metal hydride batteries have been made 30% more compact by volume. Considering the harsh operating conditions of SUVs, the batteries have been divided into three groups, with each group provided with a cooling fan in order to enhance cooling performance. The batteries themselves use metal cases that provide a high level of cooling efficiency. As a result, these compact and efficient nickel-metal hydride batteries boast a maximum output of 45 kW.

6. On-Vehicle Equipment

6.1 Equipment unique to hybrid vehicles

(1) Power meter and multi display

The power meter is located at the left end of the row of three instruments. It is provided in place of a tachometer and indicates in kilowatts (kW) the amount of power consumed by the vehicle during driving. The driver can improve fuel economy by going easy on the accelerator pedal and making sure that the indicator on the power meter does not move too high. In addition, the power meter allows the driver to monitor the regenerative function, i.e., whether the vehicle is recovering energy (**Photo 9**).

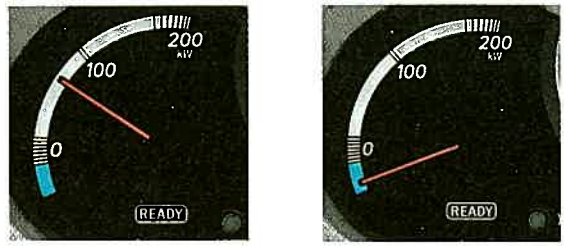

Photo 9 Power Meter: Power Output Display (Left) and Regenerative Display (Right)

The multi display is located at the center of the row of three instruments, at the bottom of the speedometer. The driver can choose to display various items of information, such as the energy flow of the hybrid system, current fuel economy, mileage, and outside temperature. If a door is ajar or the parking pedal brake has not been released, a warning and an alarm will interrupt whatever information is currently being displayed (**Photo 10**).

Photo 10 Display Example of Row of Three Instruments and Multi Display (Some Japanese Specifications Shown)

(2) Energy monitor

The multi display in the speedometer (standard for all models) or (optional) Electro Multi Vision (EMV) displays the appropriate option from 1 to 4 below, as well as either option 5 or 6 at the same time (**Photos 11** and **12**).

(1) The vehicle is running only on the motor using the battery (EV driving mode)
(2) The vehicle is running on the engine using gasoline
(3) The vehicle is running on both types of energy
(4) The battery is being charged (regenerative function)
(5) The vehicle is running in the front-wheel drive mode
(6) The vehicle is running in the four-wheel drive mode

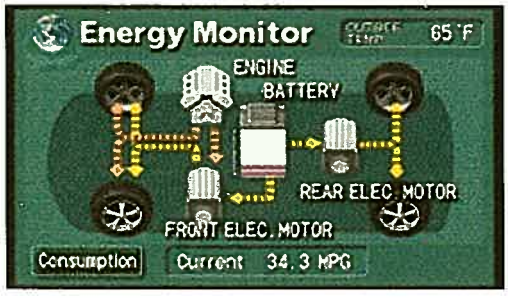

Photo 11 Energy Monitor Display Example (Full Acceleration in AWD Mode)

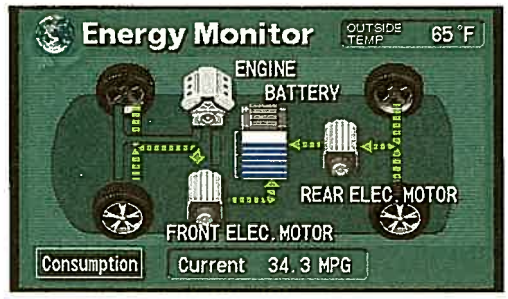

Photo 12 Energy Monitor Display Example (Regenerative Function Display)

6.2 Comfort equipment (Japanese specifications)

Various items of comfort equipment are provided with the convenience of the customer in mind. These include the following:

1. Power meter
2. Multi display with selector switch on steering wheel
3. VDIM
4. High-Intensity Discharge (HID) headlights (with intelligent Adaptive Front Lighting System (AFS), depending on model grade)
5. Humidity control air conditioner with separate right-left controls
6. SRS airbags (for driver and front passenger)
7. Cruise control
8. High performance sound insulation glass
9. Accessory power socket for AC100 V, 100 W (depending on model grade)
10. Seat heaters (on specifications with genuine leather seats)

7. Conclusions

The RX400h, the first hybrid SUV from the Lexus brand, encapsulates the enjoyment of a truly powerful driving experience, while maintaining the environmental performance of previous Toyota hybrid models. Under the IDEAL keyword, the individual performance features of this vehicle have created a level of quality that far exceeds the expectations of the customer. **Table 3** shows the specifications of this system.

Starting with the readers of this article, the authors would like as many people as possible to actually drive the RX400h and experience for themselves the brand new world of the hybrid SUV.

Table 3 Hybrid System Specifications

Item		RX400h (THS II)	New Prius (THS II)	Estima HV (THS-C)	Alphard HV (THS-C)
Vehicle model code		DAA-MHU38W	ZA-NHW20	ZA-AHR10W	ZA-ATH10W
Hybrid system*1		Fr: parallel/series Rr: series	Parallel/series	Fr: parallel Rr: series	
Engine	Model	3MZ-FE	1NZ-FXE	2AZ-FXE	
	Type	Water-cooled, V6, transversely mounted	Water-cooled, inline 4, transversely mounted	Water-cooled, inline 4, transversely mounted	
	Engine displacement (cc)	3311	1496	2362	
	Max. power output (kW(PS)/rpm)	155(211)/5600	57(77)/4500	96(131)/5600	
	Max. torque (N·m(kg·m)/rpm)	288(29.4)/4400	115(11.7)/4200	190(19.4)/4000	

*1 See attached diagram 1, page 15.

Item			RX400h (THS II)	New Prius (THS II)	Estima HV (THS-C)	Alphard HV (THS-C)
Motor	Fr	Transaxle model	P310	P112	P210	
		Max. power output (kW(PS)/rpm)	123(167)/4500	50(68)/1200 to 1540	13(17.7)/1130 to 3000	
		Max. torque (N·m(kg·m)/rpm)	333(34)/0 to 1500 (Output shaft: 825(83)/ 0 to 1500)*2	400(40.8)/ 0 to 1200 (same as output shaft)	110(11.2)/0 to 1130	
	Rr	Transaxle model	Q211		Q210	
		Max. power output (kW(PS)/rpm)	50(68)/4610 to 5120		18(24.5)/1910 to 2500	
		Max. torque (N·m(kg·m)/rpm)	130(13.3)/0 to 610		108(11.0)/0 to 400	

*2 The motor reduction mechanism amplifies torque by approximately 2.48 times and transmits it to the output shaft.

Item		RX400h (THS II)	New Prius (THS II)	Estima HV (THS-C)	Alphard HV (THS-C)
System*3	Max. power output (kW(PS)/vehicle speed in km/h)	200(272)/ 100 or more	82(111)/ 85 or more		
HV battery	Type	Nickel-metal hydride	Nickel-metal hydride	Nickel-metal hydride	
	Rated voltage	288 V (3-group battery)	201.6 V	216 V	
	Number of modules	9.6 V × 30	7.2 V × 28	7.2 V × 30	
	Capacity (Ah)	6.5	6.5	6.5	
Boost converter (in inverter assembly)	Boost voltage	288 V←→650 V	201.6 V←→500 V		

*3 Power output and torque produced by system consisting of engine and motor.

Authors


O. SADAKATA Y. IKUTA

Development of Hybrid System for SUV

Akihiro Kimura*

Abstract

The Toyota Hybrid System (THS) combines a gasoline engine and an electric motor, and has been installed in the Prius, which was introduced in 1997 as the world's first mass-produced hybrid passenger car. The Prius was vastly improved in 2003, and has since gained status as a highly innovative and practical vehicle. Combined with a V6 engine, the THS further evolved into a hybrid system for SUVs in 2005, and has been installed in the RX400h set for world launch. This article will describe the new THS achieving V8 engine power performance.

Keywords: *hybrid, power performance, 4WD*

1. Introduction

Faced with growing public concern about atmospheric contamination and global warming by carbon dioxide (CO_2), automobile manufacturers are now required to further reduce automobile exhaust gas and CO_2 emissions through improvement of fuel efficiency. A hybrid system that combines an internal combustion engine and an electric motor is recognized as a very effective means for satisfying the above requirements. Toyota developed in 1997 the world's first mass-produced hybrid system, called the Toyota Hybrid System (THS). Since then, vehicles incorporating a hybrid system (hybrid vehicles) have rapidly expanded the market (**Fig. 1**) and thus contributed to conservation of the global environment. However, only a limited number of hybrid passenger vehicle models are available today, making it difficult for some customers to find the models they need. Most hybrid systems produced today are installed in small-sized vehicles. Their performance is insufficient for driving the type of heavy-duty vehicles that emit a larger amount of CO_2 than small- and medium-sized vehicles. This article presents and discusses a new hybrid system that Toyota has developed by further improving the Toyota Hybrid System II (THS II) in order to expand the use of hybrid systems to sports utility vehicles (SUVs).

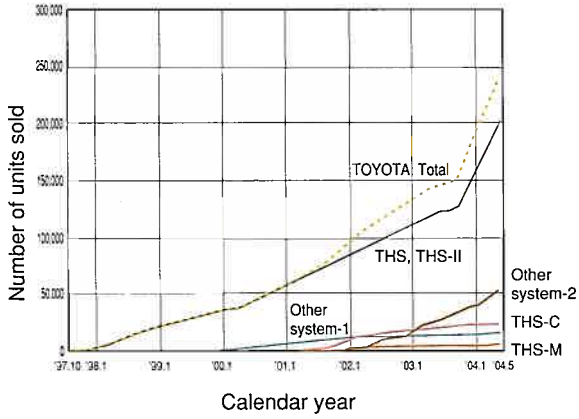

Fig. 1 Sales Volume

2. Toyota Hybrid System II for SUV

2.1 Objective of the development

In 2003, Toyota completely redesigned the Prius and integrated the THS II into the new model. The THS II was superior to the THS in terms of fuel efficiency, exhaust gas reduction performance, and power performance. In this article, the THS II for the Prius is called THS II (Prius). The THS II for SUVs is Toyota's latest hybrid system (and called the THS II (SUV) in this article) and was developed by further improving the fuel efficiency and power performance of the THS II (Prius). It was developed with the objective of expanding the use of hybrid systems in SUVs and other heavy-duty vehicles, thereby sweeping away the conventional wisdom in the market, that the acceleration performance of hybrid vehicles is lower than that of conventional gasoline-driven vehicles. Another objective of the development was to introduce a hybrid system that can be installed in a front-engine front-wheel-drive (FF) vehicle of the heaviest class, and then to serialize the system in the future so that it can also be mounted on any medium- or small-sized FF vehicle. The major specifications of the system components are shown in **Table 1**.

* Hybrid Vehicle System Engineering Div.

Table 1 Specification of THS II for SUV

	Item	THS II (SUV)	THS II (Prius)
Engine		3.3 L gasoline	1.5 L gasoline
	Max. output (kW/rpm)	155/5600	57/5000
	Max. torque (Nm/rpm)	288/4400	115/4200
Front motor		Permanent magnet motor	Permanent magnet motor
	Max. output (kW/rpm)	123/4500	50/1200-1540
	Max. speed (rpm)	12400	6400
	Max. torque (Nm/rpm)	333/0-1500	400/0-1000
Rear motor		Permanent magnet motor	–
	Max. output (kW/rpm)	50/4600-5100	–
	Max. speed (rpm)	10500	–
	Max. torque (Nm/rpm)	130/0-610	–
Battery		Nickel-metal hydride	Nickel-metal hydride
	Max. output (kW/rpm)	45	25
	10 second rated output (kW)	36	21

2.2 Engine

Increasing engine output is most important for improving the power performance of a vehicle. A 3.3 L, V6 engine was designed so that it could drive even a heavy-duty SUV with a FF system. This engine was basically the same as the RX330 engine, with the exception of intake and exhaust systems that were redesigned for further reduction of exhaust emissions. The variable valve timing (VVT) of the new engine was also changed to decompress the engine, thereby minimizing engine vibration during starting and stopping.

2.3 Front motor

As in the case of the THS II (Prius), the THS II (SUV) uses a permanent magnet motor. Since the motor produces most of the driving power as shown in **Fig. 2**, a large-torque, high-power motor is required to increase the power performance. On the other hand, due to limited allowances for space and weight a vehicle does not allow the mounting of a large electric motor. The following two techniques enabled THS II (SUV) to resolve the above contradictory problems. One is use of a system operating voltage higher than the rated voltage of the battery. Using the same technique as that used in the THS II (Prius), the electric power voltage from the battery is boosted to drive the motor and generator. For the THS II (SUV), the power density has been enhanced further by boosting the voltage of the motor and generator from 500 V in the THS II (Prius) to a maximum of 650 V. The other is installation of a gear for reducing motor speed. This speed reduction gear allows the motor to run at a high speed with a low torque value, even when the transmission of large output torque is required to the drive shaft. **Figs. 3** and **4** shows the motor specifications. The THS II (SUV) has an output power 2.5 times and a power density 3 times higher than those of the THS II (Prius).

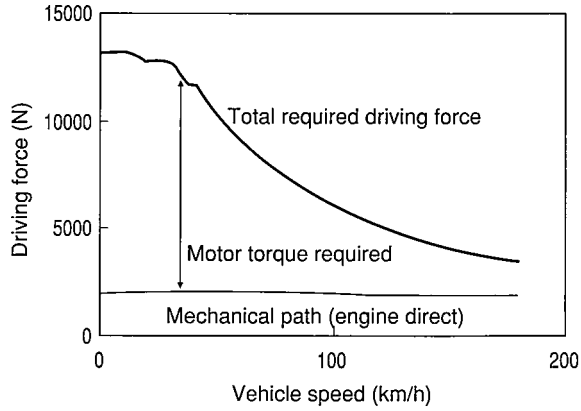

Fig. 2 Vehicle Driving Force

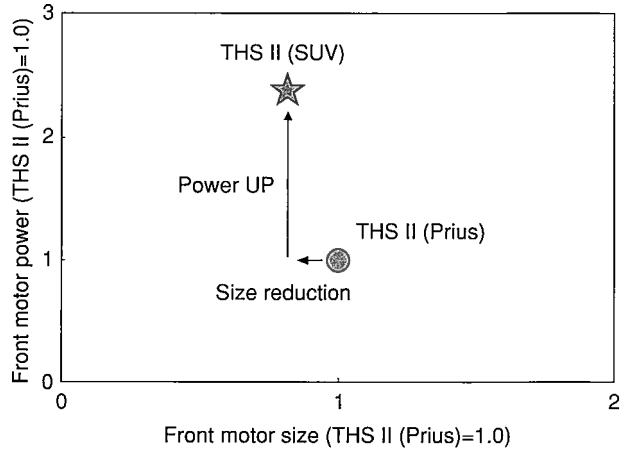

Fig. 3 Motor Size

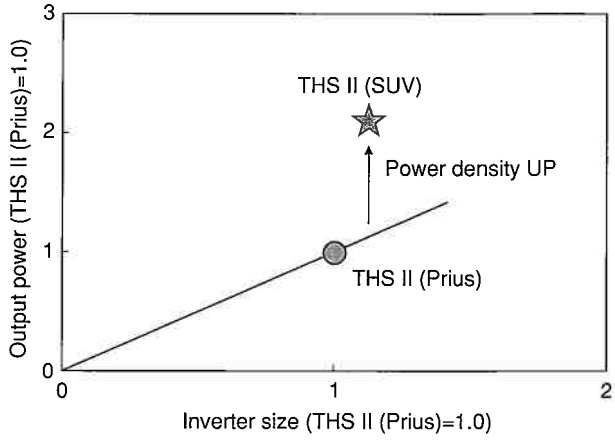

Fig. 4 Inverter Size

2.4 Generator

The generator is a permanent magnet motor with a maximum operating voltage of 650 V. An output torque larger than that in the THS II (Prius) was required for the generator to be compatible with the output torque of the 3.3 L, V6 engine, which would usually cause both the generator dimensions and weight to increase. In designing the THS II (SUV), the torque margin of the generator for engine output torque was reduced as much as possible to minimize the generator dimensions and weight. The generator is also required to supply sufficient electric power to drive the front motor and the rear motor, as will be discussed later. To meet this requirement, the generator has been designed so that it runs at a higher speed than the THS II (Prius) generator. For the generator, the same material, magnetic steel sheet, and the same coil turns as those for the front motor are used in order to reduce the cost and the number of parts. The overall dimensions of the THS II (SUV) generator per engine output has been reduced more than 30% compared to the THS II (Prius) generator (**Fig. 5**).

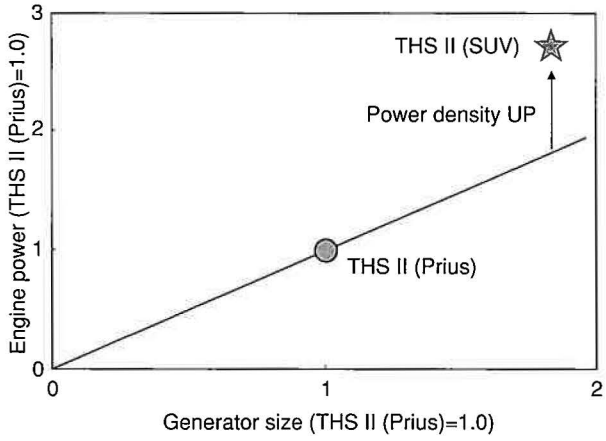

Fig. 5 Relation of Engine Power and Generator Size

2.5 Rear motor

For installation in an SUV, the hybrid system should be of a 4WD design. When compared with 2WD vehicles, conventional 4WD vehicles are disadvantageous in acceleration performance, passenger space, and vehicle weight due to the installation of an additional propeller shaft and related components. To overcome these shortcomings, the THS II (SUV) uses a motor-powered rear wheel drive unit as does the Estima Hybrid which began mass production in Japan in 2001. Similar to the Estima Hybrid, a permanent magnet motor drives the rear wheel drive unit. The motor has dramatically increased its output thanks to an increase of the maximum operating voltage to 650 V and the use of optimal coil turns for this voltage (**Fig. 6**).

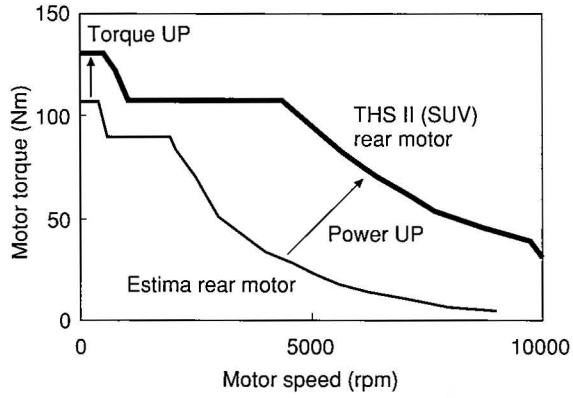

Fig. 6 Rear Motor Torque Profile

2.6 Boost converter circuit

The THS II (SUV) also uses the same boost converter circuit as that used in the THS II (Prius). This circuit boosts the voltage to a maximum of 650 V to dramatically increase the output power of the front motor, generator, and rear motor, while at the same time making them easy to install due to size and weight reductions.

2.7 Battery

Similar to the THS II (Prius), the THS II (SUV) uses a nickel-metal hydride battery. In order to secure an acceleration performance sufficient for the weight of an SUV, a battery composed of 240 cells is used. This battery has a short time rating of 45 kW and a 10 second rating of 36 kW. The size of each cell has been minimized to allow for installation in an SUV equipped with three rows of passenger seats. The above design considerations have made it possible to locate the battery beneath the second passenger seats without sacrificing the passenger space, as shown in **Fig. 7**.

To reduce the battery pack dimensions, the main relay, rush-current suppressing resistor, and current sensor have also been rearranged.

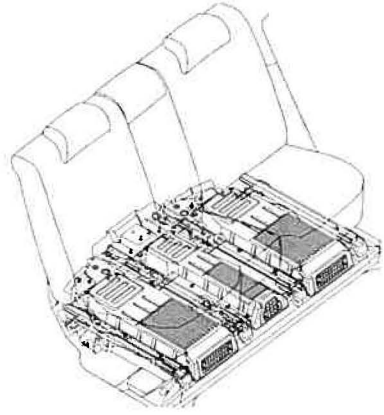

Fig. 7 Battery Pack

2.8 System configuration

The arrangement of ECUs, which has been substantially modified from the THS II (Prius) design, is shown in **Fig. 8**.

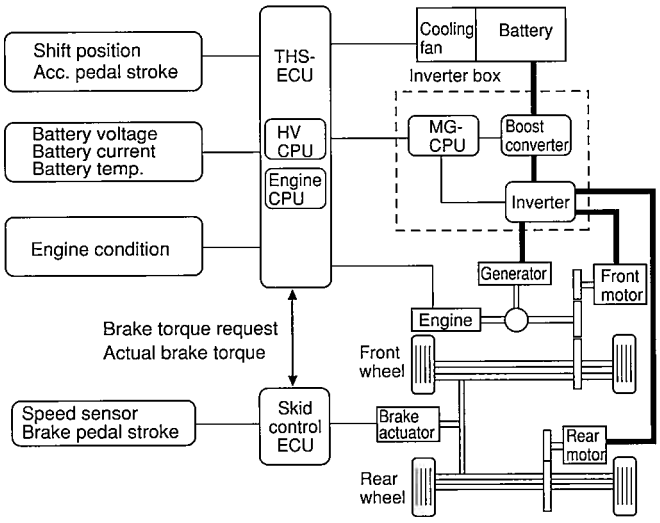

Fig. 8 System Configuration

- Relocation of MG-CPU in inverter box

Differing from the THS II (Prius) design, in which the HV-ECU comprised an HV-CPU and MG-CPU, the MG-CPU has been relocated in the inverter box to integrate the front motor, generator, and rear motor controls. As a result, the need for an inverter-powering wire harness has been eliminated.

- Integration of HV-CPU and engine CPU into single ECU (THS-ECU)

To simplify installation and reduce cost, the engine CPU and HV-CPU have been integrated into a single ECU with a common power source circuit.

- Elimination of battery ECU

Except for sensing functions, the SOC processor, cooling fan controller, and other functional units have been separated from the battery pack and relocated in the HV-CPU. As a result, the need for the battery ECU has been eliminated, which has led to reduced cost and dimensions of the battery pack.

As previously discussed, the output power of electric components has been dramatically increased from the THS II (Prius). In the THS II (SUV), the measures taken for balancing motor power with generator power, as well as the scheme for controlling the system within the rated specifications of electric components are greatly changed.

3. 4WD Control

The new hybrid system is installed in FF type 2WD vehicles and 4WD vehicles consisting of a specially designed rear wheel drive unit.

3.1 Allowable ratio of power split between front and rear wheel drive units

Front wheel drive units have been designed to allow FF vehicles to achieve the fullest performance. On the other hand, the output power of the rear wheel drive unit is slightly limited due to restricted installation space in the body. However, since the rear motor has an output power of 50 kW or 130 Nm, power can be delivered to the front and rear wheel drive units at a ratio of nearly 1 to 1, as long as the accelerator pedal is held at about 50% stroke (**Fig. 9**).

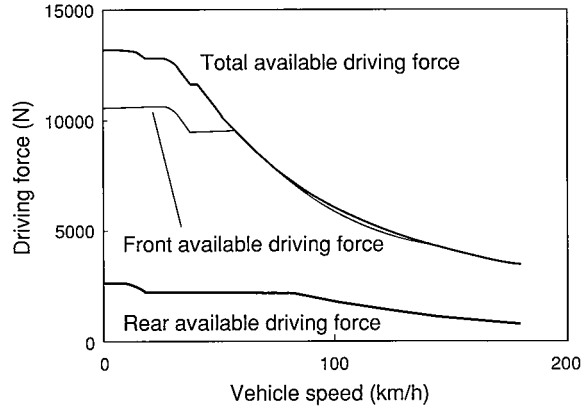

Fig. 9 Ability of Rear Unit

3.2 Response to power split command

The new hybrid system uses an electronic 4WD system. Its front and rear wheel drive units are driven independently by two electric motors (front and rear motors). The power split ratio between the front and rear motors is managed by controlling the output torque of these motors. Differing from conventional 4WD vehicles that use a hydraulic control system, the new hybrid system directly controls the electric power to be transmitted to the front and rear wheel drive motors. Therefore, the new hybrid system quickly responds to power split ratio command signals (**Fig. 10**) and thus maximizes fuel efficiency, as well as the stability and controllability of the vehicle.

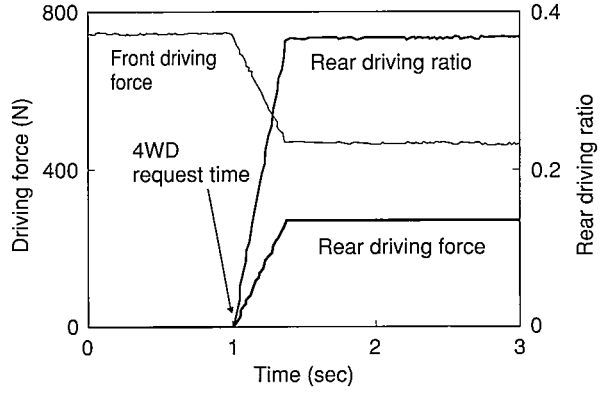

Fig. 10 Rear Driving Force Change Speed

3.3 General description of 4WD control scheme

To ensure high power transmission efficiencies, the new hybrid system installed in a 4WD vehicle is basically operated in the FF 2WD mode. 4WD operation mode is used only when necessary. The rear wheel drive unit is driven by electric power only. Therefore, to allow the rear wheel drive unit to continuously drive the wheels, the front wheel drive unit is required to generate electric power. When driving a vehicle in the 4WD mode, it is advantageous from the viewpoints of overall power consumption and battery charging/discharging efficiency to reduce the output torque of the front motor and supply the saved torque to the rear motor, which is different from driving a vehicle in the FF mode. Meanwhile, the front wheel drive unit has been designed to select its gear ratio so that the output torque of the front motor is reduced to nearly zero when the vehicle travels at a constant speed, in order to maximize the overall power transmission efficiency. In other words, under normal conditions, a vehicle mounted with the new hybrid system is driven by the power directly transmitted from the engine. Reducing the motor output torque to nearly zero minimizes transmission of power between the generator and motor. Thus, power loss in the electrical system decreases and, in turn, power transmission efficiency is maximized.

When a vehicle runs at a constant speed in the 4WD mode, the front motor is driven by the engine and generates the rear motor drive power. This causes electrical energy to flow between the front and rear motors and increases power loss in the electrical system, resulting in overall efficiency reduction. To eliminate this disadvantage, the new hybrid system has been designed to operate in the FF mode when the vehicle runs at a constant speed. Since either the FF or 4WD mode can be selected quickly as has already been discussed, sufficient vehicle stability and controllability are always obtained, even if the vehicle runs in the 4WD mode only when necessary. To keep proper stability and controllability, the vehicle is driven in the 4WD mode during acceleration, skidding, and right/left turns. The 4WD mode is also used during deceleration in order to recover kinetic energy as electrical energy.

The front and rear wheel drive units have individual performance limits. Taking this fact into account, the power split ratio is finally determined so that the fuel efficiency and power performance are maximized while giving the top priority to vehicle stability and controllability.

4. Power Performance

As discussed in Section 2, the output of each electrical component has been dramatically increased from that in the THS II (Prius) while suppressing weight increase to a minimum. Thus, a new hybrid system suitable for installation in SUVs has been developed successfully.

4.1 System output power

In the THS, the engine and battery produce the vehicle drive power, while the electric motors and generator are used to merely transmit the power, as can be understood from **Fig. 11**. A combination of the engine and battery can produce a maximum output power of 200 kW, which is comparative to the output capacity of a gasoline engine having a displacement of nearly 4 L (**Table 2**).

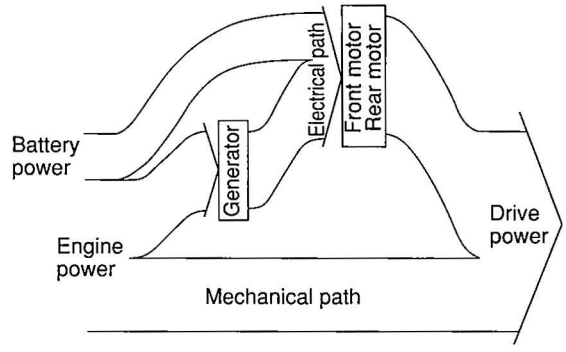

Fig. 11 Power Flow

Table 2 System Power

	THS II (SUV)	LS430 (US)
Engine type	V6	V8
Displacement	3.3 L	4.3 L
Engine max. power	155 kW	216 kW
Battery max. power	45 kW	–
Total power	200 kW	216 kW

4.2 Stepless speed reduction gear

The continuous speed reducing function of the THS permits a wide engine speed range, which implies that the engine speed can be controlled independently of vehicle speed. Therefore, unlike a step change gear type vehicle in which the engine speed drops immediately after up-shifting, the THS does not stall the engine power (**Fig. 12**). A hydraulic system, such as a CVT, is not used in the THS to change the engine speed. Therefore, the engine speed can be changed very quickly and hence a necessary amount of engine power can be obtained in a moment (**Fig. 13**).

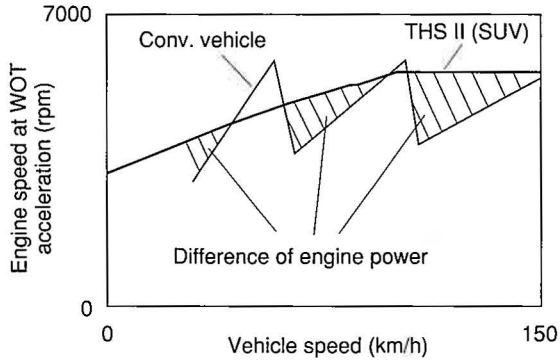

Fig. 12 Engine Speed at WOT Acceleration

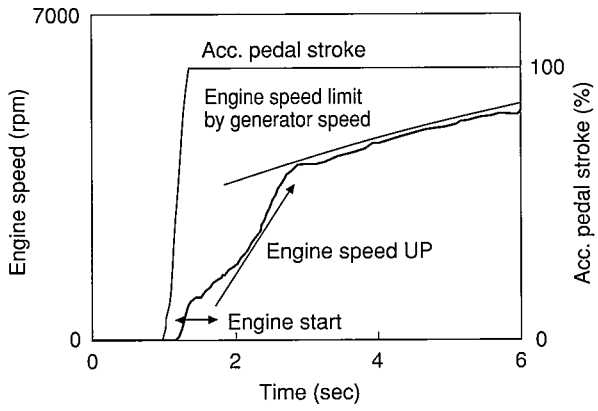

Fig. 13 Engine Speed Up Rate

4.3 Assist by rear motor

Since a 4WD model system consists of a rear motor, the excess electric power that would be generated by the generator or stored in the battery in a 2WD model system when it is driven at a low-speed can be transformed by the rear motor into drive power (**Fig. 14**). It is a matter of common knowledge that the power performance of a 2WD model system is higher than that of a 4WD system mainly because the former is lighter than the latter. However, in the case of this system, a comparison of the 4WD and 2WD model systems reveals that the 4WD has higher power performance than the 2WD, despite the fact that the former is heavier than the latter by the weight of the rear wheel drive unit.

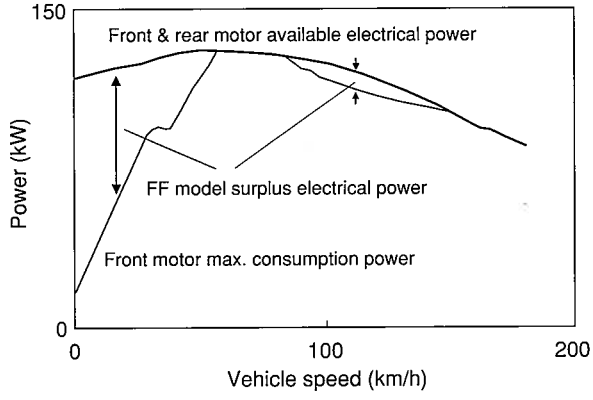

Fig. 14 Surplus Power on FF Model

4.4 Acceleration time

As discussed above, the 3.3 L, V6 engine of the new hybrid system can provide a power performance equivalent to that of a 4 L gasoline engine (**Fig. 15**). In particular, the acceleration of the new hybrid system from 30 mph is far better that that of a 4 L gasoline engine. 2WD model systems also exhibit an excellent power performance since they include a high-powered front motor.

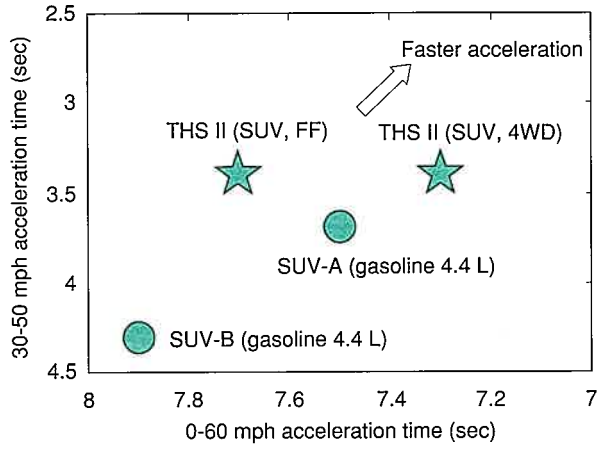

Fig. 15 Acceleration Time

5. Conclusions

A new power train containing two electric motors has been developed aiming at its application to FF type vehicles of the heaviest class.

- Introduction of a speed reduction gear and the use of higher operating voltage have increased the output density of the electrical system, yielding a power performance equal to or higher than that of conventional vehicles.
- The new 4WD design, in which the front and rear wheels are independently driven by two electric motors, has improved fuel efficiency while maintaining optimum vehicle stability and controllability. The rear motor assist function has also improved the power performance.

Author

A. KIMURA

Development of Engine for New Hybrid SUV

Ikuo Ando*
Kazuhiro Ichimoto*
Kenji Itagaki*
Daigo Ando*
Shigeru Suzuki**

Abstract

A new hybrid SUV combining the Toyota Hybrid System II (THS II) with a V6 engine for greater power output was launched in the North American, European and Japanese markets in March of 2005. An engine with high power was required for the hybrid SUV, while at the same time maintaining the high fuel economy and low emission levels that are the hallmark of hybrid vehicles. Satisfying these three requirements has achieved a new hybrid SUV with a fuel economy matching that of compact cars, and whose emissions meet the strictest levels set by each country.

Keywords: *SUV, hybrid vehicle, gasoline engine, emissions, fuel economy*

1. Introduction

With the coming into effect of the Kyoto Protocol for the prevention of global warming in February 2005, the automobile industry is required to develop technologies to further improve fuel economy and make exhaust emissions cleaner.

It was in this context that Toyota introduced its hybrid SUV in the North American, European, and Japanese markets. The hybrid SUV is equipped with the Toyota Hybrid System II (THS II), a higher-powered version of the hybrid system that is highly effective in reducing CO_2 emissions from heavy-duty vehicles like SUVs. The vehicle was developed to meet fuel economy targets of a combined 33.4 miles per gallon (North America) and 17.8 kilometers per liter in the 10-15 mode (Japan). The targets for Europe were a fuel consumption rate of 8.1 liters per 100 kilometers and CO_2 emissions of 192 grams per kilometer in the European EC mode. The emission targets were set so as to satisfy the most demanding regulations in each country/region (SULEV in North America, J-SULEV in Japan, and Euro4 in Europe).

This article describes the technologies that were incorporated into the hybrid SUV engine, with the focus on engine control.

2. Engine Selection

The engine used in the THS, THS-C, and THS II systems employs a high expansion ratio cycle to dramatically improve the specific fuel consumption (SFC), but with the trade-off of a drop in engine power.

However, one of the features of the hybrid SUV is that it should have noticeably superior driving performance at a level not seen before in a hybrid vehicle, and that requires a more powerful engine.

Fig. 1 shows the results of calculations that were made to select the engine displacement. The engine power necessary for vehicle performance is 155 kilowatts, and it can be seen that that requires a displacement of at least 3.0 liters. It is also clear that the 3.3-liter high-expansion engine is incapable of achieving the 155-kilowatt target.

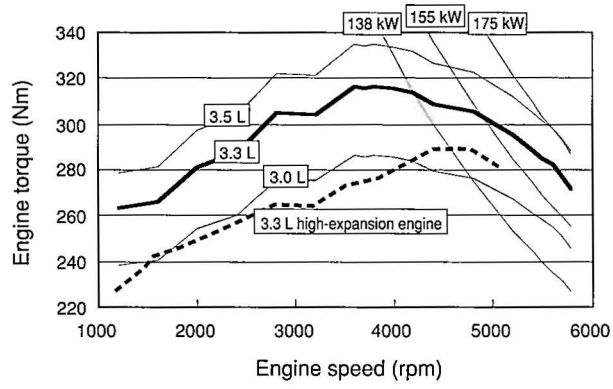

Fig. 1 Calculations for Selecting Engine Displacement

The engine was selected to meet targets for power, fuel economy, emissions, and cost. The final choice was the 3.3-liter Toyota 3MZ-FE engine that is used in the base vehicle, but the decision was made to forgo the use of the high expansion ratio cycle. Note that although the vehicle itself is specified differently for the three destinations of North America, Europe, and Japan, the same engine is used in all specifications.

Table 1 compares the new engine specifications to those of the base engine. At the same time that the changes required for use in a hybrid were made, unnecessary items were eliminated.

The next section provides a detailed description of the changes that were made to the base engine specifications.

* Hybrid Vehicle System Engineering Div. ** Engine Engineering Div. 1

Table 1 Comparison of Specifications

	New Engine	Base Engine
Engine model	3MZ-FE (V6)	←
Emission control (North America)	SULEV	LEV2/ULEV
Displacement [cc]	3,311	←
Bore × Stroke (mm)	φ92.0×83.0	←
Mechanical compression ratio	10.8	←
Intake valve closing timing (°ABDC)	92–32	64–4
Max. power (kW/rpm)	155/5600	172/5700
Max. torque (Nm/rpm)	288/4400	328/3600
ACIS	None	2-stage
Air cleaner	Special air cleaner mounted on top of engine	–
Start Catalyst	9R-08 2 mil/900 cel TWC	9R-07 3 mil/600 cel TWC
Under Floor Catalyst	13R-08 3 mil/600 cel TWC	13R-13 4 mil/400 cel TWC

3. Changes to Engine Hardware

3.1 Exhaust system

The exhaust system specifications were revised so that the hybrid SUV could satisfy the SULEV standards, the most demanding of North American emission regulations.

The base material of the start catalyst was changed to a thin-walled material with high cell density to improve the catalyst warm-up performance during cold starting. The base material of the under floor catalyst was also changed to a thin-walled material with high cell density, both to ensure good warm-up and to improve exhaust performance. The catalyst's cross section was also optimized.

These changes to the exhaust system increase the exhaust pressure to 20% greater than that of the base engine, while holding the drop in power performance to approximately 5%.

3.2 Air intake system

In order to open up space to mount the hybrid vehicle's inverter, the air cleaner was made more compact and was relocated to a position on top of the engine.

This change to the air intake system increased the intake air pressure loss by about 35% over the base engine, but the drop in power performance was held to around 6%.

3.3 Valve system

In order to reduce the vibration that accompanies the intermittent starting of the hybrid vehicle's engine, the crank angle at which the intake valve closes was retarded 28° further than in the base engine. The major consideration in determining this timing was to ensure the engine starting performance at extremely low temperature.

3.4 Elimination of acoustic control induction system

The base engine uses an acoustic control induction system (ACIS) that varies the amount of intake air to increase torque at low to medium speeds. The torque characteristics of the hybrid SUV engine when the ACIS is added are shown in **Fig. 2**. Although the ACIS does increase the torque, the required power can be obtained even without the ACIS by taking advantage of the THS II's capacity to select its own operating point. The ACIS was therefore eliminated.

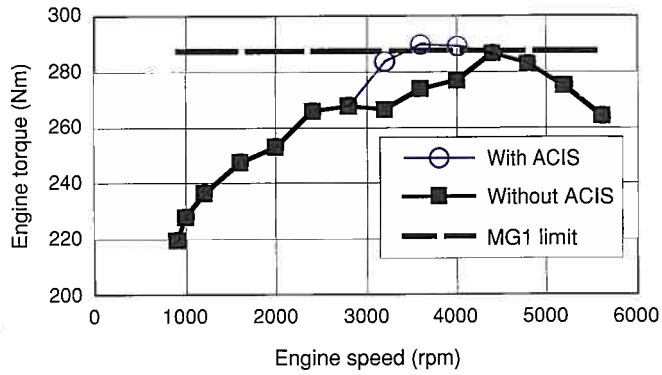

Fig. 2 Change in Torque when Using ACIS

3.5 Countermeasures against wear due to intermittent starting and stopping

To counter the wear that results from the intermittent operation of the hybrid vehicle's engine, physical vapor deposition (PVD) was used to coat the top piston ring, the 3-piece oil ring was changed to a 2-piece ring, and a plastic coating was added to the crank bearings for cylinders 1 and 4.

3.6 Elimination of V-ribbed belt to drive accessories

In the conversion of the SUV to a hybrid, the alternator was eliminated, and it was no longer necessary to drive either the air conditioning compressor at the front of the engine or the power steering oil pump. And because the 3MZ engine's water pump is driven by the timing belt, there are no accessories to drive at the front of the engine, so the V-ribbed belt was eliminated.

4. Engine Performance and Fuel Economy

4.1 Concept of environmental measures in the new engine

In order to make the emissions cleaner and improve the fuel economy, the new engine continues the concept used in the THS, THS-C, and THS II and does not increase the amount of fuel to increase torque in the low-to-medium speed range. And although the torque does drop at low to medium speeds as a result, the SFC is dramatically improved.

4.2 Engine performance and SFC

The performance and SFC of the new engine are shown in **Fig. 3**. As a consequence of the changes that were made to the air intake system for conversion to the hybrid system and compliance with the U.S. SULEV standard, the power dropped approximately 11% below that of the base engine, and the torque dropped around 14%. But conversely, the fuel economy in the low-to-medium speed range improved approximately 11%.

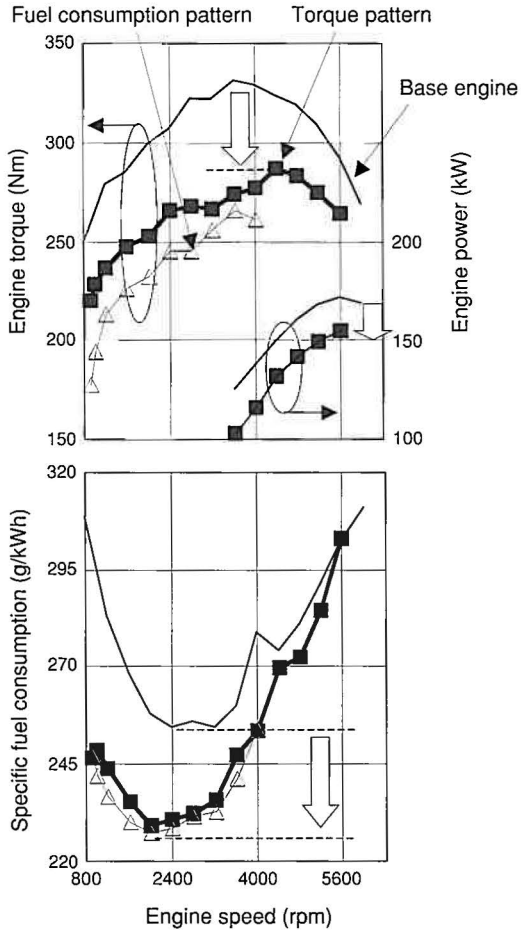

Fig. 3 New Engine Performance and Specific Fuel Consumption

4.3 Optimization of engine operating point

Looking at the selection of the engine operating point from the standpoint of fuel consumption, it is fine to choose a point that yields the lowest possible SFC while still providing the required engine power, but other requirements must also be met. These include the efficiency of the system as a whole, the suppression of booming noise, resistance to engine stalling, and good response during acceleration. As **Fig. 4** shows, the engine operating point was set to achieve good results for fuel economy, noise and vibration, and driveability.

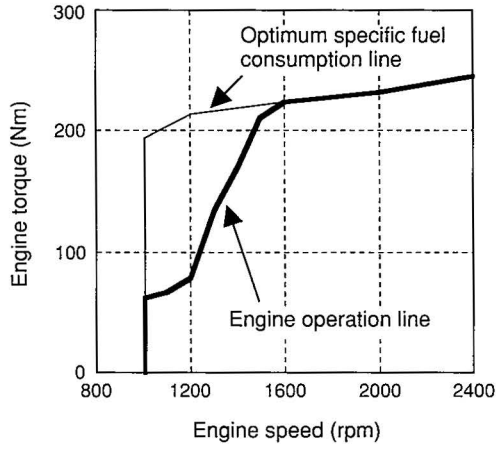

Fig. 4 Engine Operation Line

4.4 Fuel economy evaluation results

Table 2 shows the results of evaluations of the new engine's fuel economy in the North American, European, and Japanese markets. **Fig. 5** shows the fuel economy evaluation results in comparison to other gasoline-powered vehicles in the North American market. It can be seen that through the use of the higher-powered THS II and the engine improvements described above, and improvements in overall vehicle fuel economy, it is possible for large-sized vehicles like SUVs to demonstrate fuel economy equaling that of compact cars. [1]

Table 2 Fuel Economy Evaluations

Vehicle	Engine	Transmission	Fuel Economy		
			US Comb.	10•15 Mode (Japan)	EC Mode
New SUV	V6/3.3 L	THS-II/4WD	33.4 mpg	17.8 km/L	8.1 L/100 km
RX-330	V6/3.3 L	5AT/4WD	23.9 mpg	—	—
RX-300	V6/3.0 L	5AT/4WD	—	9.2 km/L	12.2 L/100 km

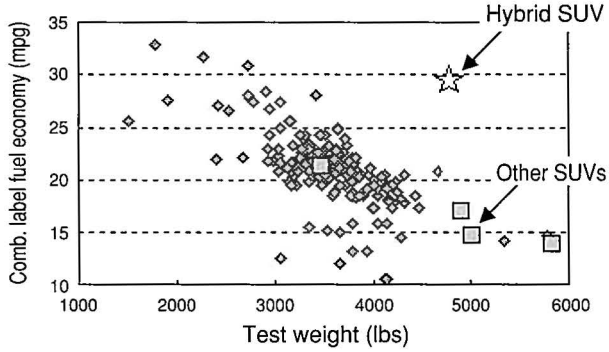

Fig. 5 Comparison of Fuel Economy in North American Market

5. Technology to Reduce Exhaust Emissions

5.1 Exhaust system

The exhaust system for the hybrid SUV is shown in **Fig. 6**.

The exhaust system was constructed to ensure that its performance would comply with the most demanding regulations in each country/region. At the same time, measures such as reducing the amount of precious metal in the catalyst and eliminating special emission-reducing devices make the exhaust system superior from both environmental and cost standpoints.

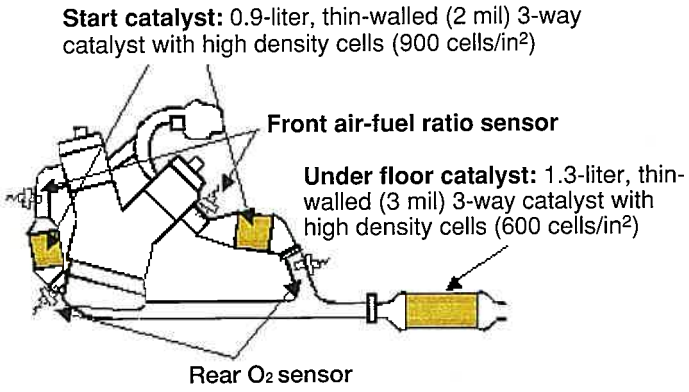

Fig. 6 Exhaust System

5.2 Rapid catalyst warm-up after cold start

The most important point in complying with the emission regulations in each country/region is to reduce the hydrocarbons that are emitted during a cold start.

As **Fig. 7** shows, hydrocarbon emissions during cold start are reduced in the same manner as in the original THS, by running the vehicle on battery power after a cold start and dedicating the engine completely to warming up the catalyst with a fixed volume of air.

The volume of intake air and the retarding of the ignition timing during catalyst warm-up have also been optimized, which reduces the hydrocarbon emissions from the hybrid SUV even further than in the conventional model.

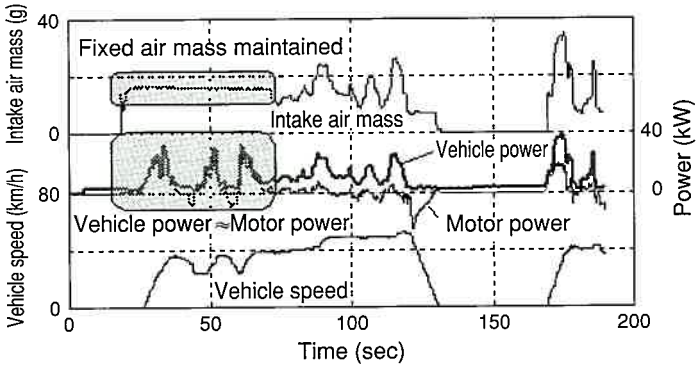

Fig. 7 Power Management after Cold Start

5.3 Suppression of catalyst deterioration

It is generally known that a 3-way catalyst deteriorates in a high-temperature atmosphere with a lean air-fuel ratio. For that reason, a control function was added that estimates the catalyst temperature based on the engine power and obtains information on the air-fuel ratio from an air-fuel ratio sensor, then uses this information to suppress catalyst deterioration.

As **Fig. 8** shows, the suppression of catalyst deterioration results in an approximately 21% reduction in hydrocarbon emissions in the LA#4 mode.

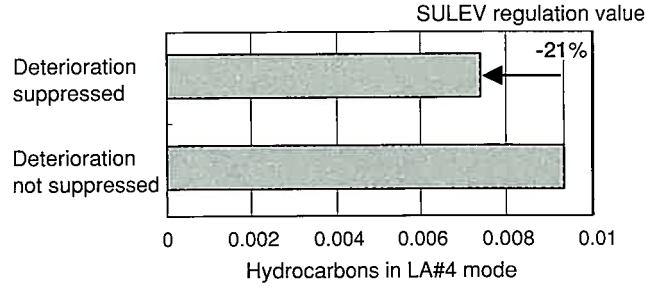

Fig. 8 Hydrocarbon Reduction Effect of Suppressing Catalyst Deterioration

5.4 Emission evaluation results

The addition of the systems and controls described above, together with the optimization of the existing controls, brings the hybrid SUV into compliance with the most demanding regulations in each country/region. The values obtained in in-house testing are shown in **Fig. 9**.

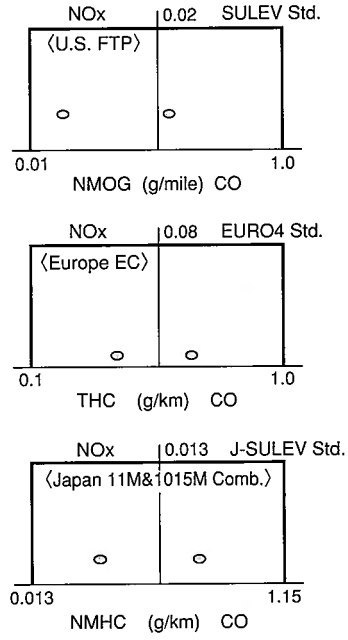

Fig. 9 Emission Evaluation Results

6. Conclusions

- The heavy-duty hybrid SUV with a 3.3-liter V-6 engine achieves fuel economy equivalent to that of a compact car by taking advantage of the features of the THS II.
- Improvements to the engine control enable the vehicle to comply with the most demanding regulations in each country/region (SULEV in North America, J-SULEV in Japan, and Euro4 in Europe).

References

(1) A. Kimura, Ando, Itagaki. "Development of Hybrid System for SUV" SAE Paper 2005-01-0273 (2005).
(2) K. Muta, Yamazaki, Tokieda. "Development of New-Generation Hybrid System THS II." SAE Paper 2004-01-0064 (2004).

Authors


I. ANDO


K. ICHIMOTO


K. ITAGAKI


D. ANDO


S. SUZUKI

Development of a New Hybrid Transmission for FWD Sports Utility Vehicles

Hiroshi Hata*
Munehiro Kamiya**
Shigetaka Nagamatsu***

Abstract
A new hybrid transmission (P310) has been developed for FWD 3-liter engine class sports utility vehicles. The development of this transmission aimed to improve power performance and fuel economy, and to achieve the most compact size in the world, while maintaining high torque capacity. In order to achieve these goals, the gear train and the motor have been newly designed, and advanced technology has been applied. This article describes the major features and performance of this transmission in detail.

Keywords: *hybrid vehicle, power train, hybrid transmission, motor, gear train*

1. Introduction

In recent years, reducing automobile CO_2 emissions and improving fuel economy have become increasingly important goals from the standpoint of the environment and energy. The hybrid vehicle, which combines an engine with a motor-generator, has been developed as one technology for improving fuel economy.

The Toyota Hybrid System (THS) was first installed in the Prius in December 1997. Since then, it has been improved, and the Toyota Hybrid System II (THS II) made its debut in the new Prius in September 2003. Now a new hybrid transmission has been developed for SUVs, based on THS II, to provide the strong power performance that SUVs require, together with good fuel economy.

This article describes the structural features of the new hybrid transmission, as well as a newly adopted motor speed reduction device, a high-power, compact motor, and other features.

2. Development Objectives

The new P310 hybrid transmission for front-wheel drive, 3-liter engine class SUVs was developed with the objectives of compact size, improved power performance, and lower fuel consumption.

(1) Compact size

The combined engine and motor power has been more than doubled over that of the P112 transmission[1] used in the Prius, but it was also necessary to make the transmission more compact to ensure its installability. In order to achieve both higher capacity and a more compact transmission, a new motor speed reduction device, a compound gear, and a higher-power, more compact motor were also developed.

(2) Improved power performance

To achieve a level of power performance that is suitable for a 3-liter engine class SUV hybrid transmission, the motor power was increased by raising the speed and the voltage of both the motor and the generator.

(3) Lower fuel consumption

To achieve the best fuel economy in the 3-liter engine SUV class, the motor loss was reduced by improving the layout of the rotor permanent magnets and making the silicon steel plate thinner, among other measures.

3. Basic Specifications and Basic Structure

Fig. 1 is a cross section of the P310, **Fig. 2** is a cross section of the P112, and **Table 1** compares the specifications of the two transmissions.

The P310 features a new motor speed reduction device and compound gear that give it a completely different structure from the P112. The new motor speed reduction device amplifies the motor torque in proportion to its gear ratio, doubling the output torque without increasing the overall length of the motor.

The compound gear, which integrates two planetary ring gears, a counter drive gear, and a parking gear into a single unit, is located to the outside of the motor speed reduction device and power split device. It allows the gear train to be made more compact by eliminating the chain used by the P112 and reducing the number of shafts from four to three.

* Power Train Engineering Div. 3
** Hybrid Vehicle Power Train Development Div.
*** Power Train & Chassis Components Production Engineering Div.

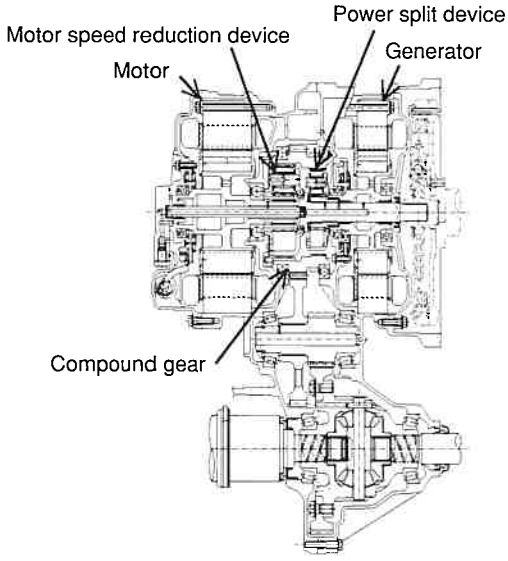

Fig. 1 Cross Section of P310

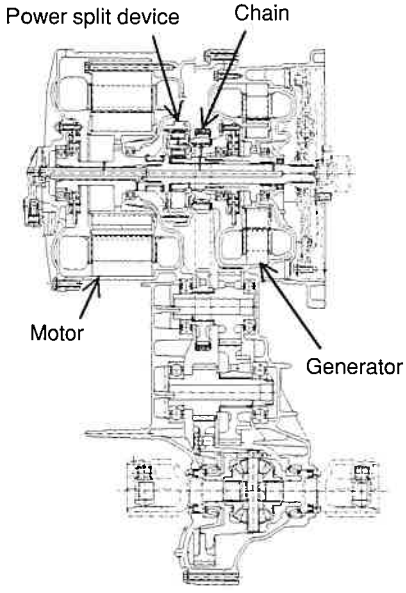

Fig. 2 Cross Section of P112

Starting from the right (the engine side) in **Fig. 1**, a damper with attached torque limiter, the generator, two planetary gears and the motor are located on shaft 1. The planetary gear on the right acts as a power split device, splitting the engine power into the driving force for the vehicle and the power that runs the generator. The planetary gear on the left acts as the motor speed reduction device. The compound gear, with its two ring gears, counter drive gear, and parking gear, is located to the outside of the two planetary gears and transmits the driving force to the counter driven gear and final drive gear on shaft 2, as well as to the ring gear and differential on shaft 3.

Table 1 Comparison of Specifications

		P310	P112
Engine	Max. power (kW)	155	57
	Max. torque (Nm)	288	115
Motor	Type	Synchronous AC motor	Synchronous AC motor
	Max. power (kW)	123	50
	Max. torque (Nm)	333	400
	Max. speed (rpm)	12400	6000
Motor reduction gear ratio		2.478	–
Differential ratio		3.542	4.113
Mass (including ATF) (kg)		125	109
Overall length (mm)		417	430

4. Compact Size

Although the engine power of the P310 is 2.7 times that of the P112, and its motor power is 2.46 times greater, using the motor speed reduction device and compound gear allows the unit to be made nearly as compact as the P112.

4.1 Motor speed reduction device

The structure of the motor speed reduction device is shown in **Fig. 3**. The planetary gear is used as the motor speed reduction mechanism. The sun gear of the planetary gear is coupled to the motor's rotor by a spline. The carrier is secured to the case by a spline fitting. The ring gear is integrated into the compound gear. The motor speed is reduced by the planetary gear, and the power is transmitted to the counter gear and differential.

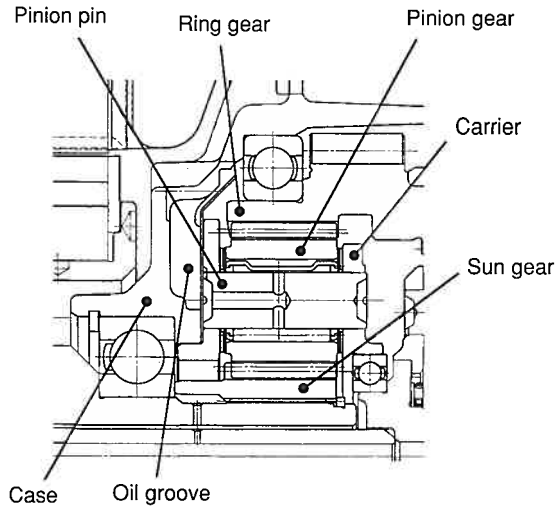

Fig. 3 Structure of Motor Speed Reduction Device

The numbers of teeth on each gear in the motor speed reduction device are as follows: 23 on the sun gear, 18 on the pinion gears, and 57 on the ring gear. The gear ratio is set to

2.478. The ring gear (compound gear) reduces the motor speed to 1/2.478 of its original value and amplifies the motor torque 2.478 times.

The operation of the motor speed reduction device allows the motor to be specified for high speed and low torque, as shown in **Fig. 4**. And because the motor size is proportional to the torque, the motor speed reduction device allows the motor to be made more compact in proportion to the reduction in maximum torque.

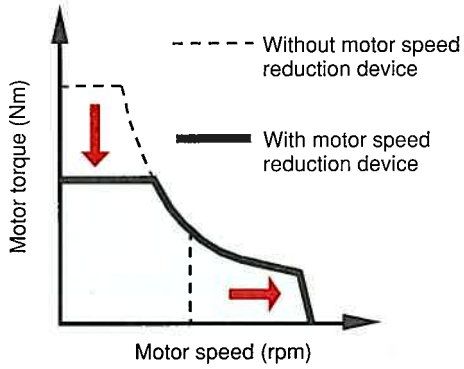

Fig. 4 Motor Size Reduction

At the same time that the motor is made more compact, its speed increases, which in turn increases the maximum revolution speed of the pinion gears in the motor speed reduction device by 50% over conventional pinion gears. **Fig. 5** shows a comparison with the maximum revolution speeds of pinion gears in other automatic transmissions. In an automatic transmission, there are times when the pinion gear revolution speed rises instantaneously during shifting, but because it is instantaneous, it has little effect on durability. However, in a configuration where the revolution speed is continuously high over an extended period of time, such as in high-speed driving, the pinion gears are exposed to harsh conditions that do affect durability. For that reason, as the P310 is operated continuously at high speed, pitting tends to occur in the tooth surface of the pinion gears and sun gear, and flaking becomes more likely on the pinion pins.

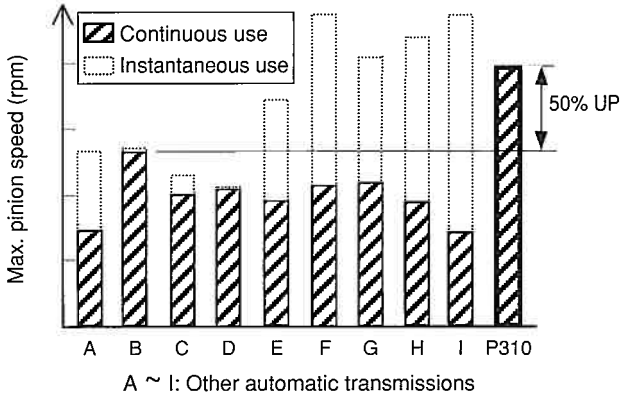

Fig. 5 Comparison of Maximum Pinion Speeds

To improve durability, improvements were made in the gears, needle bearings, and lubrication. Five pinion gears are used instead of four, thereby reducing the divided load per gear. The helix angle of each gear has also been optimized to adjust the thrust force and improve durability.

Durability at high revolution speed has also been improved by the use of cage-and-roller type needle bearings, as well as by improvements to the pinion pin material, quenching and tempering treatment, and machining methods.

Lubrication has been improved, as shown in **Fig. 6**, by providing branching oil grooves for the oil holes in the pinion pins, so that ample amounts of oil flow quickly to all five holes.

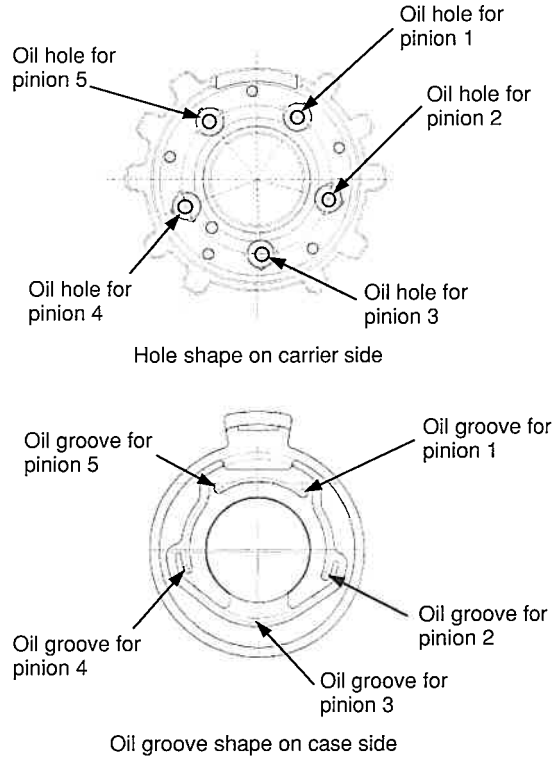

Fig. 6 Shape of Oil Groove

4.2 Compound gear

The compound gear is an integrated structure made up of two ring gears, a counter drive gear, and a parking gear, as shown in **Fig. 7**. The combining of these four parts into a single unit makes the gear train extremely compact.

The bearings that support the compound gear are located outside the planetary gear, which eliminates the need to increase the overall length of the transmission to make space for the bearings. On the other hand, the diameter of the bearings that support the counter drive gear has been enlarged, which increases the surface speed, so improvements were also made to increase durability.

The compound gear has a cylindrical shape with a large diameter, so difficulty in machining and distortion during quenching would be expected. The machining and quenching

and tempering treatment methods were therefore improved to achieve the required precision and strength.

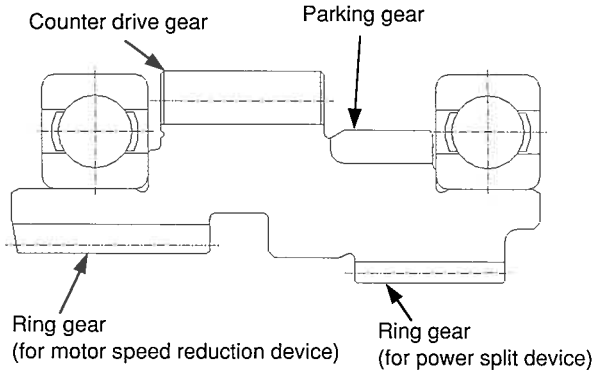

Fig. 7 Compound Gear

5. Improvement of Power Performance

Increasing the revolution speed and voltage of the motor and generator makes it possible to achieve high power in a compact unit. This section describes how the motor voltage was increased and how increasing the voltage improves the insulation performance and cooling performance.

5.1 Motor voltage increase

In the newly developed hybrid transmission for SUVs, the DC-DC converter booster system[2] that is used in the Prius has been developed further to raise the drive voltage for both the motor and the generator from 500 volts to 650 volts, as shown in **Fig. 8**.

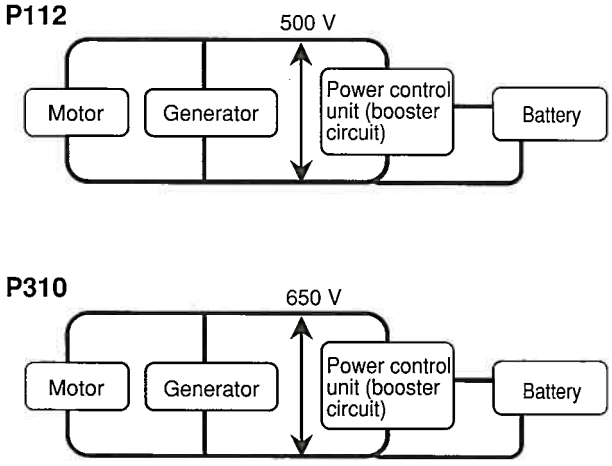

Fig. 8 Voltage Increase by Variable-Voltage System

The P310 has 30% higher drive voltage than the P112, and when the inverter switching surge is taken into account, its maximum peak voltage is at least 20% higher. An insulating paper structure has also been designed for the P310 to prevent partial discharge inception voltage between phases, even at maximum voltage. The maximum peak voltage is also affected by factors in the use environment, including the length of the high-voltage cable that connects the inverter and the motor, the temperature and humidity, the foreign matter content of the automatic transmission fluid (ATF), the degree of deterioration, and the electrical conductivity, so these were also taken into account in the design.

Automatic assembly of the insulating paper and inspection of the insulation between phases were used to ensure good insulation quality under high voltage. As **Fig. 9** shows, motors with a DC drive voltage over 500 volts have never before been produced in quantities of several thousand per month.

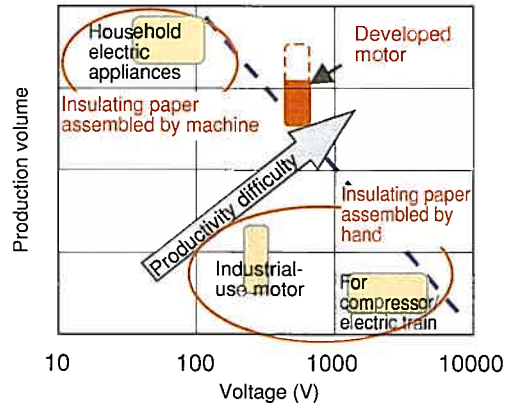

Fig. 9 Motor Voltage and Production Engineering

As **Fig. 10** illustrates, the assembly of the insulating paper uses the same insertion system that is used to insert the coil into the stator core, and the shape of the insulating paper has been optimized for easy insertion while maintaining good insulation quality. In order to ensure reliable insulation, it is necessary to confirm through measurements that the partial discharge inception voltage is not generated. To do this, a prescribed voltage is applied between phases, and measurements are taken to confirm that not even a minute electric current flows as a result. Technologies were also developed to check for factors that affect measurements of the plant environment (temperature, humidity) and the radiated noise of the production equipment and to take those measurements in a short time, so that in-line inspections could be implemented.

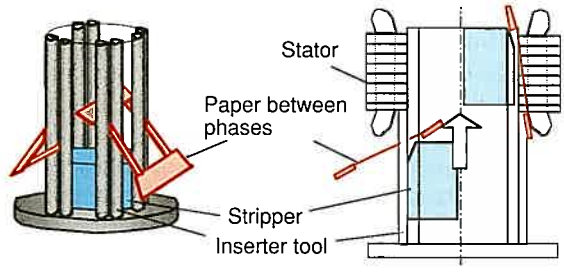

Fig. 10 Insulating Paper Assembly

5.2 Cooling performance

In the same manner as in the P112, the heat from the P310 motor is conducted to the case, where it is released to the outside. Cooling technologies used for the first time in the P310 also include the active application of ATF to the stator and coil-ends, as well as the use of the ATF to conduct the motor heat to the case.

As shown in **Figs. 11** and **12**, the ATF that is slung by the gears is collected in a catch tank that is installed on top of the case, then is supplied from the tank to the stator and coil-ends. This allows a larger amount of heat to be conducted to the case, thereby improving the cooling performance.

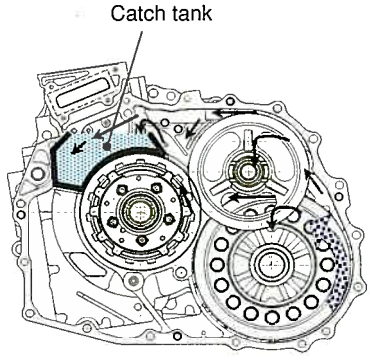

Fig. 11 Oil Slinging by Gear

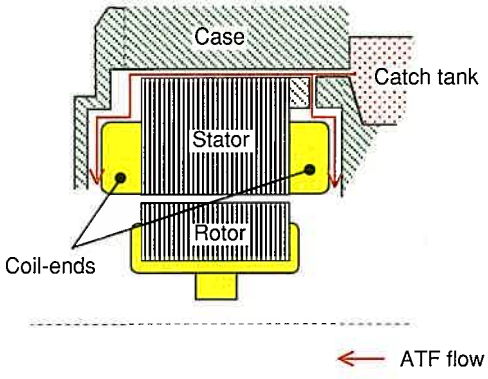

Fig. 12 Motor Cooling by ATF

As in the P112, both air cooling and water cooling are used to draw heat away from the case. Depending on the vehicle specifications, an oil cooler may also be installed to cool the ATF, thereby improving the cooling efficiency.

The release of heat from the stator and the coil-ends is accomplished by thermal conduction through contact between the stator and the case and by thermal conduction to the case through the medium of the ATF. The ratios of heat release are approximately 30% to 50% by direct contact and 50% to 70% through the ATF. The cooling effect of the ATF is extremely strong in the P310. The overall cooling performance, including air cooling, is significantly better than in the P112.

6. Low Fuel Consumption

In the P310, the major improvements to the motor make it possible to achieve compact size, high power, and low loss all at the same time. This section provides an overview of the technologies used in the new motor for the P310.

6.1 Higher motor speed

Fig. 13 is an example of a frequency map in an urban driving situation. The point to be noted here is that the frequency is high in the low-load region.

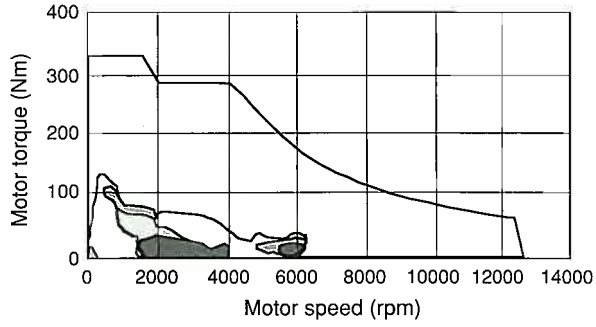

Fig. 13 Motor Frequency Map in Urban Driving

The loss in the motor consists of two types: copper loss that occurs as joule heat in the coil and iron loss that occurs in the motor core. As **Fig. 14** illustrates, iron loss accounts for a large percentage of the total loss in the low-load region, indicating that it is important to reduce iron loss to improve fuel economy in ordinary driving.

A distinctive feature of the P310 is that the use of a motor speed reduction device with a reduction gear ratio of 2.478 allows the motor to be made more compact. But conversely, that also requires the motor to operate at a speed that is 2.478 times higher.

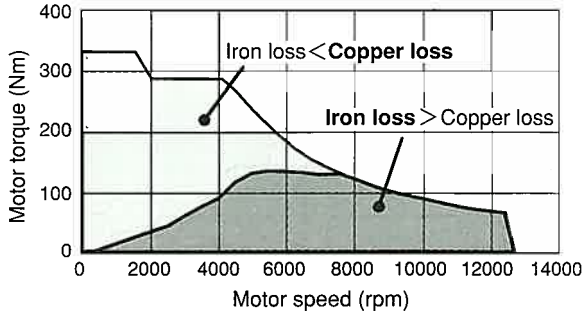

Fig. 14 Motor Loss Ratios

The iron loss in the motor increases almost proportionally to the square of the frequency, so to make high speed possible, the iron loss must be decreased without worsening the vehicle's fuel economy, and at the same time, mechanical conditions such as the strength to withstand centrifugal force must be satisfied. In

the development work reported here, a major reduction in iron loss was achieved through improvements to both the design and the materials.

A number of design improvements were made. As **Fig. 15** shows, the permanent magnets for the rotor are arranged in a V shape, which significantly improves the reluctance torque and reduces iron loss during low-load operation. At the same time, their strength has been improved by providing a rib between each pair of magnets. These steps allow the motor speed to be more than doubled. The optimization of the open angle q between each pair of rotor magnets has the effect of suppressing the harmonic components in the magnetic flux, which also makes a major contribution to reducing the iron loss. These shapes were optimized by means of the finite element method, including magnetic field and strength analyses.

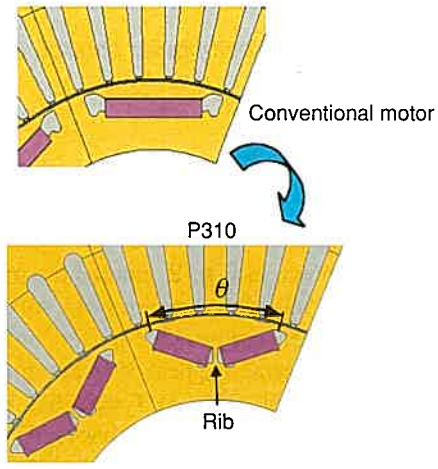

Fig. 15 V-Shaped Arrangement of Rotor Permanent Magnets

The primary improvement in materials was the development of a new silicon steel plate even thinner than the 0.35 mm plate used in the P112. Combining this with manufacturing improvements, such as an improved layering method for the stator core, resulted in much lower iron loss than in the conventional motor. **Fig. 16** shows an efficiency map for the motor that is used in the P310.

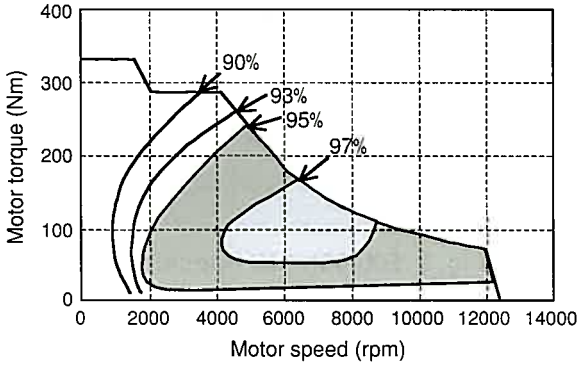

Fig. 16 P310 Motor Efficiency Map

7. Conclusions

The P310 was developed for front-wheel drive, 3-liter engine class SUVs, and the initial development objectives of compact size, improved power performance, and lower fuel consumption were all achieved. With respect to compact size and improved power performance, the motor speed reduction device, compound gear, and high-power, compact motor achieve more than twice the power of the P112 in a unit of nearly the same size. Lower fuel consumption has been achieved by using the design of the motor and improvements in the materials to dramatically reduce the motor loss.

A hybrid vehicle equipped with the P310 achieves 89% better fuel economy in the 10-15 mode than a gasoline-powered vehicle with a 5-speed automatic transmission and an engine of the same 3-liter displacement. The newly developed hybrid transmission is a major contributor to this fuel economy improvement.

References

(1) K. Yoshimura, Ohshima, Kondo, Ashida, Watanabe et al. "Improving the Efficiency of a Transaxle for Hybrid Vehicles." *Journal of Society of Automotive Engineering of Japan* Vol. 58 No. 9 (2004) pp. 68-72.
(2) M. Okamura, Sato, Sasaki. "Development of Hybrid Electric Drive System Using a Boost Converter." Evs-20 (2003).

Authors


H. HATA


M. KAMIYA


S. NAGAMATSU

Motor Control and Boost Converter Control for Hybrid Vehicles

Hideto Hanada*
Eiji Satoh*
Masaki Okamura*
Hideaki Yaguchi*

Abstract

The RX400h released in 2005 achieves outstanding power performance through use of a high-voltage/high-power motor as well as e-4WD for the rear wheels. The RX400h is based on the THS II developed for the new Prius, which enables ecology and power to be promoted simultaneously. A substantial increase in power has been achieved by adopting control for stable system operation. This article will introduce the latest motor-drive technology that allows motor power to be increased, and technology that facilitates a variable voltage system and a radical increase in output.

Keywords: *motor, boost converter, resolver, PWM control, overmodulation control, rectangular control, error correction*

1. Introduction

Amid growing concern over environmental problems such as global warming, the development of practical, environmentally friendly vehicles with better fuel economy has become a critical issue for which automotive engineers must bear the responsibility.

Toyota Motor Corporation put the world's first mass-produced hybrid car, the Prius, on the market in December 1997. The new Prius, shown in **Fig. 1**, followed in September 2003 driven by the revolutionary THS II, which uses a boost converter to increase the motor power, but still achieves marvelous fuel economy.

Fig. 1 Prius

The RX400h, shown in **Fig. 2**, entered the market in the SUV category in 2005, and delivers not only solid environmental performance and even more motor power, but also the driving pleasure that is the essential appeal of an automobile.

Hybrid vehicle development at Toyota has involved research and development on motor-drive technologies, as well as their commercialization and incorporation into mass-produced vehicles. This article describes the motor drive technologies in the latest hybrid vehicles, including a power increase and a variable voltage system, as well as additional technologies that provide even higher power in the new RX400h.

Fig. 2 RX400h (US Specifications)

* Hybrid Vehicle System Engineering Div.

2. Characteristics and Basic Control of Permanent Magnet Motor

2.1 Characteristics of permanent magnet motor

The hybrid vehicle motor is a permanent magnet (PM) motor. The reasons for using a PM motor are that it does not require a field current as an induction motor does, which increases efficiency by eliminating secondary copper loss, and that the magnet has higher magnetic flux density than a strong rare earth magnet, which allows the motor to be made more compact. The type of PM motor chosen was the inverse salient pole type that utilizes the reluctance torque, because it has a wide operating range. Equations 1 and 2 are the steady-state voltage and torque equations, respectively. Here, *vd* and *vq* are the d-axis and q-axis components of the motor voltage, *id* and *iq* are the d-axis and q-axis components of the motor current, *w* is the electrical angular velocity, *Ld* and *Lq* are the d-axis and q-axis components of the inductance, *R* is the resistance, Φ is the interlinkage magnetic flux, *p* is the number of electrode pairs, and *T* is the motor torque.

$$\begin{pmatrix} vd \\ vq \end{pmatrix} = \begin{pmatrix} R & -\omega Lq \\ \omega Ld & R \end{pmatrix} \begin{pmatrix} id \\ iq \end{pmatrix} + \begin{pmatrix} 0 \\ \omega\Phi \end{pmatrix} \quad (1)$$

$$T = p\{\Phi iq + (Ld - Lq)\, idiq\} \quad (2)$$

The second term on the right side of equation 2 is the reluctance torque.

Fig. 3 shows the torque in relation to the phase when the current amplitude is constant. Because advancing the phase increases the reluctance torque, the motor torque reaches its maximum when the current phase angle is advanced 90 degrees.

A line that connects the points at which the torque is at its maximum for various current amplitudes constitutes the optimum motor operating line, at which the current is at a minimum. A motor that is operated along this line can produce large torque very efficiently. The type of control that operates a motor along this line is called maximum torque control.

Fig. 4 shows the induced voltage constant per unit revolution speed in relation to the phase when the current amplitude is constant. The distinctive characteristic is that the induced voltage constant decreases as the current phase advances. The induced voltage is proportional to the revolution speed, so high voltage is produced at high revolution speed. If the induced voltage becomes higher than the inverter power supply voltage, the current can not be controlled, so the induced voltage must be kept low by advancing the current phase. This is called weak field control. With weak field control, the motor operating point lies to the right of the optimum operating line shown in **Fig. 3**, so torque is lower in relation to the current, and the efficiency is poorer, but it allows the motor to operate in the high speed range. **Fig. 5** shows the regions of maximum torque control and weak field control.

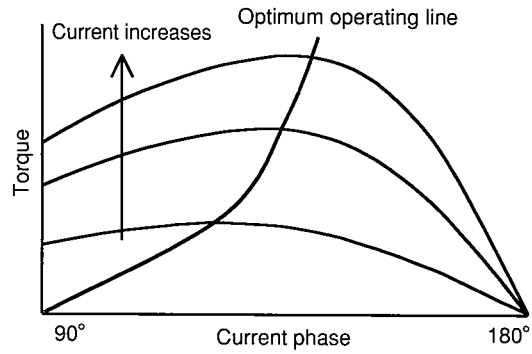

Fig. 3 Current Phase – Torque Characteristics

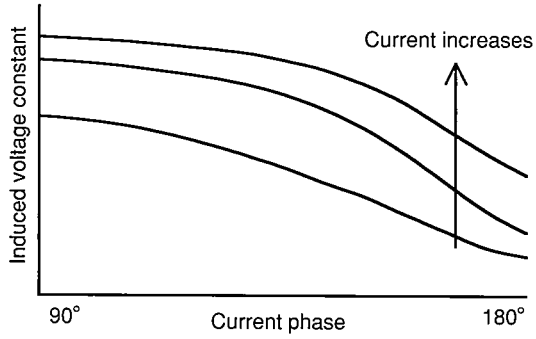

Fig. 4 Current Phase – Voltage Characteristics

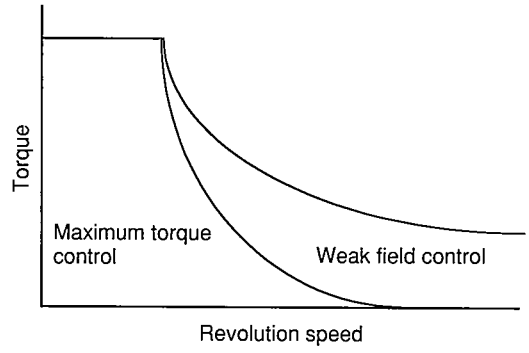

Fig. 5 Control System Regions

2.2 Current control

Fig. 6 shows the basic system configuration for PM motor control. The battery is connected directly to the inverter, and the system voltage varies according to the operating state of the battery. The inverter is a power converter made up of semiconductor switching elements that perform their task at a high frequency of several kilohertz to convert the battery voltage into alternating current voltage. Motor control requires sensors to detect the angle, current, and voltage. A resolver that measures absolute angles is used as the angle sensor.

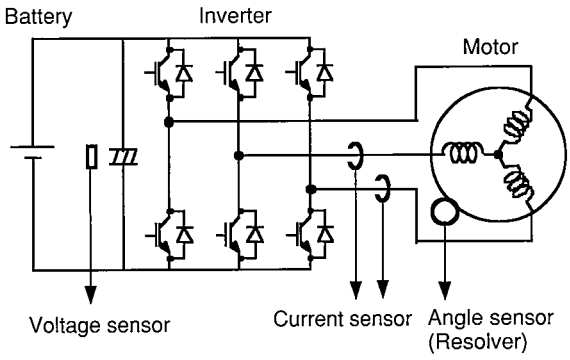

Fig. 6 Basic System Configuration

The PM motor is controlled by controlling the amplitude and phase of the current. **Fig. 7** shows the basic PM motor control configuration. A torque command from a higher level is converted into current commands (Idcom, Iqcom), and feedback control is carried out until the current detected by the current sensor matches the value of the current command. The reason for converting the value read by the current sensor from a 3-phase reading into d-axis and q-axis coordinates is that converting alternating current into direct current quantities allows feedback control to eliminate phase delays. The angle sensor value is used as a coordinate value.

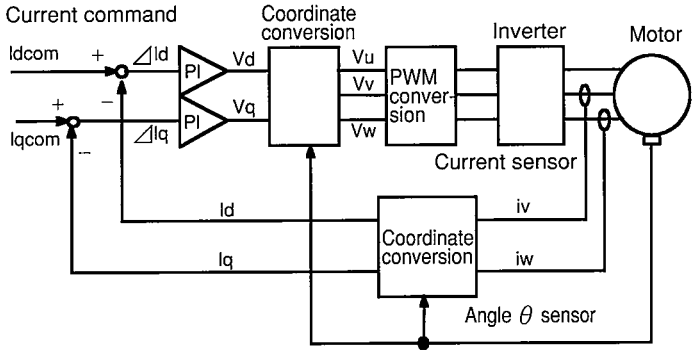

Fig. 7 Block Diagram of Current Control

2.3 Increase in motor power

Under a constant voltage, motor power drops, because the voltage restriction causes the system to switch to weak field control at high revolution speed. If the voltage that is applied to the motor could be increased, it would be possible to obtain the maximum torque at higher revolution speeds, thereby allowing the power to be increased. **Fig. 8** shows the relationship between the voltage applied to the motor and the motor power.

There are two ways to increase the voltage that is applied to the motor, both of which take maximum advantage of the limited power supply voltage. The first way is to increase the power supply voltage, and the other way is to alter the inverter switching waveform without changing the power supply voltage. These two approaches are described in detail below.

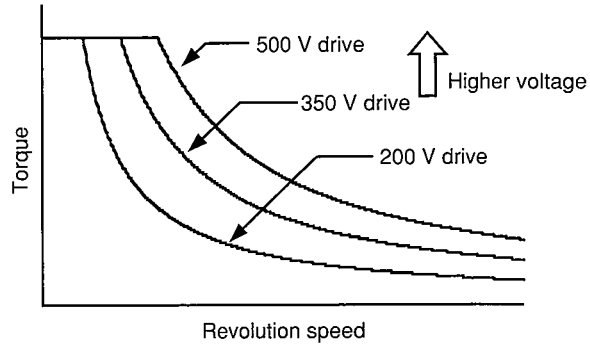

Fig. 8 Motor Applied Voltage and Torque

3. High-Power Motor Control

3.1 Voltage waveform and modulation rate

The voltage component that contributes to the motor power is determined by the basic wave component. The motor power can be increased by distorting the inverter output waveform to make the basic wave larger and magnify the basic wave component of the voltage. **Table 1** shows the inverter voltage waveforms and modulation rates. Here, the modulation rate is the ratio of the basic wave component of the output voltage waveform to the inverter power supply voltage. The voltage waveforms can be classified as sine wave PWM, overmodulation PWM, and rectangular.

Table 1 Voltage Waveform and Modulation Rate

	Sine wave PWM	Overmodulation PWM	Rectangular wave (1 pulse)
Voltage waveform	Base wave 	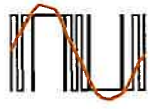	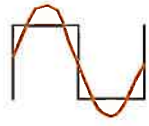
Modulation rate	0 – 0.61	0.61 – 0.78	0.78

Sine wave PWM is the most commonly used voltage waveform. Its advantage is that expressing the voltage and current as sine waves limits the torque fluctuation and makes the output smoother, but with a modulation rate only up to 0.61, the motor power is lower than with other waveforms.

The rectangular wave is the voltage waveform that, in theory, generates the maximum basic wave component. Its modulation rate is a constant 0.78. As the illustration in Table 1 shows, the voltage amplitude is not changed, so only the voltage phase can be manipulated by the control. The conventional current control algorithm assumes that both amplitude and phase can be controlled, so it can not be applied to a rectangular wave. A control algorithm was therefore developed for a PM motor that is driven by rectangular waves. A detailed description is provided below.

Overmodulation PWM is a complementary waveform with a modulation rate between those of sine wave PWM and a rectangular wave. In the hybrid system, if overmodulation PWM is not used, a drop-off in torque occurs in the medium-to-high speed range. The modulation rate can be varied from 0.61 to 0.78. Overmodulation PWM can manipulate both voltage amplitude and phase, so it can be used for current control.

Fig. 9 shows the application ranges of the different waveforms when a PM motor is driven by three types of voltage waveforms. Sine wave PWM and overmodulation PWM control the maximum torque, while the rectangular wave is used for weak field control.

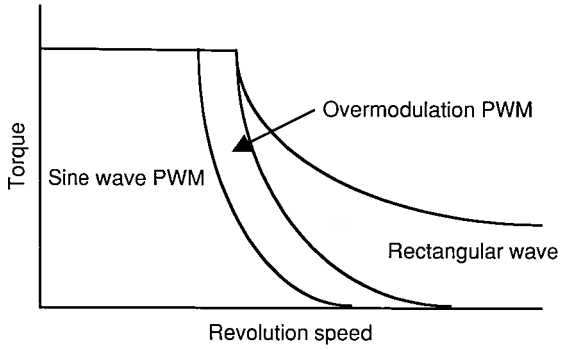

Fig. 9 Control of Each Voltage Waveform

3.2 Rectangular wave voltage phase control

To allow the PM motor to be driven by rectangular waves, a method was developed to control the torque by controlling only the voltage phase. If the PM motor voltage equation 1 and torque equation 2 are solved for the voltage phase, the relationship between the torque and the voltage phase is expressed by equation 3, in which θ is the phase angle in relation to the magnet.

$$T = -\frac{p\Phi V}{\omega Ld}\cos\theta - \frac{p(Ld - Lq)V^2}{2\omega^2 LdLq}\sin 2\theta \qquad (3)$$

Fig. 10 is a graph of the results of equation 3. There are regions in which the torque increases as the voltage phase advances. In those regions, the torque can be controlled simply by manipulating the voltage phase. **Fig. 11** illustrates the specific control configuration. The current torque is calculated in relation to the torque command from the hybrid vehicle control based on the three-phase AC power. Control of the torque by means of rectangular waves is accomplished by a torque feedback system that uses the deviations in torque as inputs to a computer, which then outputs the voltage phases.

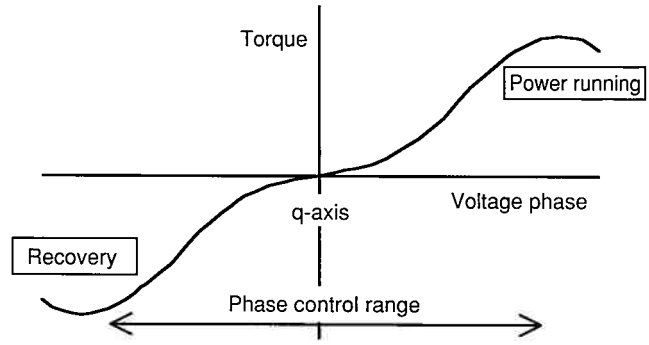

Fig. 10 Voltage Phase – Torque

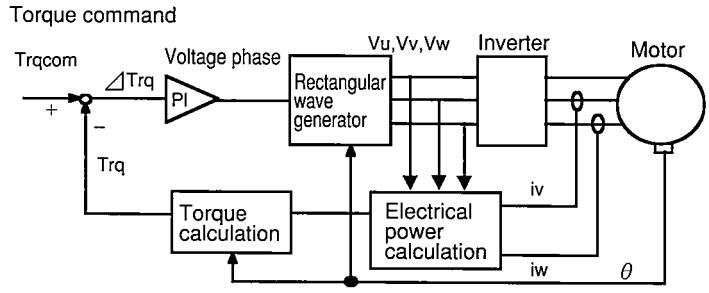

Fig. 11 Block Diagram of Rectangular Control

Fig. 12 shows the results of an evaluation of actual motor power when rectangular wave control is applied. A power increase of approximately 30% was achieved without any modifications to the motor, inverter, or battery.

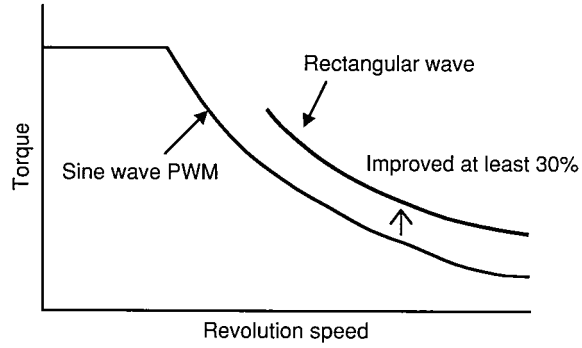

Fig. 12 Evaluation of Rectangular Wave Torque

3.3 Direct current offset feedback

In the PM motor, the angle sensor is used to control the voltage phase, but in a phenomenon peculiar to PM motors, any error on the part of the sensor causes the current to be offset. The mechanism by which this occurs is that the angle sensor error causes the switching timing to shift from its proper position, so that the rectangular wave duty is not in a 1:1 balanced state, but rather forms an unbalanced voltage waveform that is overlaid by the direct current offset. **Fig. 13** shows the offset current waveform.

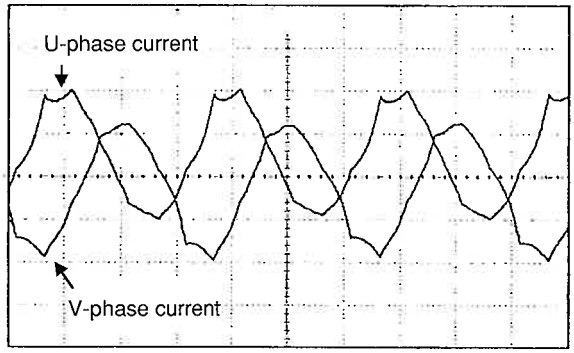

Fig. 13 Current Offset

If the PM motor current is overlaid by the direct current offset, an alternating field is added that is synchronized to the rotation of the magnet, raising concerns that eddy current will be generated, causing overheating, a drop in efficiency, and demagnetization of the magnet. To counter this phenomenon, a system was devised that detects the offset portion of the motor current and corrects the switching timing accordingly. The control configuration is shown in **Fig. 14**. First, the current waveform of the operating state is sampled for each phase, then the DC offset current is derived by computation. Next, the switching timing is corrected in the direction that will decrease the DC offset current.

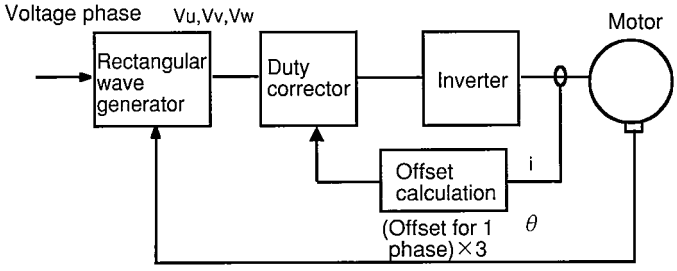

Fig. 14 Current Offset Feedback

Fig. 15 shows the current waveform that results from direct current offset feedback. It can be seen that the current offset is eliminated even when there is an angle sensor error.

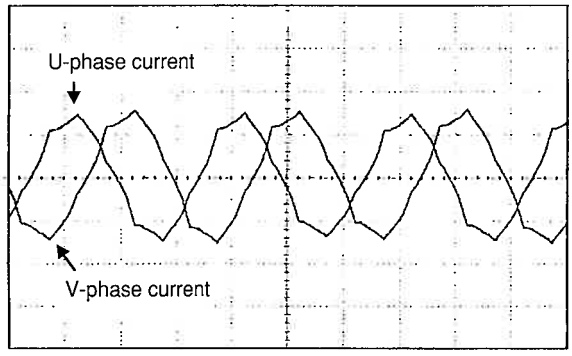

Fig. 15 Current Offset Correction

4. Variable Voltage System

4.1 System features

Increasing the inverter power supply voltage (system voltage) is one conceivable method of boosting the motor power. However, if the battery voltage is increased by adding more cells, the size and cost of the battery increase dramatically. Also, it is a property of batteries that the voltage is diminished by internal resistance due to the extraction of power (discharging), so high voltage can not be obtained when high power is desired. On the other hand, the voltage increases during charging, so the withstand voltage of parts such as the inverter element must be made higher than otherwise necessary, bringing more disadvantages in terms of size and cost. For these reasons, a variable voltage system was developed that adds a boost converter to convert the battery voltage to a higher value, instead of using the existing battery voltage. **Fig. 16** is a schematic diagram of the Toyota Hybrid System (THS), and **Fig. 17** shows an example of the system configuration and energy flow when the variable voltage system is applied to it. In this example, the battery voltage of 200 volts is boosted to 500 volts.

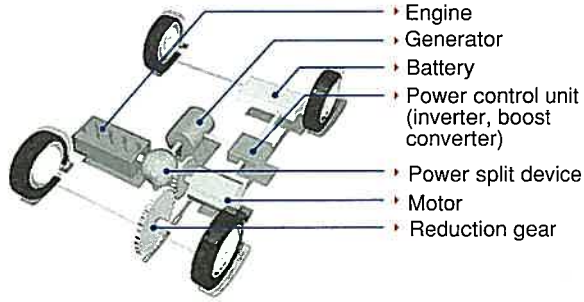

Fig. 16 Schematic Diagram of THS

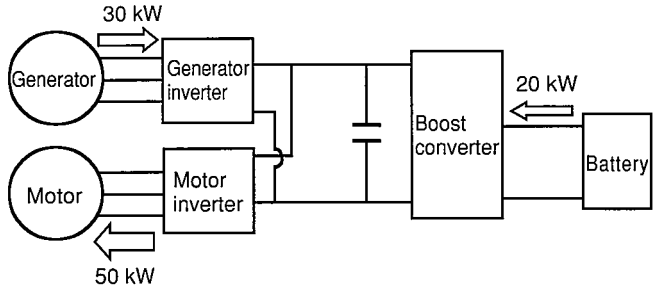

Fig. 17 Energy Flow in Variable Voltage System (Prius)

Because the variable voltage system involves adding a boost converter to the conventional system, the anticipated disadvantages would be an increase in the number of parts, a physically larger system, and an increase in loss to the extent that the boost converter is used. If the advantages of the system did not outweigh these disadvantages, it would never work. In the THS, which has both a motor and a generator, the power for the

motor is supplied mainly by the generator, with battery power accounting for a relatively small part. If the motor power is 50 kilowatts, as it is in **Fig. 17**, and the generator supplies 30 kilowatts, then only 20 kilowatts of battery power are required. The power coming out of the boost converter is essentially the power that is supplied by the battery, so a boost converter with a small capacity relative to the motor power should be sufficient. The increases in size and cost that result from adding the boost converter are more than offset by the decreases in the size and cost of the existing parts, such as the motor, inverter, and battery. The variable voltage system may thus be said to be highly compatible with the THS.

Moreover, with the variable voltage system, the system voltage and battery voltage can be varied independently, so the system design can be modified as necessary to match the vehicle power. The system voltage is determined on the basis of the motor power and the withstand voltage of the parts, while the battery voltage is determined by varying the number of cells to obtain the desired battery power and capacity. Thus, each voltage can be set independently to the optimum value.

4.2 Boost converter circuit

The boost converter circuit is shown in **Fig. 18**. The circuit is made up of a pair of IGBTs, an inductor, a main capacitor, and a filter capacitor. This circuit configuration can be operated continuously in both the charging and discharging directions relative to the battery without switching the circuit. The IGBTs operate on the basis of switching patterns that are calculated by the software, and they control the system voltage in the main capacitor by boosting the battery voltage. The range over which the system voltage can be freely controlled extends from the battery voltage at the lower limit to the withstand voltage of the parts at the upper limit. The inductor and filter capacitor are designed mainly to diminish the ripple current that is generated by switching. By reducing the ripple current that flows to the battery, they prevent loss and prolong the battery's life.

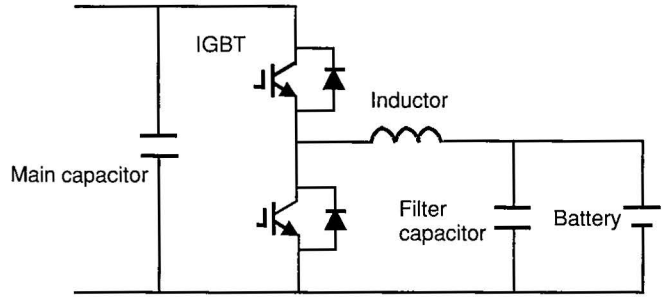

Fig. 18 Variable Voltage System

4.3 Variable voltage control

The boost converter is controlled by continuously varying the voltage according to the operating states of the motor and generator, so as to minimize the system loss. The loss generated by the motor system consists mainly of the following four types.

(1) Motor loss (copper loss plus iron loss)
(2) Inverter loss (on loss plus switching loss)
(3) Boost IGBT loss (on loss plus switching loss)
(4) Boost inductor loss (copper loss plus iron loss)

All of these types of loss are affected by the voltage, so the loss can be minimized by keeping the voltage at an optimum value.

The motor loss is the sum of the copper loss generated by the current that flows in the motor coil and the iron loss generated by changes in the magnetic flux of the iron core. The smaller the current that flows in the motor coil, the smaller the motor loss. If the system voltage falls below the induced voltage of the motor, weak field control takes over and the current increases, so the system voltage must be set to a higher value than the induced voltage.

The inverter loss consists of the loss in the switching elements like the IGBTs, and the lower the current and voltage, the lower the loss. When the current is at its minimum, the motor can not shift to weak field control, so the inverter loss is the same as the motor loss. However, the switching loss increases as the voltage rises, so loss is minimized by setting the voltage to the lowest value that does not cause a shift to weak field control. That is to say, the system voltage is made almost the same as the induced voltage.

The boost converter loss is the sum of the IGBT loss and the inductor loss. Both types of loss decrease as the current and voltage are reduced. The boost converter current is the same as the battery current, and the conditions that minimize the battery current are the same as those that minimize the system loss beyond the specified level. These conditions are essentially those that minimize motor loss and inverter loss as well.

The essential conclusion derived from the discussion above is that the condition that minimizes system loss is keeping the system voltage at almost the same level as the motor's induced voltage. The induced voltage varies according to the motor's operating state (revolution speed, torque), so loss can be minimized if the system voltage is controlled so that it also varies according to the motor's operating state.

Fig. 19 illustrates the motor voltage that is required when the motor is producing the maximum torque. When the motor operates in the low speed range, it outputs the battery voltage, which is the minimum voltage for the boost converter. When the motor operates in the high speed range, it is controlled by the system's maximum voltage. In the intermediate range, the system voltage is varied according to the motor speed to minimize the loss.

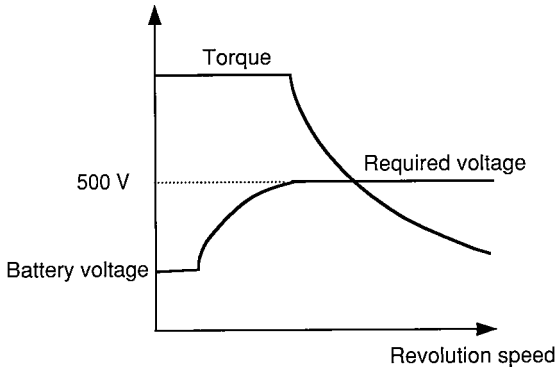

Fig. 19 Required Motor Voltage

Fig. 20 shows the flow of the system voltage calculation in the THS. In the case of the THS, where the motor and generator operate independently, the respective induced voltages do not match, so the higher of the two is selected as the system voltage. The reasons for doing so are that the desired power can not be obtained if the system voltage is too low, and increasing the system voltage reduces loss more than does using weak field control.

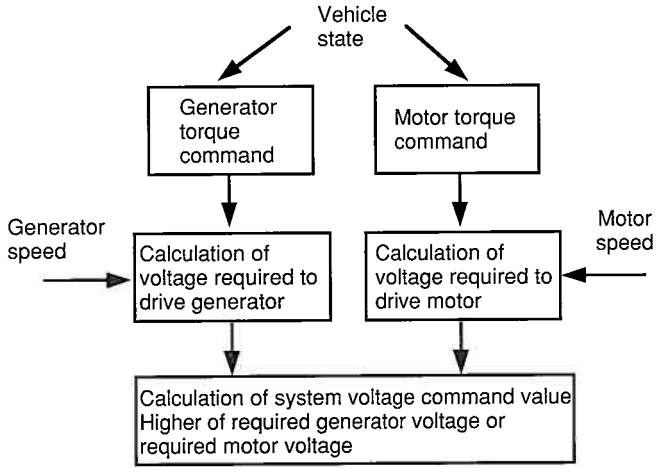

Fig. 20 System Voltage Calculation Flow

Fig. 21 shows an example of the relationship between the system voltage and the system loss. Three system voltages, 200 volts, 300 volts, and 500 volts, are compared. When the torque is at point (1) on the graph and the system voltage is 200 volts, weak field control takes over, so the loss is at its maximum. On the other hand, when comparing the system voltages of 300 volts and 500 volts, only the switching loss increases in the case of the system voltage of 500 volts. The loss at point (1) is lowest when the system voltage is 300 volts. At point (2) on the graph, weak field control takes over for the 300-volt system, increasing the loss above that of the 500-volt system. Therefore, a system voltage of 500 volts is appropriate when the torque is at point (2).

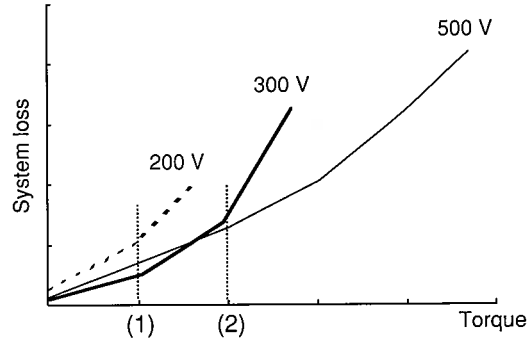

Fig. 21 Relationship Between System Voltage and System Loss

4.4 Evaluation results

Fig. 22 shows a comparison of motor performance in a Prius using the old THS and in one using the new THS II, which incorporates the variable voltage system. It can be seen that the use of the variable voltage system increases the motor power by approximately 50%, from 33 kilowatts to 50 kilowatts.

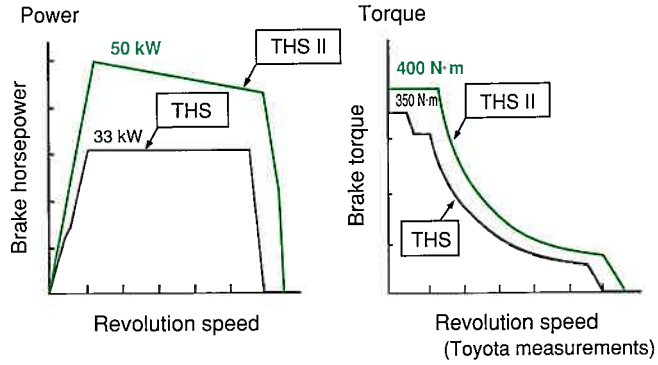

Fig. 22 Motor Performance Curve (Prius)

Fig. 23 shows the behavior of the system voltage when the accelerator is turned on and off. It is clear that the system voltage is controlled in a stable manner in response to changes in the system voltage commands.

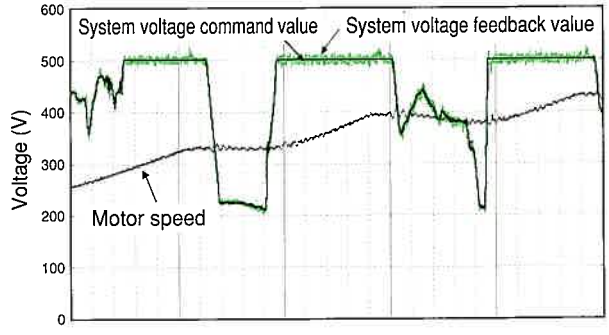

Fig. 23 Accelerator On-Off Evaluation

5. Technologies Used in the More Powerful RX400h

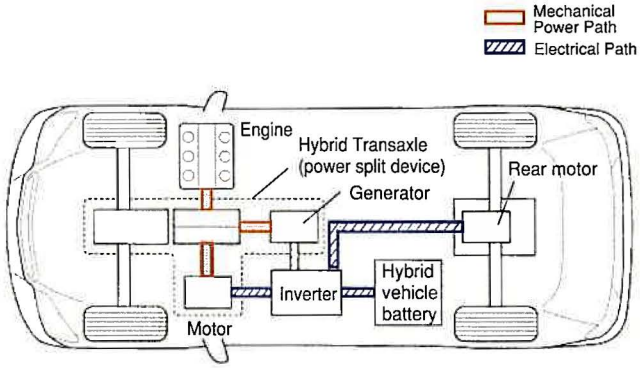

Fig. 24 Overall Structure of THS II (RX400h)

Fig. 24 shows the THS II configuration used in the RX400h. The front wheels are driven by the 3.3 L, 6-cylinder engine, the front motor, and the generator that are connected via the power split device. The rear wheels are driven only by the rear motor in this e-4WD configuration that has absolutely no drive shaft connecting the rear wheels to the front. The RX400h system is based on the THS II that is used in the new Prius, but one difference is that the reduction gear is positioned between the front motor output shaft and the power split device. The purpose of using the reduction gear is to increase the power while making the motor more compact.

The reduction gear approximately doubles the maximum front motor speed over that of the Prius, to 12,400 rpm, while increasing the maximum generator speed to 13,000 rpm.

5.1 RX400h system configuration

In the RX400h, which uses the same boost converter that is used in the Prius, the DC system voltage is increased from 500 to 650 volts. But because the rear motor is added to the system configuration, the boost converter supplies voltage to a total of three motors.

The purpose of increasing the system voltage to 650 volts was to increase the motor power. **Fig. 25** shows the output characteristics of the motor that is used in the RX400h.

The motor output (torque/power) increases in proportion to the boost in the system voltage. As **Fig. 26** shows, the front motor power of 123 kilowatts is approximately 2.5 times the 50 kilowatts of the Prius motor, but the battery power of 36 kilowatts has been limited to only approximately 1.7 times that of the Prius battery.

At the same time, it is extremely important for the three motors to operate in a stable manner on the limited battery power. Also, in order to minimize the space consumed by the three inverter units, the system is configured so that a single capacitor controls all three units. But this means that any fluctuation in the power of one motor causes the inverter input voltage to fluctuate, affecting the other two motors in turn. To avoid this problem, the fluctuation in motor power must be kept to a minimum.

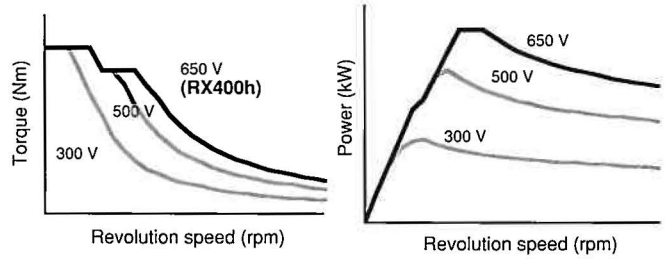

Fig. 25 Motor Output Characteristics

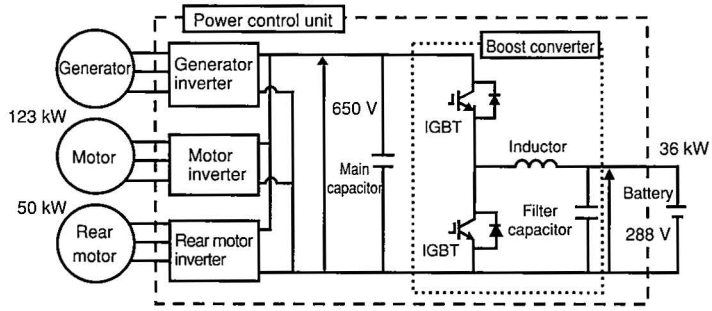

Fig. 26 RX400h System Diagram

5.2 Correction of resolver error (for even more power)

The resolver is capable of detecting absolute positions with extremely high accuracy, but due to its structure, a detection error arises that is synchronized to the rotation of the motor. **Fig. 27** is a schematic diagram of the resolver error.

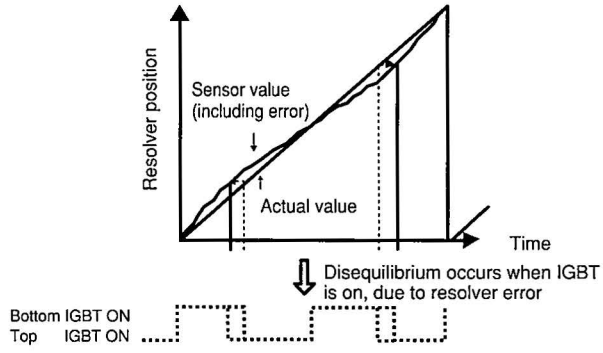

Fig. 27 Schematic Diagram of Resolver Error

The resolver error causes a phase change in the voltage vector that is input to the motor, which results in current fluctuation. For rectangular wave control, in which the voltage phase angle is 180 degrees, the resolver error causes an imbalance in the on times of the upper and lower IGBT units. As a result, the voltage input to the motor becomes unbalanced, which in turn causes the motor power to fluctuate. This effect becomes especially pronounced in the RX400h, with its high-power motor.

When the motor power is high, the power fluctuation also increases, causing the DC voltage input to the inverter to fluctuate as well. The boost converter operates so as to suppress the voltage fluctuation, but in the high-speed range, the resolver error causes the power to fluctuate at such a high frequency, so that the boost converter can not suppress the fluctuation effectively. A smoothing capacitor is therefore used to suppress the fluctuation. But if the rise in voltage that is caused by the power fluctuation is not adequately suppressed by the capacitor, the voltage fluctuates, which affects the other motors that are connected to the capacitor.

Fig. 28 shows the current fluctuation that results from the voltage fluctuation that is caused by the resolver error.

A control that corrects the resolver error was developed to solve this problem. First, when the motor speed is constant, the true angle is assumed to change in a linear manner, so that the difference between that and the detected angle is taken to be the resolver error. Next, the resolver signal is corrected based on the resolver error that was detected in the previous cycle. The current waveform after correction is shown in **Fig. 28**. It can be seen that neither the inverter input voltage nor the motor phase current fluctuates.

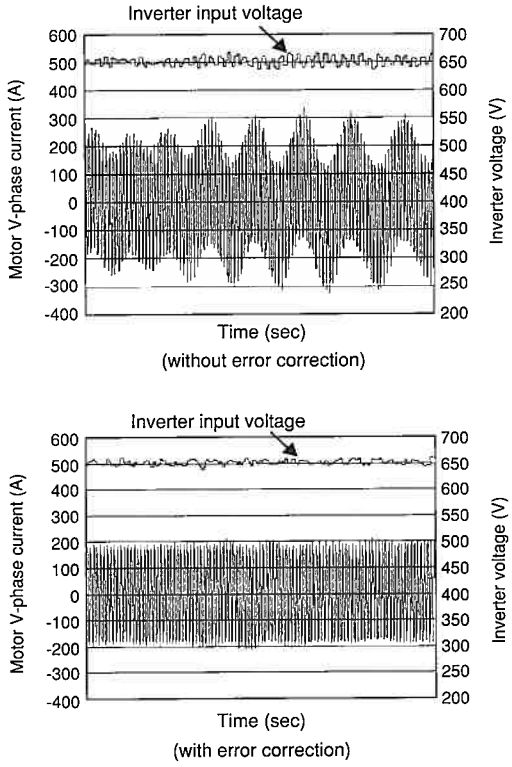

Fig. 28 Effects of Resolver Error

5.3 Power management control (for even more power)

In the RX400h system configuration, the exchange of energy among the three motors and the battery is extremely important. The proper amount of power must be supplied to the motor through the generator and battery.

Extremely large power consumption means that excessive amounts of energy are extracted from the battery, which leads to overcurrent flowing to the boost converter and a voltage drop in the battery. Particularly in a system that consumes a large amount of power, tire slippage and other factors tend to cause transient power imbalances. It is therefore necessary to correct power imbalances at a higher processing speed.

Ordinarily, the hybrid CPU controls the power by sending torque commands to the motor CPU. But because of a delay in communications between the hybrid CPU and the motor CPU, the hybrid CPU can not accurately determine the amount of power that is consumed by the motor. This communications delay constitutes a major problem for the control of the high-power system. A technique was therefore developed that prevents transient power consumption by using the motor CPU to monitor the power of each motor. **Fig. 29** shows the control configuration.

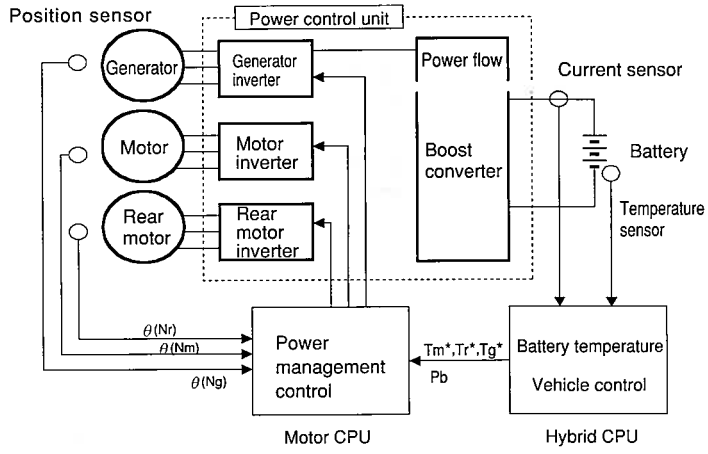

Fig. 29 Power Control Configuration for RX400h

One technique for managing power on the motor side is to define limit values based on the front motor power and the rear motor power. The motor CPU, which can monitor the energy conditions in real time, controls the amount of energy consumed so that it does not exceed the energy that is supplied. The limit values are calculated by the equations below.

$$Pm+Pr \leqq Pb-Pg-Pc-\text{loss} \quad (4)$$

$$Tm\_lim=Pm/Nm \quad (5)$$

$$Tr\_lim=Pr/Nr \quad (6)$$

The maximum value of the battery power (Pb) is defined by the state of the battery charge and the battery temperature. If power in excess of Pb is extracted from the battery, an excessively large battery current passes through the boost converter.

Pb changes more slowly than do the other control quantities, so its changes are mapped by the hybrid CPU, which then communicates them to the motor CPU.

The power accumulated and discharged by the capacitor (Pc) and the generator power (Pg) are calculated by the motor CPU, which then maps the loss based on those figures.

The torque limits (Tm_lim, Tr_lim) are calculated based on the power limit and the motor speed, which is recomputed on a moment-to-moment basis.

If the torque command from the hybrid CPU exceeds the limit value, the motor CPU acts to limit the torque.

5.4 Effect

Fig. 30 illustrates the effect of power management control.

As the data indicate, the high-speed monitoring by the motor CPU and the restriction on power effectively suppress the increase in battery current.

This prevents overcurrent from flowing to the boost converter and prevents the battery voltage from dropping.

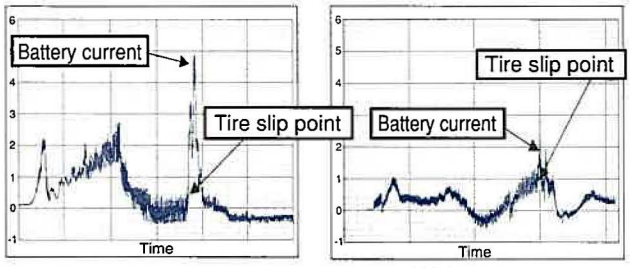

Fig. 30 Boost Converter Current

6. Conclusions

This article has described the use of high-power motor control as a motor drive technology to increase the power of the hybrid vehicle motor, as well as the variable voltage system and techniques that increase the motor power still further.

High-power motor control increases power by approximately 30% by using rectangular wave voltage to drive the motor. Two additional technologies were developed so that rectangular wave voltage control could be applied to the PM motor. One is rectangular wave voltage phase control, and the other is current offset feedback control.

In the variable voltage system, the boost converter converts the battery voltage into a high voltage, dramatically increasing the power. The system is highly compatible with the THS. Varying the voltage according to the operating state of the motor increases the power and reduces the loss at the same time.

Resolver error correction control and power management control were also developed for the RX400h to increase its power even more. These technologies are essential to making the high-power system operate in a stable manner.

It is believed that the importance of motor drive technologies in the automotive field will only increase as time goes on. Toyota will continue to develop additional technologies in the future.

References

(1) E. Satoh, Okamura, Sasaki. "High-performance Hybrid Vehicle Motor System and Its Control Technologies." *JSAE Symposium*, No. 07-04 (2004).

(2) H. Yaguchi, Sasaki. "The Motor Control Technologies for High-Power Hybrid System." *SAE* (2005).

Authors


H. HANADA


E. SATOH


M. OKAMURA


H. YAGUCHI

Development of High Output Power Control Unit for Hybrid SUVs

Takaji Kikuchi*
Kosei Matsubara**

Abstract
This article describes the power control unit installed in the RX400h hybrid vehicle. The features of this power control unit are (1) high system voltage; (2) a new system provided with a rear motor inverter; (3) high output density, achieved by enabling a high withstand voltage and reducing the size of each of the main component parts; and (4) a built-in motor controlling function separated from the hybrid controlling computer.

Keywords: *power control unit, inverter, converter, output density, soldering, wire bonding*

1. Introduction

The RX400h hybrid SUV launched in March 2005 is powered by a new generation hybrid system (**Fig. 1**). [1] This system realizes high levels of fuel economy and outstanding power by increasing the voltage and improving the control system from the Toyota Hybrid System II (THS II) used on the Prius. This article describes the latest technologies adopted in the newly developed power control unit (**Photo 1**) [1] of the THS II installed in this vehicle.

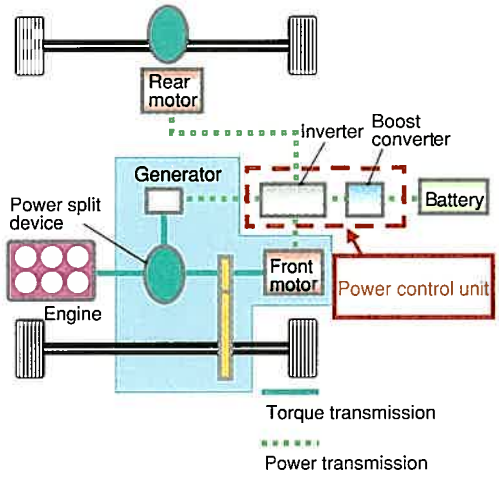

Fig. 1 Toyota Hybrid System II

Photo 1 Power Control Unit

2. Power Control Unit

The power control unit of the THS II is a high performance power conversion unit that integrates a boost converter that steps up the DC voltage supplied by a high voltage battery, inverters that convert the boosted DC voltage into AC voltage and applies it to the motors, and a DC/DC converter that converts the DC voltage supplied by the high voltage battery into 12 V DC to charge the auxiliary battery. **Table 1** [1] compares the specifications of this unit to the power control unit in the 2003 Prius.

* Hybrid Vehicle Powertrain Development Div.
** Electronic Components Dept. No. 3

Table 1 Comparison of Power Control Unit Specifications

	RX400h	2003 Prius
System voltage (VDC)	650	500
Maximum output current (Arms)	360	230
Main built-in parts	Boost converter, front motor inverter, generator inverter, rear motor inverter, DC/DC converter	Boost converter, front motor inverter, generator inverter, DC/DC converter
Mass (kg)	32	18
Volume (L)	30	20

3. Improvements to Power Control Unit

3.1 Increased system voltage

Fig. 2 [1] shows a conceptual system diagram of the power control unit. The Prius THS II used a boost circuit that effected variable control of up to 500 V. In contrast, the newly developed unit performs variable control of up to 650 V in accordance with driving state, in order to provide a boost voltage that minimizes system loss. As a result, the motor is able to achieve both high output and low power loss. Thus, along with the use of a larger sized motor, maximum motor output has been increased from 50 kW to 123 kW, an improvement of approximately 2.4 times. In addition, the system is equipped with an inverter with a maximum output of 50 kW to drive the rear motor.

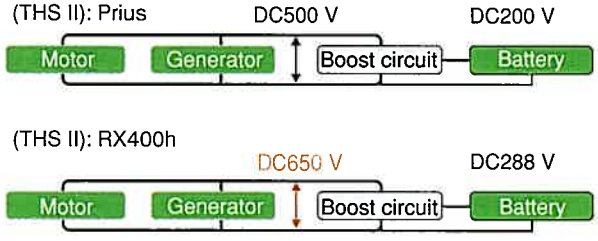

Fig. 2 Conceptual System Diagram

3.2 Configuration of power control unit primary circuit

Fig. 3 [1] shows the configuration of the primary circuit of the power control unit. The power control unit of the Prius has been supplemented with a rear motor inverter, which contributes to the enhanced dynamic performance required of SUVs. The inverters for the generator, front motor, and rear motor are voltage type inverters, which drive the generator, front motor, and rear motor by turning the switching devices ON and OFF using the voltage boosted by the boost converter. Inverter output is controlled by the voltage type PWM inverter method, which applies voltage to the generator or motor by sine wave output or square wave output in accordance with the revolution speed.

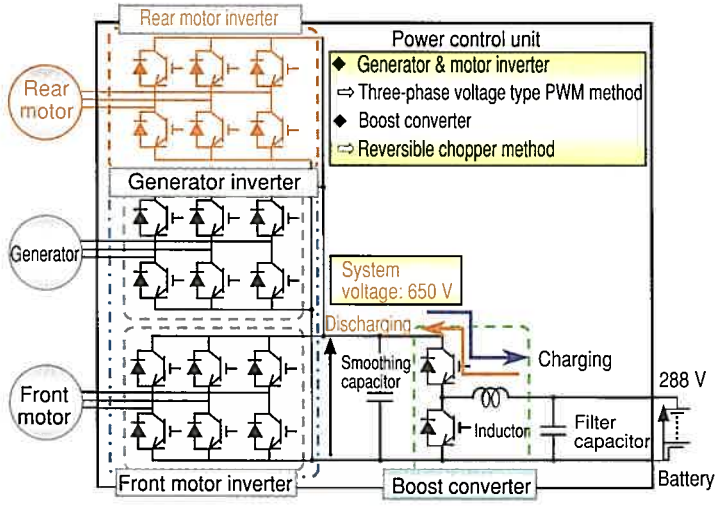

Fig. 3 Configuration of Primary Circuit of Power Control Unit

3.3 Increased output density of power control unit

Fig. 4 [1] shows the size reduction trend of the power control unit. Through the use of a higher system voltage and by making the component parts of the power control unit more compact, the output per unit volume has been improved by approximately 80% over the 2003 Prius.

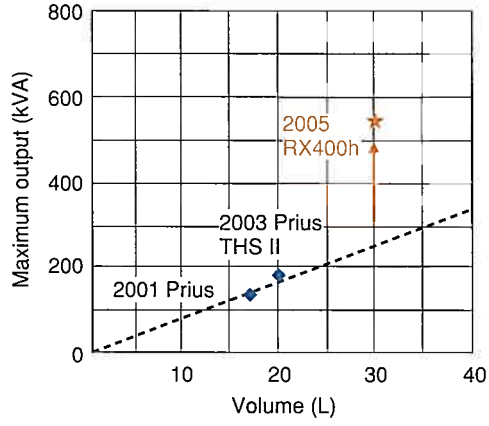

Fig. 4 Increased Output Density of Power Control Unit

3.4 Improvements to inverter-converter control system

Fig. 5 [1] shows the configuration of the control circuit of the power control unit. In the Prius power control unit, the motor controlling function to control the inverters and the boost power module was integrated in the hybrid controlling computer. However, the motor controlling function, which exchanges control information with the inverters and the boost power module in the power control unit, has now been separated from the hybrid controlling computer as a motor controlling computer and has been rearranged in the power control unit itself. As a result, the control signal wires for the inverters and the boost power module, which are used for controlling the motors, are completely enclosed in the power control unit. The wiring

between the power control unit and the hybrid controlling computer now consists only of communication signal wires, which means that the number of control signal wires has been reduced.

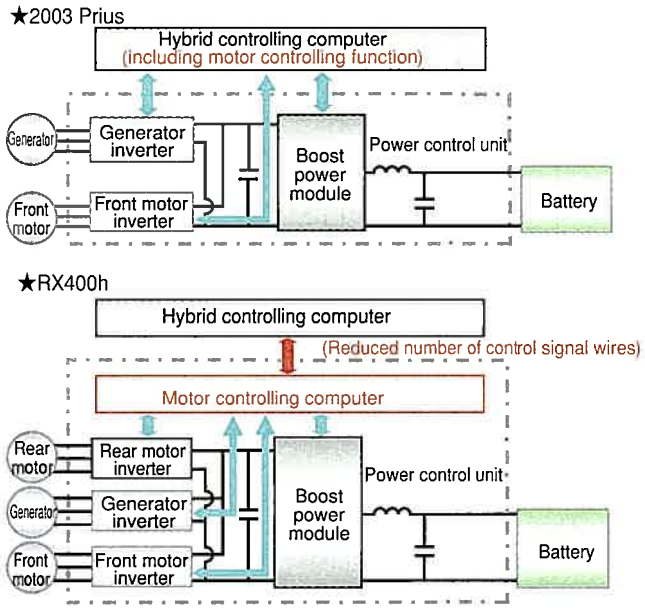

Fig. 5 Configuration of Control Circuit of Power Control Unit

4. Main Components of Power Control Unit

Fig. 6 [1] shows the structure of the power control unit. The unit is cooled by a water-cooling system that features components above and below a cooling channel. Located above the cooling channel are a front motor-generator inverter power module (integrating the generator inverter and the front motor inverter), and a rear motor inverter power module for driving the rear motor. Located below the cooling channel are the boost power module, the inductor, and the DC/DC converter. This configuration enables the system to cool the unit while maintaining a space-saving design. The capacitor is located above the front inverter power module. Furthermore, the new motor controlling computer is built into the power control unit.

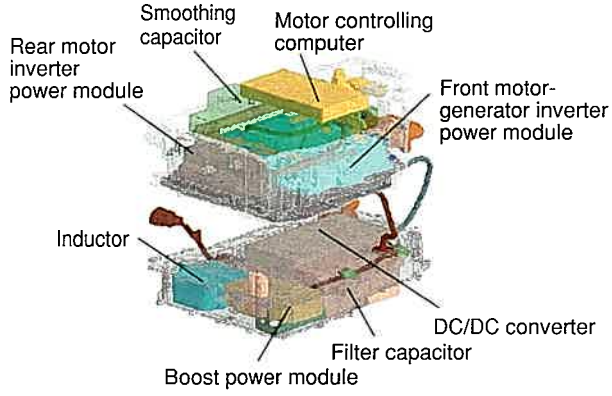

Fig. 6 Configuration of Power Control Unit

5. Technical Approaches to Higher Voltage and Output

5.1 Inverter power module

The inverters for the generator and the front motor require semiconductor switching devices in order to output power to the three-phase motors.

The new power module (**Photo 2**) [1] was developed in-house and it integrates a total of 12 of these semiconductor switching devices. Furthermore, this high performance power module contains the system voltage sensor, the output current sensor, and the device temperature sensor, all of which are required for controlling the motors.

The power semiconductor devices used in the primary circuit are 200 A class high withstand voltage trench type Insulated Gate Bipolar Transistors (IGBTs), which were also developed in-house. To support the high output, three IGBTs are connected in parallel in the front motor inverter, and two IGBTs are connected in parallel in the generator inverter (**Table 2**). [1]

In addition, the module has a self-protective operation that functions by detecting over voltage, over current, overheat, and internal power supply malfunctions of the power semiconductor devices and transmitting abnormal states to the motor controlling computer. The motor controlling computer also has a diagnosis function to detect sensor malfunctions, a design that takes system safety into consideration.

Table 2 Specifications of Front Motor-Generator Inverter Power Module

	RX400h	2003 Prius
System voltage (VDC)	650	500
Maximum output (kVA)	420	200
Front motor inverter	200 A class IGBT 3 connected in parallel	200 A class IGBT 2 connected in parallel
Generator inverter	200 A class IGBT 2 connected in parallel	200 A class IGBT
Volume (L)	3.3	3.0

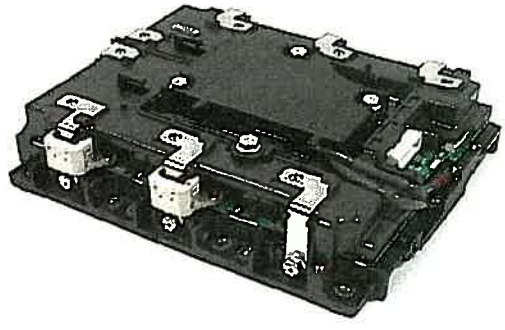

Photo 2 Front Motor-Generator Inverter Power Module

5.2 Rear motor inverter power module

The rear motor inverter power module (**Photo 3**) [1] is provided independently of the front motor-generator inverter power module. The power semiconductor devices used in six locations of the primary circuit to output power to the three-phase motor are the 200 A class high withstand voltage trench type IGBTs that were developed in-house. Like the front inverter power module, the control and drive circuits are integrated in this power module.

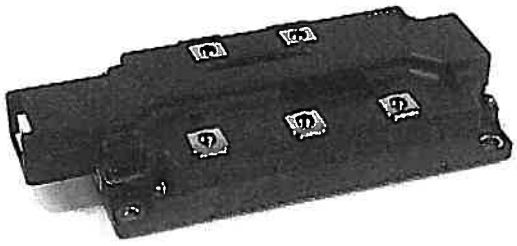

Photo 3 Rear Motor Inverter Power Module

5.3 Boost power module

The boost power module (**Photo 4**) [1] contains semiconductor switching devices in two locations to form a chopper circuit. Like the inverter power modules, the boost power module uses a special design with integrated control and drive circuits. The boost power module also uses IGBT power semiconductor devices, and contains four 150 A class IGBTs connected in parallel.

Like the inverter power module, this module is also provided with a protective function against over voltage, over current, overheat, and internal power supply malfunctions. The sensors are able to detect the battery voltage and the temperature of the power semiconductor devices.

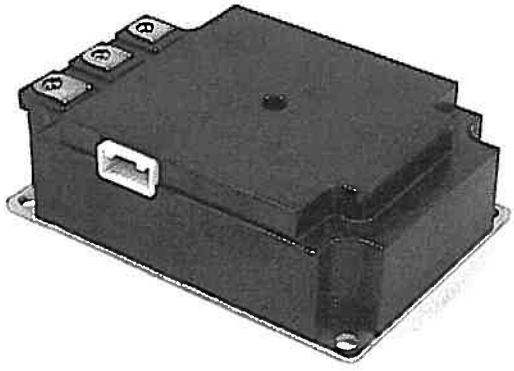

Photo 4 Boost Power Module

5.4 Capacitor module

The capacitor module contains a specially designed film type capacitor provided separately with a smoothing capacitor that smoothes system voltage, and a filter capacitor that reduces battery ripple current and noise. The capacitor devices use a newly developed, ultra-thin polypropylene (PP) film, which has enabled the capacitor unit to be reduced in size. A unique deposition pattern technique has also been developed to provide optimal patterns for achieving both high ripple support and a self-healing function. As a result of these measures, the capacitance density of the smoothing capacitor has been improved by approximately 20% from the 2003 Prius (**Fig. 7**). [1]

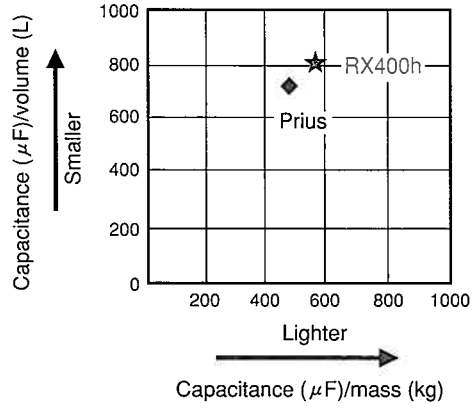

Fig. 7 Reduction in Smoothing Capacitor Size

6. Approaches to Production Technology

The power control unit used since the first-generation Prius (1997) has been kept entirely in-house, from development to production phases. High levels of productivity and quality have been attained by establishing a structural design in addition to processing and inspection technology that are highly suited for mass production. This suitability extends from individual parts of the power semiconductor devices, power modules, circuit boards, and inductors to the assembly stage.

Here is an example of the production technology applied to the power module shown in **Photo 5**. As a large current flows through the inverters in order to drive the motors, it generates a large amount of heat. To ensure the proper performance and quality of the product, heat dissipation technology (to efficiently dissipate heat) and wiring technology (to withstand the large current and heat) were essential.

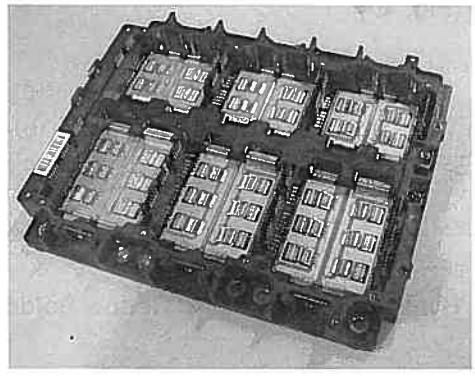

Photo 5 Power Module

6.1 High heat dissipation technology

The heat dissipation structure of the power module consists of the device, an insulating substrate, and a heat sink plate, which are joined by soldering (**Fig. 8**). The heat generated by the device is transferred to the parts and the joints, and dissipates to the aluminum case of the cooling channel through high heat dissipation grease.

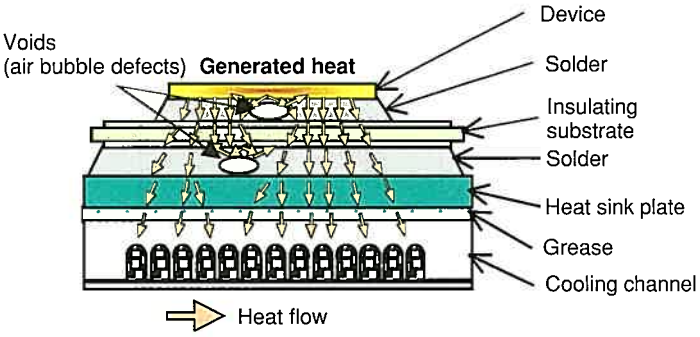

Fig. 8 Heat Dissipation Structure

6.1.1 Soldering

The voids (air bubble defects) created during soldering (hydrogen-deoxidizing reflow soldering) cause poor heat conductivity and inhibit the heat dissipation characteristic of the device. Because the present module contains a device totaling 30 cells that are joined together, the voids can greatly affect the defect rate.

The primary cause is trapped ambient gas. As a countermeasure, solder foil that exhibits a temperature difference between softening and melting is placed between the members. Heat is then applied gradually to flatten the solder while maintaining it at the softening temperature. The movement that this generates causes the gas between the members to be discharged, after which it is possible to reduce the voids by melting the solder (**Fig. 9**). However, this method requires the solder to be thoroughly softened, which involves a longer processing time. One remaining issue for the future, therefore, is to implement this countermeasure and yet still maintain productivity (**Fig. 10**).

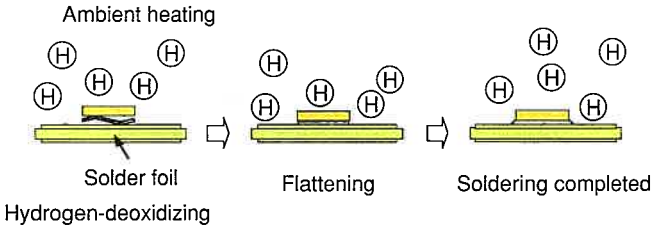

Fig. 9 Hydrogen-Deoxidizing Reflow Soldering

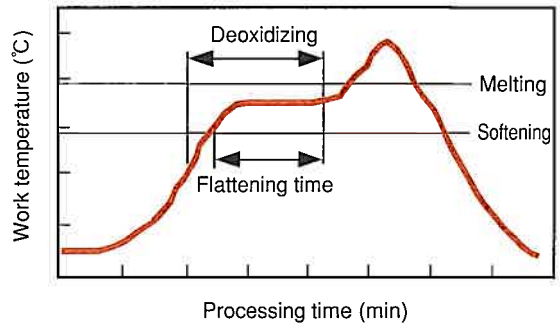

Fig. 10 Profile

6.2 Large current wiring technology

A wire bonding process using aluminum wires was used as the wiring technology for electrically joining the devices such as the IGBTs or Free Wheel Diodes (FWDs) with the electrodes or the bus bar. Wires of different diameters (ϕ150 µm, ϕ400 µm, and ϕ500 µm) were used for the different joints in the module, and approximately 900 wires were joined at over 2,500 points. This is on the largest scale of any part installed in an automobile.

6.2.1 Wire bonding

Heat is generated by the onboard environment as well as by the module itself. This generates stress and promotes cracks on joint interfaces, as a result of differences in the coefficients of linear expansion, thereby reducing the bond strength. For this reason, it was necessary to develop a bonding technology to enable the joints to withstand long periods of use.

The joints of the devices and aluminum wires are exposed to particularly severe heat generation conditions. For this reason, the area above the devices was stitch bonded to increase the bonding area without increasing the number of bonds. In addition, a wiring design (**Photo 6**) that suppresses temperature rise by, for example, optimizing the locations of the welding points and making the temperature distribution on the device surface more uniform, has been adopted to ensure a longer life.

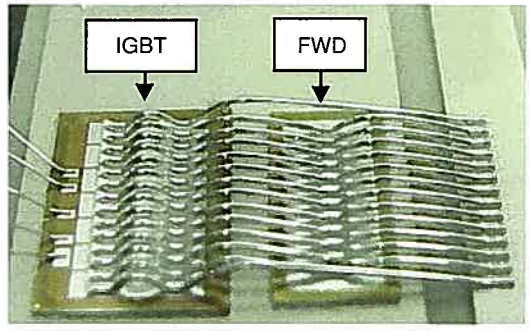

Photo 6 Wiring Above Devices

Moreover it was also necessary to deal with a conflicting issue in terms of the bonding conditions during processing. While a longer life can be attained by increasing the initial bond strength, application of excessive energy can harm the electrical characteristics of the device due to joint damage.

Photo 7 [2] shows the shape of the tip of the tool used in the processing equipment.

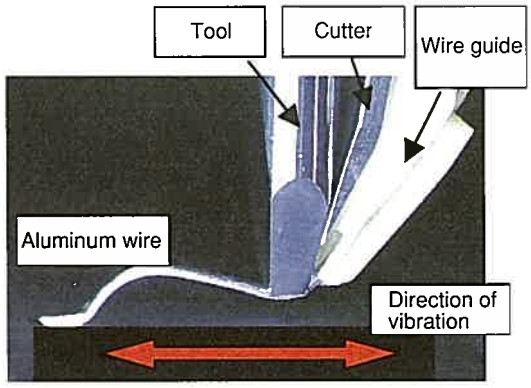

Photo 7 Tip of Tool During Bonding

As shown in **Fig. 11**, there are three bonding parameters: (1) vibration of the tool (power), (2) pressure applied by the tool (force), and (3) bonding duration (time). [2] The operating conditions have been set to optimize the joint interface state by controlling the power and force in stages. This reduces the joint damage inflicted on the device and ensures the proper bond strength.

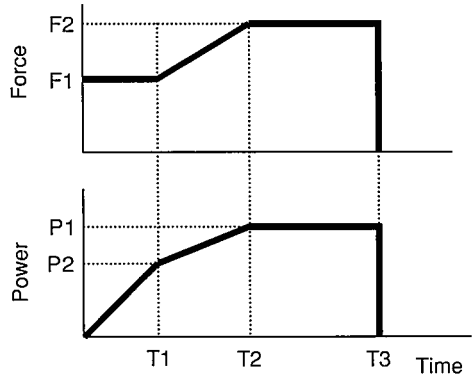

Fig. 11 Wire Bonding Parameters

6.2.2 Development of inspection technology

The shape of the wire after bonding is an important parameter in terms of reliability. However, because this condition cannot be inspected electrically, it has to be inspected visually. In response to this issue, an automatic inspection device (**Fig. 12**) was developed that uses optics to perform high-speed image matching. This device has shortened the inspection time and improved the inspection quality.

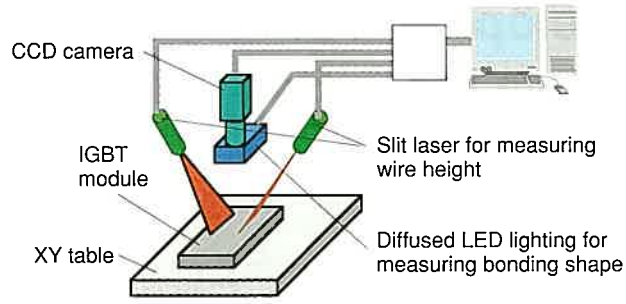

Fig. 12 Outline of Automatic Inspection Device

7. Conclusions

The development of a high output power control unit for SUVs involved the adoption of the following new technologies in addition to the aforementioned production technology, in order to realize a compact unit with a low cost and a high quality performance.

(1) System voltage was increased from DC 500 V to DC 650 V.
(2) A new system provided with a rear motor inverter was developed.
(3) A higher output density was achieved by increasing the withstand voltage and reducing the size of the main components of the power control unit.
(4) The motor controlling function has been separated from the hybrid controlling computer as a motor controlling computer and has been rearranged in the power control unit, thereby enabling the number of control signal wires and the cost to be reduced.

References

(1) T. Kikuchi, Shinmura. "Development of Power Control Unit for SUVs." *EVS21 Paper* (2005) pp. 1-8.
(2) T. Kimura, Inagaki, Shirai, Tada. "Analysis of the Wire Bonding Joints of an IGBT Module." *SAE Paper* 2003-01-1352 (2003).

Authors

T. KIKUCHI **K. MATSUBARA**

Development of Intelligent Power Module for Hybrid Vehicles

Makoto Imai*
Shinji Nakagaki**
Satoshi Hirose**

Abstract

Toyota developed a first generation Intelligent Power Module (IPM) for the inverter of the 1997 model Prius. Subsequently, a second generation IPM adapted for the high voltage and output of the THS II system, an Insulated Gate Bipolar Transistor (IGBT) and a Free Wheel Diode (FWD) have been developed for the inverter of the 2003 model Prius. In the second generation IPM, a boost converter has been added to the inverter to boost the power supply voltage and enable a reduction in current based on the relationship, power = voltage × current. The IPM has been reduced in size by measures including combining the IPMs for the motor and the generator, and continuing the integration of internal component parts, such as by combining the power supply circuit and the current sensor. In addition to the second generation 50 kW class IPM for the Prius, Toyota has also completed development of a 120 kW class IPM for the 2005 model RX400h, and plans have been made to expand the application of IPMs to other models. This article outlines the newly developed IPM and describes the new technology applied during the development.

Keywords: *hybrid vehicle, inverter, IPM, IGBT, FWD*

1. Introduction

Inverters are used as power converters in a variety of applications, but in a hybrid vehicle, the inverter converts direct current power from the battery into alternating current to drive the AC motor.

The key device within the inverter is the intelligent power module (IPM), which uses pulse width modulation to control DC/AC and AC/DC conversion in accordance with signals from the ECUs.

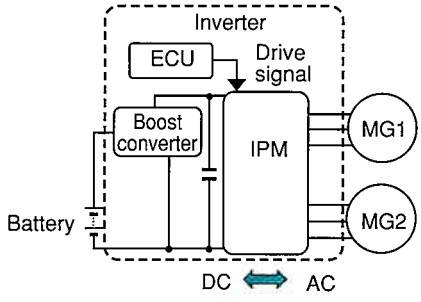

Fig. 1 Hybrid Vehicle System Diagram

In the THS II, as shown in **Fig. 1**, a DC/DC boost converter has been incorporated into the inverter to increase the input voltage to the IPM and reduce the current, thereby allowing the IPM to be made more compact.

The insulated gate bipolar transistor (IGBT) that serves as the switching device for DC/AC conversion was developed internally at Toyota to handle the higher voltage of the THS II. The IGBT was reduced in size more than 20% compared to THS by making it more efficient while generating less heat.

2. Basic IPM Structure

As shown in **Fig. 2**, the IPM consists of a module portion, which handles high voltage and current, plus a control circuit portion that controls the module. The module portion is made up of a heat sink that increases heat dispersion, an insulating substrate that ensures insulation, the IGBT power semiconductor that actually turns the current on and off, and a free wheeling diode (FWD).

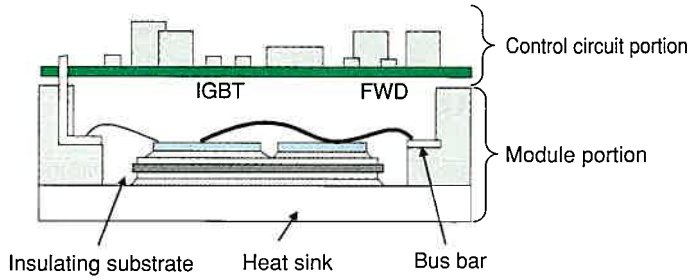

Fig. 2 Structure of Intelligent Power Module

* Electronics Engineering Div. 2
** Electronics Engineering Div. 3

2.1 Module portion

The original Prius had two separate, specially designed modules, one for the motor (288V/600A) and one for the generator (288V/200A).

In the second-generation Prius, the THS II booster system increases the voltage to reduce the IPM loss, as shown in **Fig. 3**, which allows the module to be made more compact even as its power is increased. The result is a decrease from 24 to 18 in the total number of IGBTs.

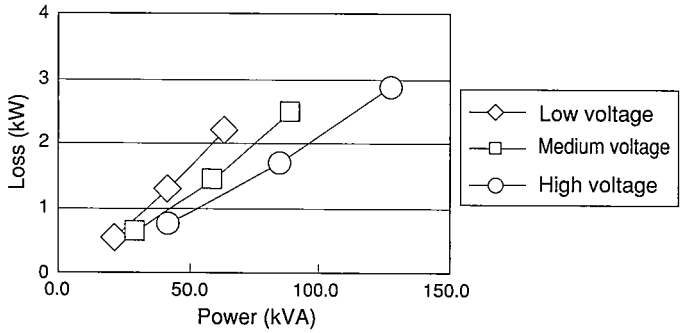

Fig. 3 Power-Loss Characteristics

The IPM is designed with dedicated circuits for each function, eliminating unnecessary terminal space. The circuits also share an optimized bus bar, allowing the generator (MG1) and motor (MG2) circuits in the RX400h to be housed in a single module, as they are in the new Prius. The result is the compact, high-power module shown in **Fig. 4**, with 320% more IPM power than in the original Prius, but occupying only 130% more surface area.

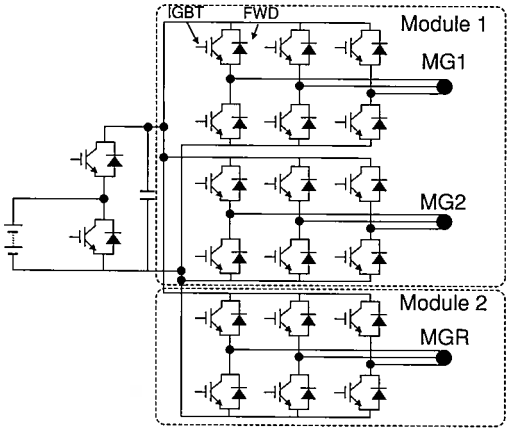

Fig. 4 Hybrid System Diagram for RX400h

Other changes that were made to adapt to the higher power included revisions to the heat sink material and the shapes of component parts to provide better heat dissipation at high temperature, as well as increasing the power density per unit surface area, as shown in **Fig. 5**. In this manner, the second-generation Prius 500V/200A+400A module was developed into the 650V/400A+600A module for the RX400h.

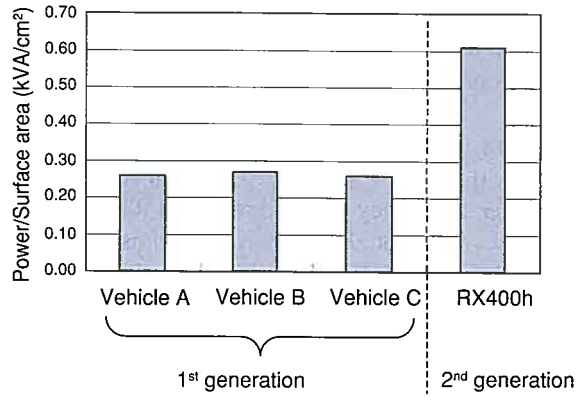

Fig. 5 Power Comparison

2.2 Control circuit

Conventionally, the inverter's internal control circuits are divided among three boards: a power supply and dead time generator board to control the IGBT, plus one IGBT driver board each for the motor and generator. Each driver board drives its power semiconductor based on logic signals and has an IGBT safety circuit to protect against short circuit current, heating, and other hazards.

For the second-generation IPM, the circuit configuration was revised to incorporate a power supply circuit that the first-generation IPM lacked, and a new IC was developed for the power supply and dead time generator circuits. More layers were added to the board itself to increase the parts mounting density, so that the number of parts was reduced to 75% and the board surface area to 52% of the first-generation IPM. Combining the motor and generator circuits in a single module opened up enough space that the same functionality could be provided in a single control board, with space left over to add a current sensor to the board. This has brought the benefits of fewer connectors, a smaller wiring harness, a more compact IPM, and higher productivity.

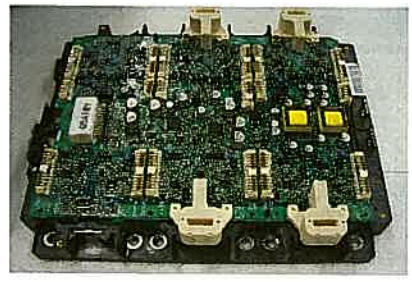

Fig. 6 Intelligent Power Module for RX400h

2.3 Power semiconductor

An internally manufactured IGBT and an FWD are used for the power semiconductor, as shown in **Fig. 7**. IGBTs play the role of the IPM switching device, generating three-phase power to drive the motor. The roles of the FWD are to freewheel the

energy that is accumulated by the motor load when IGBTs are off and to serve as a current path for taking the surplus energy that results from deceleration and braking and using it to charge the battery.

For the THS II, the goals were to increase the power supply voltage to 650 volts to give the motor more power, and to provide higher efficiency than the original THS. To achieve these goals, it was essential to increase the withstand voltage and decrease the loss in the IGBT and FWD, the key devices in the IPM. But in a power semiconductor, there is a trade-off between withstand voltage and loss, so the development of the new devices focused on how to achieve both goals at the same time.

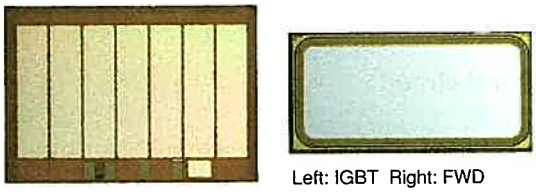

Fig. 7 Power Semiconductor for RX400h

2.3.1 IGBT

As **Fig. 8** illustrates, IGBTs have an emitter electrode on top and a collector electrode on the bottom. It controls the current by applying voltage to the gate electrode and has the switching performance of a MOSFET together with the high current processing capacity of a bipolar transistor.

The internally manufactured IGBT is the first power semiconductor in the world to be successfully produced on large-diameter 8-inch wafers. This creates a 2.8-fold increase in production capacity over 5-inch wafers and lowers the cost (converted to the unit cost of a 13-millimeter square device).

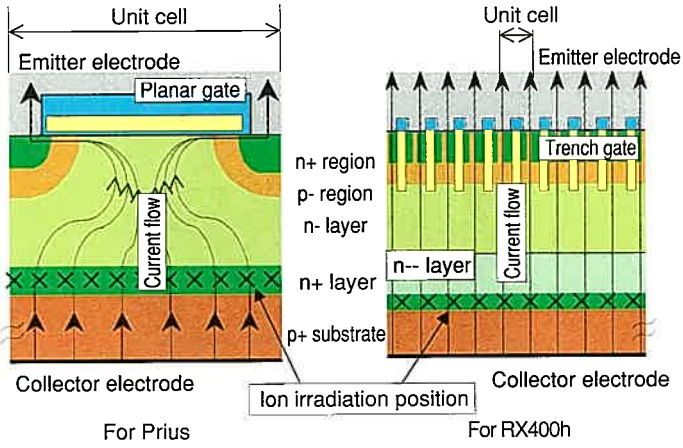

Fig. 8 IGBT Cross Section

2.3.1.1 Higher withstand voltage

A cross section of the IGBT used in the RX400h is shown on the right in **Fig. 8**. The wafer structure features a second withstand voltage holding layer (n— layer) in addition to the existing n- layer, giving the device two locations for holding the withstand voltage. The withstand voltage is thus increased without making the n- layer thicker and thereby increasing the loss.

2.3.1.2 Lower loss

The trench structure of the gate reduces the surface area of a device cell to one-ninth that required by the planar gate structure in the Prius IGBT, dramatically reducing the resistance per unit surface area. As for the increase in the short circuit current that is the penalty for using the trench structure, the short circuit capability is ensured by the design of the device top face. As **Fig. 9** shows, this is done by using a striped structure for the emitter and thereby narrowing the gate width, so as to suppress the short circuit current.

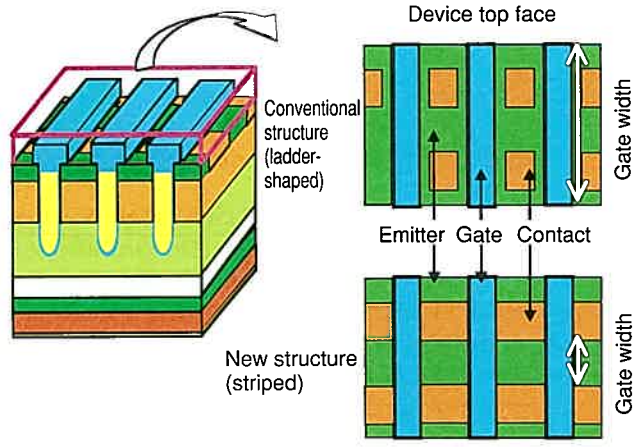

Fig. 9 IGBT Surface Structure

Local lifetime control [2] was implemented by means of helium ion irradiation to improve the switching characteristics. One characteristic of IGBTs is that the residual electric charge in the device causes the collector current to continue to flow immediately after the gate turns off. This leads to an increase in loss in the IGBT for the IPM, which requires high-speed switching. Lifetime control is a technology that creates localized defects in the interior of the device, as shown in **Fig. 8**, so that the residual charge will be efficiently dissipated. The advantage of controlling the process by means of helium ion irradiation, as opposed to other means of defect formation, is that it makes high-speed switching possible without significantly affecting steady-state loss.

2.3.1.3 Summary

Fig. 10 shows the withstand voltage in relation to the steady-state loss for the IGBT in each generation of the Toyota Hybrid System. The optimization of the device structure of the internally manufactured IGBT has achieved both higher withstand voltage and lower loss, characteristics generally thought to be mutually exclusive.

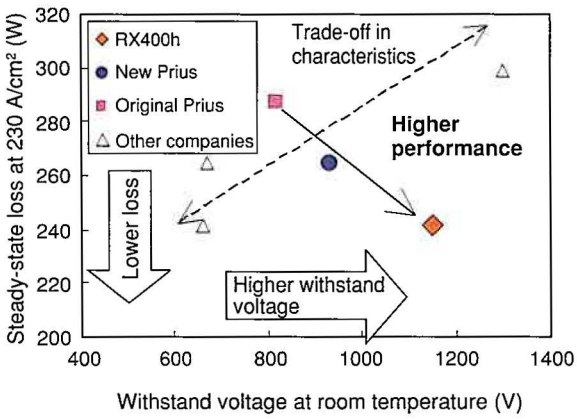

Fig. 10 IGBT Withstand Voltage and Steady-State Loss

2.3.2 Free wheeling diode

The FWD uses the PIN structure shown in **Fig. 12**, in which making the intrinsic layer thicker allows the withstand voltage to be increased. However, making the intrinsic layer thicker also increases the loss (in the form of forward voltage drop Vf and reverse recovery charge Qrr). The surge voltage (Vakp) that is generated in the FWD during the switch from forward voltage to reverse voltage also had to be reduced. The sections below describe how the loss and surge voltage were reduced. (The required characteristics are shown in **Fig. 11**.)

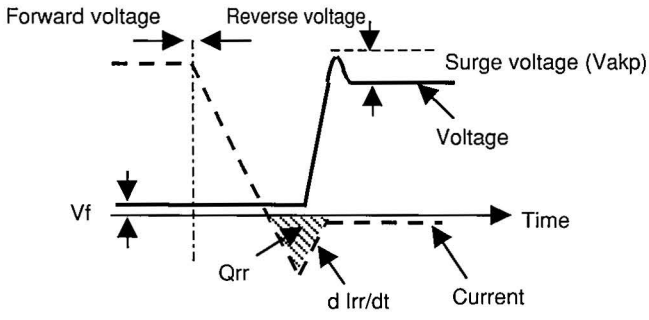

Fig. 11 Recovery Waveform for FWD

2.3.2.1 Loss reduction

The cross section of the FWD is shown in **Fig. 12**. The p+ structure is striped to increase the p+ surface area and make it more efficient to move a charge from the p+ region to the intrinsic layer. This decreases the loss (Vf) under forward voltage. Also, during the switch from forward voltage to reverse voltage, the time when current flows in the reverse direction has been shortened and Qrr has been reduced by passing the electric charge through the p- region.

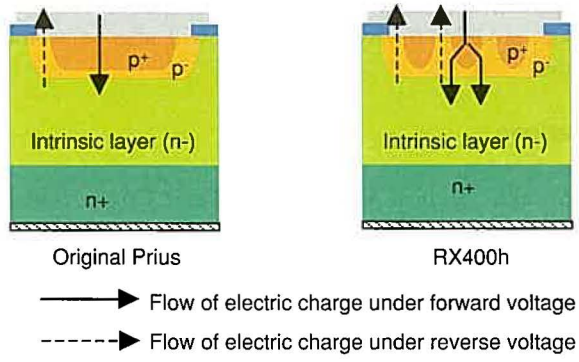

Fig. 12 FWD Cross Section

2.3.2.2 Surge voltage reduction

The surge voltage (Vakp) is expressed by equation 1.

$$Vakp = L \times dIrr/dt \qquad (1)$$

Here, L represents the system load, while dIrr/dt is the gradient of the current (as shown in **Fig. 11**). Localized defect formation by helium ion irradiation is used as a technique to reduce the value of dIrr/dt. The time it takes to dissipate the charge by forming defects (the current gradient) can be controlled. Helium ion irradiation makes it possible to form defects locally (within the intrinsic layer), gradually dissipate the charge (make dIrr/dt smaller), and reduce the surge voltage.

2.3.2.3 Summary

Fig. 13 shows a comparison of the Toyota FWD with FWDs from other companies. The Toyota FWD achieves both higher withstand voltage and lower loss.

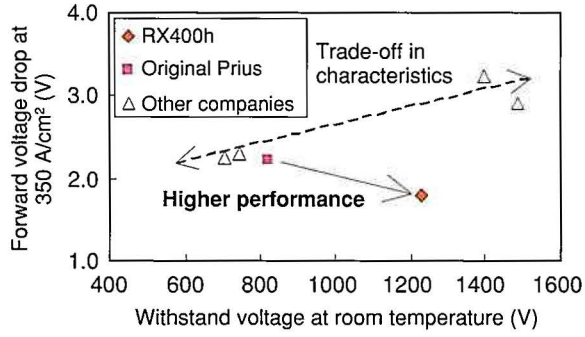

Fig. 13 Comparison of FWD Characteristics

3. Conclusion

A compact, higher-performance, second-generation IPM for hybrid vehicles has been developed through the original

development of a new power device. The development of additional products for hybrid vehicles will also be promoted in the future.

References

(1) S. Sasaki. "Hybrid Vehicles and Their Component Parts." *Jidousha Gijutsu* Vol. 59 No. 2 (2005) pp. 74-77.
(2) A. Mase, Nishiwaki, Kushida. "Development of IGBT for Hybrid Vehicles." *Toyota Technical Review* Vol. 48 No. 1 (1998) pp. 82-87.
(3) K. Nishiwaki, Kushida, Kawahashi. "A Fast and Soft Recovery Diode with Ultra Small Qrr Using Local Lifetime Control by He Ion Irradiation." *ISPSD '01* (2001) p. 235.

Authors


M. IMAI


S. NAKAGAKI


S. HIROSE

Development of a New Battery System for Hybrid Vehicles

Masanori Ito*
Shuuichi Nagata*

Abstract
In order to address environmental concerns, Toyota has developed various models including the new Prius released in September 2003, and a hybrid SUV, the Lexus RX400h which was launched in March 2005. These hybrid vehicles feature the Toyota Hybrid System II (THS II). This article discusses the development of a new battery system, which is a key component of the THS II. To simultaneously improve mountability and cooling performance of the new battery system, development activities focused on reducing the size of the battery and its packaging, and improvement of the cooling system.

Keywords: *battery, hybrid vehicle, Ni-MH*

1. Introduction

Toyota Motor Corporation initially released the Prius, the world's first hybrid vehicle (HV), for sale in December 1997. This vehicle, which achieved a landmark improvement in fuel consumption and a dramatic reduction in emissions, was later launched in North America and Europe in 2000. Following the September 2003 launch of a completely made over new model, the Prius has won broad support from people all around the world.

Going a step further, we developed the Lexus RX400h (**Fig. 1**) and the Highlander Hybrid. These vehicles are powered by the next generation THS II (**Fig. 2**), which was developed in pursuit of the world's ultimate environmental performance, while also aiming to escalate the "fun to drive" aspect, which is the essential appeal of automobiles.

Fig. 1 Lexus RX400h (US Specifications)

The vehicles are equipped with a new battery system and nickel metal hydride batteries that play important roles in the THS II. This article describes the batteries and the battery system based primarily on the Prius and the Lexus RX400h.

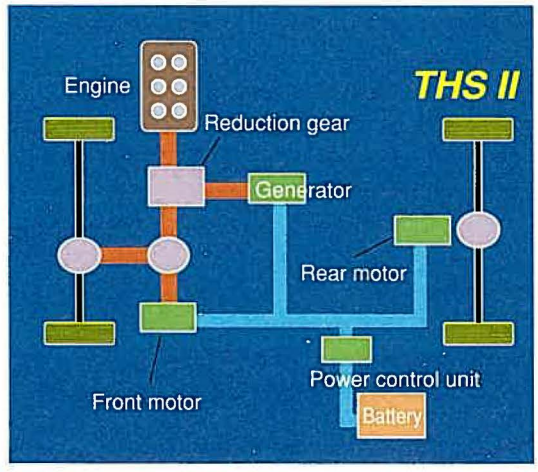

Fig. 2 Toyota Hybrid System II (4WD-i)

2. Prius

2.1 Battery module

The Prius and the Lexus RX400h use compact, high output, long life nickel metal hydride batteries. **Fig. 3** shows the charge-discharge mechanism of the nickel metal hydride battery.

* Hybrid Vehicle Power Train Development Div.

The nickel metal hydride battery is a type of rechargeable battery that primarily employs nickel hydroxide for the positive electrode and a hydrogen-absorbing alloy for the negative electrode. Its electrolyte is an alkaline solution containing potassium hydroxide as the primary component.

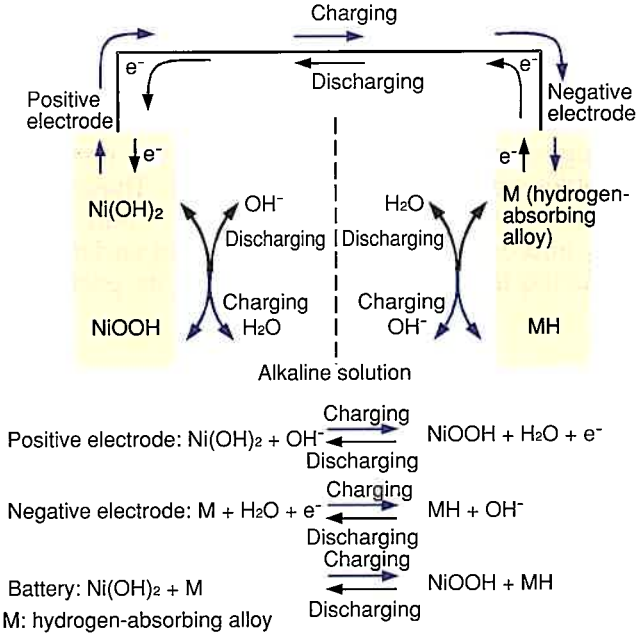

Fig. 3 Charge-Discharge Mechanism of Nickel Metal Hydride Battery

Table 1 shows the specifications for the battery module. The modules used on the 1997 Prius consisted of cylindrical, 6-cell, inline nickel metal hydride batteries.

Starting with the 2000 Prius, a prismatic shape was adopted for the battery module to realize superior heat dissipation and ease of installation. The module consists of 6-cell, inline nickel metal hydride batteries housed in a plastic battery case.

Furthermore, the internal electrical resistance of the battery module and cells of the 2003 Prius (**Figs. 4** and **5**) has been reduced 30% from the 2000 Prius. This was achieved through the following measures: using improved electrode material to reduce the reactive resistance of the electrode, and improving the cell interconnection structure to reduce the resistance of the parts (**Fig. 6**). [1]

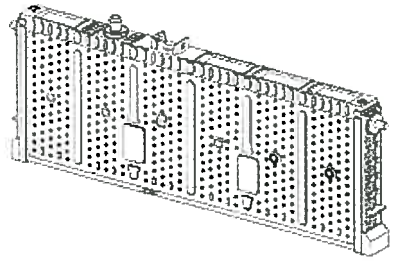

Fig. 4 Battery Module for 2003 Prius

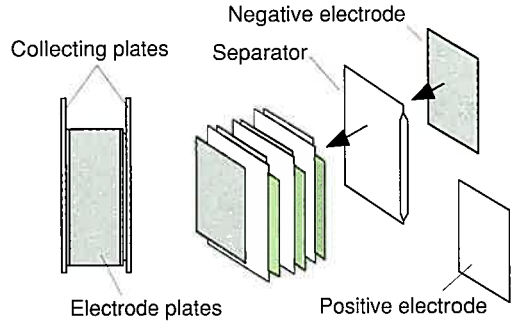

Fig. 5 Battery Cell for 2003 Prius

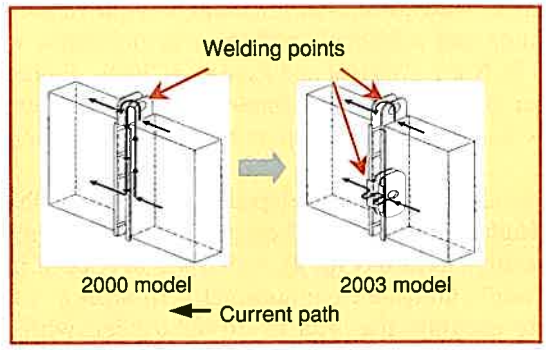

Fig. 6 Current Path in Prius Battery Module

Table 1 Battery Module Specifications

	2005 Lexus RX400h	2003 Prius	2000 Prius	1997 Prius
Shape	Prismatic	Prismatic	Prismatic	Cylindrical
Voltage	9.6 V	7.2 V	7.2 V	7.2 V
Capacity	6.5 Ah	6.5 Ah	6.5 Ah	6.5 Ah
Weight	1510 g	1040 g	1050 g	1090 g
Size	382 mm(L) 15.6 mm(W) 86 mm(H)	285 mm(L) 19.6 mm(W) 106 mm(H)	275 mm(L) 19.6 mm(W) 106 mm(H)	35 mm(ϕ) 384 mm(L)

2.2 Battery pack

Fig. 7 shows the configuration of the 2003 Prius battery pack. (2)

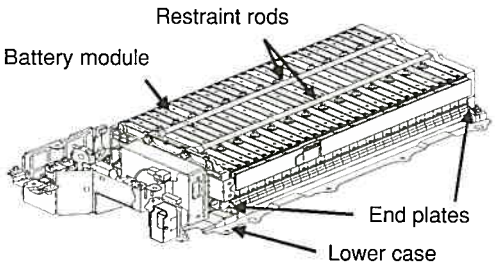

Fig. 7 2003 Prius Battery Pack

The 2003 Prius battery pack is configured such that lateral pressure exerted by the battery modules is borne by the end plates at both ends of the pack, the restraint rods, and the lower case. Forces (vertical and longitudinal forces) applied by the vehicle are borne by the lower case and the battery module fasteners.

Through improvements made to the battery module, this battery pack is able to produce the same amount of output as the previous model with fewer battery modules. However, decreasing the number of battery modules leads to a drop in power supply voltage, which poses the problem of reduced efficiency of the motors and generator.

To counter this problem, the 2003 Prius uses a variable voltage system (**Fig. 8**), which boosts the battery voltage to 500 V. Thus, even with a reduced number of battery modules, the system can use the battery pack efficiently to drive the motors and generator. Consequently, it was possible to reduce the number of battery modules from 38 on the 2000 Prius to 28, while at the same time maintaining the proper output performance of the battery pack.

As a result of reducing the number of modules and using end plates made of plastic, the battery pack as a whole has been made 15% more compact in terms of volume, and its weight has been reduced 25%.

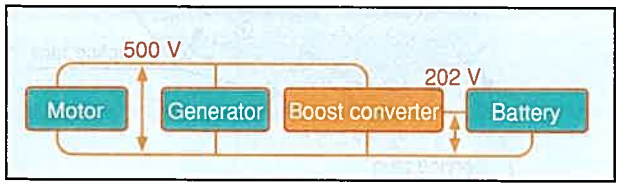

Fig. 8 Variable Voltage System for 2003 Prius

Fig. 9 shows the configuration of the battery pack for the 2003 Prius, and **Fig. 10** shows its schematic diagram.

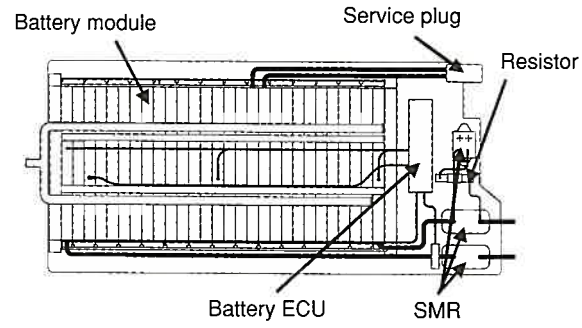

Fig. 9 Configuration of Battery Pack for 2003 Prius

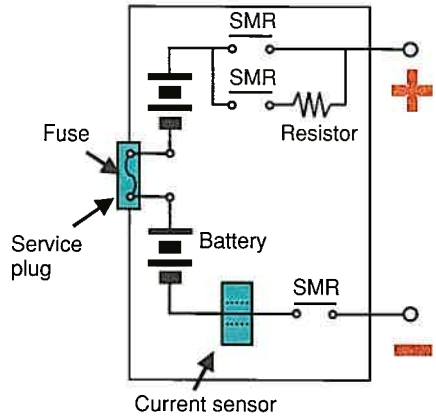

Fig. 10 Schematic Diagram of Battery Pack

To ensure the safety of the batteries, the high-voltage components are built into the battery pack for the 2003 Prius. They consist of system main relays (SMRs), a service plug with a built-in fuse, a battery electronic control unit (ECU), and a current sensor. These components have also been made more compact and lightweight.

(1) SMR

The SMR, whose primary function is to shut off current, opens and closes in unison with the ON/OFF operation of the ignition key. When the ignition key is turned to OFF, it cuts off the high-voltage system to ensure safety. It functions in the same manner in case of a vehicle collision or system failure.

(2) Service plug with built-in fuse

The fuse prevents electrical shocks and vehicle fires in the event the batteries become shorted as a result of a collision or the like. The service plug, which mechanically cuts off the circuit, ensures the safety of the technician servicing the vehicle.

(3) Battery ECU, current sensor

The battery ECU calculates the state of charge of the battery based on the battery current, voltage, and temperature, and transmits this information to the control systems on the vehicle. It also monitors the batteries for malfunction. The current sensor is used for calculating the state of charge of the batteries.

2.3 Cooling

The battery pack of the Prius is installed behind the rear seat. Following suit from the previous model, the 2003 Prius uses an air-cooled system that circulates cabin air to cool the batteries.

As a result of fewer battery modules on the 2003 Prius, their current input and output while charging and discharging a given amount of power have increased over the previous model. Nevertheless, the generation of heat has been suppressed to the level of the previous model by reducing the internal electrical resistance of the battery modules.

Fig. 11 shows the flow of the cooling air. As a result of reducing the number of battery modules and optimizing the configuration of the ducts and the pack, the temperature variance among the battery modules has decreased compared to the previous model.

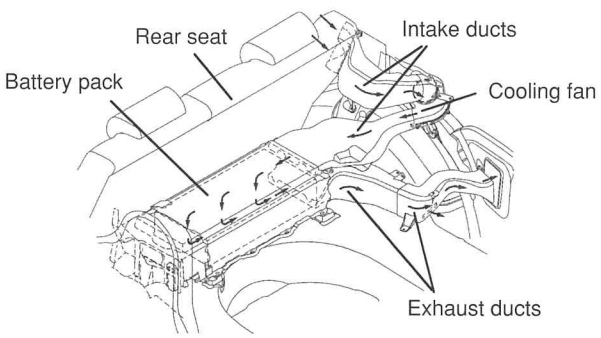

Fig. 11 Flow of Battery Cooling Air on 2003 Prius

3. Lexus RX400h

3.1 Battery module

Figs. 12 and **13** show the battery module and a single cell for the Lexus RX400h. Like the 2003 Prius model, a prismatic shape has been adopted for the battery module on the Lexus RX400h. In addition, a metal battery case that excels in heat dissipation and ease of installation was adopted. As a result, a 20 mm reduction in height compared to the previous battery module was achieved.

Two separate positive terminals for the battery cells have also been provided in the battery module for the Lexus RX400h in order to reduce the internal electrical resistance. Because the cells are single, independent cells, they offer freedom of selection for the number of cells in a module. The new module consists of 8 inline cells.

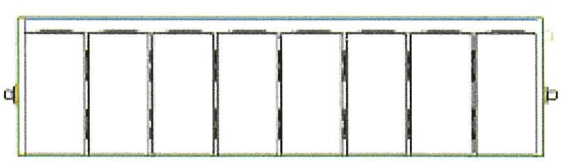

Fig. 12 Battery Module for Lexus RX400h

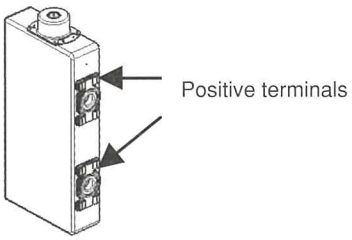

Fig. 13 Battery Cell for Lexus RX400h

As a result of these measures, the battery module has achieved the world's highest level of output density, with an improvement of over 30% per volume compared to the 2003 Prius (**Fig. 14**).

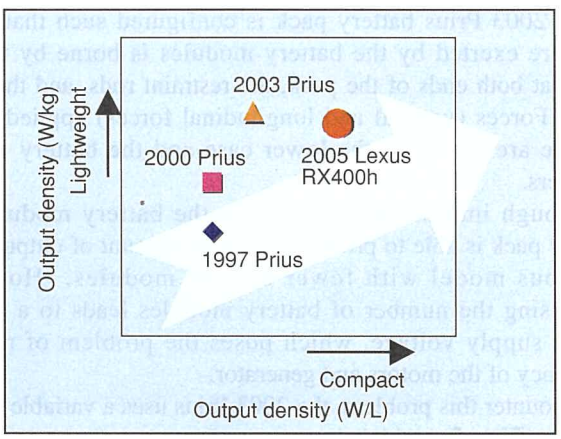

Fig. 14 Output Density

3.2 Battery pack for Lexus RX400h

Fig. 15 shows the battery pack for the Lexus RX400h.

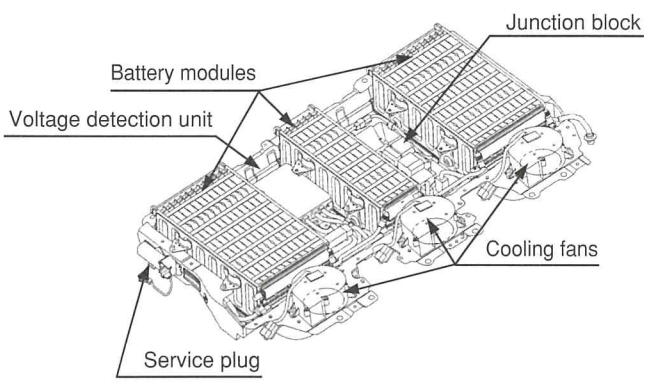

Fig. 15 Battery Pack for Lexus RX400h

Like the Prius model, the high-voltage components are built into the battery pack for the Lexus RX400h. In addition, the cooling fan is also built in.

The battery pack for the Lexus RX400h contains 30 battery modules for improved battery output. Like the Prius, the Lexus RX400h uses a variable voltage system to boost the battery

voltage to 650 V. This enables the system to operate the motors and generator in an efficient manner.

The battery pack is divided into three parts: one assembly of 6 modules, and two assemblies of 12 modules. The modules are arranged in a single row and restrained by end plates at both ends, as well as upper and lower metal bands. Moreover, as a result of developing thin, high-strength end plates, their thickness has been reduced 50% (**Fig. 16**).

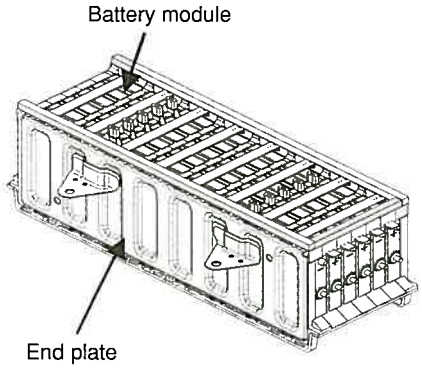

Fig. 16 Battery Module Assemblies

(1) Junction block

Components including the three system main relays (SMRs), resistors, and current sensors, which were previously provided separately, have been integrated into a junction block. This has improved the ease of installation and maintenance.

(2) Battery smart unit

Starting with the Lexus RX400h, the battery ECU has been discontinued. Instead, the vehicle control ECU handles the state of charge calculations and the monitoring of the batteries for malfunction. For this reason, the unit consists of a simple function to transmit battery voltage, temperature, and current information to the vehicle control ECU.

Through optimal packaging of the aforementioned parts, the height of the battery pack has been reduced 40 mm compared to the battery pack used on previous hybrid vehicles, thus improving its ease of installation.

These features enable the Lexus RX400h to provide the same utility and trunk space as the model with a normal power train, which greatly contributes to enhancing the product appeal of the vehicle (**Fig. 17**).

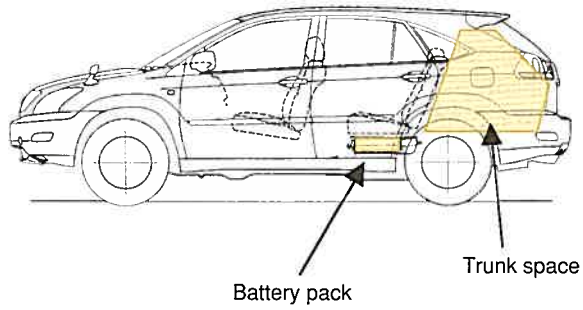

Fig. 17 View of Battery Pack Installed

3.3 Cooling

On the Lexus RX400h, the battery pack is installed below the vehicle's rear seat. Like the Prius, it uses an air-cooled system that circulates cabin air to cool the batteries. One cooling fan for each of the three battery module assemblies is built into the pack. The cooling fans are controlled individually in order to reduce the temperature variances among the battery module assemblies.

Fig. 18 shows an airflow diagram of the battery pack. To counter the increase in heat generated by the battery, the ducts, pack configuration, and the cooling fans have been optimally designed to reduce the pressure loss by 10%. And by improving heat dissipation through the placement of the battery modules in metal cases, cooling performance has been improved 20%. These features enable the system to maintain the battery temperature below a certain level (**Fig. 19**).

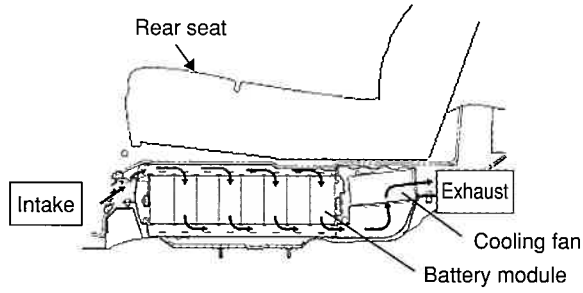

Fig. 18 Flow of Battery Cooling Air on Lexus RX400h

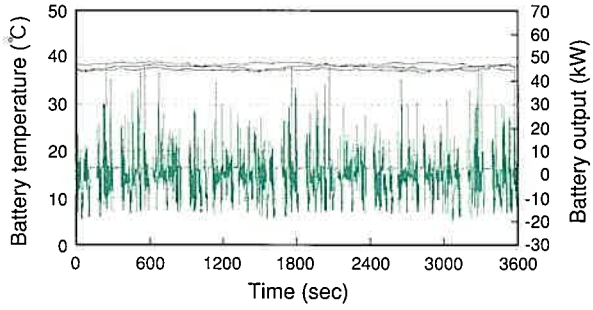

Fig. 19 Vehicle Running Data

4. Conclusion

This article described the batteries and the battery system based primarily on the Prius and the Lexus RX400h.

As the total number of automobiles increases around the world, reducing their environmental impact and lowering their fuel consumption will become increasingly important. Thus, we believe the demand for hybrid vehicles will continue to grow. For hybrid vehicles to come into wide use, developing high performance batteries, making them more compact, and reducing their cost are essential requirements. We will continue to advance our technological development efforts to meet those requirements.

Lastly, we would like to express our sincere gratitude to the representatives of the companies who extended their cooperation in the development of the present system.

References

(1) M. Ohnishi, Ito, Yuasa, Fujioka, Asahina et al. "Development of Prismatic Type Nickel/Metal-Hydride Battery for HEV." *AABC* (2003).
(2) S. Nagata, Umeyama, Kikuchi, Yamashita. "Development of New Battery System for Hybrid Vehicles." *EVS20* (2003).

Authors


M. ITO **S. NAGATA**

Noise and Vibration Reduction Technology on New Generation Hybrid Vehicles

Kazunori Miyamoto*
Masashi Komada*
Takayoshi Yoshioka*
Eiji Umemura*

Abstract

Since the world's first mass production gasoline hybrid passenger car, the Prius, was introduced in 1997, hybrid vehicles have enjoyed dominant market share among environmentally friendly vehicles and have entered into large-quantity production phase. On the other hand accomplishing good NV performance has become a significant task in hybrid vehicle development as vehicle quietness has greatly contributed to improving the marketability of vehicles. Using new generation hybrid vehicles, the new Prius and the RX400h, as subjects, this article describes NV reduction technology for solving problems peculiar to the hybrid vehicle such as boost converter system noise, engine start vibration, motor/generator noise and vibration, and drone noise and vibration at low engine speed.

Keywords: *hybrid vehicle, vibration, noise, boost converter system noise, engine start vibration, motor/generator vibration and noise, drone noise and vibration at low engine speed*

1. Introduction

In 1997, Toyota Motor Corporation introduced the Prius, the world's first mass-production hybrid vehicle, as a means of addressing global environmental issues. Subsequently, the Toyota Hybrid System (THS) has also been installed in luxury models, such as the Alphard Hybrid and the Crown Mild Hybrid. In these vehicles, technologies were required not just to address the NV problems peculiar to hybrid vehicles, but also to achieve a superior NV performance that is an important factor in improving marketability.

This article focuses on the new Prius equipped with the THS II, which was introduced in 2004, and the RX400h equipped with the high-power THS II, which came onto the market in 2005. First, it describes the new features of the THS II and the high-power THS II. This is followed by a description of the NV reduction technology applied to counter engine start vibration and drone noise and vibration at low engine speed.

2. NV Issues for Hybrid Vehicles

The engine of the THS used in the Prius was configured to improve the total fuel efficiency of the hybrid vehicle. It adopts a high expansion ratio cycle and a lowered maximum engine speed, and achieves a low level of friction loss. Moreover, the engine is stopped in the low thermal efficiency area of light load operation, allowing the vehicle to be driven by an electric motor. The engine is operated in high torque areas even at low engine speeds. [1] These measures to improve efficiency, however, have generated NV phenomena that are peculiar to hybrid vehicles. Among these NV problems are vehicle vibration during frequent engine starting and stopping, body vibration and drone noise caused by torque fluctuation at low engine speed, and motor/generator vibration and noise. Finding solutions for these problems are key points for making hybrid vehicles practical for consumers. [2][3]

The THS II adopted in the new Prius was developed for the purposes of further improving fuel economy and power performance over the previous model. While the basic configuration of the system is the same as the THS (**Fig. 1**), the THS II increases the power supply voltage to 500 V by adding a boost converter system in order to supply higher power and efficiency. [4] Reducing the resulting high frequency noise generated by radiation noise and vibration from the boost converter system has been identified as a new NV issue for hybrid vehicles.

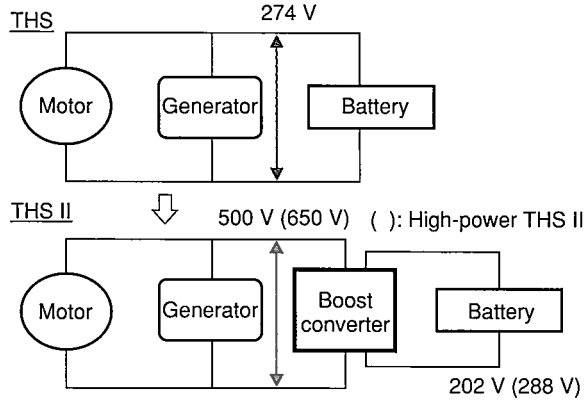

Fig. 1 THS II Block Diagram

* Vehicle Performance Development Div. 1

Moreover, the high-power THS II used in the RX400h (**Fig. 2**) uses a reduction gear for the motor/generator No. 2 (MG2) in order to increase motor speed and power while enabling a reduction in size. Increasing the motor speed, however, broadens the frequency range of electromagnetic noise. As a result, changes in electromagnetic noise frequency during regenerative braking have become more noticeable than on the THS II.

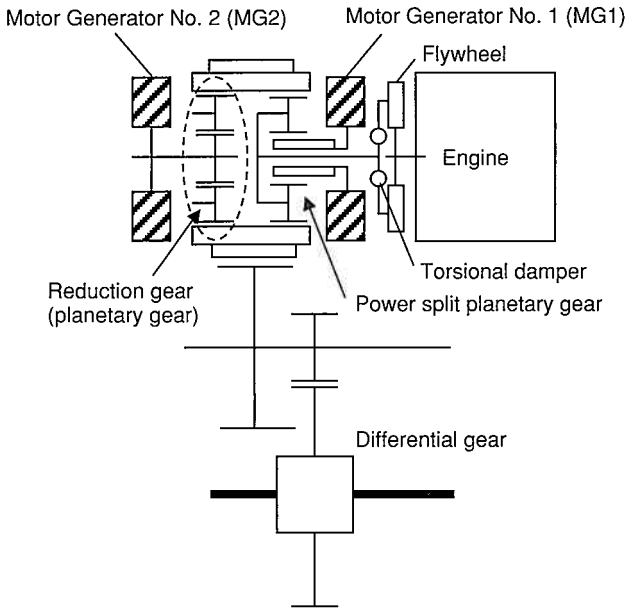

Fig. 2 High-Power THS II Drive Train Configuration

Table 1 shows the various features of the THS, THS II, and high-power THS II, and also includes a summary of the related NV phenomena.

Table 1 Noise and Vibration Issues for Hybrid Vehicles

	Technologies to improve fuel economy/power performance		THS	THS II	High-power THS II	Related noise and vibration phenomena
			Previous Prius	New Prius	RX400h	
Fuel economy performance	Engine efficiency improvement	High expansion ratio cycle	○	○		Engine noise
		Friction loss reduction	○	○		
	Optimized engine operating area	High torque operation at low engine speed	○	○	○	Drone noise and vibration at low engine speed
		Engine stops during vehicle stops	○	○	○	Engine start and stop vibration
		EV driving in light load area	○	○	○	Motor electromagnetic noise
	Energy regeneration	MG2 regenerative braking	○	○	○	Electromagnetic noise during regenerative braking
Power performance	High-voltage supply	Battery voltage boost		○	○	Boost converter system noise
	Electric 4WD	Rear motor drive & regenerative braking			○	Rear motor unit vibration and noise
	High-power, compact MG2	Reduction gear to increase revolution speed			○	Electromagnetic noise during regenerative braking (frequency varies)

3. Boost Converter System Noise

3.1 Issues to be solved

The boost converter system employed in the THS II consists of an inductor and a chopper circuit (**Fig. 3**).

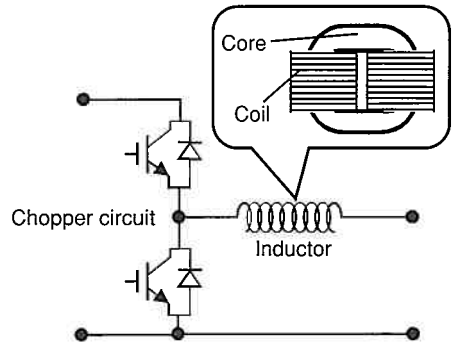

Fig. 3 Boost Converter System

When the battery voltage is boosted by this system, the high frequency switching performed in the chopper circuit generates an AC magnetic field in the inductor, accompanied by phenomena such as magnetostriction, expansion and contraction of the core, and vibration of the coil. The resulting radiation noise and vibration from the boost converter system becomes a source of high frequency vehicle interior and exterior noise that may cause discomfort to passengers in the vehicle.

When the relationship between the radiation noise generated by the boost converter system and its electric current was examined, it was found that the radiation noise from the boost converter system increases in proportion to the electric current (**Fig. 4**). It is likely, therefore, that boost converter noise would become an issue when a large current is flowing in the motor, such as during high load acceleration or regenerative braking. Moreover, when the vehicle is being driven by only the electric motor, boost converter noise would be more noticeable because the level of high frequency background noise is lower than when the engine is operated (**Fig. 5**). Effective countermeasures in consideration of the lower background noise level were therefore required to improve both the boost converter system and body sensitivity. [4]

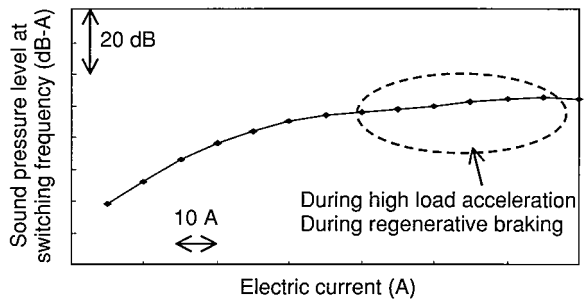

Fig. 4 Relationship Between Radiation Noise from Boost Converter and Electric Current

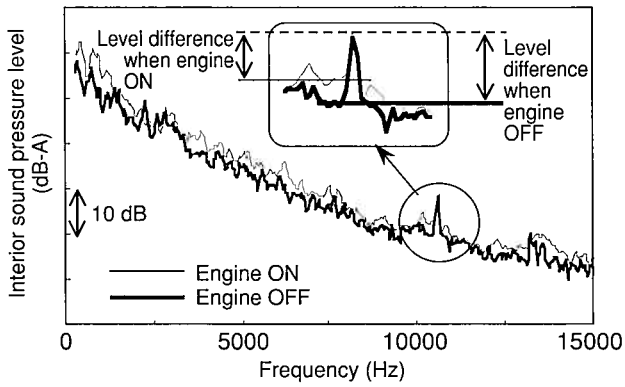

Fig. 5 Differences Between Boost Converter Noise and Background Noise in Vehicle

3.2 Countermeasures for boost converter system and body

To reduce vehicle interior noise, it was necessary to apply countermeasures against both air-borne noise and structure-borne noise from the boost converter system. The inductor core material was changed to reduce the compelling forces from magnetostriction and expansion and contraction of the core. Then, countermeasures to improve the vibration characteristics of body parts, such as the case and attachment bracket of the boost converter system, and countermeasures to improve the noise absorption and insulation of the body were applied. As a result, it was possible to achieve the target interior sound pressure level (**Fig. 6**).

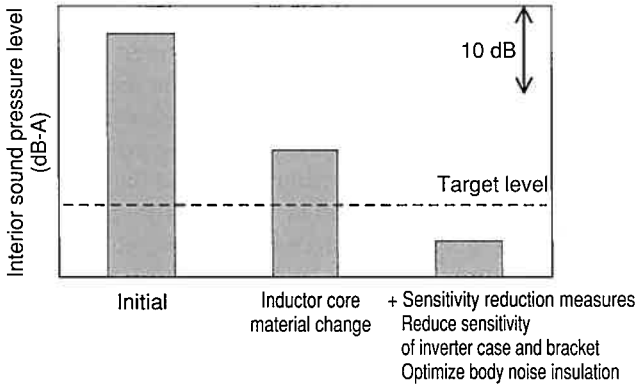

Fig. 6 Effect of Countermeasures Against Boost Converter System Noise

4. Engine Start Vibration

Vehicles equipped with the THS II are able to achieve a substantial improvement in fuel efficiency by stopping the engine frequently at low speeds where thermal efficiency is poor. However, this means that discomforting vibrations that accompany frequent engine start/stop operations become an issue. In the previous Prius model, various countermeasures were implemented, such as reducing the forces that compel engine start vibration to be generated by optimizing the engine/hybrid control, and improving the vibration characteristic of the transfer path by optimizing the engine mounting system. [5]

Some cases of improvements made to engine start vibration in the new Prius and RX400h are described below.

4.1 Compelling forces

Engine start vibration occurs during motoring and on ignition. The forces that compel engine start vibration to be generated during motoring are the reaction force of motor driving and pumping pressure. It is possible to reduce the pumping pressure by delaying the intake valve close timing using VVT-i, but since one aim of the new Prius was to improve engine starting performance under cold engine conditions, the intake valve close timing was modified from 115° to 105°. As a result, it was predicted that the engine start vibration would worsen by approximately 2 dB (**Fig. 7**).

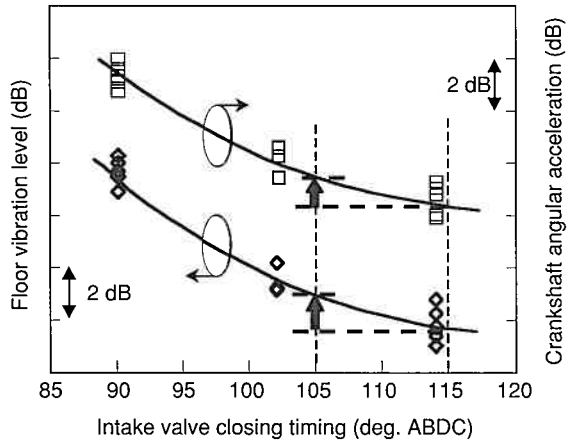

Fig. 7 Influence of Intake Valve Closing Timing on Floor Vibration

4.2 Reduction of compelling forces

Pumping pressure during motoring is determined by the intake valve close timing. On the other hand, for the first compression stroke right after motoring start, it was predicted that the pumping pressure changes in accordance with the piston position before motoring start.

For this reason, the relationship between the piston position (i.e., the crank angle) and the engine start vibration due to motoring was investigated. As a result, it was confirmed that vehicle floor vibration decreases when the piston is stopped after the intake valve close timing and the piston position is close to top dead center (**Fig. 8**). MG1 was therefore controlled during engine stop in order to concentrate the piston stop position near top dead center (TDC). This control enabled a reduction in floor vibration dispersion.

Other countermeasures applied were to improve the cranking torque raise rate by approximately doubling the MG1 motoring

torque in comparison with the previous model, and to make the floor vibration generated by the torsional resonance of the power plant and the resonance of the engine mounting system less susceptible to excitation.

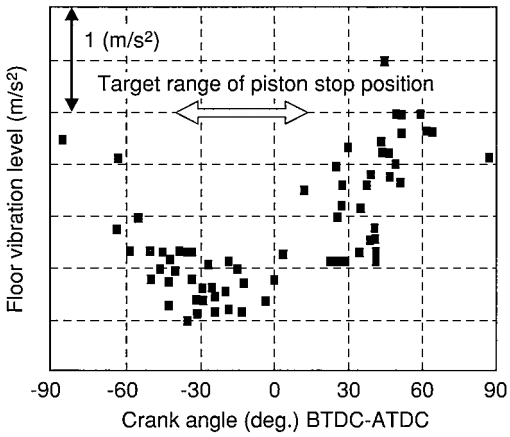

Fig. 8 Relationship Between Piston Stop Position (Crank Angle) and Floor Vibration

4.3 Optimization of engine mounting systems

4.3.1 New Prius

The engine mounting system used in the new Prius is the same pendulum mounting system as found on the previous model, but commonization was achieved with other model types for the under body. It was predicted that engine vibration would worsen during torque input if the right- and left-hand engine mountings were provided in the existing side member attachment positions. The mounting positions were therefore reviewed and, in addition, an optimization study was performed for the engine mounting system by examining the spring constant of the engine mounting within a range that minimized compromise of other performance factors. Moreover, by reducing the distance between the principal elastic axis and the center of gravity with regard to rolling and yawing of the power plant, it was possible to ensure an engine mounting vibration performance better than the previous model (**Fig. 9**).

As a consequence of the MG1 control for the engine piston stop position and the engine mounting system optimization described above, it was possible to reduce engine start vibration substantially over the previous model (**Fig. 10**).

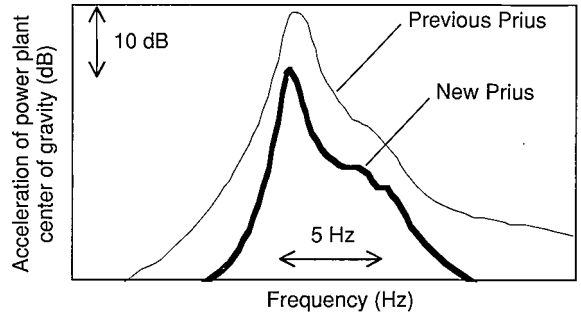

Fig. 9 Simulation Results of Power Plant Vibration by Torque Input

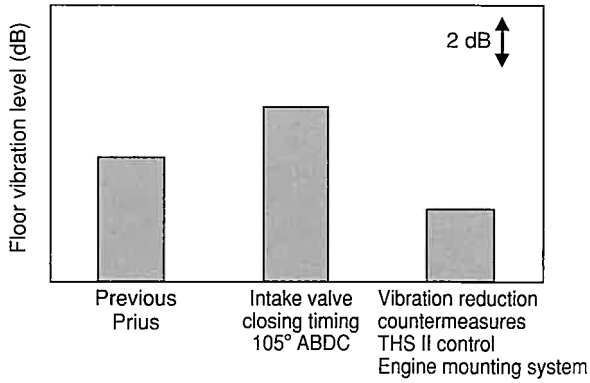

Fig. 10 Effect of Countermeasures for Floor Vibration During Engine Cranking

4.3.2 RX400h

The engine/hybrid control countermeasures to reduce the compelling forces in the RX400h are based on the technology of the new Prius, and the engine mounting system was also optimized using the same technology as in the new Prius. Under the condition that the basic structure had to be the same as in the original RX330, an optimization study was performed for the engine mounting system to decrease the distance between the power plant center of gravity and the principal elastic axis of rolling. As a result, the front engine mounting was moved upward, creating power plant vibration characteristics in which vertical vibration with regard to the center of gravity is only minimally excited under torque input conditions (**Fig. 11**).

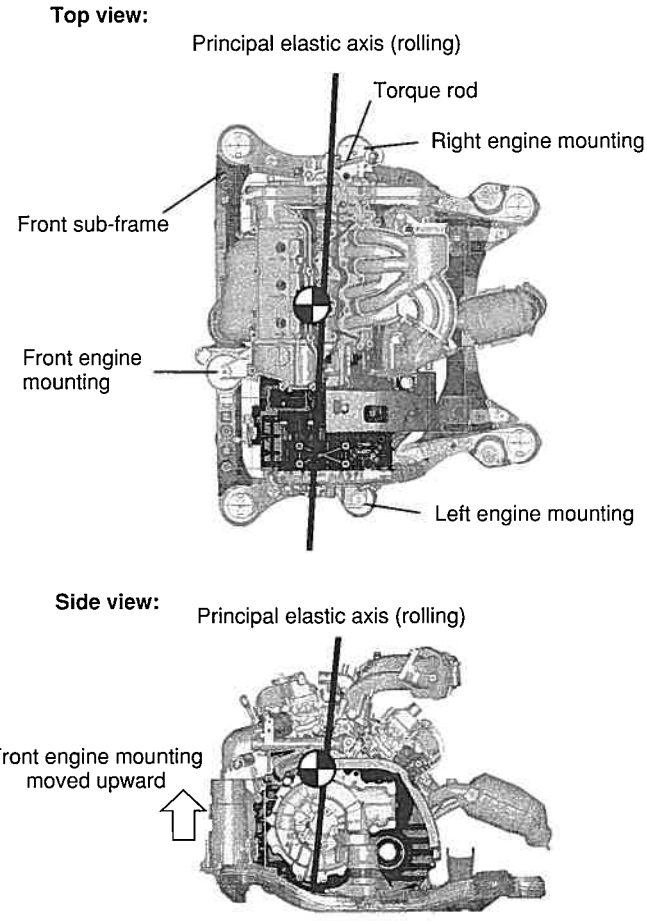

Fig. 11 Engine Mounting System

5. Motor/Generator Vibration and Noise

Issues that arose during the development of vehicles equipped with the THS and THS II included vehicle vibrations from start to very low speed motor driving, and motor electromagnetic noise on regenerative braking. The 24th order component of motor revolution (electric angle 6th order × 4 pairs of NS magnetic poles) was found to greatly affect these two issues. Controlling the electric current and changing the rotor/stator electromagnetic design were found to be effective ways of reducing the torque ripple compelling force. Moreover, for structure-borne noise, it was possible to reduce electromagnetic noise by optimizing the vibration characteristic of the case/housing and rotor/stator. **Table 2** shows a summary of the principles for improving electromagnetic noise as applied to the development of the THS and THS II.

Table 2 Summary of Countermeasures for Motor Electromagnetic Noise

Countermeasure items		THS	THS II
Reduce compelling forces	Superimpose high order components to basic current	○	○
	Optimize rotor/stator shapes	○	○
	Optimize permanent magnet shapes/layout		○
Improve vibration transmission characteristics	Optimize resonant frequencies of rotor/stator/transaxle case	○	○
	Increase transaxle case stiffness	○	○
	Separate MG1/MG2 resonant frequencies from usual rotor speed		○

The following section describes the technology that was applied to reduce electromagnetic noise on regenerative braking in the RX400h.

5.1 Electromagnetic noise on regenerative braking

Electromagnetic noise tends to be more noticeable during regenerative braking because of the lower level of background noise when the engine is stopped. Moreover, in the high-power THS II, the reduction gear increases the speed of MG2, thereby approximately doubling the frequency of the 24th order component of motor revolution (**Fig. 12**). As a result, remarkable frequency changes are generated, which make the electromagnetic noise more noticeable and create issues related to subjective perception of discomfort.

Fig. 13 shows the level of electromagnetic noise on regenerative braking, comparing the new Prius with the RX400h. The electromagnetic noise of the new Prius is generated in the middle frequency range, but the noise of RX400h extends from the middle frequency range to the high frequency range. Moreover, the interior sound pressure levels of the RX400h fluctuate remarkably during regenerative braking. New targets for interior noise were therefore set taking into account the effects of these changes in frequency range and noise level fluctuation.

Cases of improvements made to the electromagnetic noise performance of the RX400h on regenerative braking, particularly just before stopping at speeds approximately 10 km/h, are described below. Contribution analysis for interior noise showed that the major contributors to vibration were the left engine mount and the left drive shaft. Dynamic dampers were therefore installed in these locations, which enabled the new target for the interior sound pressure to be achieved while keeping weight increase to a minimum (**Fig. 14**).

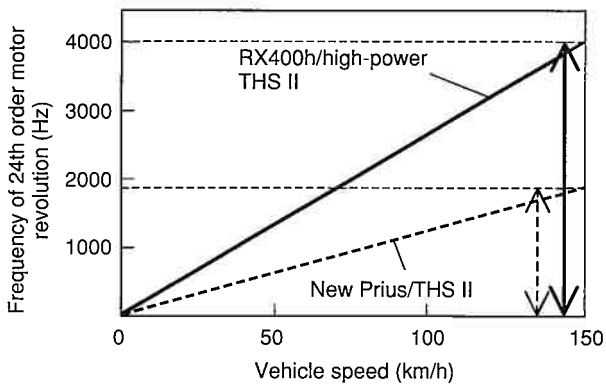

Fig. 12 Relationship Between Vehicle Speed and 24th Order Motor Revolution

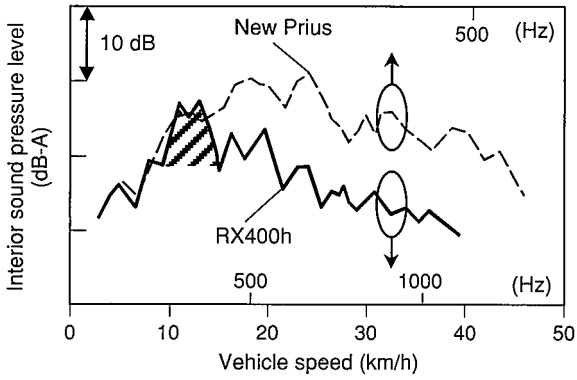

Fig. 13 Electromagnetic Noise During Regenerative Braking: Comparison Between New Prius and RX400h

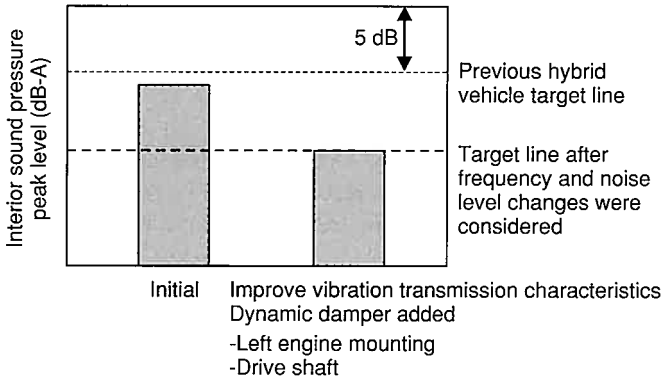

Fig. 14 Effect of Countermeasures for Electromagnetic Noise During Regenerative Braking

6. Drone Noise and Vibration at Low Speed

In lock-up condition on a conventional automatic transmission vehicle (usually at 40 km/h or faster), body vibration and drone noise due to primary engine torque fluctuations of engine combustion may become problems.

The same sort of phenomena occur in a hybrid vehicle because the engine is operated in high torque areas to allow better thermal efficiency. Additionally, since the engine is linked directly to the drive train in the THS II, the same phenomena tend to become problems at low speed driving just after take off. Improvements in drone noise performance at low speed were developed by considering the differences in noise occurrence conditions between conventional automatic transmission vehicles and hybrid vehicles.

Fig. 15 shows a comparison of the interior sound pressure levels in the drone noise frequency range between a hybrid vehicle and a conventional vehicle. It was found that the background noise level at below 5 km/h (where drone noise occurs on a hybrid vehicle) is approximately 7 dB lower than the background noise level at approximately 40 km/h (where drone noise occurs on a conventional automatic transmission vehicle). These results were taken into consideration when reducing drone noise in the RX400h, as described below.

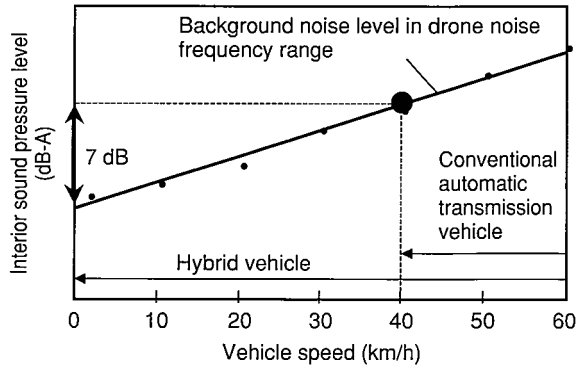

Fig. 15 Background Noise Level in Drone Noise Frequency Range

The torsional damper that is installed between the engine and the transaxle employs the same optimization technology that was used for the previous Prius equipped with the THS, while achieving the lower torsional stiffness and wider torsional angle required by the high torque engine in the RX400h (**Fig. 16**). It lowers the torsional resonant frequency of the whole drive train system, reducing the input force from the drive train system to the body. Installing a dynamic damper for the front sub-frame and optimizing the spring constant of the engine mounting have reduced the input force from the power plant to the body. Moreover, the engine operation torque area was also optimized within an area compatible with fuel economy. The final result, as shown in **Fig. 17**, is a drone noise level that does not cause discomfort to passengers at lower vehicle speeds.

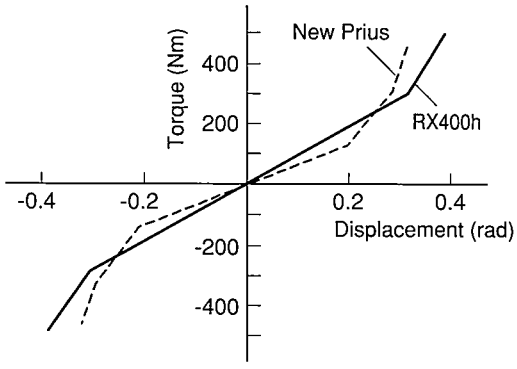

Fig. 16 Torsional Damper Characteristics

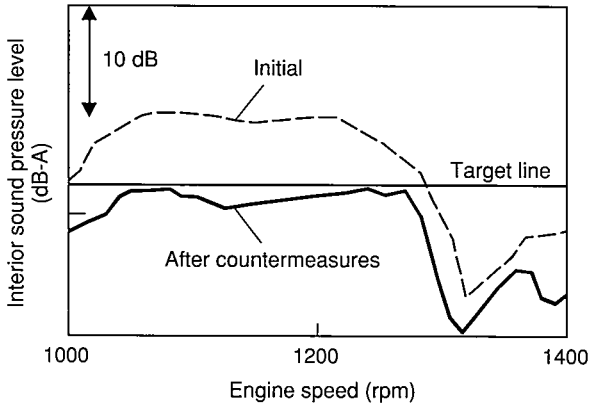

Fig. 17 Effect of Countermeasures for Drone Noise at Low Speed

7. Conclusion

In the development of the new Prius equipped with the THS II and the RX400h equipped with the high-power THS II, improvements were made to the basic component characteristics, THS control, and body characteristics to solve the distinctive NV problems of the respective hybrid vehicles. As a result, it was possible to achieve simultaneous improvements in power performance and fuel efficiency as well as in NV performance.

References

(1) S. Abe et al. "Development of Hybrid System for Mass Production Passenger Car." *JSAE Autumn Convention Proceedings* No. 975, 9739543 (1997).
(2) T. Yoshioka. "Noise and Vibration Reduction Technology in Hybrid Vehicle Development." *SAE* 2001-01-1415.
(3) M. Komada et al. "Noise and Vibration Reduction Technology in New Generation Hybrid Vehicle Development." *JSAE Autumn Convention Proceedings* No. 10-4, 20045298 (2004).
(4) Y. Kawashima. "Future Prospects of Hybrid Vehicles Development Technology." *Jidosha Gijutsu* Vol. 58 No. 1 (2004) pp. 47-51.
(5) H. Kanai et al. "Reduction of the Engine Starting Vibration for the Parallel Hybrid System." *JSAE Autumn Convention Proceedings* No. 983, 9833467 (1998).

Authors


K. MIYAMOTO


M. KOMADA


T. YOSHIOKA


E. UMEMURA

"Virtual and Real Simulator": Support Equipment for Hybrid Vehicle Development

Yasushi Kojima*
Koji Shirota**
Shoji Sakai***

Abstract

Toyota is pushing ahead with the development of hybrid vehicles. One item of equipment being used to support this development is the "virtual and real simulator (VRS)", which is already applied in conventional drivetrain development. Some of the issues involved during the application of VRS to hybrid vehicle development included the reproduction of characteristics specific to hybrid vehicles, such as regenerative braking and slip control using motors. These issues were addressed by the addition of a virtual model of a brake system. The introduction of VRS has enabled driving evaluations to be performed from the initial stage of hybrid vehicle development without the use of completed vehicles.

Keywords: *hybrid vehicle, VRS, regeneration, slip control, wavy road, low traction road*

1. Introduction

In conventional automobile development, vehicle evaluations are conducted using completed vehicles on chassis dynamometers or test courses. However, chassis dynamometer tests are incapable of evaluating transient occurrences such as tire slippage. In addition, test courses not only impose limited test conditions, but are also affected by weather, thus creating issues related to poor reproducibility of conditions. On the other hand, a difficulty with simulation evaluations using Computer-Aided Engineering (CAE) is the requirement for high precision component models. To solve these evaluation-related issues, the power train development field of Toyota Motor Corporation uses a system bench called the Virtual and Real Simulator (VRS), as shown in **Fig. 1**. This is a simulator bench that reproduces vehicle driving conditions by using actual (i.e., "real") parts for the power train portions to be evaluated and integrating them with "virtual" models that simulate the dynamic characteristics of vehicles. The VRS bench uses newly developed low-inertia, high-response dynamometers that absorb the driving force under evaluation. This enables the bench to perform transient evaluations under a variety of road surface conditions that could not be easily reproduced in the past. Therefore, the VRS bench is able to perform driving evaluations from the initial stages of development, without requiring the use of completed vehicles.

This article describes the improvements that have been made to the VRS bench and presents examples of its application in the development of hybrid vehicles (HVs), the model range of which is expected to expand.

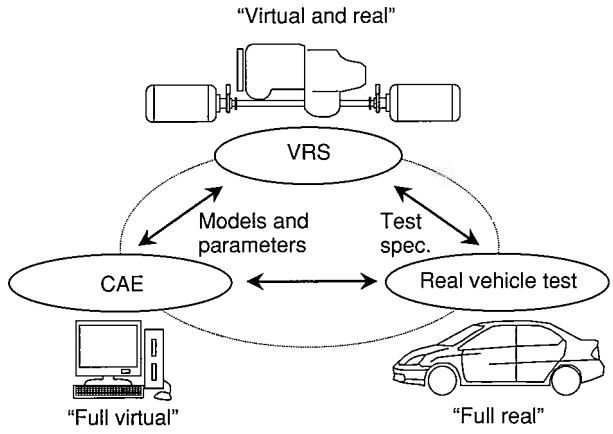

Fig. 1 Concept of VRS Bench

2. VRS Bench [1]

The main pieces of equipment on the VRS bench comply with the International Association for Mathematics and Computers in Simulation (IMACS). The bench primarily consists of an operation unit application, a management unit, an instrumentation unit, and a control unit, which allow the system to centrally manage driving control, measurement, as well as data collection and processing for the purpose of conducting various types of tests (**Fig. 2**). Moreover, a Versa Module Eurocard (VME) bus is used in the instrumentation and control units.

The VRS bench utilizes the following three features in evaluations.

* Hybrid Vehicle Power Train Development Div.
** Instrumentation Engineering Div.
*** Nippon Soken, Inc.

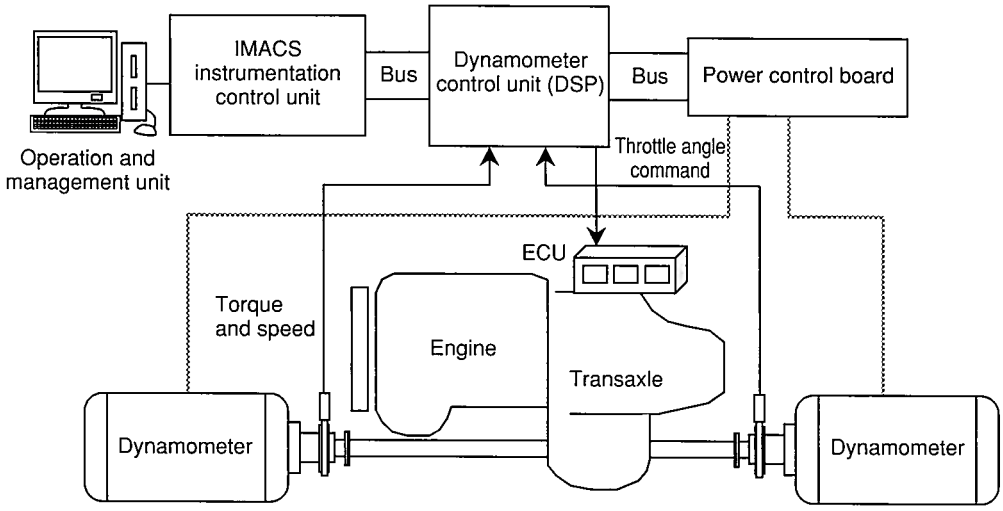

Fig. 2 Overview of VRS Bench Configuration

(1) Simulation of dynamic characteristics of vehicles using models
(2) Creation of desired temperature environment within short periods of time
(3) Low-inertia, high-response dynamometers
These features are described in more detail below.

2.1 Simulation of dynamic characteristics of vehicles using models

The load conditions of an actual vehicle can be reproduced on the VRS bench by setting the parameters for a model that represents the dynamic characteristics of that vehicle. This feature enables the VRS bench to implement and verify various types of evaluations that cannot be accomplished using conventional benches. For example, the specifications for other vehicles can be simulated on the VRS bench by changing the parameters, thereby facilitating the evaluation of power trains deployed on different vehicle models.

2.2 Creation of desired temperature environment within short periods of time

As is the case with vehicle evaluation equipment using conventional chassis dynamometers, a temperature adjustment device has been added to the VRS bench. Moreover, the VRS bench is able to recreate environments with particularly desired temperatures within short periods of time by placing the object of the evaluation in an environmental chamber that is provided with simple thermal insulation.

2.3 Low-inertia, high-response dynamometers

The most striking feature of the VRS bench is its use of the newly developed dynamometers that have a lower inertia and a higher response than conventionally used dynamometers. These dynamometers enable the VRS bench to reproduce slippage behavior that cannot be recreated easily using the conventional dynamometers (**Fig. 3**). This allows the VRS bench to be used to evaluate transient slip control. The VRS bench connects the two dynamometers to either end of the drive shaft, which enables the right and left dynamometers to act independently to virtually reproduce the braking and driving resistance of the vehicle, in accordance with the settings on the operation unit.

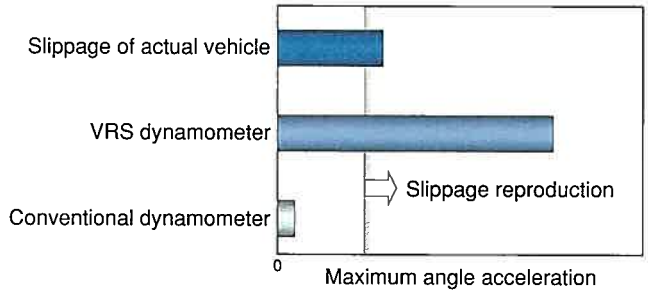

Fig. 3 Newly Developed Dynamometers

3. Hybrid Vehicle Application

3.1 Issues associated with HV application

Conventionally powered vehicles, which have been the intended object of VRS bench evaluations until now, generate braking torque through hydraulic brakes. In contrast, HVs supplement the hydraulic brakes by generating braking torque through regeneration using an electrical motor.

In the conventional configuration of the VRS bench (**Fig. 2**), the intended object of evaluation does not possess hydraulic brakes, and the VRS bench control unit issues commands that cause the dynamometers to generate braking torque. With this

configuration, the dynamometers generate the braking torque that should actually be generated by regeneration. Furthermore, because the VRS bench control unit does not provide information such as the speed data of individual wheels for evaluation, slip control cannot be performed on the conventional VRS bench using the motor. Moreover, the interposition of the motor has made it necessary to improve the reproducibility of road surfaces to enable controllability evaluations during sudden changes in motor torque. These occur, for example, on road surfaces such as wavy roads where tires repeatedly slip and grip during driving.

3.2 Addressing application issues

In response to the issues described above, a virtual brake system model was added to the conventional VRS bench to transmit the information required for evaluating regeneration and slip control. A model that can apply a virtual exciting force was also added. These models are created using MATLAB and Simulink (**Fig. 4**).

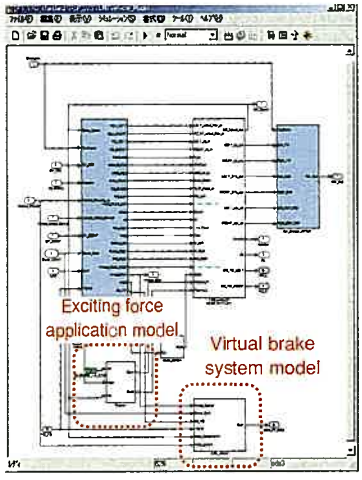

Fig. 4 Virtual Models

The system uses Controller Area Network (CAN) communication to exchange information between the virtual models and the evaluation objects (**Fig. 5**). This enables the VRS bench to be stopped automatically based on abnormal data provided by the evaluation objects, thus improving the safety level of the VRS bench during automatic operation.

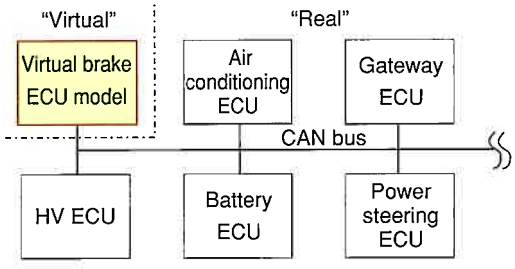

Fig. 5 CAN Communication

3.2.1 Exciting force application function

This function, which aims at improving the reproducibility of road surfaces, is described below. The reproduction of wavy road conditions is presented as an example.

When a vehicle is being driven on a wavy road, vertical forces act on the vehicle in accordance with the shape (pitch, amplitude, and lateral phase difference) of the wavy road. In other words, repeated slip-and-grip cycles take place at the point of contact between the tires and the road surface. A simulation was therefore performed using a vehicle model to analyze these forces and enable this function to be added to the VRS bench. The modeled vehicle was a front/rear two-wheel model provided with independent, vertical front and rear suspension. In addition, the vehicle body was provided with two degrees of freedom: pitch movement and translational movement (**Fig. 6**). The suspension was modeled after a simple spring and damper system.

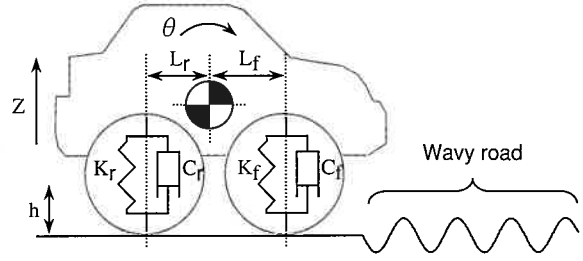

Fig. 6 Front/Rear Two-Wheel Vehicle Model

Equation 1 shows the effect exerted by the front suspension of the vehicle on the translational movement degree of freedom, i.e., the vertical direction movement.

$$F_{Fr} = 2K_{Fr}(L_{Fr} \cdot \theta - z) + 2C_{Fr}(L_{Fr} \cdot \theta' - z') \quad (1)$$

where,

F_{Fr} (N): force acting from suspension to vehicle body
K_{Fr} (N/m): spring constant of suspension
C_{Fr} (N·s/m): damping coefficient of suspension
L_{Fr} (m): horizontal distance from vehicle body center of gravity to suspension
θ (rad): pitch (rotation) angle
θ' (rad/s): angular acceleration
z (m): translational (vertical) displacement
z' (m/s) translational (vertical) direction

Equation 2 shows the effect exerted by the pitch movement of the front suspension, i.e., the pitch moment M_{Fr} (N·m) of the front suspension.

$$M_{Fr} = -L_{Fr} \cdot F_{Fr} \quad (2)$$

In the same way, equations 3 and 4 show the effects exerted by the rear suspension.

$$F_{Rr} = 2K_{Rr}(L_{Rr} \cdot \theta - z) + 2C_{Rr}(L_{Rr} \cdot \theta' - z') \quad (3)$$

$$M_{Rr} = -L_{Rr} \cdot F_{Rr} \quad (4)$$

The equations described above establish the following relational expressions:

$$M_b \cdot z'' = F_{Fr} + F_{Rr} - M_b \cdot g \quad (5)$$

$$I_{yy} \cdot \theta'' = M_{Fr} + M_{Rr} \cdot g \quad (6)$$

where,

M_b (kg): vehicle weight

g (m/s^2): gravitational acceleration

I_{yy} (kg·m^2): moment of inertia around vehicle center of gravity

The vehicle model created in this manner was used to verify the vehicle behavior on a wavy road, whose surface changes are simulated with sine waves (**Fig. 7**). The diagram shows that the force F_{Fr} applied by the front suspension to the vehicle body acts vertically in the same cycle, with a slight time lag from the changes occurring in the road surface height.

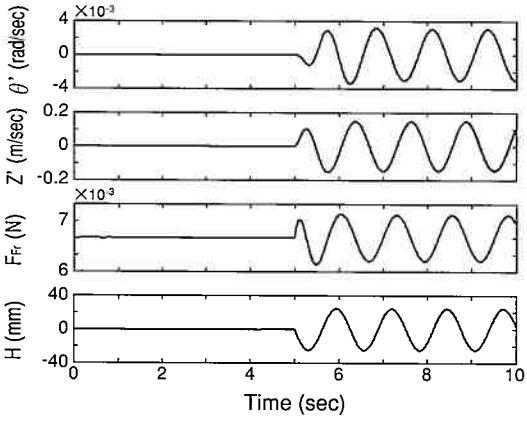

Fig. 7 Simulation Results of Wavy Road Driving

The state of a vehicle driven on a wavy road is reproduced on the VRS bench based on the results of the studies conducted using this vehicle model. This is accomplished by applying virtual torque fluctuations with the same frequency as the pitch of the wavy road to the evaluation object for the front wheel load, something which is necessary for calculating the front and rear forces of the vehicle. Note that the torque gain fluctuations were set using vehicle speed, acceleration, and unsprung mass resonance values obtained with reference to actual vehicle measurement data.

Fig. 8 shows a comparison of frequency analysis results for wheel speeds obtained from an actual vehicle driven on an in-phase wavy road at a constant speed with the results from the VRS bench. The diagram shows that the gain peak is steeper on the VRS bench.

The difference is caused by the lower impact of outside disturbance on driving conditions on the VRS bench. However, it is possible to change the settings of the model in the control unit in accordance with the purpose of the evaluation to allow the inclusion of external disturbances.

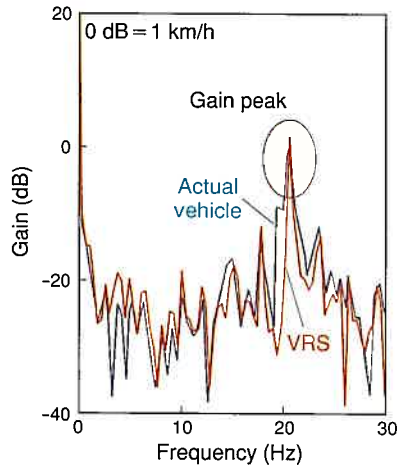

Fig. 8 Results of Wheel Speed Frequency Analysis of Vehicle Driven on Wavy Road

3.3 Application results

Before the addition of the virtual model, only regenerative current equivalent to engine braking flowed in the HV evaluation object during gradual braking. After the addition, the flow of regenerative current equivalent to actual vehicle conditions was verified, as shown in **Fig. 9** (a). Furthermore, a full throttle acceleration test conducted on the VRS bench presuming low traction road surface conditions verified that slip control could be performed using the motor, as shown in **Fig. 9** (b).

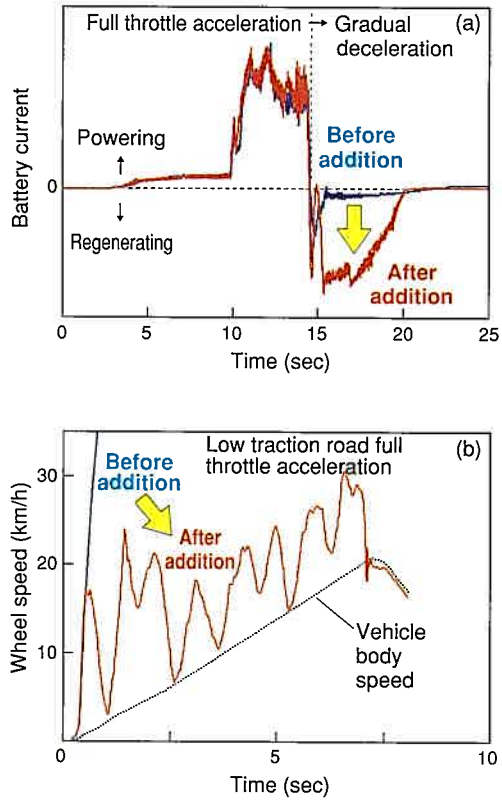

Fig. 9 Effects of Virtual Model

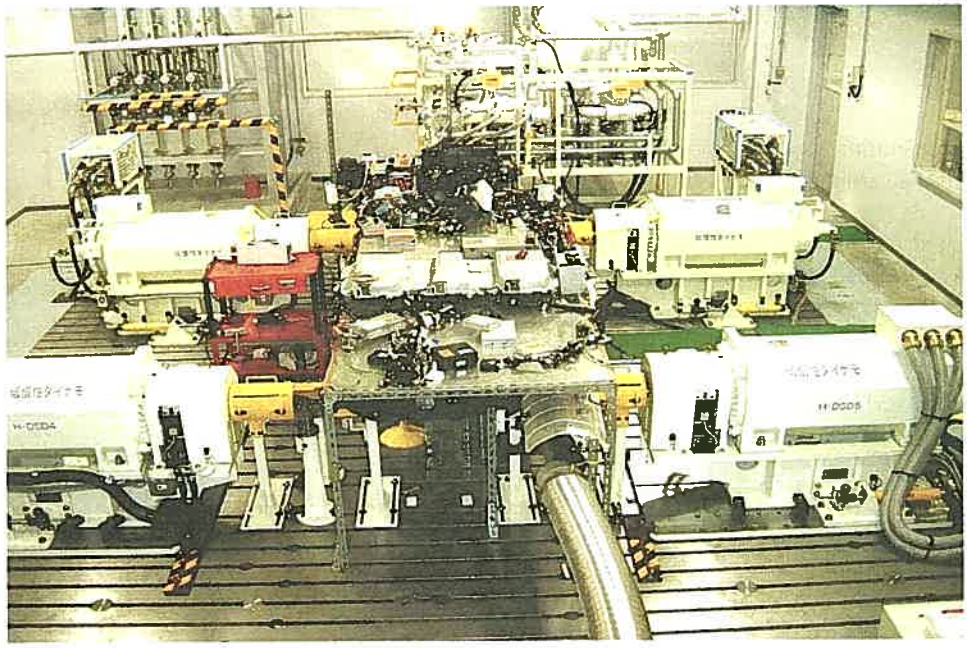

Fig. 10 VRS Bench for Hybrid Vehicles Compatible with Four-Wheel Drive

3.4 Other added functions

One of the other additional functions allows evaluations that simulate typical mountain road driving conditions in order to improve the reproducibility of motor thermal evaluations, which is a necessary factor for the development of HVs. The following new functions have been added to improve the road surface reproducibility of the conventional VRS bench, as well as to support the future expansion of HV technology to a wider range of models.

(1) Road gradient setting function in accordance with the vehicle mileage
(2) Compatibility with four-wheel drive vehicles

These functions are described below.

3.4.1 Road gradient setting function

The VRS bench uses the models that simulate the dynamic characteristics of vehicles to calculate the vehicle speed, which can then be used to obtain the vehicle mileage. A function that can vary the road gradient in accordance with mileage was therefore added, based on a road gradient map that is created in advance according to the distance. This function facilitates the creation of driving pattern files for the evaluation object, as well as the reproduction of field driving conditions of actual vehicles on the VRS bench.

3.4.2 Compatibility with four-wheel drive vehicles

To support the future expansion of HV development, both the equipment and the models that simulate the dynamic characteristics of vehicles have been made compatible with four-wheel drive vehicles. Thus, the VRS bench has the specifications to evaluate HVs that use all power train systems (**Fig. 10**).

4. Utilization Examples and Future Development

4.1 Utilization examples

This section describes the advantages of VRS bench evaluations in HV development and some utilization examples.

In the process of HV evaluations, the VRS bench is able to verify the control response during sudden changes in motor torque by applying full throttle acceleration on a wavy or a low traction road surface, in order to measure the electrical behavior of the individual units in the HV. In the past, these evaluations were performed on the evaluation road surfaces provided at test courses, but this method is limited both in terms of the pitch and amplitude of the available wavy roads and in terms of the friction coefficients of the available low traction roads. In addition, the reproducibility of conditions in these tests is inferior due to the effects of the weather on the evaluations. VRS bench evaluations have the following advantages over evaluations performed on a test course.

(1) VRS enables repeated evaluations under identical test conditions, and offers clearly superior reproducibility.
(2) Because the motion points of the vehicle can be set freely, VRS can perform precise evaluations efficiently by making minute changes to the driving state and the road surface conditions.
(3) Even on the wavy and low traction road surface evaluations mentioned earlier, VRS is capable of performing evaluations in short periods of time, in which road surface specifications such as the pitch and amplitude of wavy

roads and the friction coefficients of low traction roads are changed (**Fig. 11**).

(4) VRS enables driving evaluations that simulate field conditions by making good use of its high level of road surface reproducibility.

Since the introduction of the VRS bench, these merits have been exploited to perform precise driving evaluations from the initial stages of HV development.

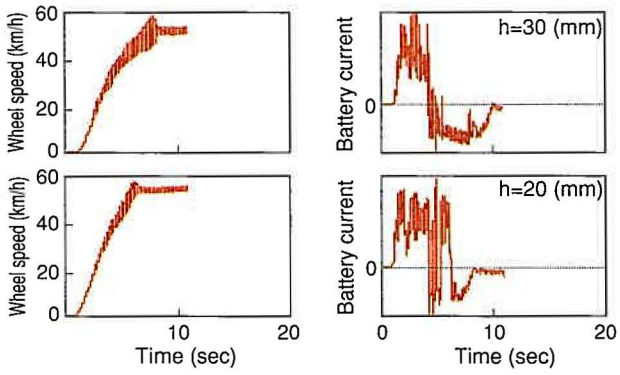

(a) Wavy road (amplitude h: 30, 20 mm)

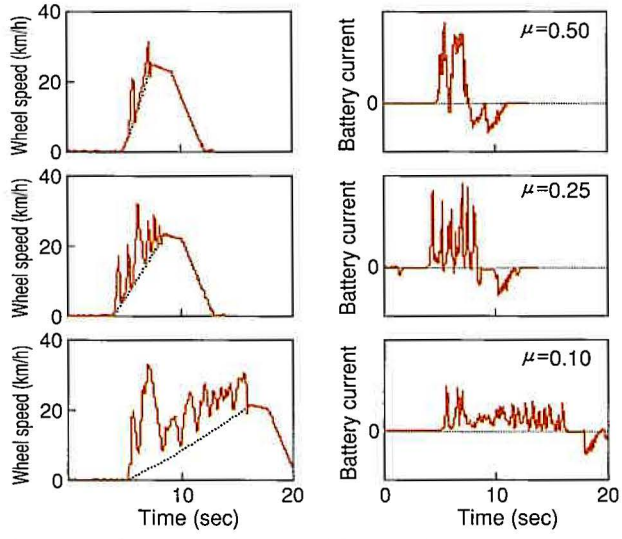

(b) Low traction road (road surface friction coefficient μ: 0.5, 0.25, 0.10)

Fig. 11 Wavy and Low Traction Road Evaluation on VRS Bench

4.2 Future development

The following are among the functions that will be added to enable the VRS bench to be used even more effectively (**Fig. 12**).

(1) A driver model that can reproduce faithfully the throttle and brake operations of a human.

(2) A model for the dynamic characteristics of vehicles that takes steering into consideration.

Currently, proportional, integral, derivative control (or "PID control") is used for the model described in point 1. Instead of this typical example of classic control theory, however, it is planned to try out a modern control theory. In addition, a method will be studied to incorporate the model described in point 2 into the VRS bench by integrating studies based on "full virtual" simulations and the measurement results of "full real" actual vehicles.

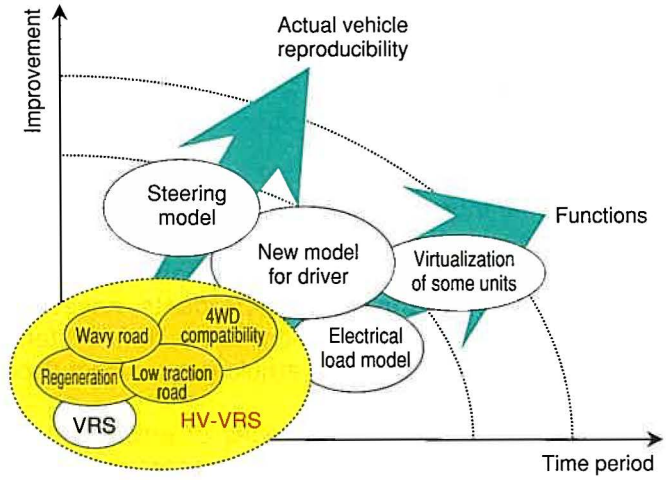

Fig. 12 Function Development of VRS Bench

5. Conclusion

HV control systems have become ever more complex as these vehicles have evolved since the launch of the first-generation Prius in 1997. Under these circumstances, it is believed that VRS, which can perform driving evaluations without the use of completed vehicles, is the most effective tool for supporting HV development.

Reference

(1) F. Baba, Shirota et al. "Development of 'Virtual and Real Simulator' for Engine." *SAE Paper* 2001-01-1355 (2001).

Authors

Y. KOJIMA **K. SHIROTA** **S. SAKAI**

Eco-Vehicle Assessment System (Eco-VAS): A Comprehensive Environmental Impact Assessment System for the Entire Development Process

Masako Yamato*

Abstract

Calls for the increased greening of automobiles have grown more diverse to include improved recyclability, less use of substances of environmental concern and lower life cycle environmental impact, in addition to the past issues of better fuel economy, lower emissions and reduced vehicle exterior noise. In order to improve the overall environmental performance of products, necessary databases and computer systems were built to enhance the system for impact assessment. The new system was named "Eco-VAS" and its usage has been successively expanding since 2005. This article gives a brief description of Eco-VAS focusing on LCA.

Keywords: *recycling, substances of environmental concern, life cycle assessment (LCA), development process, environmental impact assessment system*

1. Introduction

The automobile is implicated in a variety of environmental issues as it passes through its life cycle, as shown in **Fig. 1**.

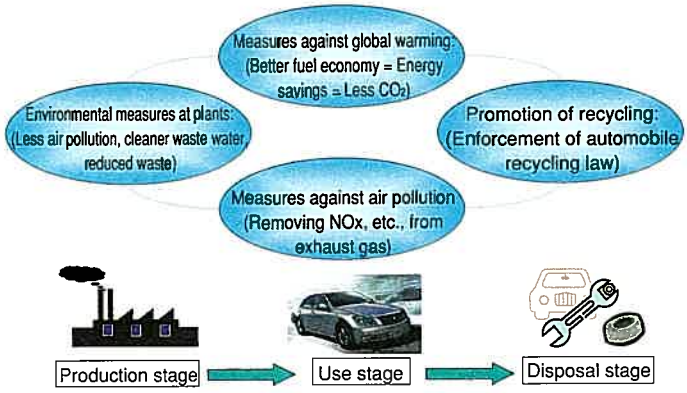

Fig. 1 Automobiles and Environmental Issues

In the 20th century, the number of automobiles in use increased rapidly, reaching a worldwide total of more than 800 million vehicles by 2002. The trend is forecast to continue in the 21st century. To date, automobile manufacturers have implemented environmental measures in their production plants and in individual vehicles, but these efforts must be strengthened if the automobile industry is to continue growing.

Conventional environmental measures for automobiles have concentrated on improving fuel economy and reducing exhaust emissions and noise. Growing concern over environmental issues in the 1990s led to demands for new efforts in the areas of recycling, reduction of substances of environmental concern, and reduction of environmental impact over a vehicle's entire life cycle, in order to construct a sustainable recycling-oriented society. Action was taken in each of these areas.

Toyota seeks to make its various environmental actions even more effective by establishing environmental targets for the vehicle development process and following through to see that they are achieved. In 2005, a comprehensive environmental assessment system was introduced under the title of Eco-Vehicle Assessment System, or Eco-VAS.

This article describes both Eco-VAS and a new assessment tool called life cycle assessment (LCA), which seeks to reduce environmental impact over the entire vehicle life cycle.

2. Life Cycle Assessment (LCA)

2.1 LCA method

LCA is a method of assessing the environmental impact of a product through quantitative analyses of the resources and energy that the product consumes, and the substances of environmental concern that it emits, over its entire life cycle, from the extraction of resources through manufacturing, use, and recycling to disposal. The method was incorporated into the ISO14000 series of environmental standards in 1993 and is now used internationally as an environmental management tool.

Fig. 2 shows the automobile life cycle. At each stage from material manufacturing to disposal, various resources and forms of energy are consumed, resulting in large emissions of atmospheric pollutants like CO_2 and NOx, as well as waste water contaminants and solid wastes.

* Environmental Affairs Div.

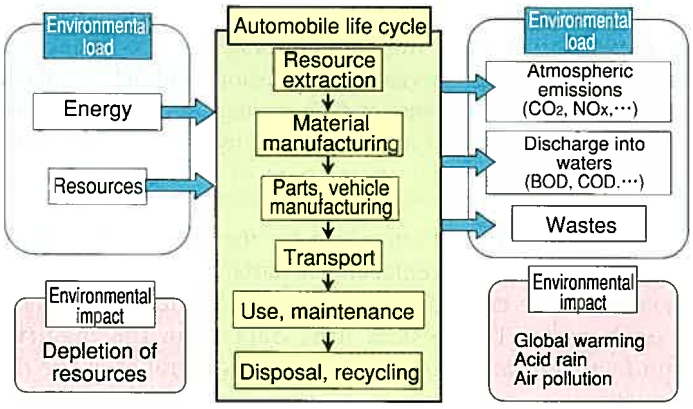

Fig. 2 Automobile Life Cycle

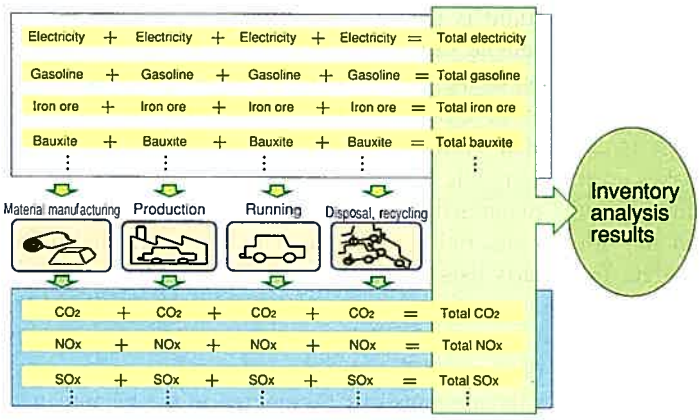

Fig. 3 LCA Method (Inventory Analysis)

The LCA method is divided into two stages: inventory analysis and environmental impact assessment. Inventory analysis, illustrated in **Fig. 3**, is a quantitative survey and analysis of the resources and energy consumed and the amounts of CO_2 and other substances emitted.

The environmental impact assessment, shown in **Fig. 4**, categorizes the data collected by the inventory analysis according to the environmental impact, such as global warming or air pollution, then assesses the degree of impact.

It should be noted that the methods of categorizing different types of substances of environmental concern, such as CO_2, NOx, and fluorocarbons, as well as the approaches to use in the ranking of environmental impacts within a category and the weighting of impacts across categories (comparing the environmental impacts of global warming and air pollution, for example), are currently the subjects of international research and have not yet been standardized.

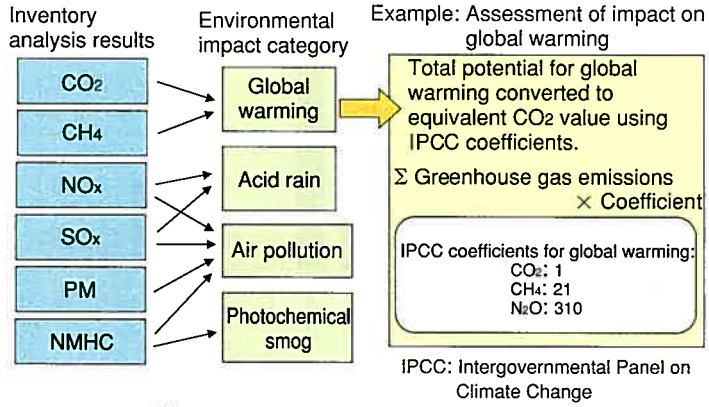

Fig. 4 LCA Method (Environmental Impact Assessment)

At Toyota, LCA is currently being used mainly for inventory analysis. **Fig. 5** illustrates the flow by which the LCA

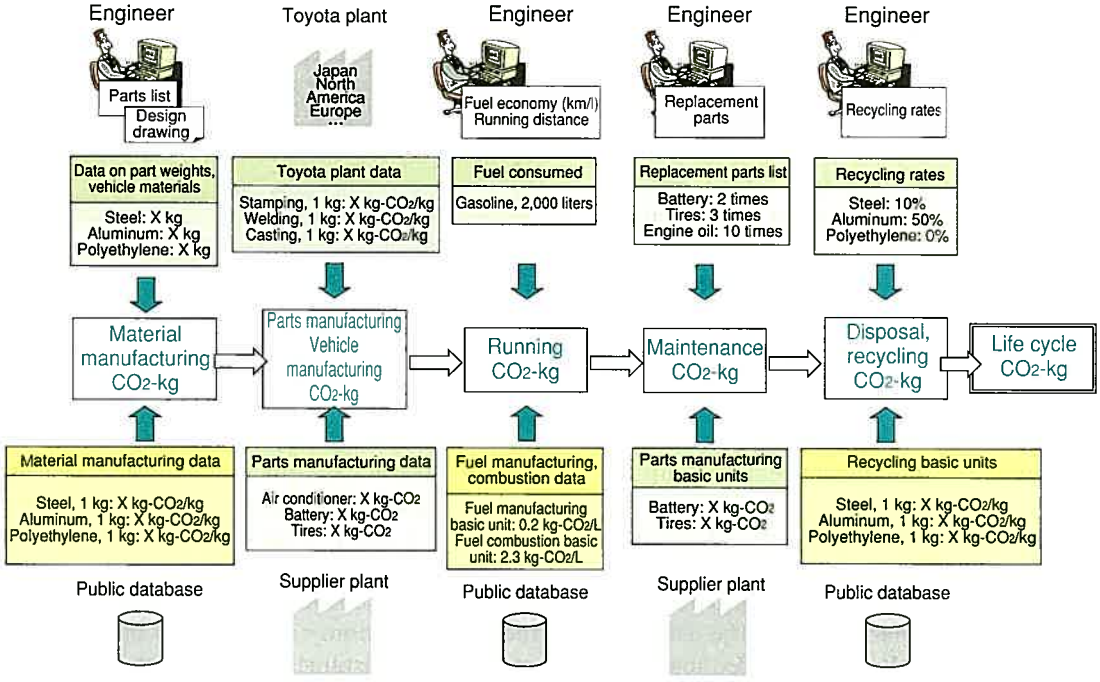

Fig. 5 LCA CO_2 Calculation Flow

calculation method is used to determine the amount of CO_2 emitted over a vehicle's life cycle.

The calculation of the total CO_2 emissions proceeds in stages. First, the amount of CO_2 emitted at the material manufacturing stage is calculated by taking the amount of each material that makes up an automobile and multiplying it by the amount of CO_2 emitted in the manufacture of 1 kilogram of the material. The amount of each material used in one vehicle is calculated based on data from parts lists and drawings. To create the material manufacturing database, data was collected from public databases and incorporated into an automotive materials manufacturing database at Toyota.

Fig. 6 shows the amounts of CO_2 emitted in the manufacture of 1 kilogram of some of the main materials used in automobiles.

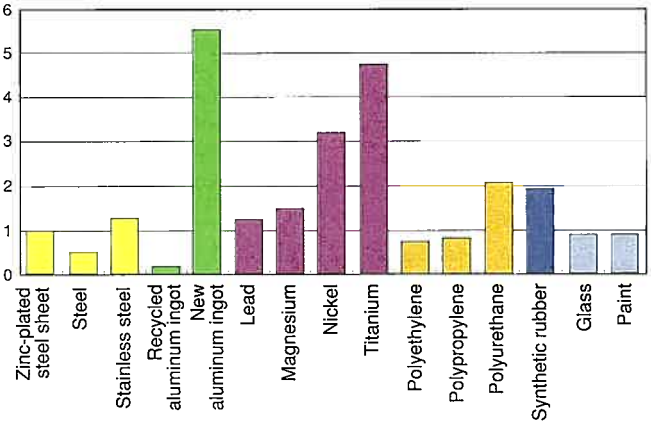

(Relative values when defining CO_2 emissions of zinc-plated steel manufacturing as 1)

Fig. 6 CO_2 Emissions in Manufacture of 1 Kilogram of Material

The amounts of CO_2 emitted vary considerably according to the type of material. For example, the amount of CO_2 emitted in manufacturing 1 kilogram of new aluminum is roughly double the amount for steel sheet. There is a possibility that changing materials or adopting new materials could alter the environmental impact at the manufacturing stage. In this sort of case, LCA can be used to assess the environmental impact before a change is made.

Next, the calculations are made for the parts manufacturing and vehicle manufacturing stages. The CO_2 emissions for internally manufactured parts are calculated by multiplying the amount of each material used by the amount of CO_2 emitted in processing 1 kilogram of the material. Manufacturing data from each Toyota plant has been surveyed and collected for incorporation into a database of CO_2 amounts emitted during processing.

For the main externally manufactured parts, manufacturing data is collected with the cooperation of the suppliers. The manufacturing database currently holds data on approximately 60 parts, mainly ones that are particularly heavy. The data for internally and externally manufactured parts are added together for use as parts and vehicle manufacturing data.

For the running stage, the total fuel consumption is calculated by multiplying the total life cycle running distance by the fuel consumption rate for the vehicle in question. Publicly available coefficients for the amounts of CO_2 emitted in the manufacture and combustion of fuel are multiplied by the life cycle fuel consumption to calculate the amount of CO_2 emitted in the running stage.

To calculate the CO_2 emissions for the maintenance stage, LCA defines specific replacement parts, then calculates the amounts of CO_2 emitted in manufacturing the required number of each part. The system uses data from the material manufacturing and parts manufacturing databases for the calculations.

CO_2 emissions at the disposal stage are calculated as the total CO_2 emissions from the shredding of an end-of-life vehicle and the landfill of the shredder residue. CO_2 emissions for the recycling stage are calculated by determining the amounts of CO_2 emitted in the recycling and reuse of the scrap steel and aluminum that is recovered from an end-of-life vehicle. A database for steel, aluminum, and plastic recycling has been assembled by surveying and collecting environmental data on representative recycling processes. The amount of CO_2 emitted in the recycling stage can be calculated just by multiplying the appropriate coefficient by the amount of scrap.

The total amount of CO_2 emitted over the entire life cycle is the sum of the emissions at the individual stages.

2.2 Use of LCA at Toyota

Toyota started using LCA in 1997, and its history is divided into three phases, as shown in **Fig. 7**.

	Developments	Vehicle assessed
Phase 1 (1997-1999)	- LCA method established - Existing clean energy vehicles assessed	- Prius - RAV4EV
Phase 2 (2000-2003)	- Use of LCA starts with developed parts - LCA implemented for representative vehicles* and results published in catalog (*2010 fuel economy target + U-LEV) - LCA system established	- Premio - Allion - Ist - FCHV - New Prius
Phase 3 (Since 2004)	- LCA extended to all vehicles - LCA system operation - Eco-VAS introduced in 2005	All vehicles

Fig. 7 History of LCA Use and Future Plans

During the three years of Phase 1, the LCA method described in Section **2.1** was established, and the necessary databases were created. In 1997, LCA was used to assess clean energy vehicles such as the original Prius and an electric vehicle. **Fig. 8** shows the Phase 1 LCA results for an electric vehicle and hybrid vehicle. The assessment was based on a lifetime running distance of 100,000 kilometers (10 years' use), with 10-15 mode fuel consumption. The electric and hybrid vehicles were compared to gasoline vehicles of the same class to determine how much they reduce environmental impact.

In the graphs in **Fig. 8**, a value of 1 is assigned to the gasoline vehicle for each LCA assessment item, and values are assigned to the electric and hybrid vehicles in relation to that standard.

The graph for CO_2 shows that the electric vehicle's emissions in the running stage are extremely low. But because electric vehicles use motors and nickel-metal hydride batteries weighing several hundred kilograms, the CO_2 emissions at the manufacturing stage, the sum of the material manufacturing and vehicle manufacturing emissions, are approximately double those for a gasoline vehicle.

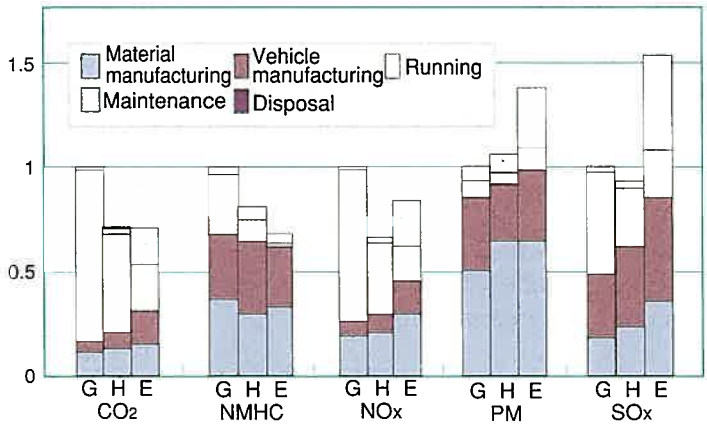

Hybrid (H) and electric (E) vehicles compared to gasoline (G) vehicles of the same class

NMHC: Non-methane hydrocarbons
PM: Particulate matter

Fig. 8 LCA Results for Electric Vehicle and Hybrid Vehicle

Moreover, because the batteries must be replaced after five years, a large amount of CO_2 is emitted in the maintenance stage.

The hybrid vehicle also uses motors and nickel-metal hydride batteries weighing close to a hundred kilograms, so its manufacturing-stage CO_2 emissions are also higher than for a gasoline vehicle.

The total results for CO_2 indicate that the electric and hybrid vehicles achieve about the same level of reduction in CO_2 emissions in comparison with a gasoline vehicle. The hybrid reduces emissions in a well-balanced manner for the other assessment items as well. This shows that it is a clean vehicle, even from the LCA perspective.

In Phase 2, assessments began for certain development parts and vehicles. In 2001, the Premio/Allion became the first of several representative models with good fuel economy and emissions performance to have its LCA results published in the catalog.

Phase 3 started in 2004, with LCA being implemented for all new passenger car models, as well as those undergoing a model change.

The nucleus of an LCA system that networks all of the necessary databases was completed and first put into operation for the new Vitz that went on the market in February 2005.

As **Fig. 9** illustrates, the LCA system networks a series of databases, including manufacturing databases for Toyota plants, externally manufactured parts, and material and energy, with the LCA calculation system. This allows the chief engineer and the design staff to use their computers to check LCA data for vehicles in development whenever the need arises. The network will also be made available to suppliers in the future, so that LCA assessments of parts can be done at any time. Completion of the entire LCA system is planned for 2005.

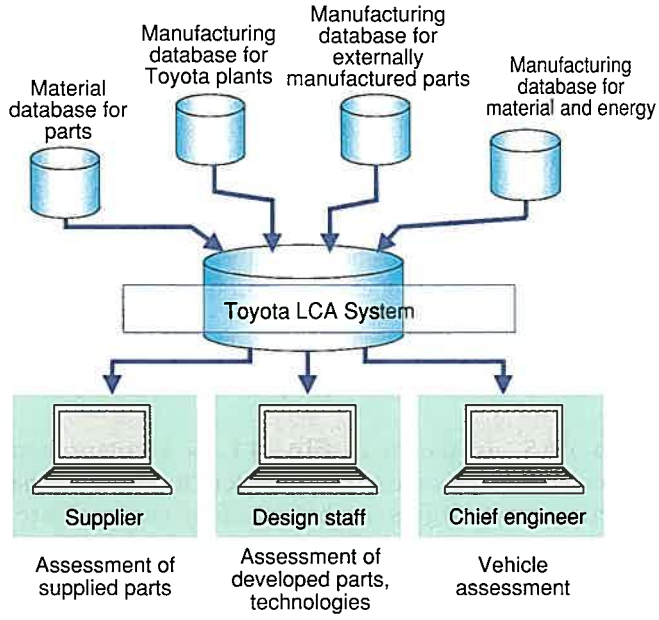

Fig. 9 LCA Network System

The LCA results for the new Vitz are shown in **Fig. 10**, with the old model labeled "A" and the new model labeled "B." The assessment was based on a 1.0 L engine and a lifetime running distance of 100,000 kilometers (10 years' use) in the 10-15 mode. The graph for CO_2 is in tons, while those for the other items are in kilograms. The CO_2 results are expressed in relation to a level of 1,000 tons for the old model, while the results for the other items are relative to a value of 1 for the SOx emissions of the old model.

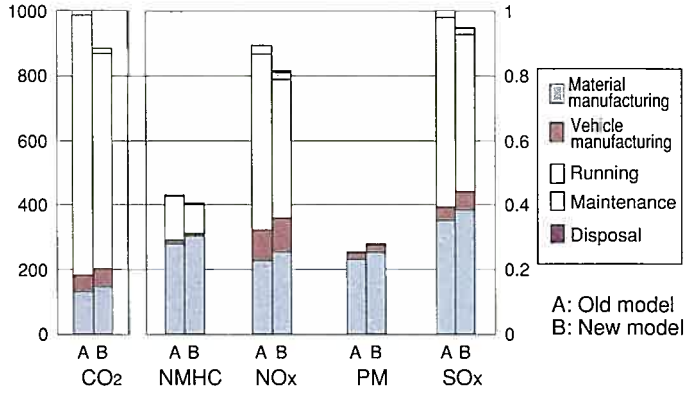

Fig. 10 LCA Results for New Vitz

The vehicle weight of the new Vitz is greater than that of the old model, but the 10-15 mode fuel economy is approximately 20% better. The LCA results indicate that the manufacturing-stage emissions of all items are higher for the new Vitz than for the old model. However, the new Vitz has better fuel economy and exhaust emissions performance, so its total emissions are lower.

Improvements in fuel economy and exhaust emissions performance have been established as the most important targets in new vehicle development, which means that the amounts of lightweight materials and electronic control parts are expected to increase. This means that the environmental impact in the manufacturing stage may increase, so if the environmental impact over the total life of a vehicle is to be continuously reduced, it is important for LCA to be utilized starting in the initial stage of development.

Operation of Eco-VAS started in 2005 with the new Vitz. LCA is used as an assessment tool for reducing the life cycle environmental impact, which is one part of Eco-VAS.

3. Eco-Vehicle Assessment System (Eco-VAS)

Eco-VAS, as shown in **Fig. 11**, is a comprehensive environmental impact assessment system for ensuring that the environmental targets set by the chief engineer are met throughout the development process, from the planning stage to the start of production.

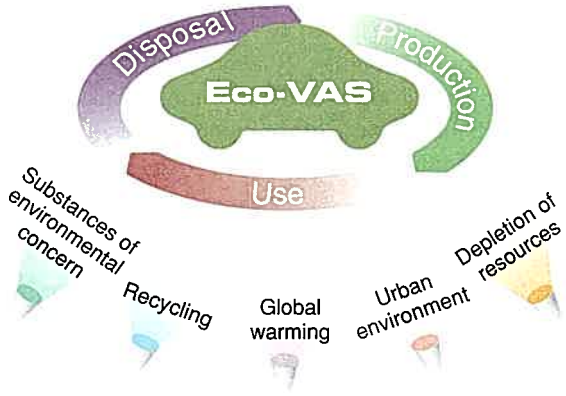

Fig. 11 Eco-VAS

A wider range of environmental measures have been devised in recent years, and in the 1990s, the automobile industry came under pressure to improve its recycling performance, cut back on substances of environmental concern, and reduce the life cycle environmental impact. A chief engineer must consistently promote a broad range of environmental measures for a vehicle in development.

The conventional approach at Toyota to recycling, substances of environmental concern, and LCA has been for the respective promotion departments to communicate with the chief engineer, so that environmental measures are incorporated into the design. Now, under the framework of Eco-VAS shown in **Fig. 12**, targets are established not only for fuel economy and exhaust emissions, but also for the impacts on (LCA values for) air pollution, global warming, and resource depletion from the viewpoint of the entire life cycle, as well as for recycling performance and the reduction of substances of environmental concern when a vehicle is dismantled. Moreover, the achievement of the targets is monitored throughout the development process. The system illustrated in **Fig. 13** was introduced in 2005 with the hope that it will help to achieve the targets in a balanced and reliable way.

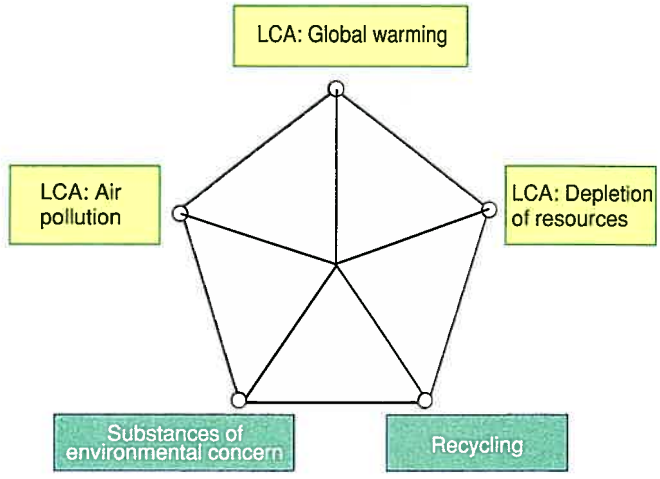

Fig. 12 Eco-VAS Environmental Targets

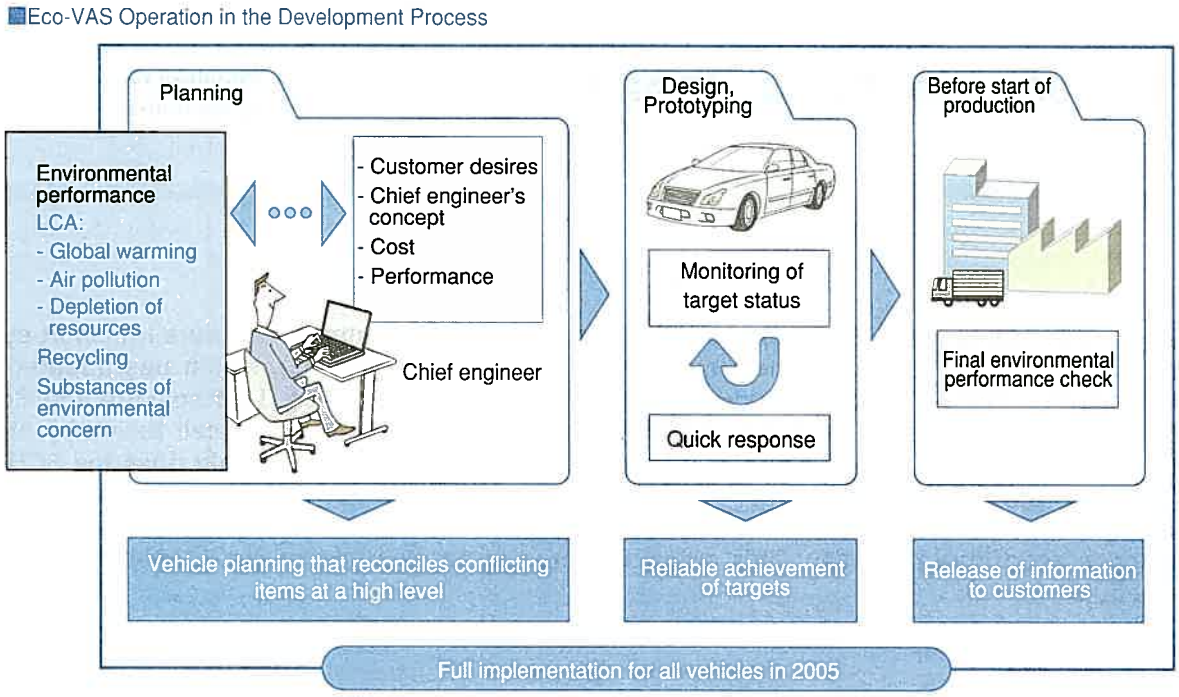

Fig. 13 Use of Eco-VAS in the Development Process

Toyota will use Eco-VAS to continuously improve its environmental performance in the future and will provide customers with environmental information that has been confirmed in the final stage.

Author

M. YAMATO

Introduction of FCHV-BUS for The 2005 World Exposition, Aichi, Japan

Yoshiyuki Miki*
Hideaki Mizuno*
Masataka Esaki**
Akira Iwatsuki***

Abstract

A fuel cell hybrid vehicle bus (FCHV-BUS) has been introduced as an example of a future transport system at The 2005 World Exposition, Aichi, Japan (hereinafter referred to as EXPO 2005), which has adopted the theme, "Nature's Wisdom." The FCHV-BUS provides a transportation link between the Nagakute and Seto areas of EXPO 2005, and utilizes a hybrid system in which a motor is driven using a fuel cell fueled by high pressure hydrogen gas and a battery (a hydrogen nickel battery) as power sources. Not only does the FCHV-BUS have zero CO_2 and harmful substance emissions, but it also offers high energy efficiency and excels in terms of quietness. Eight of the buses are being used at EXPO 2005, which will give many people a chance to experience their advantages and future potential. This article will provide an overview of the FCHV-BUS, and describe its running schedule.

Keywords: *fuel cell, hybrid, bus, EXPO 2005*

1. Introduction

Toyota Motor Corporation started developing fuel cell vehicles in 1992. Fuel cell buses for urban transport not only offer environmental advantages (**Fig. 1**), but also play a major role in popularizing fuel cell vehicles as a whole because they can be ridden by a large number of people.

Toyota began developing the FCHV-BUS1 fuel cell bus in 1999 as a joint enterprise with Hino Motors, Ltd. (**Fig. 2**).

Hino took charge of the vehicle body and other areas specific to buses, while Toyota took charge of the areas pertaining to the fuel cell system. This was the best way to capitalize on the hybrid technology, knowledge, and know-how that both companies have nurtured over the years.

Based on the success of the FCHV-BUS1, development of the FCHV-BUS2 was initiated in 2001. The FCHV-BUS2 was certified by the Ministry of Land, Infrastructure and Transport in September 2002, a first for a bus. Public road tests started in October of the same year, and it was operated commercially from August 2003 to December 2004 as a city bus run by the Tokyo Metropolitan Government, primarily between the Yaesu exit of Tokyo Station and Odaiba.

As a result, the bus logged approximately 17,000 kilometers of commercial runs, enabling a large number of people to experience a vehicle powered by fuel cells.

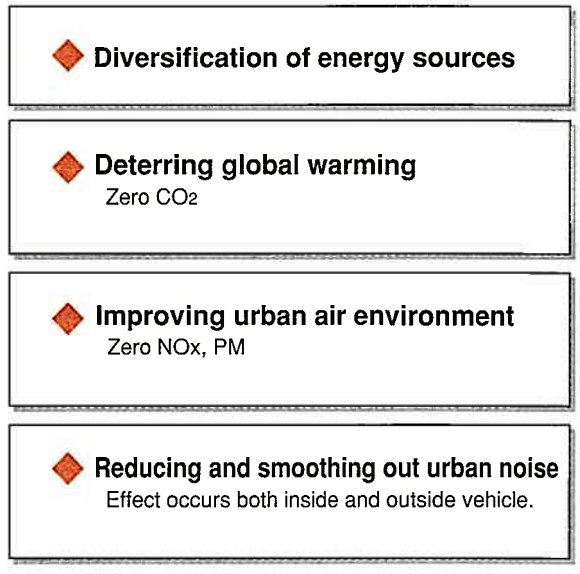

Fig. 1 Advantages of Fuel Cell Bus

* Fuel Cell System Engineering Div.
** Product Development Group
*** Toyota Development Center 1

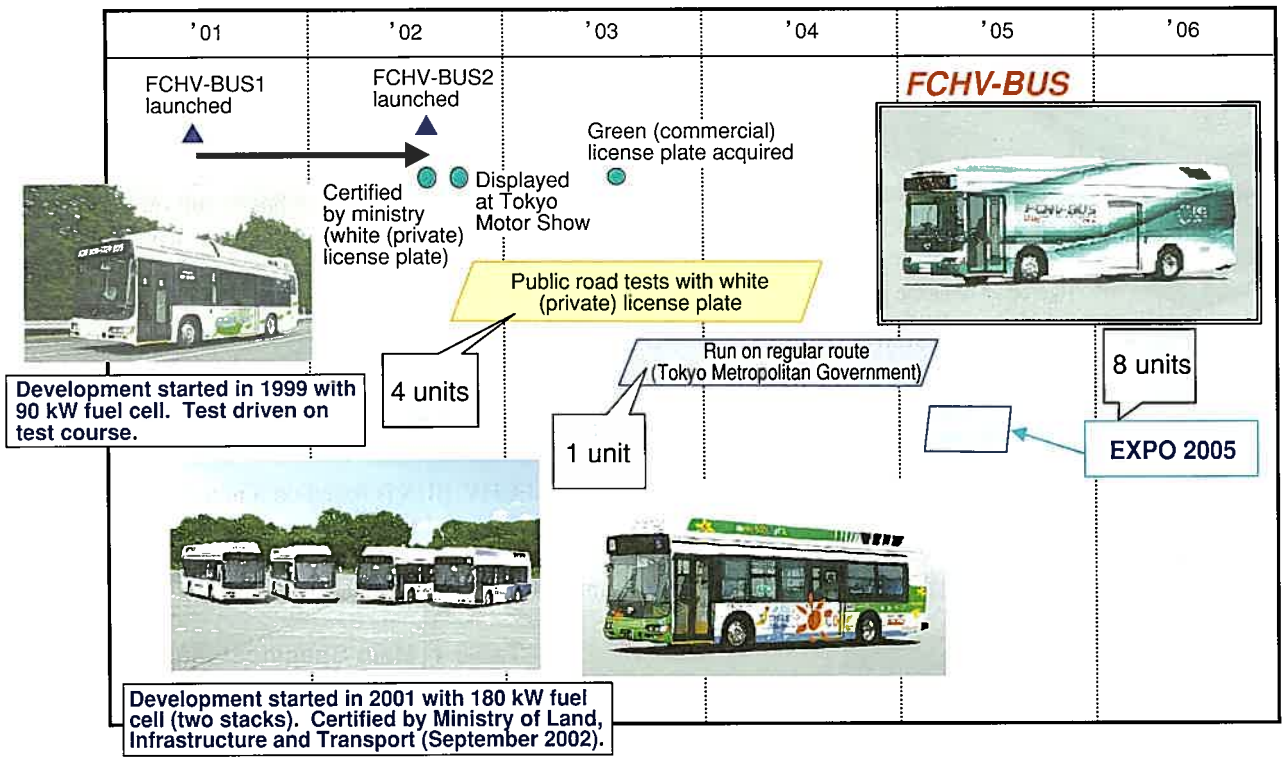

Fig. 2 Development of Fuel Cell Hybrid Bus

2. Fuel Cells

A fuel cell produces electricity through a chemical reaction between hydrogen and oxygen in the air (**Fig. 3**). When hydrogen is supplied to a catalyst on the negative electrode, electrons are discharged. These electrons then flow from the negative electrode to the positive electrode, generating electricity. The hydrogen that discharged the electrons is converted into hydrogen ions, which pass from the negative side to the positive side via a polymer electrolyte membrane. Oxygen, hydrogen ions, and electrons recombine on the catalyst of the positive electrode to form water. Resembling a small generating plant, a fuel cell produces electricity through a chemical reaction between hydrogen and oxygen. It is highly efficient because it extracts electricity directly from hydrogen without burning it. Theoretically, a fuel cell discharges only water, without emitting CO_2 or other harmful substances. This is the reason why a car that uses a fuel cell is said to be the ultimate eco-car.

In a fuel cell, the electrodes and the polymer electrolyte membrane are sandwiched between separators. Together, these three items are called a cell, with each cell producing a low voltage of 1 V or less. Therefore, several hundred cells must be stacked serially to generate high voltage. A single package of these stacked cells is called a fuel cell stack, or simply an FC stack. Ordinarily, the term "fuel cell" refers to an FC stack.

The fuel cell developed in-house at Toyota is called the "Toyota FC Stack."

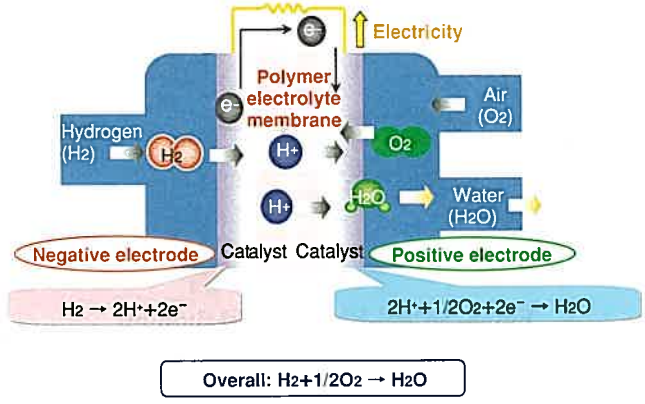

Fig. 3 Workings of Fuel Cell

3. FCHV System

The FCHV-BUS utilizes a hybrid system in which a motor is driven using a fuel cell fueled by high pressure hydrogen gas and batteries as power sources. Seven high pressure hydrogen tanks are provided on the roof, and two Toyota FC Stacks and other major components, are located at the rear of the vehicle (**Figs. 4** and **5**).

As **Fig. 6** shows, the bus contains two electrical systems, each consisting of a Toyota FC Stack, batteries, and power control units. Each system operates independently and cooperates with each other to control the motor. The power output of the motor is connected mechanically through gears.

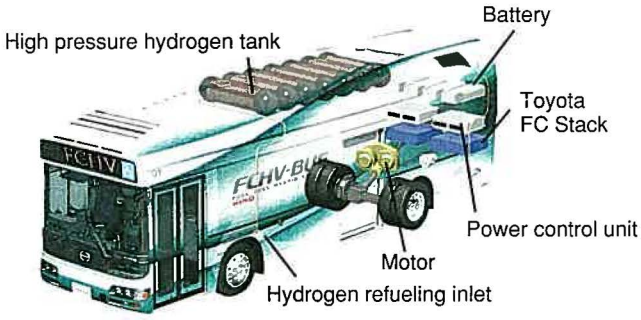

Fig. 4 FCHV-BUS System

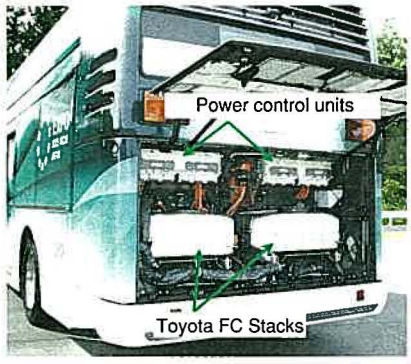

Fig. 5 Toyota FC Stacks

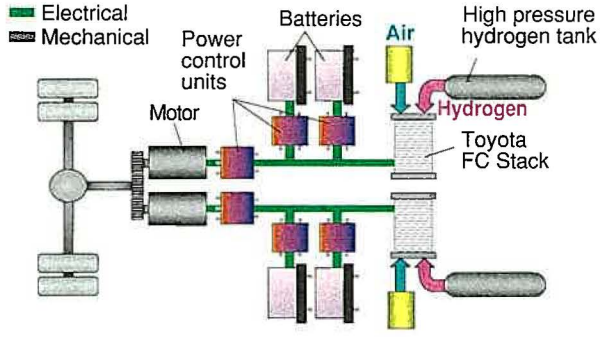

Fig. 6 FCHV-BUS Hybrid System

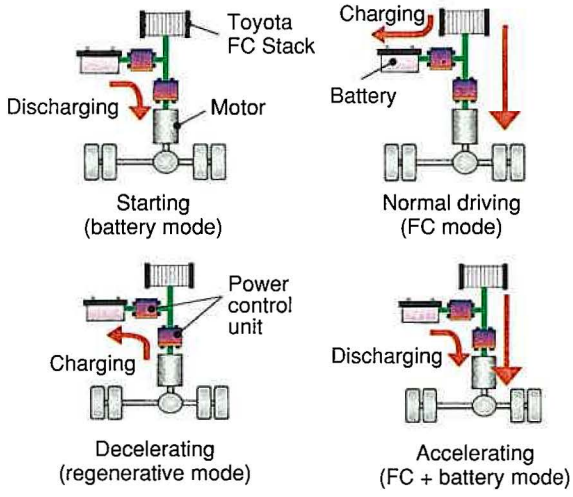

Fig. 7 Energy Management

Hybrid technology that has been developed as part of the Prius and Hino hybrid systems has been applied to system control. The inclusion of batteries in the system allows the bus to be operated more efficiently. This is because the batteries are charged using power generated on deceleration by the motor, thus allowing regeneration of energy, and because the system strictly controls whether the bus is run on either the Toyota FC Stacks or the batteries, depending on driving conditions and the most efficient region of the power sources (**Fig. 7**). Each electrical system contains two nickel-metal hydride batteries, making a total of four batteries.

4. FCHV-BUS Overview

The FCHV-BUS is based on a non-step large-sized Hino route bus. It delivers high dynamic performance, with a fuel cell stack output of 90 kW×2, maximum motor output of 80 kW, and maximum torque of 260×N·m² (**Table 1**).

Table 1 Main Specifications of FCHV-BUS

Vehicle	Base vehicle	Blue Ribbon City (non-step large-sized Hino route bus)
	Overall length/width/height	10,515/2,490/3,360 mm
	Max. speed	80 km/h
	Passenger capacity	65 people
Fuel cell stack	Type	Solid polymer type
	Output	90 kW×2
Motor	Type	AC synchronous motor
	Max. output	80 kW×2
	Max. torque	260 N·m×2
Fuel	Type	Pure hydrogen
	Storage system	High pressure hydrogen tanks
	Max. refueling pressure	35 MPa (350 bar)
Batteries	Type	Nickel-metal hydride

In addition to advanced fuel cell technology, the exterior of the bus has been designed to express a futuristic feeling and environmental friendliness (**Fig. 8**). The interior utilizes the concept of Universal Design, which emphasizes user-friendliness for a maximum number of people.

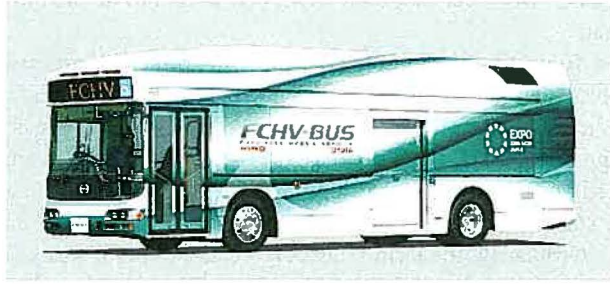

Fig. 8 Exterior of FCHV-BUS

5. Driving Schedule

The buses were used to shuttle visitors to the EXPO 2005 between the Seto and Nagakute pavilions free of charge (**Figs. 9** and **10**). The schedule was set up to allow the buses to be ridden by 300,000 people during the period.

This was the first opportunity in the world for fuel cell vehicles to be ridden by such a large number of people during a six-month period. It enabled the visitors to experience the usefulness of this technology and the great promise that a hydrogen-powered society holds for the future.

Operation period: March 25 to September 25, 2005 (185 days)
Route: Seto Pavilion to Nagakute Pavilion, approx. 4.4 km
Operation time: 9 am to 6 pm (matching the opening time of the pavilions)
Number of buses in operation: 8 units
Trip duration: approx. 10 minutes (one-way)
Operation intervals: approximately every 8 minutes
Transport capacity: 800 to 1,000 roundtrip passengers per hour

As a project carried out by the Engineering Advancement Association of Japan, a hydrogen station was set up at the bus terminal of the Seto Pavilion where the buses were refueled with hydrogen gas. The hydrogen station contained two refueling units: one that produced hydrogen by reforming city gas, and one that utilized by-product hydrogen gas obtained from a steelworks.

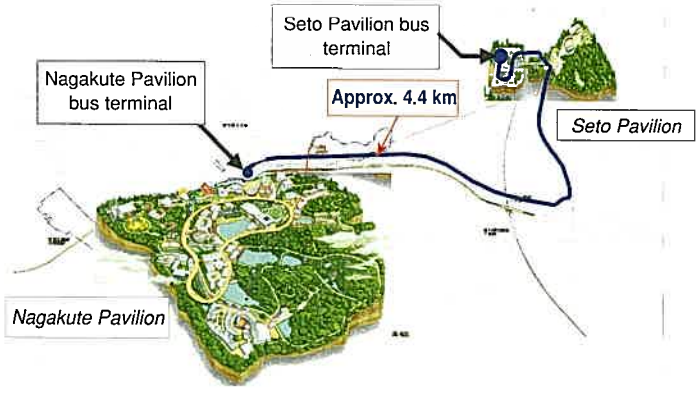

Fig. 9 Route Diagram

Fig. 10 Nagakute Pavilion Bus Terminal

6. Toward the Hydrogen-Powered Society of the Future

In contrast to the limited resources available on Earth, hydrogen is believed to possess unlimited possibilities as a new source of energy.

However, for automobile manufacturers, issues remain to be solved before fuel cell vehicles become widespread (**Table 2**). Measures must be taken to counter the freezing of the water produced by the reaction between hydrogen and oxygen at low temperatures. Technology must also be developed to store an adequate amount of hydrogen in order to ensure a driving range appropriate for a passenger car in spite of limited installation space. Ensuring reliability, improving durability, and reducing costs are also some of the issues that must be solved before fuel cell vehicles can enter widespread use.

Moreover, the maintenance of an infrastructure to supply hydrogen, and the development of basic technologies are also essential for achieving a hydrogen-powered society. It is hoped that society as a whole will act in concert toward the materialization of this goal (**Fig. 11**).

Table 2 Issues Facing the Widespread Use of Fuel Cell Vehicles

Item	Issues	Responsibility
Technological issues	**Low temperatures, high temperatures,** high efficiency, compactness, reliability, durability, salt water, dust, hot spring areas (hydrogen sulfide), high altitude, radio waves, etc.	Car manufacturers
Marketability	**Driving range** (hydrogen storage), **cost** (vehicle cost)	
Environmental concerns	Recyclability, Life Cycle Assessment (LCA)	
Safety	Hydrogen, high voltage, collision	
Social base	**Hydrogen production, transport, storage, infrastructure maintenance,** hydrogen cost	Governments and energy producers

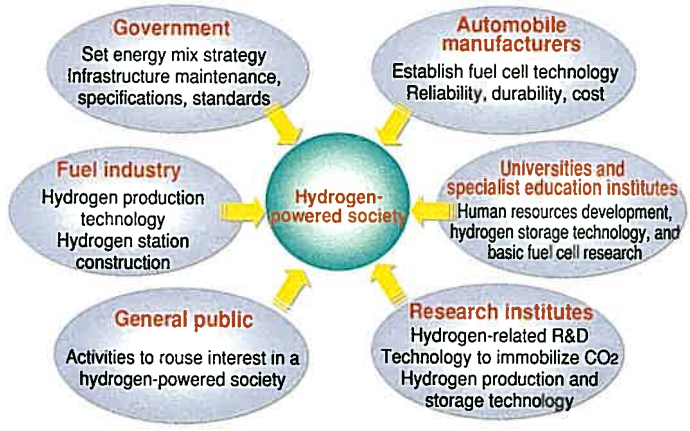

Fig. 11 Toward a Hydrogen-Powered Society

7. Conclusion

The authors hope that the EXPO 2005 has made more people familiar with the fuel cell, and helped spread the idea that it can be used as the power source for their dream car.

Authors


Y. MIKI


H. MIZUNO


M. ESAKI


A. IWATSUKI

Development of Light Weight and Low Fuel Consumption 3-Cylinder 1.0 L Engine

Akio Okamoto*
Kimioki Yasunaga**
Tadashi Nara**
Naoki Sugita**
Eiji Mishima***
Eiichi Komatsu***

Abstract

Reduction of CO_2 is essential to prevent global warming, and the development of small engines with good fuel consumption is an urgent task. In order to address these requirements, Toyota and Daihatsu have jointly developed the 1KR-FE 3-cylinder 1.0 L engine. This compact engine simultaneously achieves low fuel consumption and high performance through adoption of features like a spined cast iron liner with thin wall thickness, resin coated pistons, a unified intake system, and optimized intake port design. Moreover, as countermeasures against vibrations that are a concern for 3-cylinder engines, a crank shaft with three counter weights, and two mountings and a torque rod system with optimized spring constant and positioning have been adopted. As a result, vibrations have been reduced to an extremely good level.

Keywords: *new type, gasoline engine, 3-cylinder, light weight, excellent fuel economy*

1. Introduction

In recent years, much attention has been focused on global environmental issues, and the reduction of CO_2 emissions in particular has become one of the biggest challenges facing the automotive industry. The development of small engines with excellent fuel economy is an urgent task for addressing this issue. In order to fulfill this need, Toyota and Daihatsu have jointly developed a new 3-cylinder 1.0 L gasoline engine named 1KR-FE. This article presents an outline of the new engine.

2. Assessment

A or B segment vehicles weighing 1.0 t or less require an engine with a maximum power output of approximately 45-50 kW to provide an acceptable highway driving performance. Based on specific power output, it was determined that a 1.0 L naturally aspirated gasoline engine is capable of achieving this output level.

Recently, 3-cylinder engines have been drawing attention in this vehicle class. Before starting the development of the new 1.0 L engine, the appropriate number of cylinders for the engine was investigated from the perspectives of output performance, fuel economy, and noise and vibration (NV).

2.1 Weight and size

Designing lighter and more compact engines is an issue for all classes of vehicles. In small cars in particular, it is very important for an engine to be light and compact because of fuel economy, driving performance, and package restrictions (**Fig. 1**). Comparisons of 3- and 4-cylinder layouts with the same displacement demonstrated that greater reductions in weight and size can be achieved with a 3-cylinder layout.

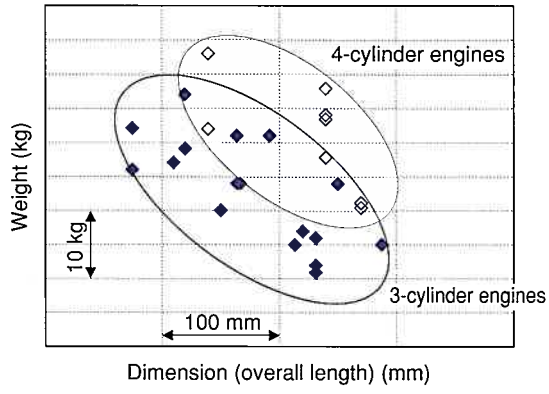

Fig. 1 Trends for Engine Dimensions and Weight

* Engine Engineering Div. 2
** Engine Engineering Div. 1
*** Daihatsu Motor Co., Ltd.

2.2 Fuel economy

Fig. 2 shows the results of a simulation of indicated heat efficiency and heat loss against displacement. The calculation was performed using a single cylinder engine with a square bore/stroke. It is a well-known fact that a bigger displacement per cylinder or a smaller S/V ratio (the ratio of the combustion chamber surface area to displacement) leads to lower heat loss and higher indicated heat efficiency. **Fig. 2** demonstrates that this tendency is stronger for small 1.0 L engines.

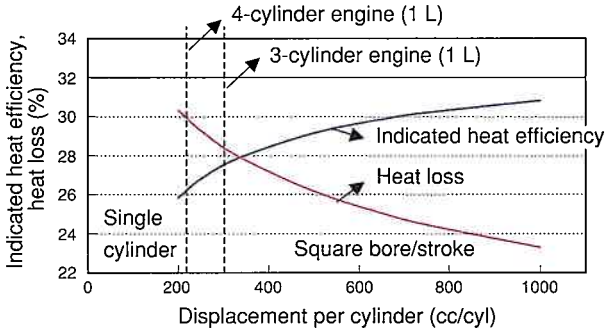

Fig. 2 Heat Efficiency Calculation Results

Fig. 3 shows the relationship between displacement per cylinder and fuel economy, obtained from a regression line created using data of 16 types of engines. Based on these results, it was estimated that the fuel economy of a 3-cylinder engine would be approximately 5% better than a 4-cylinder engine in the 1.0 L class. Key factors in this difference include the combined effect of the smaller S/V ratio and lower friction.

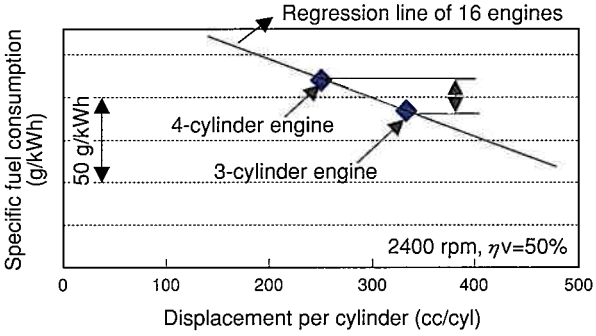

Fig. 3 Fuel Consumption Test Formula

2.3 Volumetric efficiency

Because the volumetric efficiency of three cylinders is higher than four in the low- to mid-speed range, a 3-cylinder engine has higher low- to mid-speed torque potential. **Fig. 4** shows results for volumetric efficiency calculated by BOOST (a simulation tool for the intake and exhaust systems).

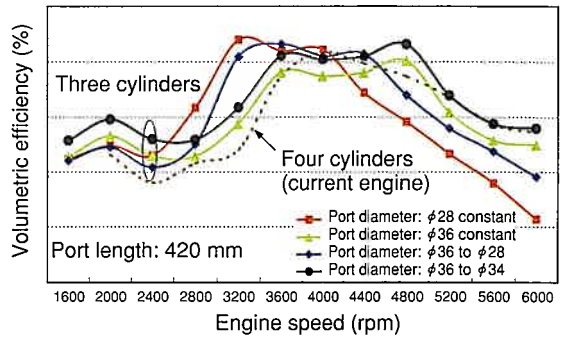

Fig. 4 Volumetric Efficiency Calculation by BOOST

2.4 Idle vibration

The biggest concern for 3-cylinder engines is vibration when idling. First order vibration caused by rotation and 1.5 order vibration rotation caused by engine combustion are known issues in the development of a mounting system for a 3-cylinder engine. **Fig. 5** shows the power plant resonance relationships in a 3-cylinder engine mounting system. Controlling the spring constants clearly suppresses the vibration level at approximately 800 rpm between the 1st and 1.5 order peaks.

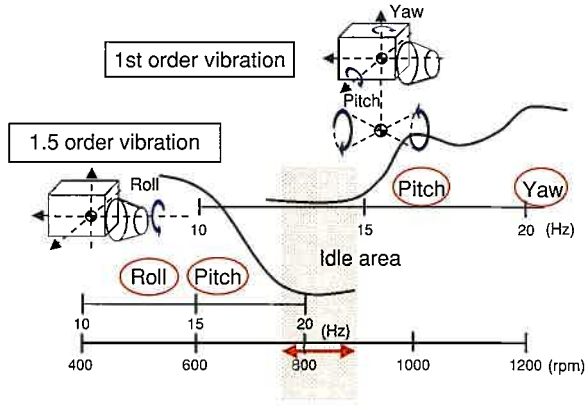

Fig. 5 Power Plant Rigid Resonance

Good potential for suppressing idle vibration was demonstrated in a simulation of vehicle floor vibration (**Fig. 6**).

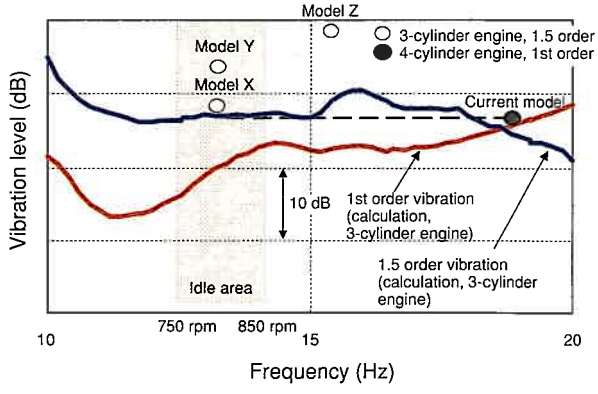

Fig. 6 Floor Vibration Simulation

2.5 Summary of assessment

Based on the above assessment, idle vibration was determined to be controllable. Consequently the 3-cylinder concept was chosen for reasons of weight, size, fuel economy and low- to mid-speed torque.

3. Features of the 1KR-FE Engine

Table 1 shows the base specifications of the 1KR-FE engine. **Fig. 7** shows an overall view of the engine and the new features. The development targets for this engine were top-of-class fuel economy, high output, low weight, and compactness. This engine incorporates the features of recent Toyota engines, including a DOHC with chain-drive, four valves per cylinder and a compact pent roof combustion chamber.

Table 1 Features of 1KR-FE Engine

Engine code	1KR-FE	Current engine
Number of cylinders	3	4
Displacement (cc)	998	998
Bore (mm) × stroke (mm)	φ71×84	φ69×66.7
Bore center distance (mm)	78	78
Compression ratio	10.5	10
Valve train system	DOHC 4-valve with VVT (direct tappet)	DOHC 4-valve with VVT (direct tappet)
Max. power (kW/rpm)	50/6000	48/6000
Max. torque (Nm/rpm)	93/3600	90/4100
Low-speed torque (Nm) @2,000 rpm	85	78
Dry weight (with alternator, kg)	67	83

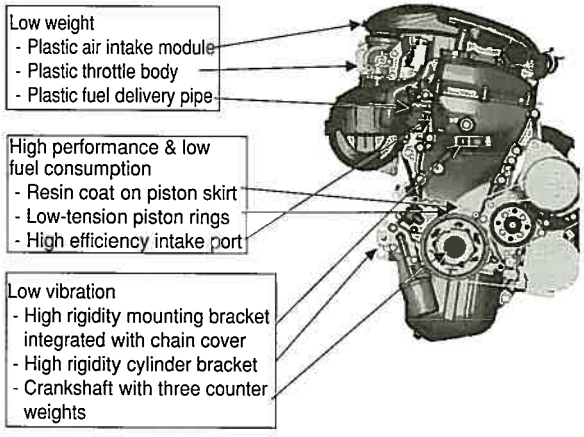

Fig. 7 Overall View and Main New Features of 1KR-FE Engine

3.1 Low weight and compactness

All intake air system components including the throttle body are made of plastic and are provided in a compact package (**Fig. 8**). The air cleaner cover forms one unit with the intake air duct and the engine cover, and the air cleaner housing is integrated into the cylinder head cover. As a result, the intake air system is about 18% lighter than a conventional model (**Fig. 9**).

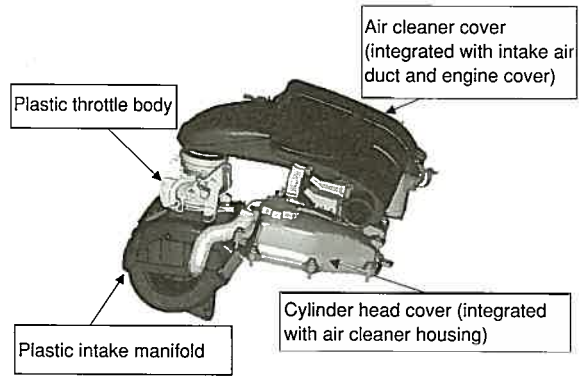

Fig. 8 Plastic Air Intake Module

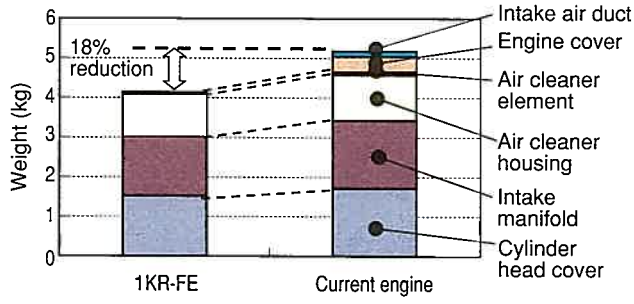

Fig. 9 Weight Reduction of Intake System

The 1KR-FE engine uses thin cast iron cylinder liners as cast inserts within an aluminum alloy cylinder block (described below). This reduces the spacing between bores, making the engine more compact (**Fig. 10**).

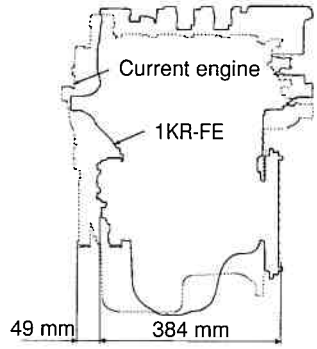

Fig. 10 Engine Dimensions

The implementation of the light weight and compact design has achieved a weight reduction of about 20% from a conventional engine, making the 1KR-FE the lightest engine in its class (**Figs. 11** and **12**).

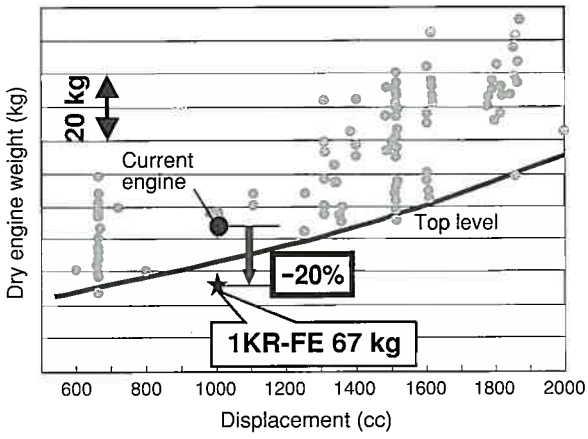

Fig. 11 Engine Weight

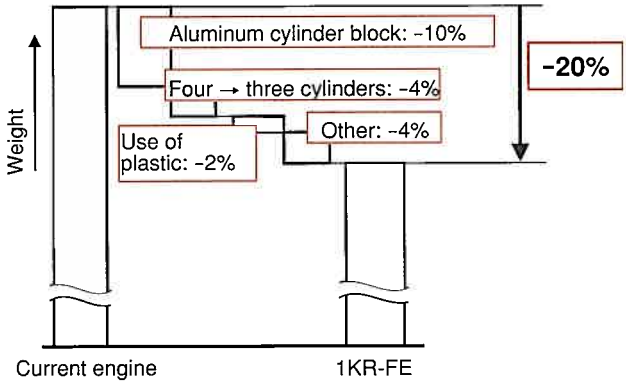

Fig. 12 Weight Reduction Analysis

3.2 Excellent fuel economy

In addition to the friction reduction achieved with the 3-cylinder design, the 1KR-FE engine also includes several other features that improve fuel economy (**Table 2**).

Table 2 Fuel Economy Improvement Features

Items	1KR-FE	Current engine
Intake port	High flow and high tumble	High flow
Total tension of piston rings (N)	14	28
Piston ring width (mm)	Top, 2nd: 1.0 Oil: 1.5	Top, 2nd: 1.2 Oil: 2.0
Piston resin coating	New resin coating	None
Crankshaft main journal diameter (mm)	44	46
Crankshaft offset (mm)	8	8
Compression ratio	10.5	10

As mentioned above, the new cylinder liner (**Fig. 13**) is a spined cast iron liner with thin wall thickness. The new liner has a lower peripheral protrusion height and a more uniform protrusion density than a conventional model, enabling dimensional precision to be improved. The thickness of the liner has been reduced to 2.3 mm and the height of the spines has been kept to a maximum of 0.9 mm. As a result, a spacing of 7 mm has been achieved between the bores. By reducing surface roughness at the bottom of the protrusion periphery, metal flow is improved during the aluminum die-casting process. As a result, the bonding strength between the iron liner and the aluminum block is better than in the conventional model. This reduces cylinder bore distortion after engine running (**Fig. 14**), thereby reducing the piston ring tension.

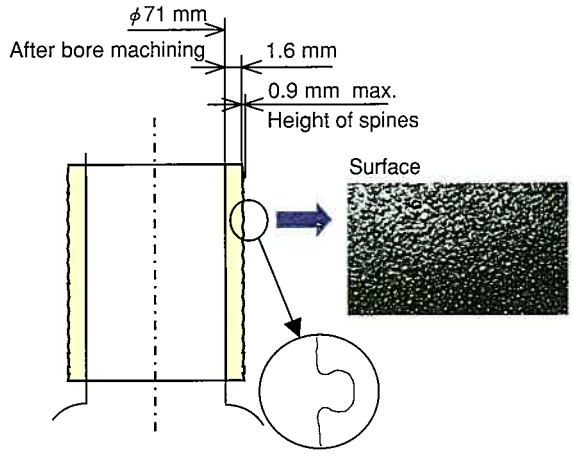

Fig. 13 New Cylinder Liner

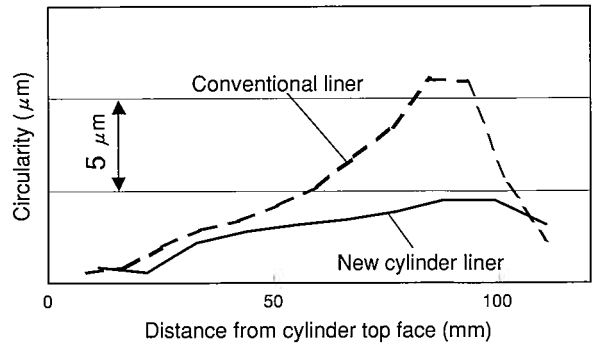

Fig. 14 Cylinder Bore Circularity (4th Order)

The width of the piston rings has been reduced to 1.0 mm for the top and second rings and to 1.5 mm for the oil ring. Adopting the newly developed cylinder liner ensures cylinder bore circularity after engine running. This reduces the total tension by 14 N, which represents a piston ring force reduction of approximately 50% over the conventional model (**Fig. 15**).

Furthermore, a new type of resin coat is used on the piston skirt. This new coat contains aluminum oxide to improve wear resistance. **Fig. 16** shows the results of friction analysis. Despite an increased piston speed, the friction of the piston system has been reduced by the adoption of the low-tension rings and new resin coat. The friction of the valve train system has also been reduced.

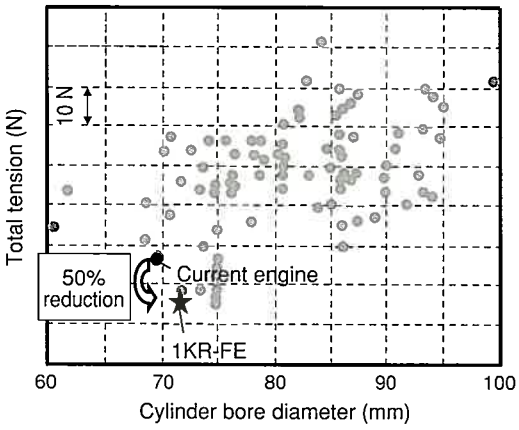

Fig. 15 Total Tension of Piston Rings

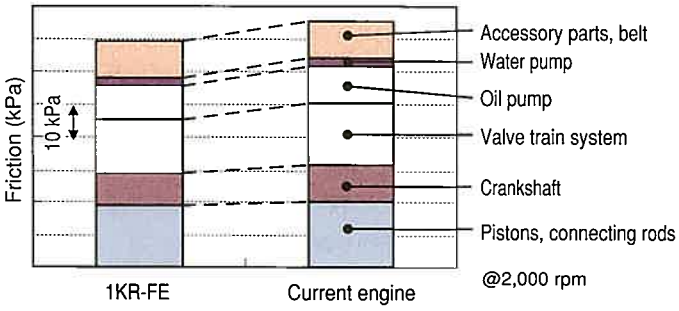

Fig. 16 Friction Analysis Results @2,000 rpm

Based on these results, fuel consumption has been reduced by approximately 10% over the current engine, as shown in **Fig. 17**.

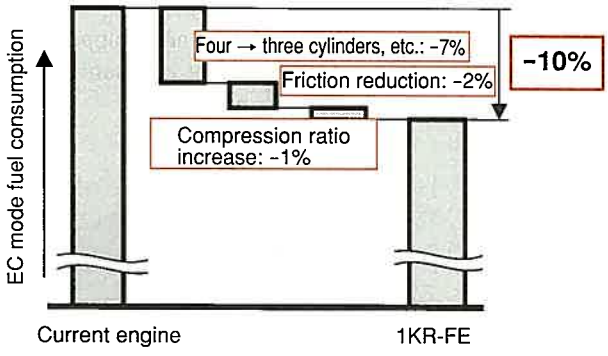

Fig. 17 Fuel Consumption Reduction

3.3 High performance

The use of a long reach type spark plug (**Fig. 18**) allows a sufficient water jacket space at the center of the combustion chamber for improved cooling in the chamber. This minimizes the possibility of self-ignition around the spark plug and ensures anti-knock performance at a high compression ratio of 10.5. The slant squish combustion chamber improves the combustion speed.

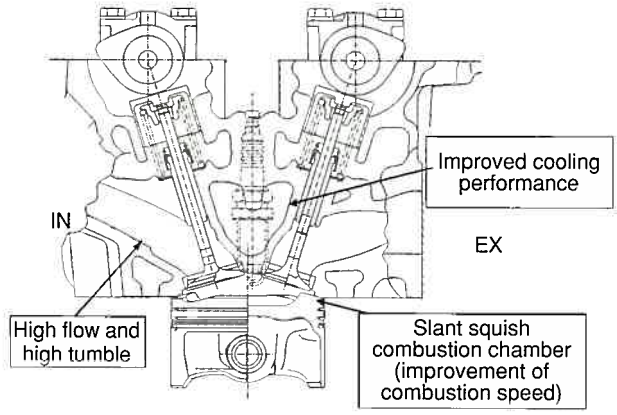

Fig. 18 Section View of Cylinder Head

VVT-i has also been introduced to optimize low- to mid-speed torque and high-speed performance.

Fig. 19 shows the performance curves of this engine. The 1KR-FE engine has a maximum power output of 50 kW/6,000 rpm, a maximum torque of 93 Nm/3,600 rpm, and a low-speed torque of 85 Nm/2,000 rpm.

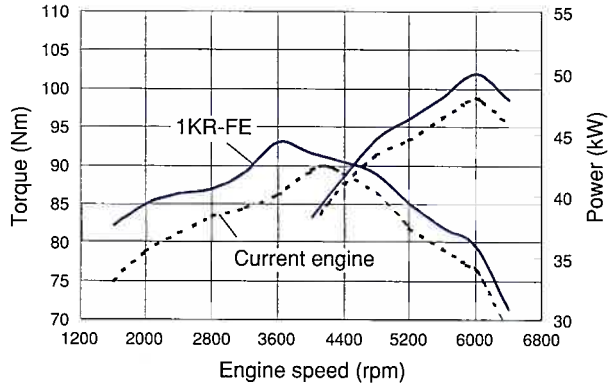

Fig. 19 Performance Curves

3.4 Vibration

This engine uses a forged crankshaft. It has a three-counter weight design for improving NV performance, despite the fact that this is heavier than the normal two-counter weight design. The cylinder block is a deep skirt type, which has the merit of better rigidity, and is reinforced with ribbing to achieve the required strength. The weight of moving parts has also been minimized by, for example, reducing the piston weight to 169 g.

As a result, the 1KR-FE achieves vibration levels comparable to a 4-cylinder engine (**Fig. 20**).

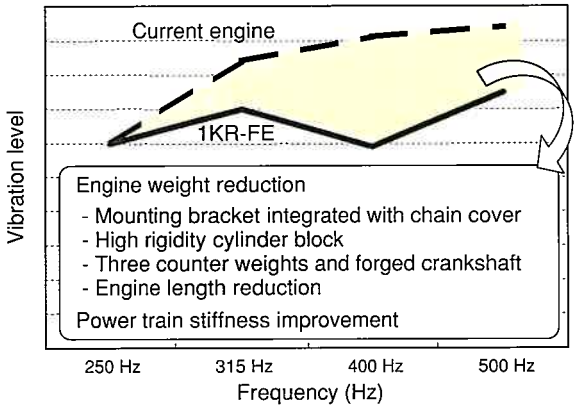

Fig. 20 Vibration Level at Engine Mounting Ends

The 1KR-FE engine has two mountings and a torque rod system. The engine mountings on the left and right are located near the center of gravity of the power plant (**Fig. 21**). As mentioned above, 1st and 1.5 order vibration from engine rotation focus were identified as key factors. Consequently, the up-down, left-right and front-rear spring constants of the mountings and the spring constant of the torque rod were optimized by simulation and road tests. The up-down positions of the left and right mountings and the torque rod were also optimized. As a result, it was possible to isolate the resonance points of engine pitching, yawing and rolling from the idle area of approximately 800 rpm, thereby achieving a top level of idle vibration in the 3-cylinder engine class (**Fig. 22**).

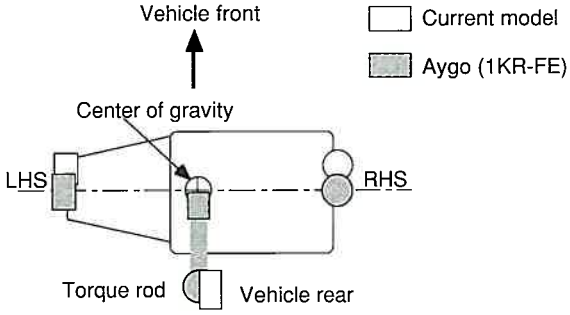

Fig. 21 Mounting Layout

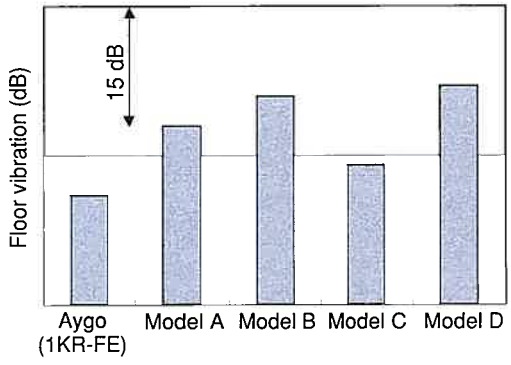

Fig. 22 Comparison of Floor Vibration when Idling (3-Cylinder Engines)

4. Conclusions

Toyota and Daihatsu have jointly developed the 1KR-FE, a new 3-cylinder 1.0 L gasoline engine for A or B segment vehicles. All intake air system components have been made of plastic and integrated into a compact package to reduce the weight and size of the engine. A newly developed cylinder liner design minimizes cylinder-bore distortion, making it possible to use thin, low-tension piston rings. Additionally, a new type of resin coat with excellent wear resistance is used. As a result, friction has been reduced, and the CO_2 emissions of the Toyota Aygo have been suppressed to 109 g/km (**Fig. 23**).

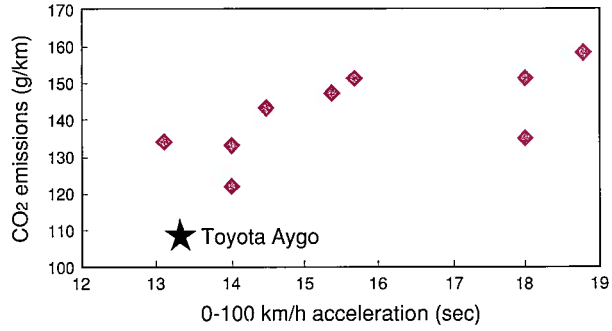

Fig. 23 Aygo CO_2 Emissions and Acceleration

Introducing a three-counter weight design for the crankshaft, increasing the rigidity of the cylinder block, reducing the weight of moving parts, in addition to adopting a design featuring two mountings and a torque rod with optimized spring constants and positions have all contributed to reducing vibration to an optimum level.

Finally, we would like to express our sincere appreciation to Daihatsu Motor Co., Ltd. and all relevant companies for their valuable contributions to the 1KR-FE project.

Authors

A. OKAMOTO K. YASUNAGA T. NARA

N. SUGITA E. MISHIMA E. KOMATSU

Development of New 2.2 L Direct Injection Diesel Engine

Masao Suzuki*
Naoyuki Tsuzuki**
Yoshihiro Teramachi***

Abstract

Two types of L4, DI diesel engines (2AD-FTV and 2AD-FHV) have been newly developed in order to achieve on a higher order the conflicting goals of greening emissions and reducing CO_2 emissions, while also securing high output and high torque. The 2AD-FTV engine uses an open-deck aluminum cylinder block, balance shaft and roller rocker valve train, and solenoid injectors used in the common rail system were optimized. The 2AD-FHV engine builds on the 2AD-FTV and utilizes a wealth of advanced technology, including a low power-compression ratio, piezo injectors, increased pressure (180 MPa), injection interval optimization, Diesel Particulate-NOx Reduction System (DPNR), and passage-switching Exhaust Gas Recirculation (EGR) cooler. Although this involved difficult research and development with high hurdles, the resulting 2AD-FHV has attained a level of emissions considerably lower than the Euro4 regulation value, while also achieving top output and torque for a 1.9 L to 2.2 L class engine.

Keywords: *diesel engine, common rail system, low compression ratio, piezo injector, open-deck aluminum cylinder block*

1. Introduction

It has become increasingly important for engines to satisfy two separate requirements. Exhaust emissions must be made cleaner and CO_2 emissions reduced from the perspective of protecting the global environment, but at the same time, there is an increasing demand from customers for higher performance to enhance the driving experience. In response to these needs, the number of diesel engines in Europe has increased over the past few years because of advantages such as better fuel economy, lower CO_2 emissions, and higher output performance. However, both NOx and PM must be reduced before diesel engines can become even more popular.

For these reasons, two types of new 2.2 L direct injection common rail diesel engines have been developed, the 2AD-FTV and 2AD-FHV. This article presents an outline of these new engines.

2. Aims of Development

The 2AD engine series was developed with emphasis on the following items in order to create class-leading diesel engines for passenger vehicles in the European market.

(1) Exhaust emissions performance far better than the Euro4 emissions standard
(2) Class-leading high output performance
(3) NV performance comparable to gasoline engines
(4) Class-leading low weight
(5) Class-leading reduced friction performance

3. Base Specifications

Table 1 shows the base specifications of these new engines.

Table 1 Engine Specifications

	2AD-FHV	2AD-FTV
Cylinder arrangement	In-line 4-cylinder	
Displacement (cc)	2231	
Bore × stroke (mm)	86 × 96	
Max. power (kW/rpm)	130/3600	110/3600
Max. torque (Nm/rpm)	400/2000-2600	310/1800-3000
Mean effective pressure (MPa)	2.26	1.75
Min. specific fuel consumption (g/kWh)	200	200
Fuel injection system	Common rail, piezo injector	Common rail, solenoid injector
Valve train system	4-valve, DOHC, chain	
Specifications of intake and exhaust systems	Variable blade turbocharger with intercooler	
Dry weight (dry/kg)	168	165
Exhaust emissions standard	Euro4*1	Euro4
Exhaust emissions control system	DPNR and passage-switching EGR cooler	Oxidation catalyst and EGR cooler

*1 NOx and PM are far below the levels specified in the Euro4 emissions standard.

4. Engine Features

Fig. 1 shows the main technologies adopted in the new engines. The weight of the 2AD-FTV has been reduced due to the use of a newly developed aluminum die-cast cylinder block.

* New Engine Development Div.
** Engine Engineering Div. 2
*** Engine Administration Div.

Noise reduction has been achieved by using a balance shaft, and fuel consumption has been reduced by using a roller rocker valve train system with a hydraulic lash adjuster. Maximum power output is 110 kW, and maximum torque is 310 Nm.

Furthermore, the 2AD-FHV uses such new technologies as DPNR, piezo injectors, a high-pressure injection system, and a low compression ratio to achieve a maximum power output of 130 kW and a maximum torque of 400 Nm. Both of these values are class-leading. In exhaust performance, the 2AD-FHV has achieved a drastic reduction in emissions, attaining a level far below that specified in the Euro4 emissions standard.

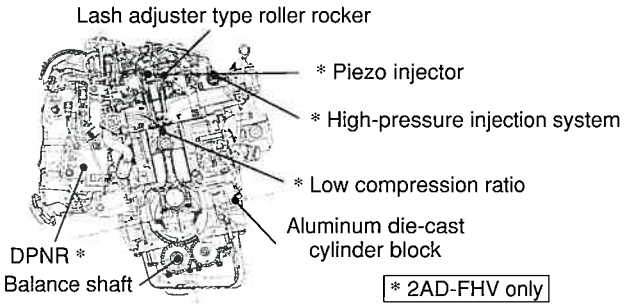

Fig. 1 New Technologies Incorporated into 2AD Engines

The output and exhaust performance of both engines are shown in **Fig. 2** and **Fig. 3** respectively.

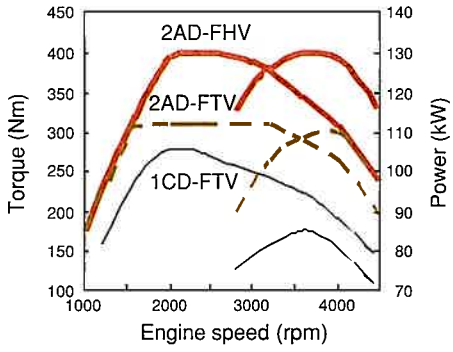

Fig. 2 Power and Torque Performance

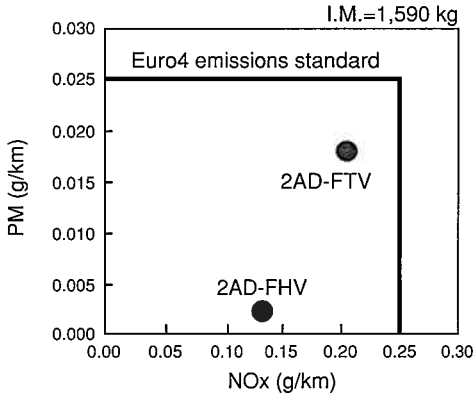

Fig. 3 Emissions

4.1 Low compression ratio

Reduction of the compression ratio enables output performance to be improved without increasing the pressure inside the combustion chamber (**Fig. 4**). It also enables the proportion of EGR gas in the total volume of intake air to be increased. Consequently, NOx reduction is achieved without affecting fuel efficiency (**Fig. 5**).

Low-temperature startability with the reduced compression ratio is ensured by the use of a ceramic material that enables the temperature of the glow plug tip to be increased, and piezo injectors that enable high-precision control of the multi-stage injection.

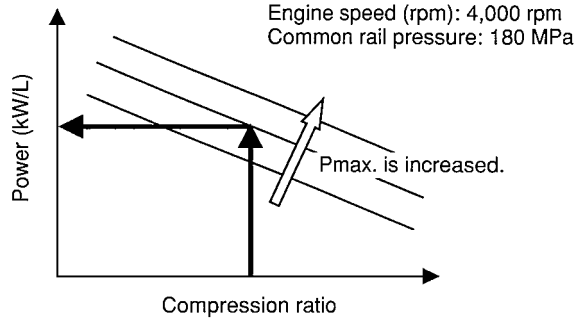

Fig. 4 Power-Compression Ratio

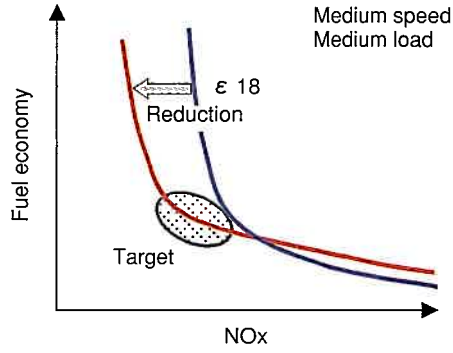

Fig. 5 Fuel Economy-NOx

4.2 Piezo injectors

Use of a piezo electric device has improved the response and speed of needle control, and radically improved injection properties on start-up and completion of injection (**Fig. 6**). Moreover, the improved controllability during multi-stage injection has enabled a reduction in combustion noise (**Fig. 7**).

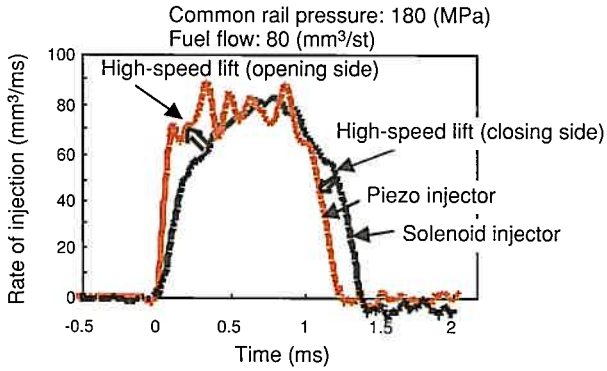

Fig. 6 Rates of Injection

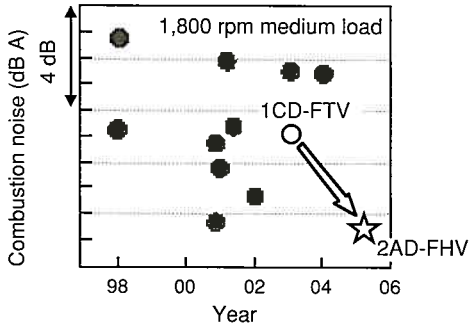

Fig. 7 Combustion Noise

4.3 Cylinder heads

The water flow in the cylinder heads has been optimized to reduce the temperature between the valve seats. Since the output of these engines is high, cylinder head reliability has been ensured by using a vertical-flow water jacket structure designed independently for the intake and exhaust sides (**Fig. 8**).

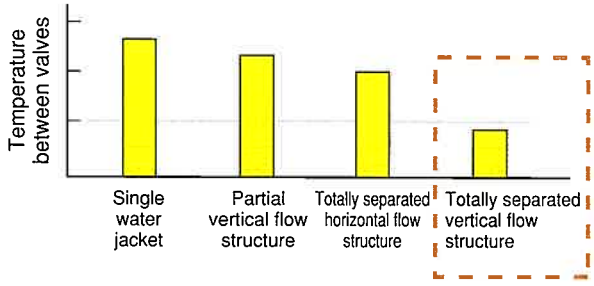

Fig. 8 Temperature Between Valves

4.4 Cylinder block

These new engines use an aluminum die-cast open deck structure that is commonly adopted for gasoline engines. High rigidity, low weight, and good casting performance were enabled by optimizing the structure using Finite Element Method (FEM) analysis and by evaluating various individual parts. Bore movements in the vertical and radial directions tend to be larger in an open deck structure than a closed deck structure. This movement has been suppressed and head gasket surface pressure losses reduced by tuning the head bolt tension and head gasket shape. In addition, the head bolt tightening structure has been optimized to reduce cylinder bore distortion (**Fig. 9**).

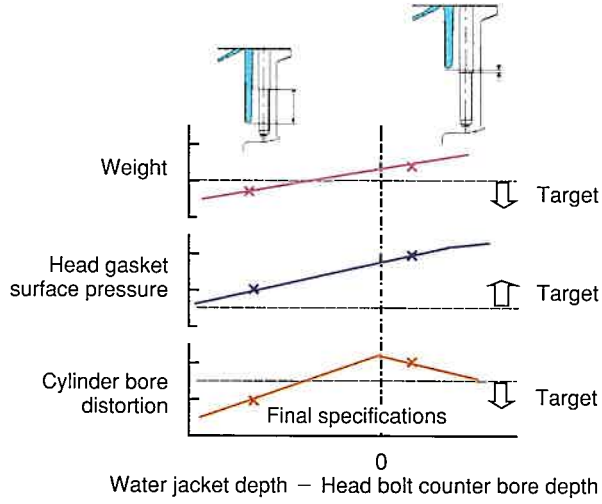

Fig. 9 Head Bolt Bore Shape

4.5 Turbocharger

A cassette type nozzle structure has been adopted for the variable nozzle turbocharger to reduce nozzle-side clearance, and improve low-speed torque and exhaust performance. In addition, the acceleration performance of the 2AD-FHV has been improved substantially by reducing the inertia moment of the turbine wheel by 30% over a conventional model (**Fig. 10**).

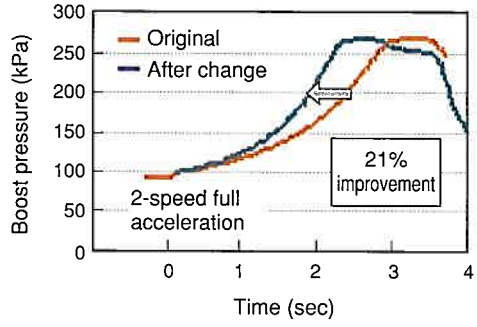

Fig. 10 Effect of Reducing Turbine Wheel Inertia

4.6 EGR system

Use of a high-response linear solenoid in the EGR valve drive has reduced transient smoke and combustion noise, and achieved stable combustion during switching of DPNR control. The 2AD-FHV also contains an additional bypass circuit in the EGR cooler to attain high output and low emissions in all operational conditions (**Fig. 11**).

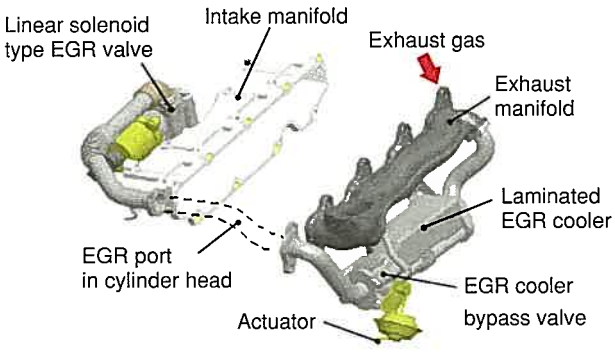

Fig. 11 EGR System

4.7 Balance shaft

A cassette type balance shaft has been used to reduce 2nd order vibration caused by engine rotation (**Fig. 12**). In addition, a scissors gear has been adopted in the drive system between the crank and the balance shaft to reduce noise caused by backlash (**Fig. 13**).

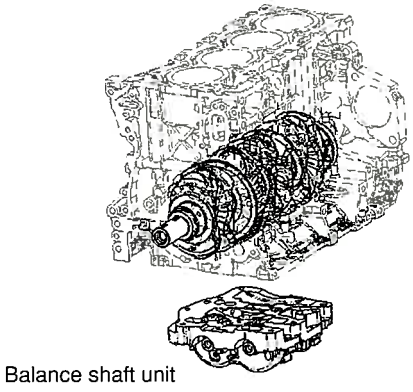

Fig. 12 Cassette Type Balancer Unit

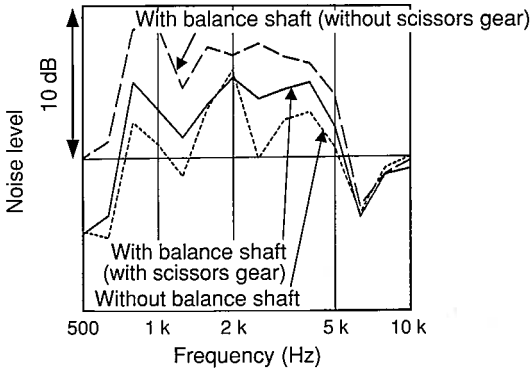

Fig. 13 Idling Engine Noise

5. Low Weight

The weight of the 2AD-FHV engine is extremely low. Aside from the adoption of the open-deck aluminum cylinder block, this has been accomplished by measures such as optimizing the shapes of the crankshaft and connecting rod, and adopting a plastic oil strainer (**Fig. 14**).

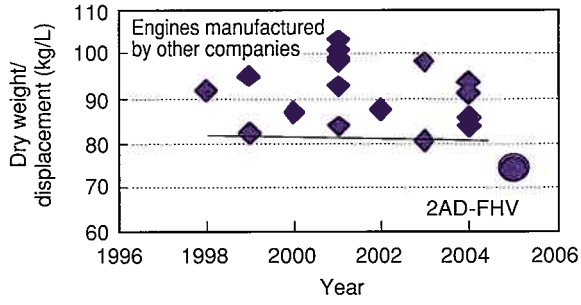

Fig. 14 Dry Weight

6. Low Friction

Technologies such as the roller rocker valve train system, and a 2 mm-wide oil ring have been adopted. CAE was also utilized to optimize the delivery capacity of the oil pump. As a result, an extremely good level of friction loss has been achieved, especially during low-speed operation. This level is clearly superior to models without a balance shaft (**Fig. 15**).

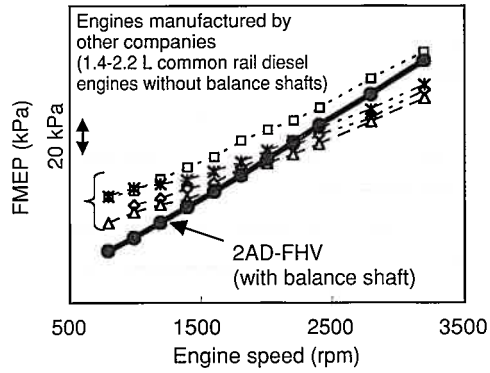

Fig. 15 Engine Friction

7. Conclusions

These new engines have extremely good output performance and NV levels that are comparable to gasoline engines, both of which are requirements for leading the ever-expanding European diesel passenger vehicle market. In addition, the 2AD-FHV has achieved an exhaust emissions performance that is far better than

the level specified in the Euro4 emissions standard. In the future, efforts will be made to further develop technology in order to improve the output performance and fuel economy, and to reduce exhaust emissions.

Finally, we would like to express our sincere appreciation to Toyota Industries Corporation and all relevant companies for their valuable contributions to the development of these new engines.

Authors


M. SUZUKI


N. TSUZUKI


Y. TERAMACHI

Investigation of Perovskite Type NOx Storage Materials at High Temperature

Yuichi Sobue*
Masahiko Takeuchi**
Masaru Ishii***
Mamoru Ishikiriyama*

Abstract

Fuel efficiency can be effectively improved using a lean burn engine, and to achieve further improvement it is necessary to widen the lean burn region as far as high speeds. However, in the high speed region, the exhaust gas temperature increases, and purification of NOx at high temperature becomes essential. However, purification of NOx in the lean burn region is problematic since there is normally a decrease in the NOx storage capability of the NOx storage and reduction catalyst. To address this, attention was focused on Perovskite type complex oxides that are supposed to have outstanding high temperature characteristics, and an investigation concerning oxidation activity, crystal structure and basicity was carried out. A NOx storage material that excels in terms of high temperature NOx storage capability was discovered. The reason for this remarkable high temperature characteristic is thought to be that the developed NOx storage material has storage sites that retain NOx up to high temperatures, unlike the conventional NOx storage materials.

Keywords: *lean burn engine, NOx storage and reduction catalyst, NOx storage material, high temperature, Perovskite type oxides*

1. Introduction

In recent years, simultaneous improvements have been sought in the fuel efficiency and emissions of automobiles. Lean burn systems used in direct injection gasoline or diesel engines are an effective means of improving fuel efficiency. However, there is an excess amount of oxygen to fuel in the exhaust gas of these engines. If a conventional three-way catalyst is used in the lean burn (hereinafter referred to as "lean") range, it is difficult to remove NOx, one of the harmful substances that are present in exhaust gas. For this reason, NOx storage and reduction catalysts (hereinafter referred to as "NSR catalysts") have been in practical use on lean burn engines since the 1990s. [1] As **Fig. 1** shows, an NSR catalyst uses storage materials consisting of alkaline earth metals or alkaline metals such as barium (Ba) or potassium (K) to store and retain NOx in a lean atmosphere. Then, in an excess fuel atmosphere (hereinafter referred to as "rich") in the vicinity of stoichiometry, the stored NOx is reduced into N_2.

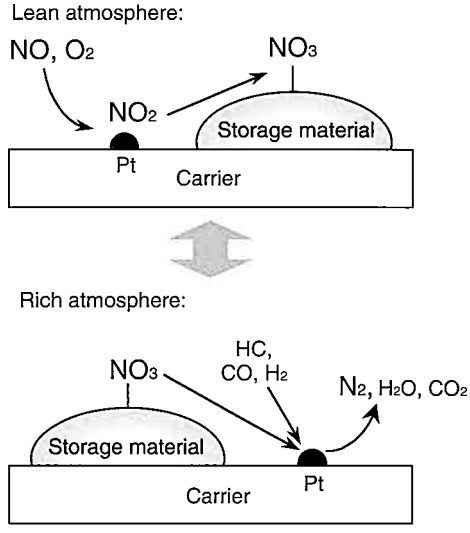

Fig. 1 Removal Mechanism of NOx Storage and Reduction (NSR) Catalyst

* Material Engineering Div. 3
** Material Engineering Div. 1
*** Material Engineering Div. 2

Fig. 2 shows the NOx storage characteristics of Ba and K, the NOx storage materials currently used in NSR catalysts. The NOx storage amount of Ba decreases suddenly at temperatures above 350°C, and that of K at above 500°C. At temperatures above 600°C, the NOx storage amount of both Ba and K is virtually zero. It has therefore not been possible to operate engines under lean conditions in the high temperature range, that is to say, under high-speed driving conditions in which the exhaust gas temperature rises, because of the inability to remove NOx.

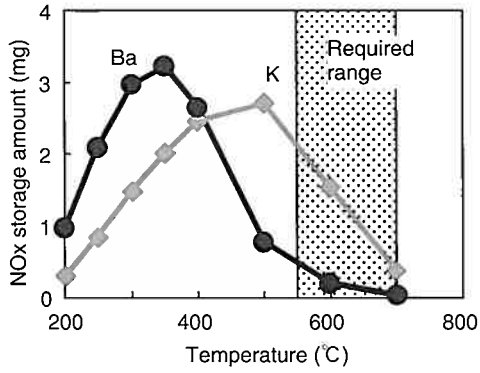

Fig. 2 NOx Storage Amount of NSR Catalysts with K and Ba as Storage Materials

The purpose of this study was to find and develop storage materials able to store NOx in this high temperature range.

2. Experiments

2.1 Experimental method

The NOx storage amounts were measured in a conventional fixed bed reactor as shown in **Fig. 3**. The gas flow rate was 5 L/min, and the sample was 1 g of a pellet catalyst loaded with a given amount of platinum (Pt). The composition of the model gas, as shown in **Table 1**, simulated the composition of exhaust gas obtained on a gasoline engine bench.

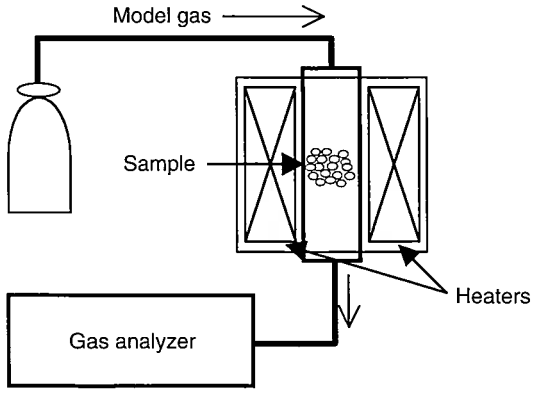

Fig. 3 Outline of Model Gas Catalyst Evaluation Equipment

Table 1 Model Gas Composition

	NO (ppm)	HC (ppmC)	CO (%)	CO_2 (%)	O_2 (%)	H_2O (%)	N_2
Rich	500	667	0.6	10	0.4	5	Residual
Lean	500	667	0.1	10	6.5	9	Residual

2.2 Experiment indices

As **Fig. 4** shows, the NOx storage amount is obtained from the NOx storage time t, NOx_{IN}, and NOx_{OUT}, which are the concentrations of NOx contained in the inlet and outlet gas of the catalyst, respectively. The NOx storage amount was calculated from the amount of NOx stored over 2 minutes. In this study, all the NOx storage amounts were measured at 600°C, in order to examine the suitability of storage materials for high temperature applications.

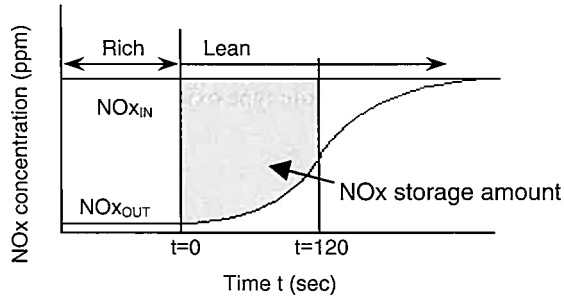

Fig. 4 Measurement of NOx Storage Amount

The oxidation activity of the catalyst was evaluated by measuring the H_2 oxidation temperature. The same equipment as for measuring the NOx storage amount was used to measure the temperature at which the amount of H_2 reduction reaches the maximum level when a gas mixture containing H_2 (1%) and N_2 is introduced into the catalyst, as shown in **Fig. 5**.

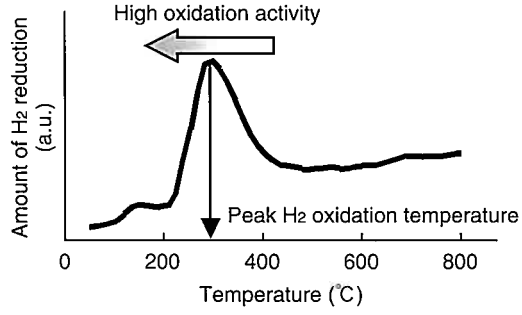

Fig. 5 Measurement of Oxidation Activity

3. Approaches to NOx Storage Materials for High Temperature Applications

Among the conventional storage materials, potassium compounds have favorable high temperature characteristics. NOx storage performance was therefore measured on 12 types of

materials containing potassium oxide. The measured NOx storage amounts are shown in **Fig. 6**.

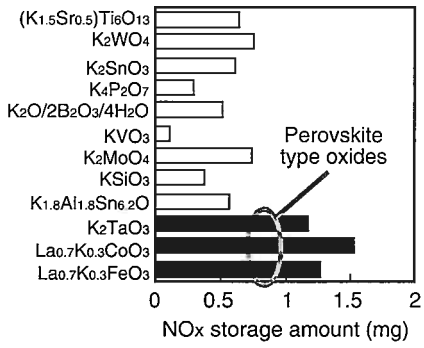

Fig. 6 NOx Storage Amount of NSR Catalysts Including Various Types of Storage Materials

NSR catalysts containing Perovskite type oxides (typical example: $La_{0.7}K_{0.3}CoO_3$) as the storage material exhibited a superior NOx storage performance to other materials. Therefore, the study focused on Perovskite type oxides.

4. Results and Discussion

4.1 Improvements in oxidation activity

The crystal structure of Perovskite type oxides is shown in **Fig. 7**.

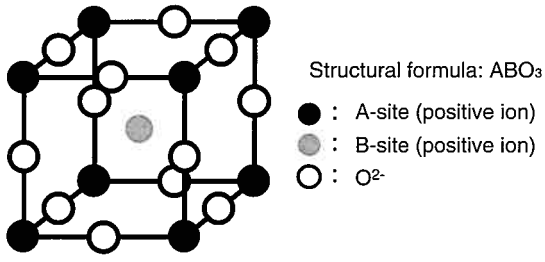

Fig. 7 Schematic Diagram of Structure of Perovskite Type Oxides

There are two types of actions in the crystal structure of Perovskite type oxides. One takes place in the A-site, i.e., the body center of the cubic lattice that is coordinated by 12 oxygen atoms. The other takes place in the B-site, i.e., the face center of the cubic lattice that is coordinated by 6 oxygen atoms. The average valence of the A-site and the B-site is 3+.

With respect to the ABO_3 Perovskite type oxides that include rare earth elements in the A-site and the first transition metal series (such as Co and Fe) in the B-site respectively, it is already known that the properties of the B-site ions are reflected strongly in the oxidation activity. [2]

This study examined the first transition series, which has a fairly high level of oxidation activity. The relationship between oxidation activity and NOx storage amount is shown in **Fig. 8**.

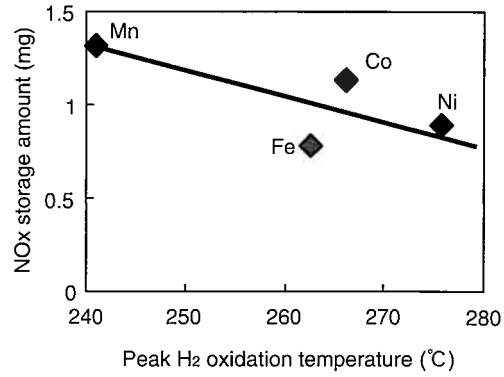

Fig. 8 Relationship Between Oxidation Activity and NOx Storage Amount

Catalysts using Mn in the B-site exhibited the highest oxidation activity and the largest NOx storage amount. As equations 1 and 2 indicate, this is believed to be because the valence of the B-site ions is susceptible to change, which facilitates the entry and exit of lattice oxygen, thereby promoting the oxidation of NO. In equations 1 and 2, A^{3+} indicates the A-site ions. A comparison of the ionization energy of the 3+ ions indicates that Mn becomes 4+ at a lower energy than the other three elements, [3] thus indicating the effectiveness of Mn.

$$A^{3+}Mn^{3+}O^{2-}_3 \rightleftarrows A^{3+}Mn^{3+}_{1-2x}Mn^{2+}_{2x}O^{2-}_{3-x} + \frac{x}{2}O_2 \quad (1)$$

$$A^{3+}Mn^{3+}O^{2-}_3 + \frac{x}{2}O_2 \rightleftarrows A^{3+}Mn^{3+}_{1-2x}Mn^{4+}_{2x}O^{2-}_{3+x} \quad (2)$$

The Mn in Perovskite type oxides normally stabilizes at Mn^{3+}. Substituting a portion of the Mn with 4+ ions results in 2+ Mn ions but, because these ions revert easily to the 3+ state, they are thought to facilitate the entry and exit of the oxygen atoms, as indicated in equation 3. [4][5] **Fig. 9** shows the results of NOx storage amount measurement after partially substituting the B-site with 4+ ions. Here, Ti^{4+}, whose ion radius is relatively close to Mn^{3+}, is used as the substitution element because the crystal structure could break if the size of the ions is too different from Mn^{3+}.

$$A^{3+}Mn^{3+}_{1-2x}Mn^{2+}_{x}Ti^{4+}_{x}O^{2-}_3 \rightleftarrows A^{3+}Mn^{3+}_{1-x}Ti^{4+}_{x}O^{2-}_{3-x} + \frac{x}{2}O_2 \quad (3)$$

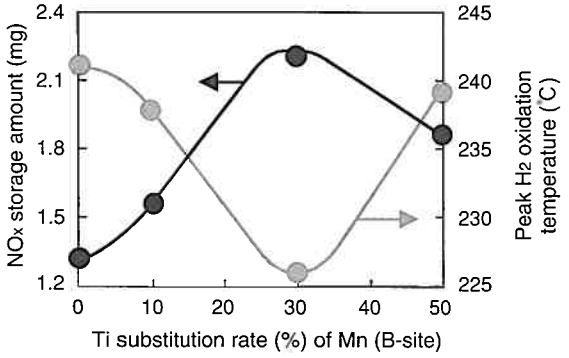

Fig. 9 Relationship Between Ti Substitution Rate and NOx Storage Amount

When the Ti substitution rate of the B-site is 30%, the oxidation activity is the highest and the NOx storage amount is also large. Although Ti promotes valence change in Mn, the optimal value for the substitution rate is believed to be 30% because the amount of Mn becomes insufficient if the rate is excessive.

4.2 Stabilizing the Perovskite crystal structure

The Tolerance Factor (hereinafter referred to as "T") was used as an index for finding a suitable structure for NOx storage. The T shown in equation 4 indicates the structural stability of Perovskite type compounds. An ideal cubic Perovskite structure is attained when T=1. Here, r_A indicates the average ion radius in the A-site, r_B indicates the average ion radius in the B-site, and r_O indicates the negative ion radius, which in this case is the ion radius of O^{2-} (0.14 nm).

$$T=\frac{R_A+R_O}{\sqrt{2}\,(R_B+R_O)} \qquad (4)$$

The rare earth elements that enter the A-site have different ion radii, but similar chemical properties. The rare earth elements in the A-site were examined to find a suitable structure for NOx storage. The results are shown in **Fig. 10**.

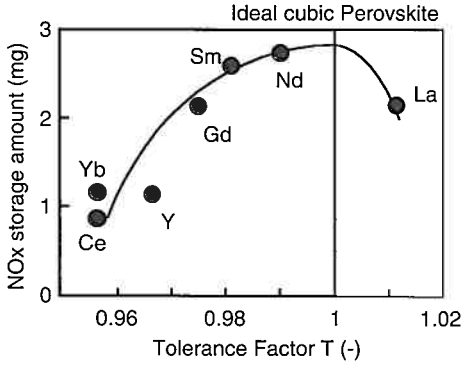

Fig. 10 Relationship Between Crystal Structure Stability and NOx Storage Amount

The study suggests that the closer the Tolerance Factor is to T=1, the greater the NOx storage amount becomes. Thus, the closer the structure is to the ideal cube, the better suited it is for NOx storage. Among those examined, the use of neodymium (Nd) exhibited the largest NOx storage amount.

4.3 Strengthening basicity

It is known that the NOx storage amount of conventional storage materials increases as basicity increases. Basicity was also expected to be an important factor when Perovskite type oxides are used as a storage material. It was therefore considered that strengthening basicity would increase the NOx storage amount. The effects of basicity were verified by replacing the alkaline elements that enter the A-site. The results are shown in **Fig. 11**.

As is the case with the conventional storage materials, the NOx storage amount trend increased in accordance with the basicity. However, when cesium (Cs) was used, the NOx storage amount decreased in spite of the strong basicity. As shown in **Fig. 12**,

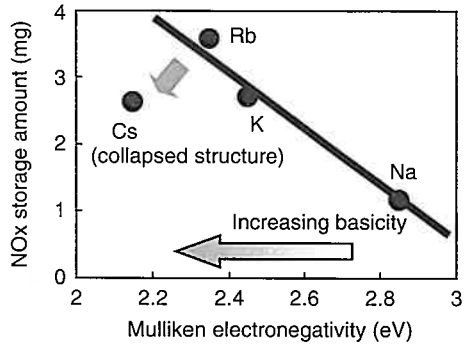

Fig. 11 Relationship Between Basicity and NOx Storage Amount in Perovskite Type NOx Storage Material

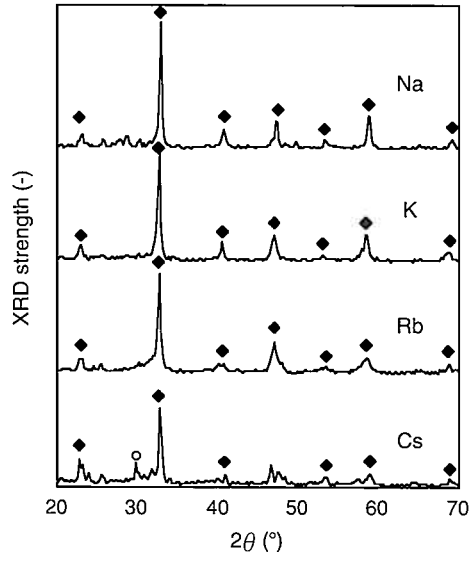

Fig. 12 Added Alkalis and Crystal Structure

○: Cs_2CO_3 ◆: Perovskite type structure

the crystal structure of the samples was verified through X-ray diffraction (XRD) analysis. The results revealed that using Cs caused the Perovskite structure to collapse.

Based on these results, it was determined that the optimal alkaline metal for the A-site in Perovskite type NOx storage materials is rubidium (Rb).

As evident from the results shown in **Figs. 11** and **12**, high basicity alone is not the only factor related to storing NOx at high temperatures, and it is extremely important for the NOx storage material to have a Perovskite structure. While the NOx storage amount increases in accordance with the addition amount of Rb, an excessive amount of Rb is thought to cause the structure to become unstable and to decrease the NOx storage amount. For this reason, the Rb addition amount was examined in order to determine the optimal value. The results are shown in **Fig. 13**.

It was confirmed that the NOx storage amount increased in accordance with the amount of Rb, and that the largest amount of NOx was stored when the addition amount of Rb was 30%. Calculation showed that the Tolerance Factor T was closest to 1 when the addition amount of Rb was 30%. At 50%, T was 1.02, indicating that the Perovskite structure had collapsed.

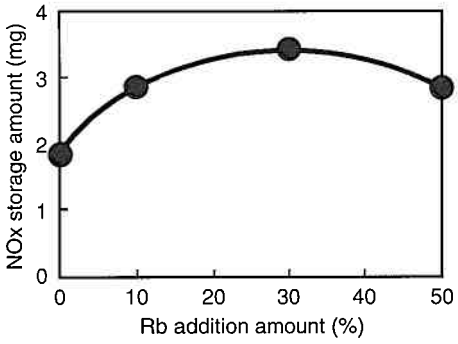

Fig. 13 Relationship Between Rb Addition Amount and NOx Storage Amount

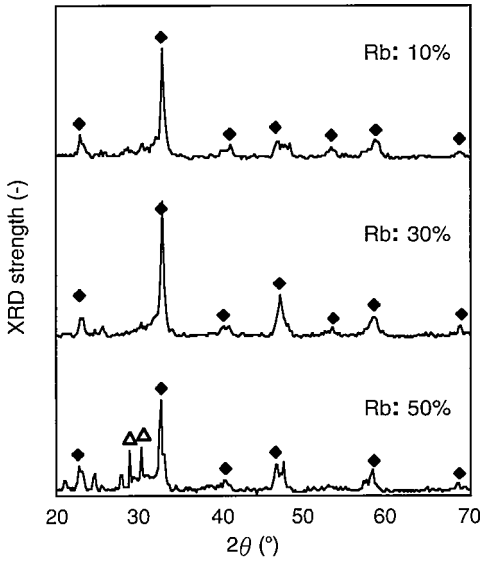

Fig. 14 Rb Addition Amount and Crystal Structure
△: Rb_2CO_3 ◆: Perovskite type structure

As the XRD analysis of the crystal structure in **Fig. 14** shows, the material with an addition amount of 50% had a collapsed Perovskite structure. This confirmed that a portion of Rb had precipitated to form a carbonate.

5. Verifying the Effectiveness of Catalyst with Optimized Composition

It was determined from the results of the studies described above that the composition of a storage material suitable for NOx storage at high temperatures is $Nd_{0.7}Rb_{0.3}Mn_{0.7}Ti_{0.3}O_3$ (hereinafter referred to as "NRMT"). The effectiveness of NRMT as a NOx storage material was then verified.

5.1 Retention of stored NOx

A temperature programmed desorption test was conducted for stored NOx to verify the difference in stored NOx retention capability between Ba and K (the conventional NOx storage materials) and NRMT. The test enabled the thermal stability of stored NOx to be observed by causing NOx to be stored at 300°C, then applying heat under a flow of He and measuring the desorbed NOx.

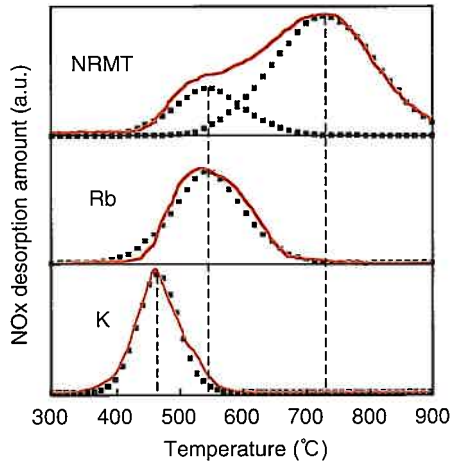

Fig. 15 Comparison of NOx Retention of Storage Materials
—: Measured value
··· : Value calculated by waveform separation

Fig. 15 shows that an NSR catalyst that uses K or Rb as the NOx storage material has only one NOx desorption peak, located at 463°C and 545°C, respectively. Because the conventional storage materials are known to store NOx as nitrates, the desorption peak for these materials is dependent upon nitrate stability. However, the tests have revealed that an NSR catalyst that uses NRMT as the NOx storage material has two NOx desorption peaks. The temperatures of the two NOx desorption peaks obtained through a waveform separation analysis were 545°C and 740°C, respectively. The lower NOx desorption peak

temperature is the same as with a catalyst using only Rb as the storage material. Therefore, it is assumed that a portion of the Rb that precipitated on the surface stored NOx in the form of a nitrate. However, the tests revealed that NRMT has a site that retains NOx up to an extremely high temperature of 740°C, something that has not been observed previously. This is assumed to be because NRMT stores NOx in a crystal lattice, instead of storing it in the form of a simple nitrate as with conventional catalysts.

5.2 NOx storage performance

Fig. 16 shows the results of the findings of the temperature characteristics of NRMT, as compared to the conventional NOx storage materials Ba and K.

The results show that the newly developed NSR catalyst that uses NRMT as the storage material provides a better NOx storage performance than one that uses Ba and K, particularly in the high temperature range between 500°C and 600°C.

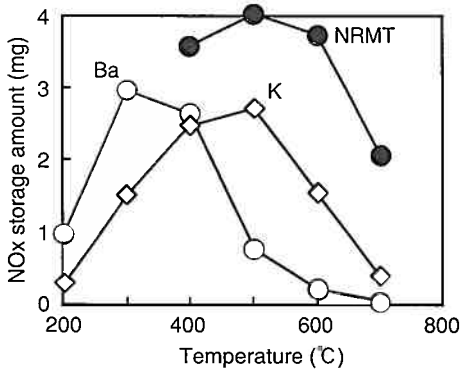

Fig. 16 Comparison of NOx Storage Amount Between NRMT and Conventional Storage Materials

6. Conclusions

This article has described research pertaining to a NOx storage material with an excellent high temperature NOx storage performance, which is necessary for further improving fuel economy and achieving cleaner emissions, as well as the effectiveness of this material. The results of the research can be summarized as follows.

(1) NRMT, which has a Perovskite structure, is effective for high temperature NOx storage.
(2) Unlike conventional materials, NRMT has a site that can retain NOx up to a high temperature range.
(3) When a Perovskite type NOx storage material is used for storing NOx at high temperatures, the NOx storage amount shows an increasing trend the closer the structure is to an ideal cube (T=1).

References

(1) N. Miyoshi et al. "Development of New Concept Three-Way Catalyst for Automotive Lean-Burn Engines." *SAE Paper* 950809 (1995).
(2) The Chemical Society of Japan. "Shokubaisekkei Kagakusousetsu No. 32" (in Japanese). *Center for Academic Publications Japan* (1997) p. 149.
(3) The Chemical Society of Japan. "Kagakubinran Kisohen II Revision 4" (in Japanese). *Maruzen* (1993) p. 618.
(4) T. Nakamura, Misono, Yoneda. "Reduction-oxidation and catalytic properties of La_1-xSrxCoO$_3$." *Journal of Catalysis* Vol. 83 (1983) p. 151.
(5) N. Yamazoe, Teraoka, Seiyama. "TPD and XPS study on thermal behavior of stored oxygen in La_1-xSrxCoO$_3$." *Chemistry Letters* Vol. 12 (1981) pp. 1767-1770.

Authors


Y. SOBUE


M. TAKEUCHI


M. ISHII


M. ISHIKIRIYAMA

Microbiological Treatment System for Volatile Organic Compound (VOC) Contaminated Soil

Toshiaki Kimura*
Yasushi Oda*
Shusei Obata*

Abstract

A quick, low-cost, safe microbiological treatment system has been developed for trichloroethylene contaminated soil. Naturally occurring microorganisms with a high degradation capacity were evaluated, and the best microorganisms from the standpoint of safety to humans and the ecosystem were selected. Conventionally, it has been difficult to apply biological treatment systems to silty soil, but this was enabled by mixing in soil amendments to create environmental conditions where the microorganisms can operate easily. Large-scale validation tests were performed to achieve the first introduction of this kind of system in the world. It has been confirmed by the Ministry of Economy, Trade and Industry in Japan that this technology conforms to bioremediation guidelines for open systems.

Keywords: *volatile organic compound (VOC), contaminated soil, microbiological treatment, trichloroethylene, soil amendments, bioremediation*

1. Introduction

In recent years, soil contamination has become more noticeable and is now regarded as a major problem for society. According to a 2002 survey by the Japanese Ministry of the Environment, 43% of the reported cases of contamination involved volatile organic compounds (VOCs). (1)

The conventional technologies to treat VOC-contaminated soil include mixing and aeration treatment, heat treatment, and chemical degradation treatment. However, each of these presents problems, such as the length of time required for treatment, the relatively high cost, or the safety of the chemicals employed. A technology is therefore needed that can treat contaminated soil safely, in a short time, and at low cost. (2)

To address these problems, Toyota focused on the ability of microorganisms to degrade VOCs, identified safe microorganisms in the natural environment that have that ability, created the conditions that maximize that ability, and developed a practical process for treating contaminated soil.

2. Overview of Microbiological Treatment System

Fig. 1 shows a schematic view of the microbiological treatment system that was developed. The system consists of a process that mixes VOC-degrading microorganisms into contaminated soil that has been excavated and a process by which the microorganisms degrade and remediate VOCs. The degradation and remediation process is an extremely simple one that requires no special processing line and completes remediation just by piling the soil and letting it sit.

* Future Project Div.

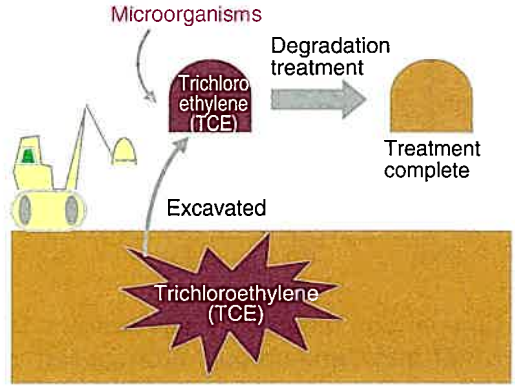

Fig. 1 Schematic Diagram of Treatment System

3. Development of A Trichloroethylene-Degrading Bacterium

3.1 Isolation of a trichloroethylene-degrading bacterium

Bacteria were isolated that degrade the most commonly reported VOC contaminant, trichloroethylene (TCE), in contaminated soil. The microbiological degradation of TCE can be accomplished by either aerobic bacteria, which require oxygen, or anaerobic bacteria, which do not need oxygen, but fast-growing aerobic bacteria were chosen in order to achieve quick remediation. **Fig. 2** illustrates the mechanism by which aerobic bacteria degrade TCE. An inducer is introduced into the bacterial cells to cause them to produce the enzyme that degrades TCE. The TCE-degrading enzyme adds oxygen to TCE to form TCE oxide. In the end, the TCE is broken down into water, carbon dioxide, and chloride ion.

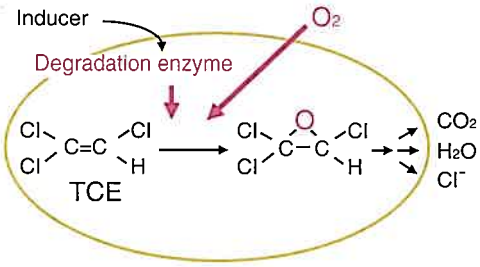

Fig. 2 How Aerobic Bacteria Degrade TCE

Fig. 3 illustrates the method by which the bacteria were isolated. Samples were collected from natural sources such as soil, sludge, and river water, then incubated in mixtures of TCE with different inducers. The growing cells were separated out, and the ability of the resting cells to degrade TCE was evaluated.

Resting cells are cells that have been separated by centrifuge from the culture medium in which the TCE-degrading bacteria are incubated with nutrients and inducer, such as phenol, and washed to remove the nutrients and phenol.

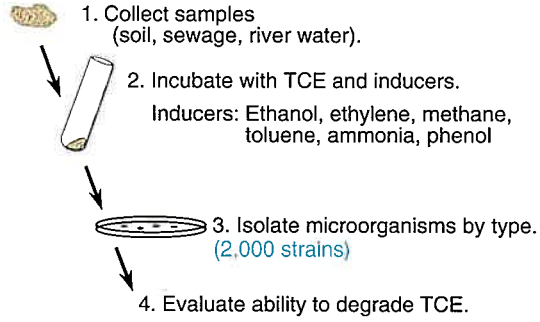

Fig. 3 Isolation of TCE-Degrading Microorganisms

The advantages of using resting cells are (1) they have been fully induced to produce TCE-degrading enzyme, so they have the capacity for quick remediation; and (2) they have been washed, so that when they are added to the soil, they do not carry harmful substances like phenol and nutrients with them.

Approximately 2,000 bacterial strains that were isolated from the natural environment were evaluated by resting-cells reactions. From these, a phenol-using TCE degrader called strain MO7 was selected. **Fig. 4** is an electron microscope photograph of strain MO7. Strain MO7 grows best in a neutral-pH environment at temperatures of 20°C to 30°C.

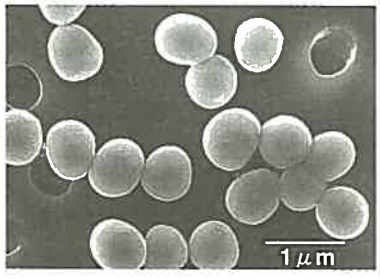

Fig. 4 Electron Microscopic Photograph of Strain MO7

3.2 Degradation performance of strain MO7

The ability of strain MO7 resting cells to degrade TCE in water was evaluated. When added at a concentration of 10^9 colony forming unit (cfu)/ml, strain MO7 completely degraded 50 mg/l of TCE in one day. The bacterium even completely degraded a high concentration of 100 mg/l of TCE without any effect on its performance, as shown in **Fig. 5**.

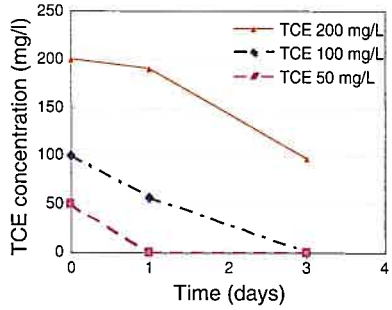

Fig. 5 Degradation of TCE in Water by Strain MO7

Strain MO7 is capable of degrading a broad range of compounds in addition to TCE, including *cis*-1,2-dichloroethylene, 1,1-dichloroethylene, *trans*-1,2-dichloroethylene, 1,3-dichloropropene, benzene, toluene, xylene, phenol, and cresol.

These results indicate that strain MO7 is a high-performance VOC degrader.

3.3 Safety of strain MO7

3.3.1 Taxonomic identification of strain MO7

Strain MO7 is gram positive, with a high G+C content (73%), *meso*-diaminopimelic acid as the main constituent of its cell walls, and menaquinone-8 (H4) as the respiratory chain quinone. **Fig. 6**

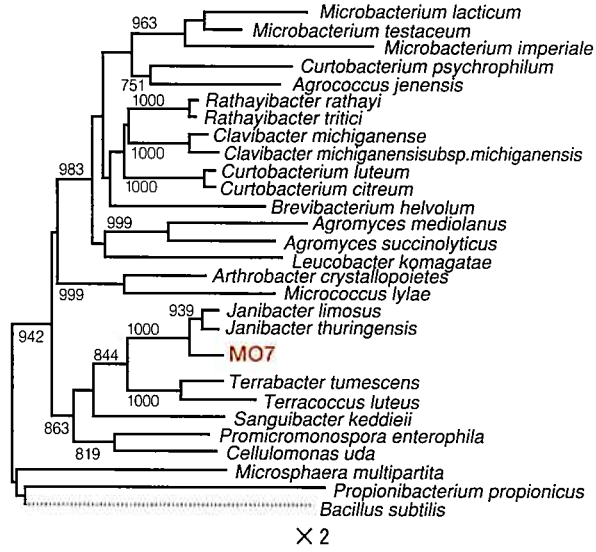

Fig. 6 Phylogenetic Tree Showing the Relative Position of Strain MO7 Based on 16S rRNA Gene Sequences

shows the results of a phylogenetic analysis of the 16S rRNA gene sequence. Based on these results, strain MO7 was identified as *Janibacter* sp. No pathogenic *Janibacter* sp. bacteria have ever been reported, so strain MO7 can be regarded as a non-pathogenic organism.

3.3.2 Safety testing of strain MO7

Strain MO7 was tested for toxicity and environmental impact. At the time the system was developed, no guidelines had been established for the remediation of VOCs by mixing microorganisms into soil, so testing was conducted according to the items used by the Japanese Ministry of Agriculture, Forestry and Fisheries in its safety testing for microbiological agricultural chemicals.

A third-party organization carried out toxicity and skin irritation tests on rabbits and rats, as well as environmental impact tests on quails, a type of fish (killifish), daphnia, and algae. The tests showed that there is no toxicity or environmental impact. These test results have been reviewed and confirmed by the safety committee of the Japanese Ministry of Economy, Trade and Industry. (4)

3.3.3 Detection of strain MO7 in soil

It was extremely important to develop a full understanding of the behavior of strain MO7 when it is added to soil and to check whether or not it grows abnormally. To do so required the development of a method to detect only strain MO7 amid the multitude of other microorganisms that are present in soil.

An MO7-specific selective culture plate was developed by incorporating four antibiotics into an inorganic salt medium that uses phenol as its sole carbon and energy source. Counts of the colonies that grew on the plate indicated that strain MO7 could be detected at levels of 10^5 cfu/g of dry soil or higher.

To provide the sensitivity to detect MO7 at 10^4 cfu/g of dry soil or lower required the capacity to distinguish it from the background of other microorganisms in the soil. A method of detecting MO7 was developed that uses the colony PCR method to select, from among the MO7 gene sequences for TCE-degrading enzymes, a particular gene sequence that is unique to MO7. Of the 50 soil samples studied to date, none has shown any amplification of DNA from colonies of soil bacteria growing on the selective culture plates, indicating that strain MO7 can be distinguished from soil bacteria.

Next, these technologies were used to study changes in the numbers of strain MO7 cells. As **Fig. 7** shows, the MO7 count declined from 10^9 cfu/g of dry soil to 10^5 cfu/g.

These results mean that when MO7 is dispersed in soil, its levels decline naturally after the TCE in the soil is degraded, indicating that it has no effect on the natural environment.

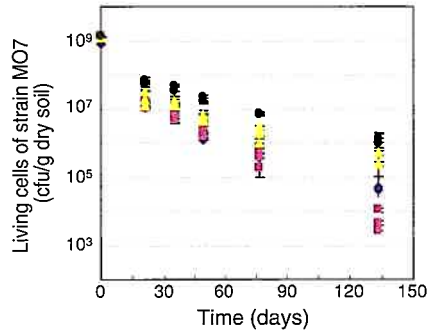

Fig. 7 Changes in Numbers of Strain MO7 in Soil

4. Development of Treatment System

4.1 TCE degradation in soil by strain MO7

The level of TCE in sandy soil decreases rapidly when strain MO7 is added, as shown in **Fig. 8**. By contrast, when MO7 is added to silty soil, almost no TCE degradation occurs.

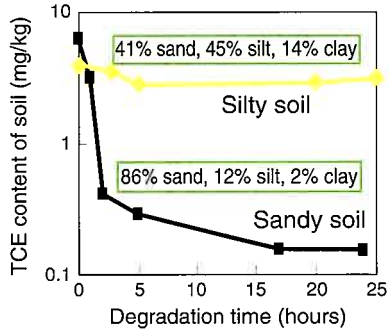

Fig. 8 Degradation of TCE in Soil by Strain MO7

Silty soil has smaller particles than sandy soil and tends to retain water. It is therefore conjectured that the degradation does not occur in silty soil because the air pockets within the soil fill with water, creating an oxygen deficiency.

Soil amendments that absorb water were therefore added to the silty soil. **Fig. 9** is a photograph from a cryo-scanning electron microscope showing soil into which soil amendments have been mixed. Air pockets were observed to form as the soil amendments absorbed the water. Strain MO7 utilizes the oxygen in these air pockets efficiently to degrade TCE.

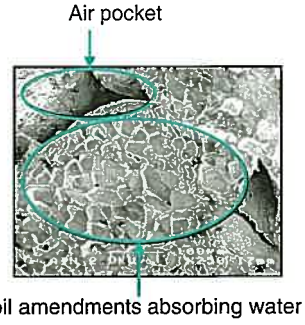

Fig. 9 Electron Microscopic Photograph of Soil with Added Soil Amendments

The results of TCE degradation in silty soil are shown in **Fig. 10**. When nothing was added or only strain MO7 was added, almost no TCE degradation occurred, but when strain MO7 was added together with soil amendments, TCE in the soil was reduced to below the Japanese environmental standard value of 0.03 mg/l within 24 hours.

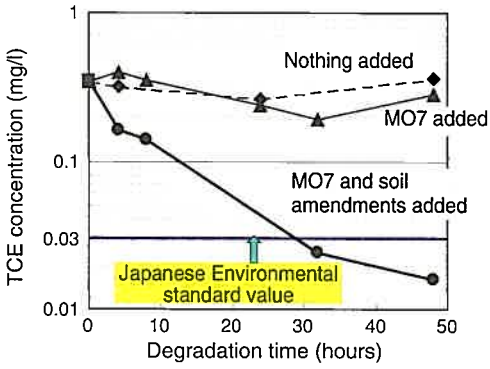

Fig. 10 Degradation of TCE in Silty Soil

4.2 Pilot-scale testing

Fig. 11 shows the pile stock bioremediation system that was developed to degrade TCE in soil.

In this extremely simple process, TCE-contaminated soil is excavated, and then mixed with strain MO7 and soil amendments by a machine like that shown in **Fig. 12**. The mixture is piled up and left for 24 hours, after which time the TCE is fully degraded and remediated.

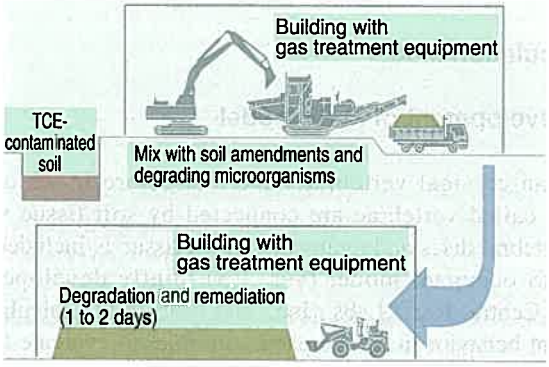

Fig. 11 Developed Treatment System - Pile Stock Bioremediation System -

Fig. 12 Mixer Used in Pilot-Scale Testing

Pilot-scale testing also demonstrated the effectiveness of the system by reducing TCE in soil to below the Japanese environmental standard value. [5][6]

5. Conclusion

Even though microorganisms are small, they possess a range of abilities, and they are useful to humans not only in the brewing industry, for example, but in cleaning the environment as well. However, a range of problems have kept methods of treating soil with specific bacteria (bioremediation) from reaching the commercial level. This article has described a system that was developed to address these issues, and economic issues as well, and that has proven to be commercially feasible. It is expected that new uses will continue to be found for these microorganisms that embody the wisdom of nature and that they will play an active role in reducing the burdens on the environment.

The treatment system described here was developed jointly with Obayashi Corporation. The authors wish to thank all those involved in the project.

References

(1) Ministry of the Environment, Environmental Management Bureau, Water Environment Department: http://www.env.go.jp/water/report/h16 - 05/full.pdf (2005).
(2) K. Fujii, Ide, Ishikawa, Toge. *Obayashi Corporation Research Paper* No. 67 (2003) pp. 1-6.
(3) Y. Oda, Kimura, Okamura, Tokuhiro, Nakayama, Numata. *Shuki no Kenkyu* Vol. 30 No. 3 (1999) pp. 22-32.
(4) Ministry of Economy, Trade and Industry, Manufacturing Industries Bureau, Biochemical Industry Section: http://www.meti.go.jp/feedback/data/i40305cj.html (2004).
(5) T. Kimura, Oda, Higuchi, Toge, Ishikawa, Fujii. *Proceedings of the 7th International Symposium of Environmental Biotechnology* (2004) p. 56.
(6) K. Fujii, Ishikawa, Toge, Oda, Yoneda, Kimura. *Abstracts of 10th Research Symposium on the Contamination of Ground Water and Soil and Measures to Prevent It* (2004) pp. 52-55.

Authors


T. KIMURA


Y. ODA


S. OBATA

Simulation of Occupant Motion in Rear Impacts using Human FE Model THUMS

Yuichi Kitagawa*
Junji Hasegawa*

Abstract

In this study, occupant motion in rear impacts was simulated with a human body model named Total Human Model for Safety (THUMS). First, the human neck structure was modeled including soft tissues such as ligaments and nerves. The model was validated against Post Mortem Human Subject (PMHS) tests that have been reported in related publications. Next, kinematics of the head and neck were analyzed using the THUMS with the detailed neck model, and the load applied to the soft tissues was investigated with the impact speed increased. Then, the model was used to evaluate the performance of a new seat system, the New Whiplash Injury Lessening (WIL) Concept Seat, which has been developed to reduce relative motion between the head and torso. Despite increasing the impact speed up to 50 kph (which is faster than that conventionally used), the load applied to the neck soft tissues was mitigated with the New WIL Concept Seat as compared to the conventional seat.

Keywords: *THUMS, human model, rear impact, whiplash injury, seat*

1. Introduction

Although the number of fatalities in automotive traffic accidents has been falling in recent years, the total number of accidents and casualties is still on the rise, and rear impacts account for a large proportion. (1) Rear impacts occurring at low speeds only result in a small amount of damage to the vehicle, however vehicle occupants involved in rear impacts often complain of a dull pain in the neck (hereinafter called cervical vertebra). This dull pain is a so-called "whiplash injury." Unlike bone fractures, a whiplash injury cannot be visually confirmed, thus making it difficult to pinpoint the cause of pain. Researchers are also still only at the stage of proposing various theories regarding how much of a load on the cervical vertebra leads to a whiplash injury. It is widely known that relative motion between the head and torso is the key to understanding whiplash injuries, and some research institutions have proposed evaluation methods using crash test dummies. Recently, there has been a spate of research (2)-(4) focusing on joint behavior in cervical vertebrae (neck bones) and the loads on soft tissues (such as ligaments and nerves). However, measuring the behavior of individual cervical vertebrae from among the overall body movement of the occupant is not an easy task.

The Total Human Model for Safety (THUMS) jointly developed by Toyota Motor Corporation and Toyota Central R&D Labs., Inc. includes most bone and joint structures of the human body. For this reason, THUMS enables a detailed analysis of behavior from the level of the overall occupant body down to behavior in units of cervical vertebrae. By adding soft tissues included in the neck to THUMS, this research was able to evaluate the load applied to the occupant's neck in a rear impact. The validity of the model was confirmed by comparison with the cervical vertebrae behavior described in the literature. Use of this model makes it possible to study variations in neck loads resulting from different rear impact speeds or seat structures. Therefore, THUMS was used to verify the impact mitigating effect of the New WIL Concept Seat developed by Toyota.

* Advanced CAE Div.

2. Calculation Model

2.1 Development of neck model

Human cervical vertebrae have a structure in which bone masses called vertebrae are connected by soft tissue such as intervertebral discs and ligaments. Such tissue is included in the THUMS occupant model (ver. 1.5) jointly developed with Toyota Central R&D Labs., Inc., and enables the calculation of occupant behavior in rear impacts. In order to evaluate the load level on soft tissue, this research newly added soft tissue such as the spinal cord, spinal fluid, dura mater, pia mater, nerve roots, vertebral arteries, and joint capsules. **Fig. 1** shows general views of the model. The soft tissue forms were created referring to anatomy literature and the like, and the material properties were input referring to values given in biomaterial literature. (5)(6) Also modeled in THUMS were the main muscles associated with movement of the head and neck. The positions where muscles are attached to bones were determined with reference to biomaterial literature; however, the muscles themselves were modeled using linear spring elements. No consideration was given to muscular contractions resulting from reflexive reactions.

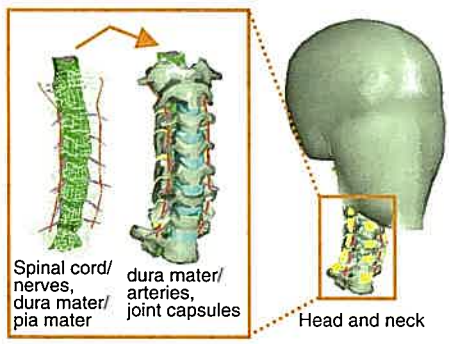

Fig. 1 Modeling of Soft Tissues in Neck

2.2 Verification in units of cervical vertebrae

Much of the data given in the literature on the material properties of human tissue were obtained by extracting the subject tissue and then setting it on a tester to measure. Simply inputting the obtained physical values into the model should enable the simulation of dynamic characteristics. However, forces acting within the actual human body are not necessarily the same as those in tests at the tissue level, so the behavior and response are not guaranteed accurate for the human body. In other words, the assembled model needed to be verified anew. Hence, this research first identified the material properties for the model in units of cervical vertebrae, using the literature data input for each tissue as initial values. Test data [7] was cited as target cervical vertebrae characteristics, which applied impact loads to extracted human (PMHS) cervical vertebrae and measured the rotational angle and moment. **Fig. 2** shows line diagrams of the rotational angle and moment when cervical vertebrae are twisted in the longitudinal direction, and compares test data given in the literature with the calculation result obtained using THUMS. The two diagrams are both in almost complete correspondence, and it is clear that the identified cervical vertebrae model simulates the test results well.

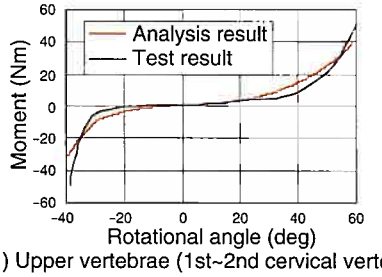

(1) Upper vertebrae (1st~2nd cervical vertebrae)

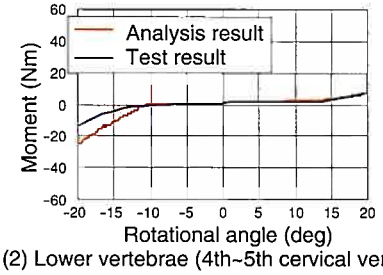

(2) Lower vertebrae (4th~5th cervical vertebrae)

Fig. 2 Verification Results in Units of Cervical Vertebrae

2.3 Verification of model including head

Next, verification of the overall behavior of the neck as well as the head was performed on the model identified in units of cervical vertebrae. With regard to the area from the head to the 1st thoracic vertebra (T1) of the PMHS in the referenced test, forward acceleration at a maximum of 10.5 G with T1 fixed to the sled resulted in a swinging movement of the head in the longitudinal direction. [8] The rotational angle and translational displacement of the head center of gravity were measured based on the output of an accelerometer set in the head. For THUMS as well, the area from the head to T1 was extracted and a calculation was performed using the same inputs as the test. Nodal displacement corresponding to the head center of gravity of THUMS was output for comparison with the time history data given in the literature. **Fig. 3** shows the comparison results. For both the rotational angle and the translational displacement of the head center of gravity, it was confirmed that the behavior of the THUMS head and neck corresponded well with the behavior of the PMHS head and neck.

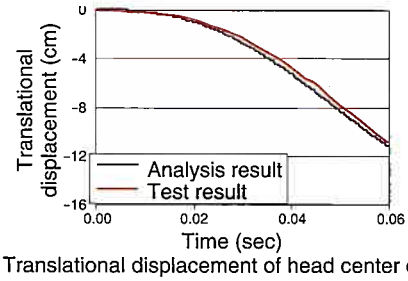

(1) Translational displacement of head center of gravity

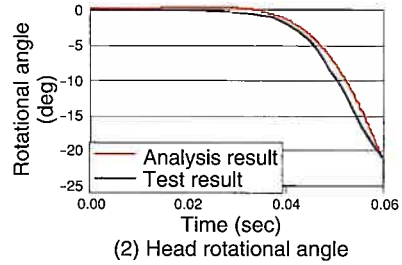

(2) Head rotational angle

Fig. 3 Verification Results of Model Including Head

2.4 Verification of full-body model

Last of all, the behavior at the level of the overall body was compared to test results [9] using human subjects (volunteers). In the test, the volunteers were seated in a rigid seat that was then tilted and slid down rails. Once the acceleration reached approximately 8 km/h, the seat was stopped by a shock absorber. According to this method, the torso decelerates first at the time of stopping, while the head tends to remain in motion due to inertia. It is therefore possible to simulate cervical vertebrae behavior resembling that of vehicle occupants in rear impacts. Note that whiplash injuries were reported not to occur in healthy test subjects at a delta-V of approximately 8 km/h, and that the research in the literature focuses on the measurement of cervical vertebrae behavior. In addition to setting an accelerometer on

the bodies of the volunteers to understand the behavior of the overall body, profiles of the volunteers' heads were recorded using a high-speed X-ray camera for image analysis. Based on the above, the movement of the cervical vertebrae was measured in units of vertebrae.

For the calculation using THUMS, a full-body model was seated in a rigid seat and the test was simulated by inputting the acceleration pulse measured in the actual test. It was possible to compare the cervical vertebrae behavior (rotation in particular) with the test data by outputting the nodal displacement of the cervical and thoracic vertebrae as time history data. **Fig. 4** shows the comparison results of the rotational angles of the cervical and thoracic vertebrae. Both the rotational angle of the head center of gravity and the rotational angles of each vertebra calculated in THUMS were confirmed to have excellent correspondence with the test results up until approximately 100 ms after the start of deceleration. After 100 ms, the rotational angles of the cervical vertebrae in THUMS tended to increase. The reason for this may be due to the fact that although muscular contraction due to a spinal reflex starts after 100 ms in human subjects, which basically applies the brakes on head and neck behavior, the THUMS calculation does not take into account muscular activation and therefore the rotation continues to increase. Based on the above, the THUMS model used in this research can be considered capable of simulating the head and neck behavior of human subjects with high accuracy, provided that the simulation is limited to approximately 100 ms after the start of muscular response.

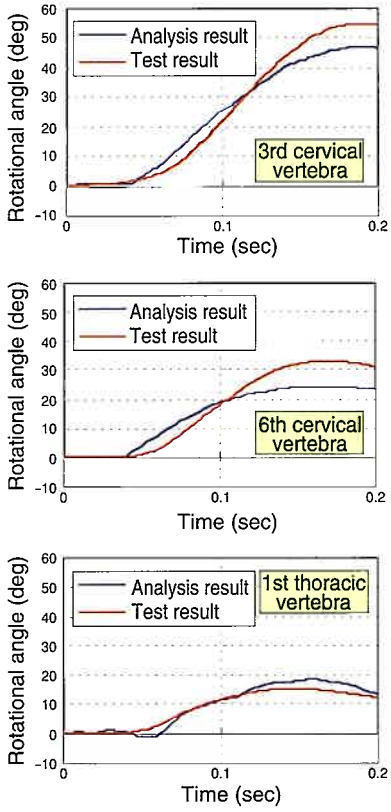

Fig. 4 Verification Results of Full-Body Model

3. Occupant Behavior in Rear Impacts

3.1 Occupant behavior characteristics

Occupant behavior was studied under conditions simulating a vehicle rear collision, using the THUMS model that was confirmed capable of simulating human head and neck behavior with high accuracy. A calculation model simulating the front seat of a passenger vehicle was created, onto which THUMS was seated in a standard position. For simplicity, the vehicle structure was omitted, and input from a rear impact was simulated by applying forward acceleration to the seat bottom. The condition for impact intensity was set as equivalent to that when a stopped vehicle is impacted from behind by another vehicle traveling approximately 30 km/h.

Fig. 5 shows the behavior of the THUMS head and neck when viewed using the seat as a reference. When observing the rear impact phenomenon using the road surface as a reference, the seat moves forward and pushes out the occupant's torso, while the head tends to stay in the same position due to inertia. As a result, a relative difference in displacement occurs between the head and torso. On the contrary, in the seat reference view of the figure the body is shown moving to sink into the seat due to the rear impact. The speed at which the torso sinks into the seat gradually decreases because of the reaction force from the seat back; however, the head still moves backward at the initial speed (because of inertia). Consequently, a relative difference in displacement occurs between the two. Furthermore, it was also confirmed that the spine ramps up once the torso receives the reaction force from the seat back, and that the seat back conversely deforms in a downward slanted direction due to pressure from the torso. At first, the head translates backward and the movement of the lower end of the cervical spine is restricted because of its connection with the torso. But as time passes, the head contacts the head restraint while rotating backward. Afterwards, the movement of the head finally decelerates as the rigidity of the stay and foam material start to support the head. Both the head and the torso ultimately return forward due to the reaction force of the seat.

3.2 Effect of rear impact speed

According to an analysis of traffic accident data conducted by the Ministry of Land, Infrastructure and Transport in Japan, approximately 60% of rear collisions occur at speeds of 30 km/h or less, and approximately 90% occur at speeds of 50 km/h or less (when a stopped vehicle is impacted from behind by another vehicle). [10] The conventional neck whiplash injury evaluation is performed under conditions mainly assuming an impact speed of 30 km/h. However, the evaluation speed was raised to 50 km/h in this research in order to further increase the technology level.

Using THUMS, the effect of an increased rear impact speed was studied. Rear impact conditions were simulated by applying a delta-V of approximately 16 km/h and 25 km/h to the bottom

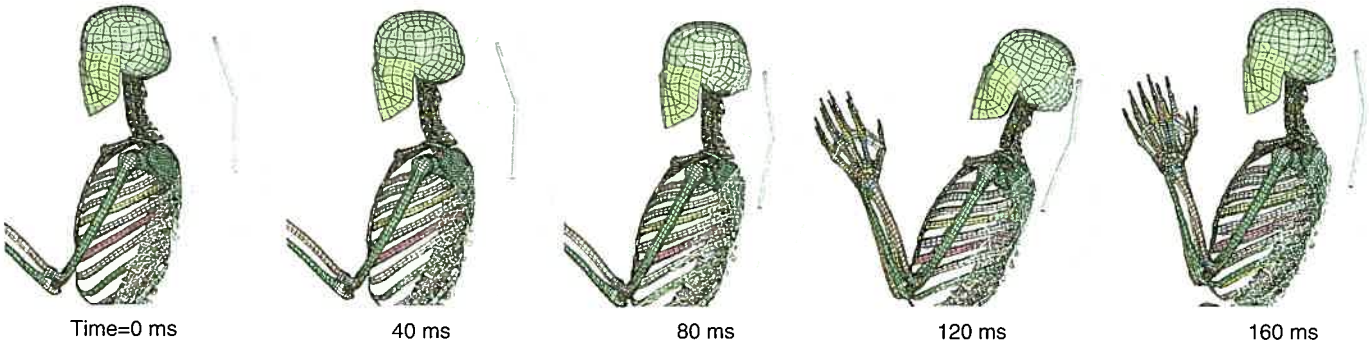

Fig. 5 Head and Neck Behavior in Rear Impact (Skin Not Shown in THUMS Calculation Result)

of the seat model in the actual calculation. This is based on the fact that if, for example, a stopped vehicle is impacted from behind by a vehicle of the same weight traveling 50 km/h, the final speed of both vehicles is 25 km/h. Therefore, the delta-V of the impacted vehicle is approximately half of the impact speed, or 25 km/h. **Fig. 6** is an enlarged view focusing on the behavior of the head and neck at rear impact speeds of 30 km/h and 50 km/h. Compared to 30 km/h, the backward tilt angle of the seat back at 50 km/h is much greater, and the rotational displacement of the head and neck is clearly increased. This indicates an increased amount of impact energy due to the rear impact, which in turn increases the kinetic energy of the body as well as seat deformation.

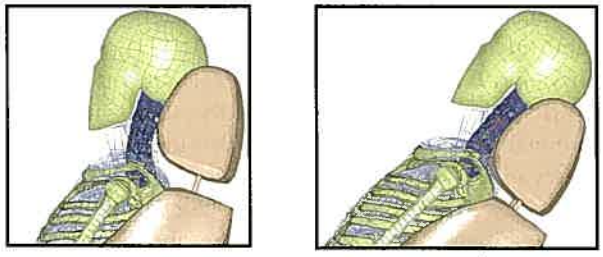

Fig. 6 Change in Head and Neck Behavior Due to Increased Rear Impact Speed

3.3 Evaluation of neck load

A comparison was made next of the loads acting on the neck at the rear impact speeds of 30 km/h and 50 km/h. An indicator called Neck Injury Criteria (NIC) was used, which is often used in evaluations with crash test dummies. The NIC are calculated from the differences in velocity and acceleration of the head and the lower end of the neck, and represents the relative differences in movement of the head and torso in numerical values. This research also evaluates the stress and strain generated in the neck soft tissues in addition to using the NIC. Soft tissue that researchers have focused on include the intervertebral disc, joint capsule, anterior longitudinal ligament, and dura mater. Load levels leading to injury have also been proposed for each tissue. [11] However, the load level values are still under debate.

Moreover, in consideration of the fact that the THUMS model used in this research does not include muscular activation, a comparative evaluation was conducted based on calculated values. **Fig. 7** shows the comparison results according to rear impact speed. Looking at the load levels of soft tissues, it is apparent that raising the rear impact speed from 30 km/h to 50 km/h also results in an all-around increase in the levels of loads acting on the neck soft tissues. Furthermore, the same trend as the soft tissues is also seen with the NIC, which rise along with the increase in rear impact speed.

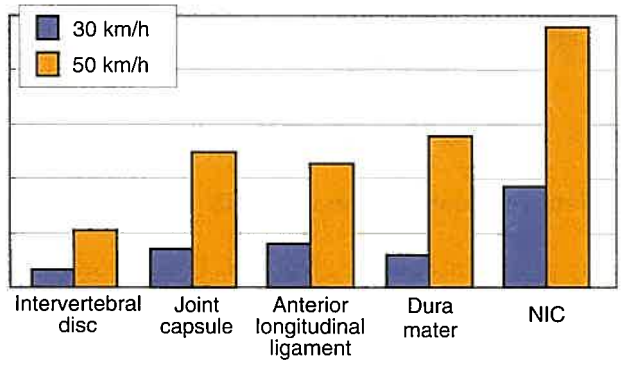

Fig. 7 Change in Neck Load Indicators Due to Increased Rear Impact Speed

4. Proposal for New Seat Structure

4.1 New WIL Concept Seat

Toyota Motor Corporation has employed the WIL Concept Seat to mitigate the loads on an occupant's neck in rear impacts. In light of raising the evaluation speed from 30 km/h to 50 km/h, this research developed a New WIL Concept Seat that builds on past technology.

Fig. 8 summarizes the technical aspects of the New WIL Concept Seat. The structure of the lower part of the seat back was reinforced to cope with the increased speed. Thus, the backward tilt angle of the seat back can be held in check and kept small, even at impact speeds equivalent to 50 km/h. On the

other hand, the part of the seat back supporting the occupant's torso was given more cushioning. Suppressing the reaction force of the seat back should have the effect of narrowing the relative difference in displacement of the head and torso. Moreover, restraining the spine from ramping up leads to better support of the head by the head restraint. The position of the head restraint was also moved closer to the head and modified for improved support. In addition, a two-layer structure was used for the foam material of the head restraint. A soft foam material was used for the outer layer to ensure that the head restraint remains comfortable during normal use, whereas the inner layer employs a harder material to securely support the head in rear impacts. The mounting stiffness of the head restraint stay was also reinforced to add further support.

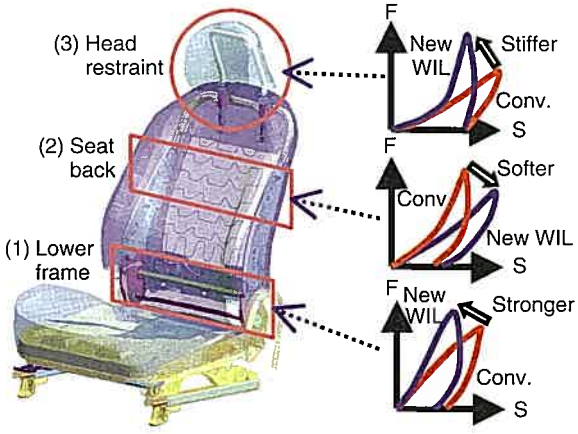

Fig. 8 Technical Aspects of New WIL Concept Seat

4.2 Effect verification using THUMS

During development of the New WIL Concept Seat, a crash test dummy called BioRID was used for effect verification in tests. Even under impact conditions equivalent to a rear impact speed of 50 km/h, it was confirmed that indicators such as NIC were held low compared to those for a conventional seat. In order to verify the mitigating effect of the New WIL Concept Seat on load levels applied to a human neck, a rear impact simulation was performed using THUMS. First, a model was created with a detailed rendering of the structural features of the New WIL Concept Seat, onto which THUMS was seated. For the seating position, the position of the lower back (hip point) of the seated dummy in actual tests and the clearance between the dummy's head and the head restraint were reproduced exactly. After inputting an acceleration pulse equivalent to a rear impact speed of 50 km/h to the seat bottom, the behavior of the seat and THUMS was calculated up to approximately 200 ms. Similar to the previous example, the NIC used in the dummy tests were also calculated in addition to the output of load levels for the soft tissues. A model of a conventional seat was also created for comparison with THUMS seated on it, and identical calculations were performed under the exact same conditions.

Fig. 9 shows a comparison of the behavior of the THUMS head and neck due to differences in seat structure. In the conventional seat, there is a relatively large backward tilt angle of the seat back, and the head contacts the head restraint in a somewhat ramped up position. On the contrary, in the New WIL Concept Seat there is a relatively small backward tilt angle of the seat back, and the head is well supported by the head restraint. The smaller backward tilt angle of the seat back in the New WIL Concept Seat is believed to be the result of reinforcing the bottom structure of the seat back, which had been modified to handle the higher evaluation speed.

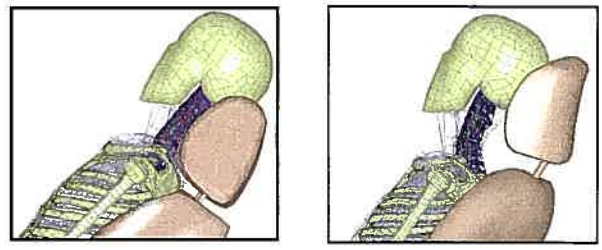

Fig. 9 Change in Head and Neck Behavior Due to Seat Structure Modifications

Furthermore, adding more cushion to part of the seat back allowed the torso to sink into the seat back, and made the head less likely to ramp up the head restraint. **Fig. 10** shows a comparison of the NIC and load levels of neck soft tissues for the conventional seat and the New WIL Concept Seat. Both are comparatively evaluated here similar to **Fig. 7**. It was confirmed that all values for the NIC and load levels on soft tissues in the New WIL Concept Seat were reduced to less than that for the conventional seat. Based on the fact that the various evaluation indicators proposed by researchers all confirm the reduction trend, the New WIL Concept Seat can be evaluated as having a large mitigating effect. In light of the above, the New WIL Concept Seat was confirmed capable of keeping load levels on soft tissue in the neck low, even under conditions equivalent to a rear impact speed of 50 km/h, by holding the occupant's torso and firmly supporting the head.

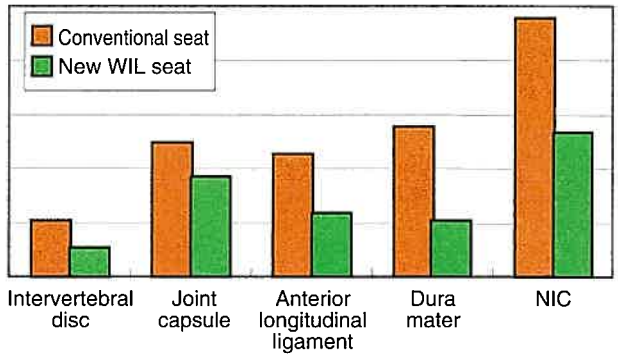

Fig. 10 Change in Neck Load Indicators Due to Seat Structure Modifications

5. Conclusions

This article described (1) the development of a neck model in THUMS including the soft tissue in a human neck, (2) a precise verification of the model by comparison with literature data, (3) an analysis using THUMS of occupant behavior in rear impacts, and (4) the mitigating effect of the New WIL Concept Seat on neck loads. The authors would also like to emphasize that the analysis using THUMS quantitatively illustrated for the first time such aspects as the rotational behavior of the occupant's head and the increased load levels on soft tissue resulting from a raised rear impact speed. The crash test dummy is a useful tool for evaluating actual seat parts, and the NIC are an effective means for examining the relative difference in displacement of the head and torso. Adding an evaluation analysis using THUMS as well thus achieved the development of safety technology that takes into account protecting human tissue, i.e., real-world safety. The effect verification of the New WIL Concept Seat has been positioned as a first case example. However, many issues still remain to be addressed in order to eliminate whiplash injuries from all traffic accidents. Future research will be planned for an analysis that considers actual conditions such as the influence of an occupant's build, age, and sex.

In closing, the authors would like to acknowledge and thank Mr. Hayato Masuki of Toyota Communication Systems Co., Ltd. who assisted in the effect verification of the New WIL Concept Seat and in the calculations of occupant behavior in rear impacts using THUMS, as well as the members of Toyota Central R&D Labs., Inc. who developed and provided the base THUMS occupant model.

References

(1) Japanese National Police Agency. Traffic Green Paper (1999) (in Japanese).
(2) K. Ono, Kaneoka. "Motion Analysis of Human Cervical Vertebrae During Low Speed Rear Impacts by the Simulated Sled." *Proc. IRCOBI Conference* (1997) pp. 223-237.
(3) B. Winkelstein et al. "Cervical Facet Joint Mechanics: Its Application to Whiplash Injury." *Proc. 43rd Stapp Car Crash Conference* 99SC15 (1999).
(4) J. Hasegawa et al. "A Study of Whiplash Injury Occurrency Mechanisms Using Human Finite Element Model." *Proc. 18th ESV Conference* 05-0288 (2003).
(5) M. deJager. "Mathematical Head-Neck Models for Acceleration Impacts." *Thesis Technishe Universiteit Eindhovenm* (1996) pp. 42-47.
(6) H. Yamada. "Strength of Biological Materials." *Williams & Wilkins Company,* Baltimore (1970).
(7) R. Nightingale et al. "Comparative Strength and Structural Properties of the Upper and Lower Cervical Spine in Flexion and Extension." *Journal of Biomechanics* Vol. 35 (2002) pp. 725-732.
(8) J. Cholewicki et al. "Head Kinematics During In Vitro Whiplash Simulation." *Accident Analysis and Prevention* Vol. 30 No. 4 (1998) pp. 469-479.
(9) K. Ono et al. "Relationship Between Localized Spine Deformation and Cervical Vertebral Motions for Low Speed Rear Impacts Using Human Volunteers." *Proc. IRCOBI Conference* (1999) pp. 149-164.
(10) Ministry of Land, Infrastructure and Transport. *The 3rd Car Safety Symposium* (2002).
(11) N. Yoganandan et al. "Biomechanical Evaluation of Human Cervical Spine Ligaments." *SAE Paper* No. 983159 (1998) pp. 223-236.

Authors

Y. KITAGAWA **J. HASEGAWA**

Development of New Whiplash Lessening Seat

Masahide Sawada*
Junji Hasegawa**
Masato Ohchi***

Abstract

Whiplash, or soft tissue cervical injury, is a common injury incurred by occupants of passenger cars in rear-end collisions. At Toyota Motor Corporation, a Whiplash Injury Lessening (WIL) Concept Seat designed to reduce the load on the neck has been developed, based on a unique concept for whiplash lessening that is achieved by simultaneously restraining the head and body of the occupant as much as possible, thereby controlling relative motions in a rear-end collision. The developed seat also reduces local strain of the neck by preventing rotation of the head, in addition to uniformly distributing loads on the cervical vertebrae (C1-C7), even in collisions that are more severe than those used in past tests. Having succeeded in reducing both the injury values to the BIO-RID II dummy and local strain of the neck of the FE model called Total Human Model for Safety (THUMS), this new seat design is expected to help reduce whiplash injury.

Keywords: *whiplash lessening, WIL Concept Seat, BIO-RID II dummy, NIC, extension moment, THUMS, strain on joint capsule*

1. Introduction

Cervical injury incurred during a rear-end collision is a typical injury inflicted on occupants of passenger cars involved in traffic accidents. Although only a small number of rear-end collisions in Japan result in fatal accidents, they make up about one-half of all accidents involving injury, as shown in **Fig. 1**. [1][2] Approximately 80% of these result in cervical injury, making the reduction of whiplash an important issue.

To date, the most commonly used whiplash test is the triangular pulse sled test performed at ΔV=16 km/h. This test is equivalent to a rear-end collision velocity of 32 km/h between two cars of the same weight, which represents only a 60th percentile collision in Japan, as shown in **Fig. 2**. [3] If collision velocities of up to 50 km/h are examined, as much as 90% of all such collisions can be represented. Converted into ΔV for a collision between cars of the same weight, ΔV=25 km/h.

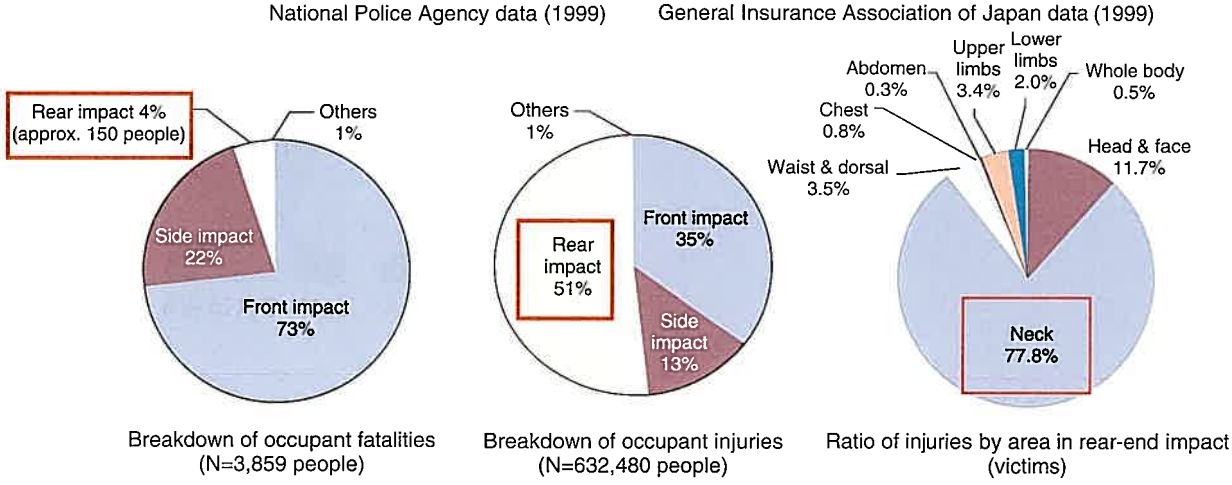

Fig. 1 Realities of Rear-End Collisions

* Vehicle Engineering Div.
** Advanced CAE Div.
*** Body Engineering Div. 1

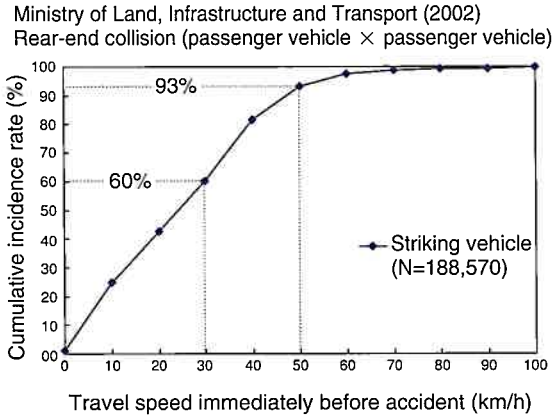

Fig. 2 Cumulative Incidence Rate of Travel Speed Immediately Before Accident

Meanwhile, vigorous studies have been undertaken to clarify the injury mechanism of whiplash. However, because whiplash injury cannot be described simply with a single mechanism, numerous criteria are currently being proposed. Typical studies conducted in the past dealt with the relative movement occurring between the head and the thorax, and the load that is acting on the neck. More recently, behavior analyses of cervical vertebrae (C1 to C7) are being conducted [4] through the use of X-ray cineradiography devices on cadavers and volunteers. Furthermore, human FEM models are being used to conduct detailed analyses [5] of the stress and strain that act on the cervical vertebrae and the soft tissue. Thus, the study of the mechanism of whiplash, which consisted of the relative movement between the head and the thorax and the load acting on the neck, has evolved into a study to clarify the relationship between the local behavior of the neck and whiplash.

Fig. 3 shows the Whiplash Injury Lessening (WIL) Concept Seat [4] developed by Toyota Motor Corporation. This seat is designed to reduce the load on the neck of the occupant by simultaneously restraining the head and body of the occupant, thus suppressing relative motions in a rear-end collision. In addition to achieving the foregoing objectives at higher levels, we have recently developed a seat that can also suppress local strain of the neck. This is accomplished by suppressing the rotation of the head and uniformly distributing the load on the cervical vertebrae. The effects of this seat have been verified through experiments using a BIO-RID II dummy and FEM analyses on the Total Human Model for Safety (THUMS).

2. Composition of New Whiplash Injury Lessening Seat

Fig. 4 shows a comparison between the newly developed seat (new type) and a conventional seat (conventional type). One of the features of the new design is a change made to the position (b) of the upper part of the frame and to the stiffness of the seat back cushion. These changes allow the thorax of the occupant to sink deeper into the seat during Phase 1 (until the head contacts the head restraint). This delays the onset of the thorax G (T1G) movement and reduces its velocity relative to the head, as shown in **Fig. 5** (a). This concept has the same objective as the active head restraint used by other companies, which aims at quickening the onset of the head G movement in order to reduce its velocity relative to the thorax G (T1G), except that the approaches are different.

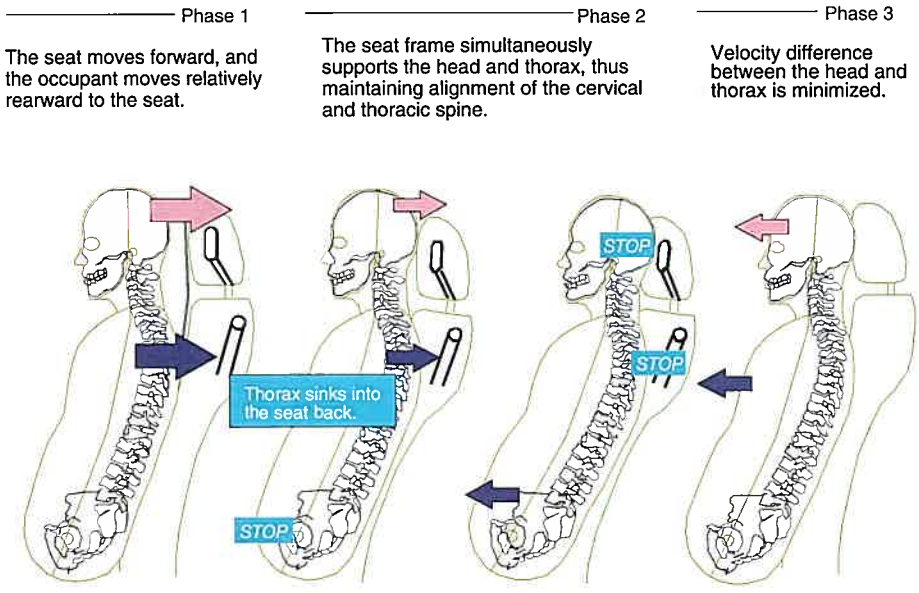

Fig. 3 Whiplash Injury Lessening (WIL) Concept

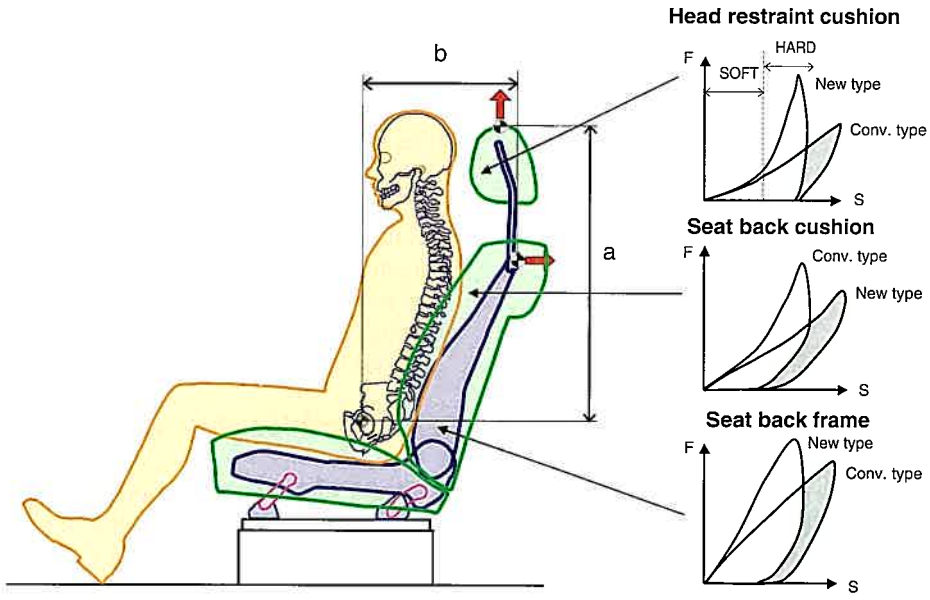

Fig. 4 Comparison Between New and Conventional Seats

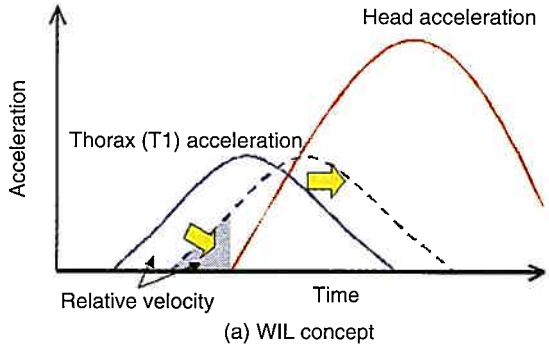

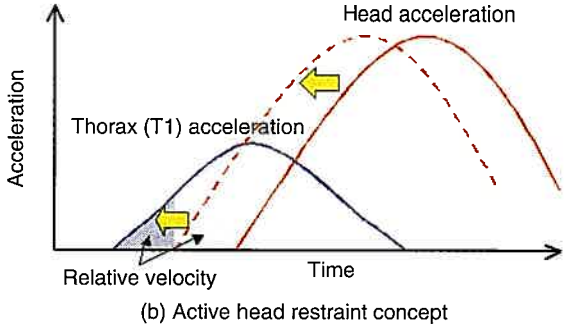

Fig. 5 Comparison of Seat Development Concepts

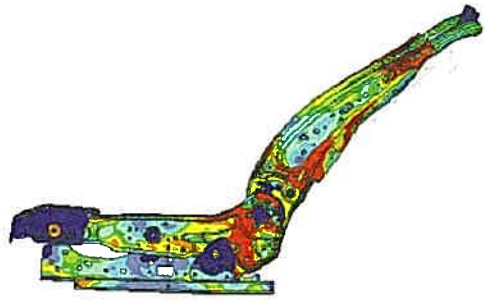

Fig. 6 Results of CAE Study on Seat Frame Strength

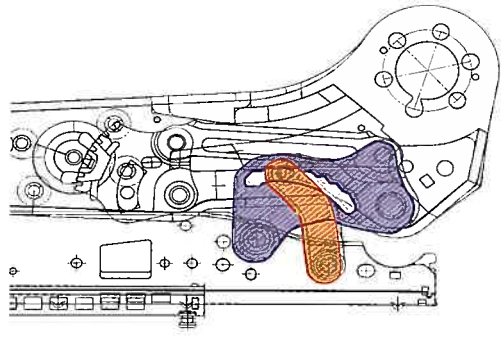

Fig. 7 Vertical Lifter Sinking Prevention Mechanism

Secondly, to ensure proper restraint in Phase 2 (after the head contacts the head restraint), the vertical position (a) of the head restraint and the load-displacement characteristic of the head restraint cushion have been revised. Also, through computer-aided engineering (CAE), the balance of the seat frame strength has been revised in order to ensure reliable restraint performance at higher velocities up to ΔV=25 km/h. This allows the energy to be absorbed by the entire seat (**Fig. 6**). The seat with a vertical lifter is provided with a stop shown in **Fig. 7**. These changes have been made to securely restrain the head of the occupant at a higher position, in order to prevent the head from extending backward over the head restraint even in a high-speed rear-end collision.

3. Test Equipment and Conditions

The seat was tested through experiments conducted at the Safety Laboratory of the Higashifuji Technical Center. An electronically controlled servo-hydraulic sled tester (**Fig. 8**) was used to reliably generate free collision acceleration pulses. A BIO-RID II dummy (**Fig. 9**), which is most widely used in whiplash evaluations, was used in the tests. The test method complies with the International Insurance Whiplash Prevention Group (IIWPG) test protocol. [6] **Fig. 10** shows the sled acceleration Pulses 1, 2, and 3 that were used in the tests. Pulse 1, which is the most widely adopted acceleration pulse, is a triangular pulse of ΔV=16 km/h, tested by ADAC, Folksam, and the respective organizations (IIHS and Thatcham) of IIWPG. Since there is no standardized sled acceleration pulse of ΔV=25 km/h, Pulse 2 is a triangular pulse of ΔV=25 km/h used by ADAC, and Pulse 3 is a trapezoidal pulse ΔV=24 km/h used by Folksam.

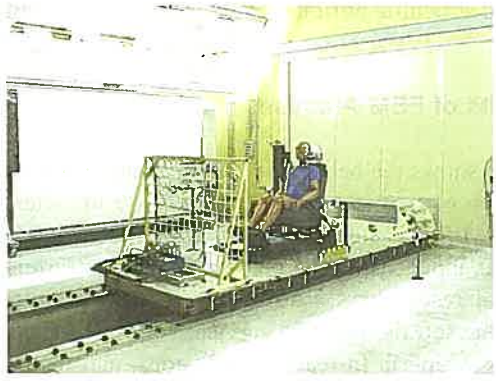

Fig. 8 Electronically Controlled Servo-Hydraulic Sled Tester

Fig. 9 BIO-RID II Dummy

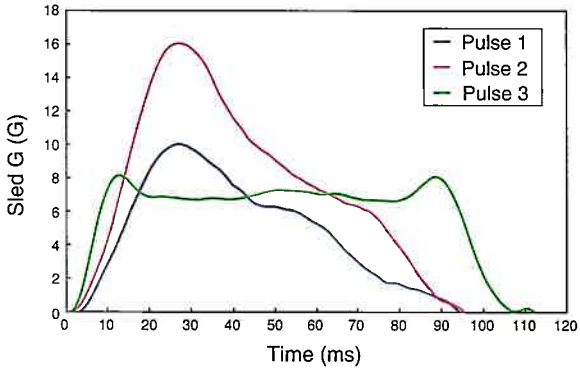

Fig. 10 Sled Pulses

4. Test Results

Fig. 11 shows test results compiled with the Neck Injury Criterion (NIC) proposed by Bostron et al [7] for evaluating whiplash through the changes in the pressure of the spinal fluid in the cervical spinal canal. The NIC is a criterion (equation 1) for evaluating Phase 1 by focusing on the relative motions of head G and thorax G (T1G) and is considered to be consistent with the WIL concept. At the three sled pulses, the NIC_{max} of the newly developed seat (new type) exhibited smaller values than the conventional seat (conventional type), indicating that the new type restrains the head and thorax more simultaneously.

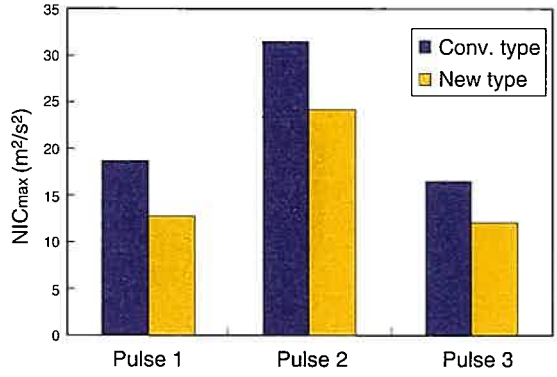

Fig. 11 Results of NIC Analyses

$$NIC(t) = 0.2 \cdot a_{rel}(t) + (V_{rel}(t))^2 \qquad (1)$$

where, $a_{rel} = a_x^{T1}(t) - a_x^{Head}(t)$

$$V_{rel} = \int a_{rel}(t)dt$$

Fig. 12 shows the maximum value of the lower neck extension moment My. Importance was attached to applying this criterion for evaluating Phase 2, as it relates to the large angular variation and strain of the lower cervical vertebrae, such as between C4-C5, C5-C6, and C6-C7, obtained from the results of the volunteer tests conducted by Sekizuka [4] and from the results of the human FEM analyses performed by Hasegawa [5] as well. At the three sled pulses, the My_{max} of the newly developed seat (new type) produced lower values than the conventional seat (conventional type), indicating a greater suppression of extension.

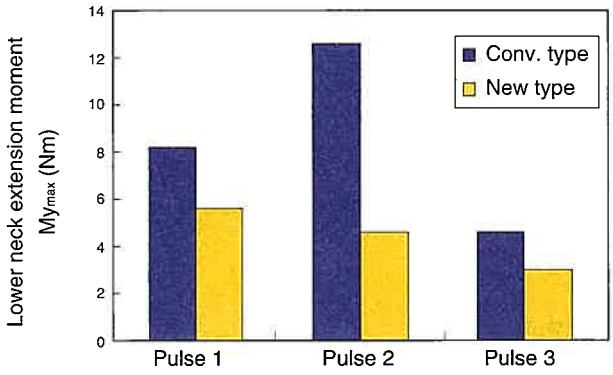

Fig. 12 Results of Analyses by Lower Neck Extension Moment My_{max}

5. FEM Analysis Method

To verify the effectiveness of the newly developed seat to reduce loads acting on the human neck and analyze the mechanism of the loads acting on the neck, rear-end collision simulations were performed using a human FEM model called a Total Human Model for Safety (THUMS). **Fig. 13** shows an enlargement of the entire body and neck of the THUMS model (ver. 1.63). This model is an upgraded version of the conventional THUMS passenger model (ver. 1.5). It has undergone significant improvements such as the added ability to represent the structure of the spinal cord and the cervical vertebrae joints in detail, in order to accurately reproduce the motions of the neck and to evaluate the strain of the various soft neck tissues in rear-end collisions. A seat model representing a conventional seat structure and one incorporating newly developed structural attributes were also prepared (**Fig. 14**).

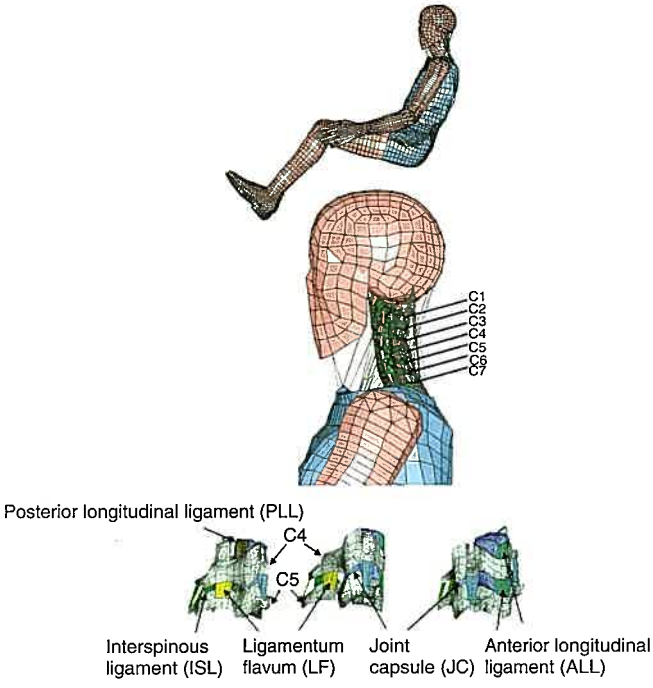

Fig. 13 THUMS (Ver. 1.63)

6. Results of FEM Analyses

Fig. 15 shows the behavior of the head and neck and the strain distribution of the neck soft tissues at 106 ms after a rear-end collision. In the calculation, Pulse 2 (ΔV=25 km/h triangular pulse) was input, using the new seat model. Currently, a large number of researchers are focusing on the strain of the joint capsule (the soft tissue of the cervical vertebral joints) associated with neck whiplash in rear-end collisions, and pinpointing their

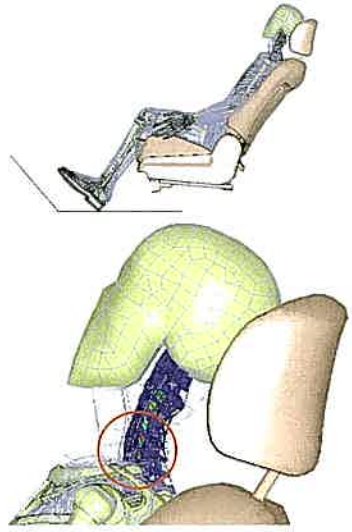

Fig. 15 Principal Strain Distribution using THUMS (New seat, Pulse 2, 106 ms)

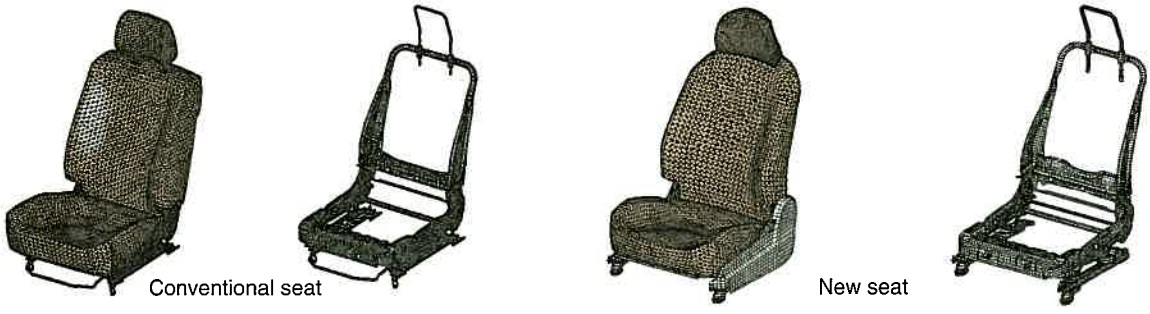

Fig. 14 Seat FE Model

cause-and-effect relationship. The analyses results indicated high values (red areas) of strain at the joint capsules of cervical vertebrae C5-C6 and C6-C7, showing a tendency similar to the results of the volunteer tests performed by Sekizuka [4] and the human FEM analyses conducted by Hasegawa [5] as well.

Fig. 16 shows the results of comparing neck soft tissue strain with the three input pulses shown in **Fig. 10**, between the new seat (new type) and the conventional seat (conventional type). The vertical axis in the figure represents the ratio between the maximum main strain that is output through a calculation and a generally proposed criterion value. The strain level of the newly developed seat was lower than the conventional seat for every input pulse.

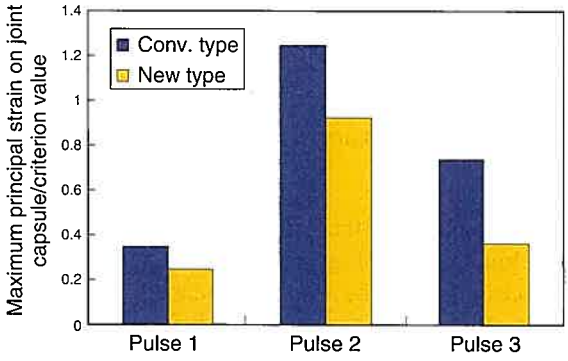

Fig. 16 Results of Analyses on THUMS (Maximum Principal Strain on Joint Capsule/Criterion Value)

7. Conclusions

(1) A seat using a design concept of simultaneously restraining the head and thorax while suppressing head rotation was developed. This seat, which uses higher strength components and a revised component layout, will be adopted on new models, starting with the new 2005 Yaris model.

(2) As intended, the newly developed seat is able to simultaneously restrain the head and thorax, while suppressing the rearward rotation of the head, for velocities up to ΔV=25 km/h (equivalent to a collision velocity of 50 km/h between two cars of the same weight). Thus, it was effective in reducing the injury value sustained by the dummy.

(3) In rear-end collision simulations using THUMS, the strain distribution of the neck soft tissues was larger in the lower neck, as observed in experiments. The strain of the neck joint capsule was also investigated, and it was confirmed that the strain level was lower for the newly developed seat than for the conventional seat. Based also on the biomechanics perspective, the newly developed seat is expected to be effective in reducing the load on the neck. The experiments and FEM analyses also proved the proposed seat development concept to be effective on humans as well.

References

(1) Japanese National Police Agency. *Traffic Green Paper* (Japanese) (1999).
(2) General Insurance Association of Japan data (1999).
(3) Ministry of Land, Infrastructure and Transport. *The 3rd Car Safety Symposium* (2002).
(4) M. Sekizuka. "Seat Designs for Whiplash Injury Lessening." *16th ESV Conference 1998* No. 98-S7-O-06 (1998).
(5) J. Hasegawa. "A Study of Neck Soft Tissue Injury Mechanisms During Whiplash Using Human FE Model." *Proc. IRCOBI Conf.* (2004) pp. 321-322.
(6) International Insurance Whiplash Prevention Group. *IIWPG Protocol for the Dynamic Testing of Motor Vehicle Seats for Neck Injury Prevention* (2004).
(7) O. Bostron, Svensson, Aldman, Hansson, Haland et al. "A New Neck Injury Criterion Candidate Based on Injury Findings in the Cervical Spinal Ganglia After Experimental Neck Extension Trauma." *Proc. IRCOBI Conf.* (1996) pp. 123-136.

Authors


M. SAWADA


J. HASEGAWA


M. OHCHI

A Silicon Micromachined Gyroscope and Accelerometer for Vehicle Control

Eiichi Nakatani*
Masaru Nagao*
Hikaru Watanabe*
Masato Hashimoto**
Kouji Shirai**
Kouji Aoyama***

Abstract

The number of traffic accidents and casualties is still on the rise, making widespread use of VSC more desirable for its anticipated effect on traffic accident reduction. Therefore, lowering the cost of gyroscopes for detecting vehicle behavior has become an urgent task. The researchers have developed a silicon gyroscope that was manufactured using silicon micromachining technology. This sensor detects acceleration in addition to an angular rate from a sensor element. A high-accuracy analog-to-digital converter has also been incorporated into the signal processing circuit for digital calibration of sensor properties using microcomputer calculations. The development of these novel technologies has succeeded in giving the sensor unit a simple structure while also reducing its cost and size.

Keywords: *vehicle control, semiconductor, gyroscope, accelerometer, signal processing IC*

1. Introduction

The automobile has become an indispensable mode of transportation in modern life. But with the number of injuries in traffic accidents continuing to rise, traffic safety has become a critical issue for society as a whole. As an automobile maker, Toyota is involved in the development of both active and passive safety technologies with the goal of reducing traffic accidents to zero. Vehicle Stability Control (VSC) is one active safety system. On slippery road surfaces like snowy roads, accidents sometimes occur when the driver turns the steering wheel too sharply on a curve, sending the vehicle into a sideways skid. VSC controls this sort of vehicle behavior by manipulating the brakes and engine power to prevent skidding and stabilize the vehicle. VSC is therefore expected to reduce traffic accidents, and its widespread use would be of real benefit.

VSC detects the behavior of the vehicle by using sensors to measure inertial forces such as acceleration and angular rate. Reducing the cost of these sensors is an urgent task, because lower costs would encourage wider use of VSC. For that reason, development of inertial sensors is being actively pursued using silicon micromachining technology, a technology that is expected to reduce cost sufficiently to make mass production practical. [1]-[7] The technology is now being used to produce almost all of the accelerometers that are used for vehicle control, but it has not been applied very often to producing practical gyroscopes to detect angular rate for vehicle control. This is because the silicon gyroscopes that have been produced to date are less sensitive than piezoelectric ceramic or quartz gyroscopes that utilize the piezoelectric effect, so their performance tends to fall short of what is required for vehicle control.

Toyota has addressed these shortcomings and utilized silicon micromachining technology to develop a sensor element and signal processing IC. The sensor element and signal processing IC are vacuum-sealed in a hermetic package to form the sub-assembly shown in **Photo 1**, which is then installed in the sensor unit. The sub-assembly is so designed that the single sensor element detects not only the angular rate, but also the acceleration. Sigma-delta analog-to-digital conversion, which is known for its high accuracy, is used to convert the sensor signals. A sigma-delta modulator is built into the signal processing IC, and a microcomputer in the sensor unit performs digital computations to calibrate the sensor characteristics. This allowed the structure of the sensor unit to be simplified, reducing its cost, and the unit went on the market in December 2003. This article describes the newly developed sensor element and signal processing IC.

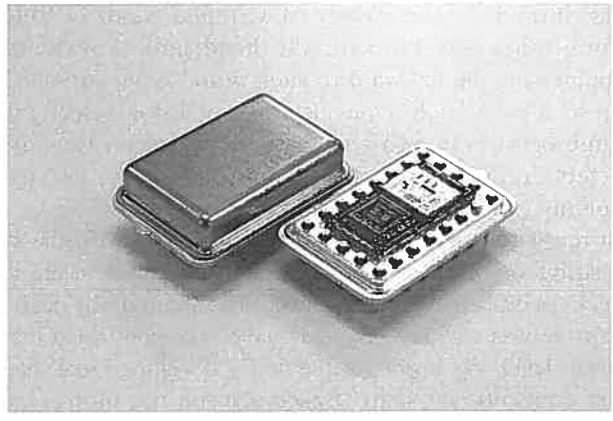

Photo 1 Sensor Sub-Assembly

* Electronics Engineering Div. 3
** Electronics Engineering Div. 2
*** Electronic Components Engineering Div.

2. Sensor Element

2.1 Detection principle

Angular rate detection works by detecting the Coriolis force that acts on an oscillating body when it rotates. **Fig. 1** illustrates how detection works.

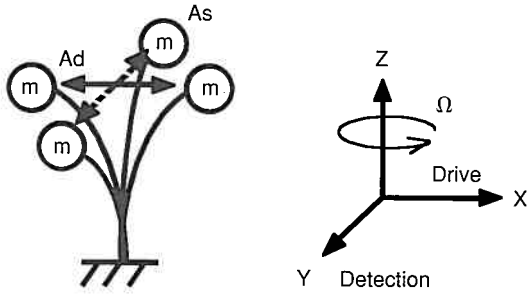

Fig. 1 Angular Rate Detection Principle

A point mass (m) is made to oscillate in the X-axis direction at a resonant frequency of ωd and a fixed amplitude of Ad. If an angular rate (Ω) is input around the Z axis at this time, a Coriolis force that is proportional to the angular rate acts on the point mass in the Y-axis direction at a frequency of ωd. The mass starts to move in an elliptical path that combines the oscillation in the X-axis direction with the Coriolis force in the Y-axis direction. The angular rate is detected by detecting the amplitude in the Y-axis direction (As).

The amplitude in the Y-axis direction (As) is expressed by equation 1.

$$As = \frac{2Ad}{\omega d} \frac{1}{\sqrt{(\alpha^2 - 1)^2 + \left(\frac{\alpha}{Qs}\right)^2}} \Omega \qquad (1)$$

Here α is the detuning ratio (the detection-side resonant frequency ωs divided by the drive-side resonant frequency ωd), and Qs is the quality factor on the detection side (the clarity of the resonance).

According to equation 1, the sensitivity of the angular rate sensor can be increased by boosting the drive amplitude Ad and keeping the detuning ratio α close to 1. A structure is therefore used that increases the drive amplitude Ad by vacuum-sealing the sensor element and raising the Q factor (the clarity of the resonance), so that a high-amplitude signal is obtained from even a small force.

By contrast, acceleration is detected based on the Y-axis displacement of the point mass that results from the acceleration that is input in the Y-axis direction. Angular rate and acceleration are thus both detected based on the Y-axis displacement; the method of separating the two is described in Section **2.3**.

2.2 Sensor element structure

Photo 2 shows the sensor element as seen through a scanning electron microscope (SEM), and **Fig. 2** is a diagram of its structure.

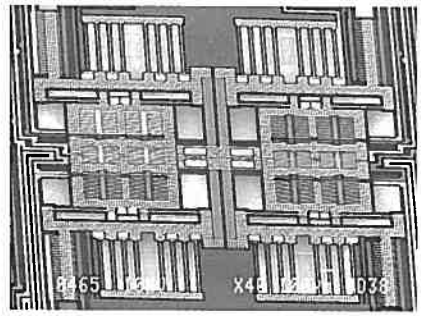

Photo 2 Scanning Electron Microscope Photograph of Sensor Element

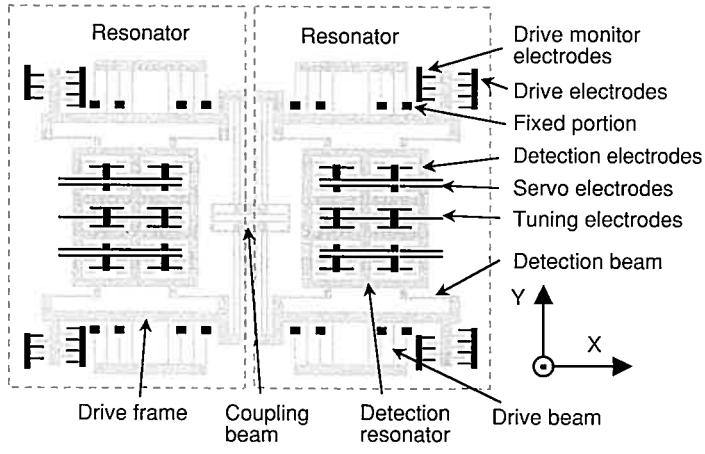

Fig. 2 Sensor Element Structure

The resonators on the left and right are joined by a coupling beam, so that they function as a tuning fork. The upper and lower ends of each resonator rest on drive frames that are themselves suspended on drive beams that are anchored in the silicon substrate. The detection resonator is suspended on detection beams that rest on the drive frames. Each of the four drive frames is provided with drive electrodes, which are anchored in the substrate and intermesh with the frame electrodes like the teeth of two combs, as well as drive monitor electrodes that detect the amplitude of the oscillation. The electrostatic force generated by the drive electrodes drives the resonators in the X-axis direction. Driving the detection resonator through the drive frames in this manner makes it possible to separate the drive oscillation from the detection oscillation, decreasing the interference that the drive oscillation imposes on the detection function so as to reduce sensor output errors.

The interior of the detection resonator is made up of detection electrodes, servo electrodes, and tuning electrodes that adjust the

detection resonator's resonance frequency. The electrodes that are anchored in the substrate and the resonator electrodes function as parallel flat-plate capacitors. When the detection resonator moves in the Y-axis direction, the distances between electrodes change, which changes the capacitance.

The angular rate is detected by detecting the changes in the capacitance of the detection electrodes when the Coriolis force causes the detection resonator, which is already oscillating in the X-axis direction, to move in the Y-axis direction as well.

2.3 Method of separating angular rate from acceleration

The gyroscope that was developed uses a single sensor element to detect both angular rate and acceleration. The two are separated as described below.

The resonators on the left and right are driven in opposite directions on the X axis. The movements of the coupling beam cause the resonators to oscillate in opposite phases at a fixed resonant frequency, in the same manner as a tuning fork. If an angular rate around the Z axis is input to the sensor element at this point, the Coriolis force acts on the left and right detection resonators in opposite phases at the same resonant frequency. On the other hand, if an acceleration is input in the Y-axis direction, the detection resonators move in the same phase on the Y axis. The phases of the left and right detection resonators are used to separate the angular rate from the acceleration. Moreover, because the Coriolis force acts at the drive resonance frequency, synchronous demodulation at that frequency is used to make the separation more accurate.

3. Fabrication Method

Fig. 3 is a schematic diagram of the sensor element fabrication process. The sensor element is fabricated on a silicon-on-insulator (SOI) wafer using micromachining technology.

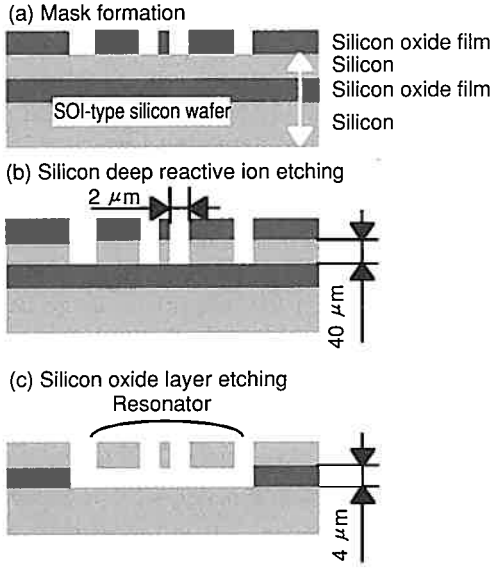

Fig. 3 Sensor Element Manufacturing Process

(a) A silicon oxide mask is formed to allow the silicon in the SOI wafer to be etched.
(b) A pattern in the shape of the sensor is etched into the silicon by means of deep reactive ion etching, with a depth/height aspect ratio of 40 μm of depth per 2 μm of gap.
(c) The buried silicon oxide layer is etched isotropically by an ammonium fluoride solution. Isopropyl alcohol, which has low surface tension, is then used to dry the element by evaporation, so that surface tension will not cause the resonators to stick to the substrate. The resonators are thus rendered functional.

The sensor element that is thus fabricated is vacuum-sealed in a hermetic package with the signal processing IC.

4. Sensor Signal Processing

4.1 Detection by means of capacitance changes

Semiconductor-based angular rate sensors are less sensitive than comparable piezoelectric sensors. If the change in capacitance that must be detected is converted to displacement of an aF (10^{-18}F) order, it works out to 1 nanometer or less. It is therefore important to reduce noise in the detection circuit.

Fig. 4 is a block diagram of the capacitance change detection circuit. When the detection resonator is displaced by the angular rate input, the opposing capacitance changes in the detection electrodes are detected and converted to voltage for output. The capacitance is detected by detecting the charge so that parasitic capacitance will not reduce the efficiency of the capacitance-to-voltage conversion. [8]

The next task was to reduce circuit noise. Circuit noise is divided into two types: frequency-independent white noise and frequency-dependent 1/f noise. The latter is dominant and therefore more important to reduce. To do this, a method was adopted in which the carrier wave for the sensor capacitance signal is amplitude-modulated to raise the frequency of the signal that the circuit handles, thereby reducing the 1/f noise.

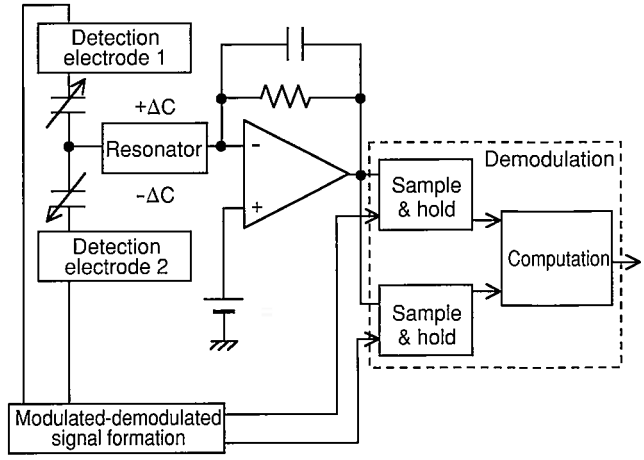

Fig. 4 Block Diagram of Capacitance Change Detection Circuit

4.2 Angular rate signal processing

Because the angular rate signal is at the same frequency as the resonator drive frequency, it can be extracted by synchronous demodulation at the drive frequency. However, in practice, variations in the degree of vacuum and the resonant frequency of the detection resonator, as well as variations in the phase of the detection resonator's response to the Coriolis force, affect the sensitivity and offset drift of the angular rate signal and so lead to errors. This section describes how those errors were reduced.

Due to the variations in the fabrication process, the drive direction of the detection resonator may not be completely parallel to the X axis and may involve some degree of Y-axis oscillation. This oscillation is the same sort that the detection resonator detects as the Coriolis force. However, this oscillation is 90° out of phase with the Coriolis force, so it should be possible to distinguish it from the Coriolis force. But in reality, it gives rise to significant error for the reasons described below.

In order to increase their sensitivity, resonance-type angular rate sensors are generally designed so that the resonant frequencies of the drive oscillation and the detection oscillation are close, as described in Section **2.1** above. **Fig. 5** shows the results of a simulation of resonance characteristics. It indicates that the phase delay in the detection resonator's response to the Coriolis force depend on changes in the degree of vacuum. Because the synchronous demodulation is done according to the phase of the drive oscillation, any variation in the phase of the detection resonator's response causes a discrepancy in the demodulation timing, creating variations in the angular rate sensitivity and offset drift.

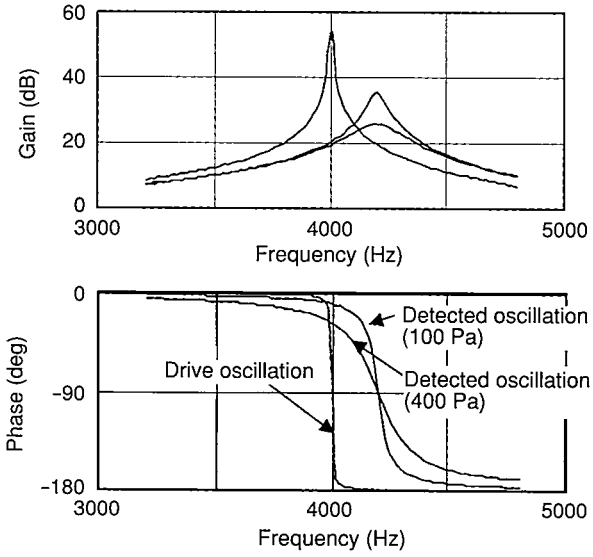

Fig. 5 Simulation of Resonance Characteristics

For the gyroscope described in this article, a servo detection circuit is used in addition to synchronous demodulation to reduce the influence of the variations in the phase characteristics. The servo force is provided as an electrostatic force by applying voltage to the servo electrodes. Applying the servo force in opposite phase to the Coriolis force controls the detection resonator so that it does not oscillate in the Y-axis direction. This makes the displacement of the detection resonator extremely small, reducing the influence that variations in the response to the Coriolis force have on the sensor characteristics. The detection resonator displacement signal is used to assess the balance between the servo force and the Coriolis force, so that the Coriolis force (angular rate) is detected based on the magnitude of the servo force.

The next issue was how to adjust the resonant frequency of the drive oscillation and the detection oscillation. Because of variations in their fabrication, resonance-type angular rate sensors generally require tuning of the resonant frequency of the drive oscillation and the detection oscillation. The sensor described here tunes the frequency of the detection oscillation by applying a DC bias voltage to the detection resonator. This makes tuning simpler than with mechanical tuning methods. The bias voltage is applied through the tuning electrodes. **Fig. 6** shows how the resonant frequency depends on the tuning voltage.

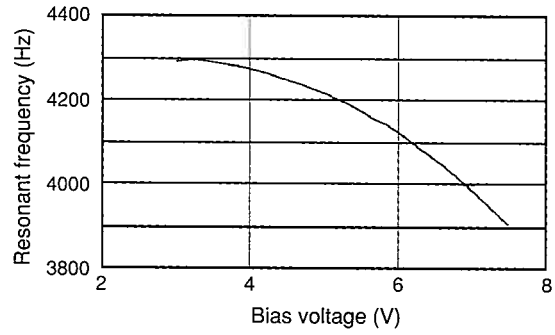

Fig. 6 Dependency of Resonant Frequency Adjustment on Voltage

It can be seen from these characteristics that the resonant frequency fluctuates according to fluctuations in the temperature and reliability of the bias voltage, and that affects the sensor characteristics in turn. The influence of these fluctuations in the resonant frequency is effectively reduced simply by using the servo circuit to assess the balance of forces, as described earlier.

4.3 Detection of acceleration signal

Acceleration is detected by its moving in phase with the detection resonator. The signal processing circuit is simpler than the one for the angular rate signal, and the changes in the detection capacitance are detected by a charge-detection type of capacitance detection circuit, as described earlier. The detection signal is first put through a low-pass filter to remove the drive signal noise, then amplified to an appropriate level for output. The acceleration detection circuit was created simply by adding a small circuit to the signal processing IC. **Photo 3** shows the signal processing IC.

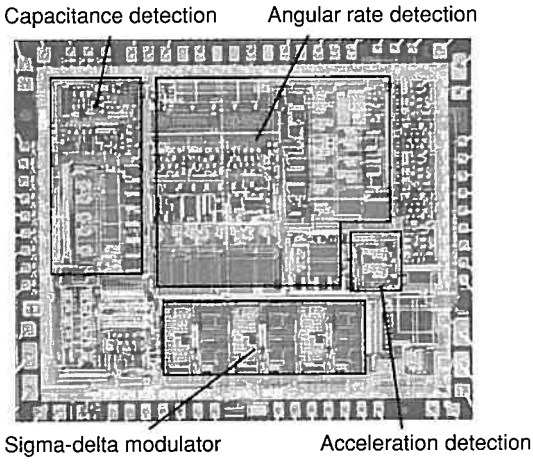

Photo 3 Signal Processing IC

4.4 Calibration of characteristics

Vehicle control sensors must be highly accurate, so initial variations in the sensor characteristics must be calibrated. Conventionally, characteristics are calibrated by analog computations using a trimming resistor and digital-to-analog conversion. For the sensor described here, digital calibration of the characteristics was achieved by using sigma-delta analog-to-digital conversion, which is known for its high accuracy. **Fig. 7** is a block diagram of the sensor unit. A sigma-delta modulator is built into the signal processing IC, where it converts the acceleration, angular rate, and temperature signals into single-bit digital signal streams that are sent to a microcomputer. A digital filter in the microcomputer restores the digital data with an accuracy of 12 bits or better, and the sensor characteristics are calibrated by digital computations based on calibration information that is stored in EEPROM.

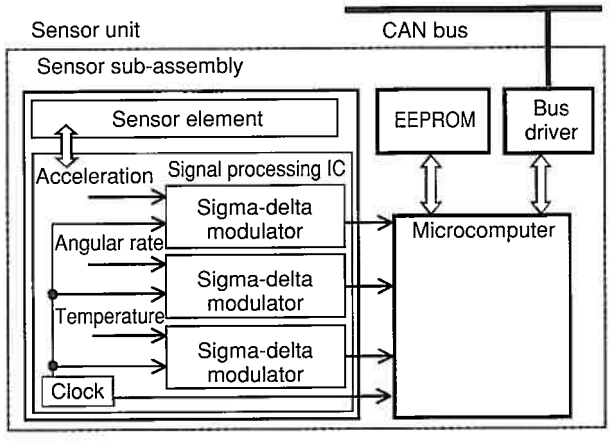

Fig. 7 Block Diagram of Sensor Unit

5. Sensor Performance

Photo 4 shows the external appearance of the sensor unit. It measures 70 by 55 by 30 millimeters.

Photo 4 Sensor Unit

Fig. 8 shows the measured characteristics of the sensor output signal. First, the sensor is mounted on a turntable, so that its axis of acceleration detection will be vertical. When the turntable rotates at a fixed speed, a fixed angular rate is applied to the sensor. On the other hand, the rotation repeatedly moves the sensor's acceleration detection axis in the vertical direction, so that acceleration is applied in the form of a sine wave at approximately 10 m/sec^2. The resulting output waveform is shown in **Fig. 8**. It was confirmed that a fixed angular rate and an acceleration that is input as a sine wave are successfully separated for output.

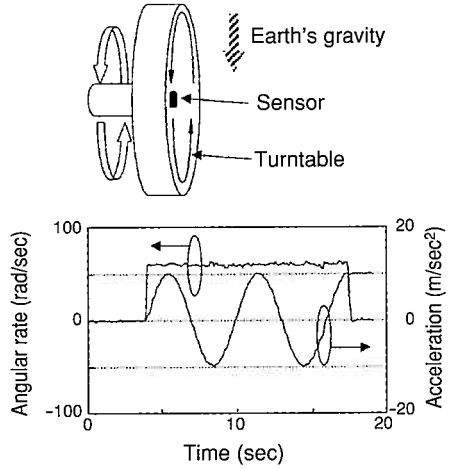

Fig. 8 Measurement of Sensor Output Signal Characteristics

Some of the most important characteristics of sensors for vehicle control vary with the temperature. **Figs. 9** and **10** show the temperature dependency of the offset and sensitivity of the angular rate signal after it has been calibrated by digital processing. It can be seen that the offset varies by no more than 0.5 degrees per second and the detection sensitivity varies by 1% or less, indicating no problem for use in vehicle control.

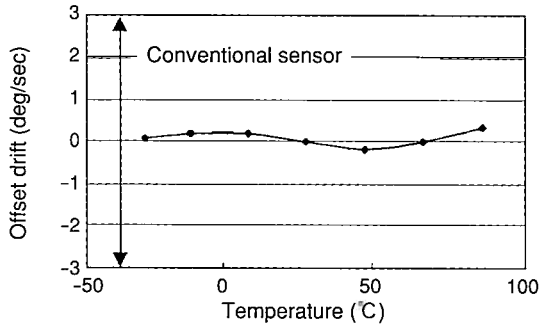

Fig. 9 Temperature Dependency of Angular Rate Signal Offset

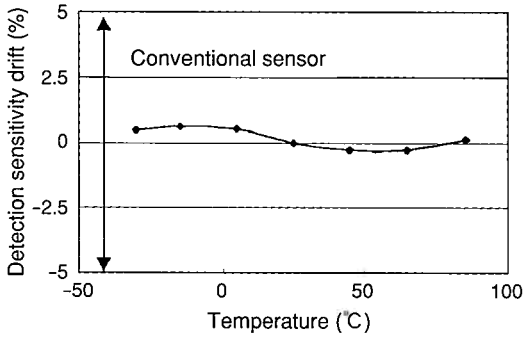

Fig. 10 Temperature Dependency of Angular Rate Signal Sensitivity

6. Conclusion

This article has described a semiconductor-based gyroscope that was successfully commercialized for vehicle stability control. The single sensor element, which is fabricated using micromachining technology, detects not only angular rate, but acceleration as well. Also, the incorporation of sigma-delta analog-to-digital conversion into the signal processing IC allows the sensor characteristics to be calibrated digitally by a microcomputer. The result is a simple sensor unit that is 30% smaller and 20% lower in cost.

Toyota will continue to pursue technical development to accelerate the spread of safety systems such as VSC, so as to contribute to the building of a mobile society with zero accidents.

References

(1) J. Berstain et al. "A Micromachined Comb-Drive Tuning Fork Rate Gyroscope." *Proceedings of MEMS Workshop* (1993) pp. 143-148.
(2) M. Putty, Najafi. "A Micromachined Vibrating Ring Gyroscope." *Solid-State Sensor and Actuator Workshop* (1994) pp. 213-220.
(3) J. Johnson, Zarabadi, Sparks. "Surface Micromachined Angular Rate Sensor." *SAE Paper* No. 950538 (1995).
(4) K. Yamashita, Minami, Esashi. "A Silicon Micromachined Resonant Angular Rate Sensor Using Electrostatic Excitation and Capacitive Detection." *Tech. Dig. Of 14th Sensor Symposium Proceedings* (1996) pp. 39-42.
(5) T. Juneau, Pisano. "Micromachined Dual Input Axis Angular Rate Sensor." *Solid-State Sensor and Actuator Workshop* (1996) pp. 299-302.
(6) M. Lutz et al. "A Precision Yaw Rate Sensor in Silicon Micromachining." *Transducers* '97 (1997) pp. 847-850.
(7) J. Geen, Sherman, Chang, Lewis. "Single-Chip Surface Micromachined Integrated Gyroscope with 50/h Allan Deviation." *IEEE Journal of Solid-State Circuits* Vol. 37 No. 12, pp. 1860-1866.
(8) Kawahashi, Sugimoto. "21st Century Automotive Electronics System and System LSI." *Keisoku to Seigyo* Vol. 40 No. 12 (2001) pp. 848-856.

Authors


E. NAKATANI


M. NAGAO


H. WATANABE


M. HASHIMOTO


K. SHIRAI


K. AOYAMA

Clarification of Grinding Crack Mechanism

Masaaki Sato*
Hiroyuki Miwa*
Takashi Eguchi*
Shuzo Yamamoto*

Abstract

The importance of improving vehicle performance necessitates constant increases in the accuracy and strength of shafts such as the crankshaft, which is a key part of the engine. Grinding is used as a finish method for bearings and other parts where the required accuracy is particularly high, but a crucial issue in this process is solving quality problems caused by so-called grinding cracks. Conventional wisdom states that the most important factors in grinding cracks are surplus grinding heat generated at the grinding point and the cooling that occurs when coolant is applied, but no general solutions have been formulated. This article describes how the temperature generated during grinding on a high-speed cylindrical grinding machine was measured successfully, thereby enabling the grinding crack mechanism to be demonstrated quantitatively. As a result, the necessary conditions for ensuring that no cracks are generated have been defined, regardless of variations in material composition or process location, making it possible to develop more efficient methods of grinding.

Keywords: *shaft, grinding, grinding crack, grinding temperature, work piece deformation*

1. Introduction

The importance of improving vehicle performance attributes like fuel efficiency and generating capacity means that it is constantly necessary to increase the accuracy and strength of shafts such as the crankshaft and the camshaft, which are key parts of the engine. Grinding is used as a finish method for bearings and other parts where the required accuracy is particularly high, but a crucial issue in this process is solving quality problems caused by so-called grinding cracks. Conventional wisdom states that the most important factors behind grinding cracks are surplus grinding heat generated at the interface and the cooling that occurs when coolant is applied. However, it has only been possible to take a qualitative approach with regard to the countermeasures for these issues and for how to judge quality. As a result, it has been a very time consuming process to build in quality to the initial production preparation phase whenever changes occur to product specifications, production capacity, or the like.

This article describes how the temperature generated during high-speed cylindrical grinding was measured successfully, thereby enabling the grinding crack mechanism to be demonstrated qualitatively. As a result, the necessary conditions for preventing the initiation of cracks have been defined, regardless of process location, and the effects of variations in material composition have been assessed. It is also felt that this will enable the development of more efficient methods of grinding.

* Engine Production Engineering Div.

2. Grinding Cracks

Grinding cracks are fractures initiated by tensile residual stress in the outer layer of the work piece after grinding has been performed (**Fig. 1**). The formation of these cracks cause the surface of shafts to take on a convex shape, which subsequently leads to bearing seizure. Grinding cracks are therefore an issue linked directly to serious quality problems, and eliminating their occurrence is considered to be crucially important.

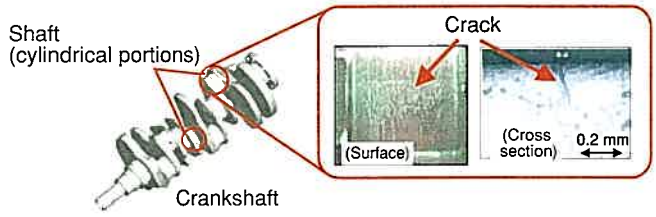

Fig. 1 Grinding Cracks in Shafts (E.g.: Crankshaft)

3. Clarification of Grinding Crack Mechanism

3.1 Conventional approaches and measures

Fig. 2 shows the conventional approach with regard to the presumed grinding crack mechanism. The application of heat followed by rapid cooling during pre-finish induction hardening causes carbon to form in solid solution in the work piece, thereby generating compressive residual stress in the outer layer. The heat generated by grinding in the finish process is then transferred to the work piece, causing the solid solution carbon to

precipitate as carbides and generating tensile residual stress in the outer layer. Cracks are then initiated if this tensile residual stress exceeds the strength of the material. Moreover, the temperature at which this kind of deformation occurs in the work piece is considered to be approximately 300°C. Therefore, accepted theory states that grinding cracks are caused by work piece deformation generated when the grinding temperature reaches this level. For these reasons, countermeasures for cracks have focused on improving both the suppression of generated heat and the cooling efficiency by reducing processing efficiency and supplying large amounts of coolant. As a result, it has been difficult to improve productivity.

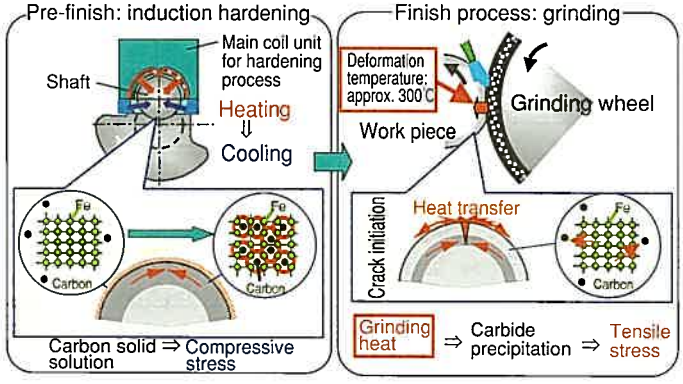

Fig. 2 Presumed Mechanism for Initiation of Grinding Cracks

3.2 Analysis procedure

A hypothesis was formulated based on the presumed mechanism described above. This hypothesis stated that, since the grinding temperature has a correlation with grinding cracks, the necessary conditions for suppressing grinding cracks might be defined by establishing control of the grinding temperature. Analysis was therefore performed in accordance with the steps shown below. The tests used cylindrical grinding in order to simulate the way that shafts are processed.

(1) Measurement of temperature during grinding process
(2) Reproduction of size of cracks
(3) Analysis of correlation between work piece deformation and temperature
(4) Verification of method of controlling grinding temperature

Various methods of measuring the temperature during the grinding process have been described in the literature, but none have been put into practical use due to issues such as the reliability of the measured values, versatility, and the like. The method described in this article was developed by revising procedures such as the method of sampling sensor signals, and it is the first time that temperature measurement technology has been applied to a high-speed cylindrical grinding machine.

3.3 Development of grinding temperature measurement technology

3.3.1 Verification of measurement method

As shown in **Fig. 3**, the four general categories of grinding temperature are (1) the interface temperature of the abrasive, (2) the interface temperature of the grinding wheel, (3) the inside temperature of the grinding wheel, and (4) the outer layer temperature of the work piece. Since the mechanism to be explained in this development has a relationship with work piece deformation, it was necessary to visualize temperature (4), the outer layer temperature of the work piece. Therefore, it was important to be able to obtain detailed data on the transfer of heat to the inside of a work piece rotating at higher speeds.

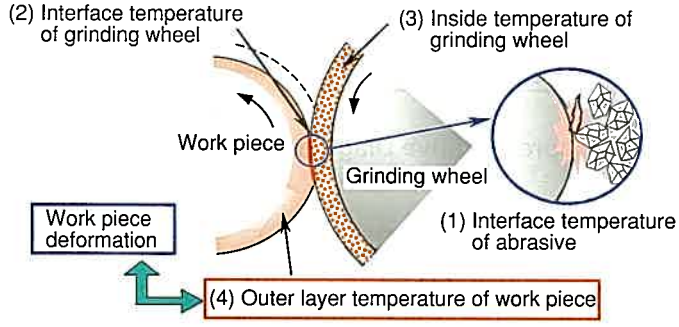

Fig. 3 Categories of Grinding Temperature

The method of temperature measurement devised for this development applied temperature measurement technology from high-speed drilling based on the use of embedded thermocouples.

3.3.2 Temperature measurement device

Fig. 4 shows the outline of the temperature measurement device and the measurement results. Multiple thermocouples were embedded inside the work piece alongside an A/D converter, and a phase detector was provided in order to acquire the signals from the thermocouples passing through the interface at higher speeds. Furthermore, non-contact type data transmission was performed by utilizing electromagnetic coupling, which enables the temperature of bodies rotating at high speed to be measured with little noise interference. As a result, it was possible to sample the temperature in accordance with a power waveform that represents the grinding load.

Thermocouple disconnection signals and data on the process diameter using a grinding machine sizing device were added based on these measurement results (**Fig. 5**). This allowed the distribution of heat generation at the interface and the heat transferred to the inside of the work piece to be visualized (**Fig. 6**).

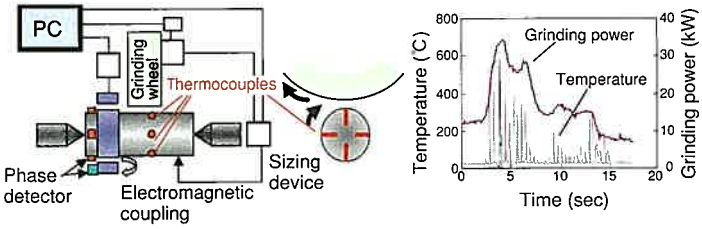

Fig. 4 Measurement Device and Measurement Results

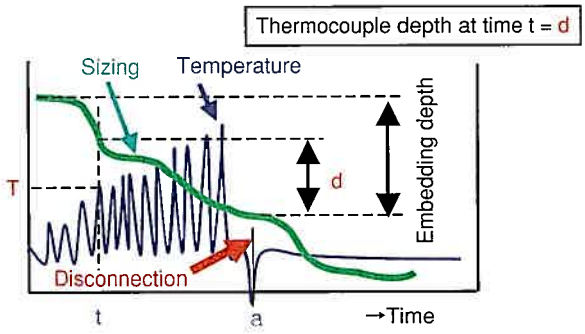

Fig. 5 Representative Diagram of Sampling Waveform

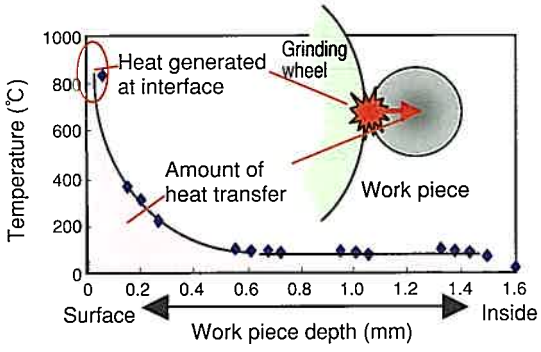

Fig. 6 Temperature Distribution

3.4 Tests and analysis

3.4.1 Reproduction of size of grinding cracks

To verify the accepted theory about cracks, conventional process conditions were set, and tests were made to reproduce large and small cracks. The key points with regard to the set conditions were generated heat and cooling efficiency. The cutting speeds and coolant flow rates were switched mainly between standard levels, and states were reproduced with large and small grinding cracks (**Fig. 7**).

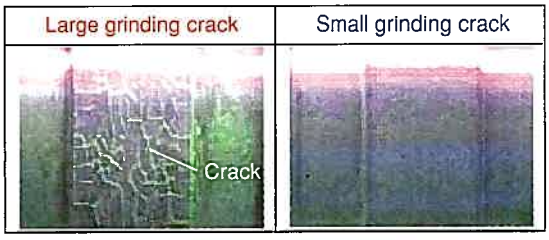

Fig. 7 States of Cracks on Work Piece Surface After Grinding

3.4.2 Analysis of correlation between work piece deformation and grinding temperature

The reproduced work pieces containing large and small cracks were examined. The carbide precipitation layer and the residual stress, which indicate the state of deformation, were observed in order to analyze the relationship with the grinding temperature. The results are shown in **Fig. 8**.

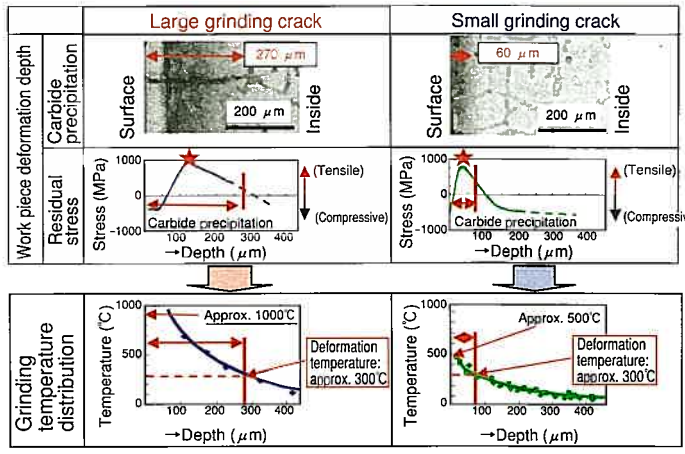

Fig. 8 Cross Sectional Structure, Residual Stress and Grinding Temperature

The results show that the smaller the crack, the shallower the carbide precipitation depth becomes. In consequence, the peak position of the tensile residual stress (indicated by the stars in **Fig. 8**) is also generated within the carbide precipitation layer.

The grinding temperature at this point indicates that the temperature close to the surface is lower the smaller the crack becomes. However, the relationship with work piece deformation confirms that the temperature of the deformation depth is approximately 300°C, regardless of whether the crack is large or small. This indicates that the work piece deformation depth is dependent on the depth to which the grinding temperature is transmitted.

3.4.3 Verification of method of controlling grinding temperature

Based on the findings described above, verification was made as to whether it is possible to control the transmission depth of the grinding temperature. The key point here is the reduction of the ratio of heat transfer to the work piece even when the temperature generated by processing close to the surface is the same. General high-speed grinding theory states that an effective way of reducing the ratio of heat transfer to the work piece is to shorten the contact time with the heat source. Consequently, the relationship with the speed at which the work piece passes through the heat source in relation to the heat source length was defined as the "work piece heating time" (**Fig. 9**). The correlation between the work piece heating time and work piece deformation was then verified.

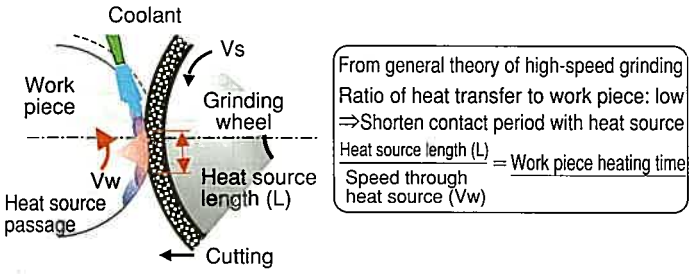

Fig. 9 Definition of Work Piece Heating Time

The factors in the processing conditions that affect generated heat and cooling efficiency, such as the feed speed and the like were fixed, and three combinations of conditions were set. These consisted of the length of the arc of contact of the grinding wheel and the revolution speed of the work piece. The results confirmed that in all cases the temperature close to the surface reached 800°C or more, but that the work piece deformation depth became shallower in accordance with reductions in the work piece heating time (**Fig. 10**). Work piece heating time was therefore judged to be an effective means of controlling deformation depth.

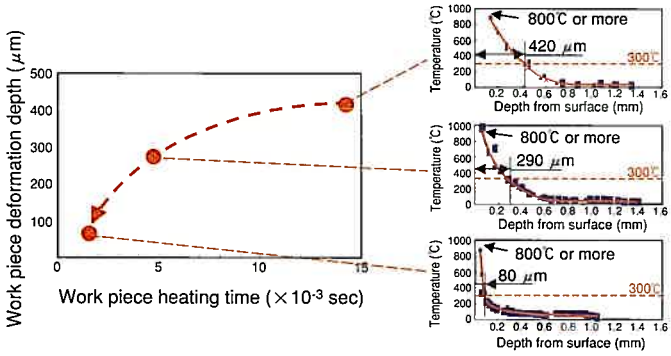

Fig. 10 Effect of Work Piece Heating Time

3.5 Summary of explanation of mechanism

Accepted theory related to cracks states that it is possible to reproduce large and small cracks by changing factors affecting generated heat and cooling efficiency. The results of the tests performed as described above were in concordance with the theory. Furthermore, visualizing the grinding temperature also enabled verification that the deformation depth of the work piece is the depth to which a grinding temperature of approximately 300°C (the deformation temperature) is transmitted. It was also discovered that the work piece deformation depth is dependent on a factor described above as "work piece heating time."

4. Application to Processing of Parts

Fig. 11 shows a grinding cycle plan during the processing of parts. After the hardening phase is complete, the work piece passes through the following stages: (1) high-efficiency grinding in a rough grinding cycle that is applied in consideration of corrections such as quenching strain and the like; (2) a fine grinding cycle where the deformed layer generated during rough grinding is removed completely; and (3) a final polishing step to secure product quality. Consequently, the method of completely eliminating grinding cracks in the processing of parts requires the control of the deformation depth in accordance with each of the cycles. It is therefore necessary to clarify the degree of impact of the control factors.

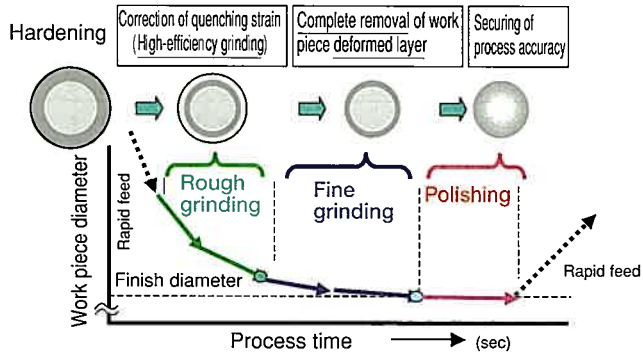

Fig. 11 Grinding Cycle Plan

4.1 Factor analysis

Fig. 12 shows a system diagram depicting the relevant factors for work piece deformation. It shows grinding conditions that control generated heat and cooling efficiency as main factors, and work piece conditions related to the hardened structure and material qualities as acceleration factors. The degree of impact of these factors has been evaluated in the past but, in this case, a heating time factor was also included in consideration of the data acquired after verification of the crack mechanism. The degrees of impact were therefore re-examined to include previously unevaluated factors.

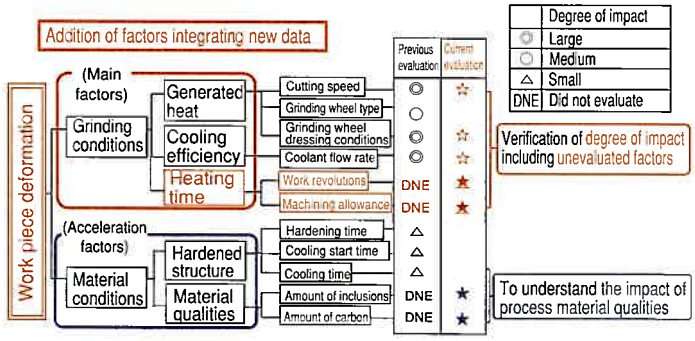

Fig. 12 System Diagram of Factors

4.1.1 Impact of work piece qualities

The concept behind this part of the evaluation was whether work piece deformation caused by the type of steel used would change in relative terms. The test conditions for this evaluation

are shown in **Table 1**. Work piece deformation depth was compared and evaluated after changing three main factors (cutting speed, work piece revolutions and coolant flow rate) in relation to two acceleration factors (steel type and hardness).

Table 1 Test Conditions (1)

	Factors	Conditions 1	2	3
Main factors	Cutting speed (ϕ mm/min)	25	15	2
	Work piece revolutions (rpm)	202	91	–
	Coolant flow rate (L/min)	70	15	–
Acceleration factors	Steel type※	Lead-free	Free cutting tri-composite steel	–
	Hardness	Upper limit	Center	–

※Both have the same carbon amounts.

The results are shown in **Fig. 13**. It was confirmed that work piece deformation depth changed in accordance with the changes in the coolant flow rate and heating time, i.e., the factors representing cooling efficiency. However, the same distribution for work piece deformation depth was acquired regardless of the steel type and hardness of the work piece. This indicates that differences in work piece qualities have a smaller impact than the main factors.

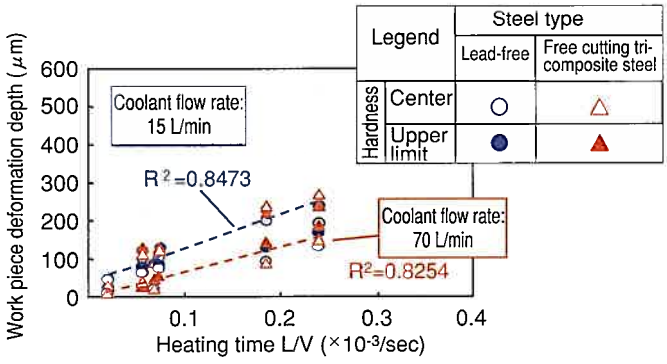

Fig. 13 Test Results

4.1.2 Evaluation of degree of impact of grinding conditions

The test method evaluated five factors considered to be related to both the conventional factors (generated heat and cooling efficiency) and the additional factor (heating time). Processing was then performed using random combinations of the conditions, as shown in **Table 2**. The evaluation utilized a statistical method and applied the standardized partial regression coefficient as an index for the degree of impact. The larger the value acquired for this absolute value, the stronger the significance with regard to work piece deformation. Multiple regression analysis was also performed at the same time to calculate a prediction formula for work piece deformation.

Table 2 Test Conditions (2)

Factors	Conditions 1	2	3
Cutting speed (ϕ mm/min)	2	15	25
Work piece revolutions (rpm)	91	202	400
Coolant flow rate (L/min)	15	50	70
Dressing lead (mm)	0.05	0.1	0.2
Machining allowance (mm)	0.2	0.8	–

The results are shown in **Fig. 14**. It was confirmed that a previously unevaluated factor (work piece revolutions) had the largest impact.

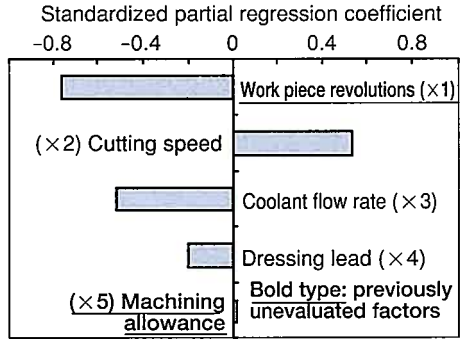

Fig. 14 Evaluation Results

4.2 Summary of factor analysis

Since work piece conditions (i.e., the acceleration factors) have only a small impact on suppressing work piece deformation, it is important that actions be focused on the main factors. Analysis that was performed after applying data newly obtained in this development discovered that an additional factor, namely work piece revolutions, has the largest impact with regard to these main factors. Moreover, the work piece deformation depth prediction formula as shown in equation 1 enables the work piece deformation depth to be controlled in each grinding cycle.

$$\underset{\text{Work piece deformation}}{Y} = \underset{\text{Work piece revolutions}}{-0.67(X_1)} + \underset{\text{Cutting speed}}{6.26(X_2)} - \underset{\text{Coolant flow rate}}{1.98(X_3)} - \underset{\text{Dressing lead}}{508.50(X_4)} + \underset{\text{Machining allowance}}{4.46(X_5)} + 262.33 \quad (1)$$

4.3 Compatibility with increased crankshaft strength

4.3.1 Optimization of shaft cylindrical grinding conditions

As the generating capacity of V8 engines increases, it has become necessary to boost the hardness of the raw materials used in the crankshaft. At the same time, environmental concerns have necessitated the application of lead-free materials.

Since these conditions are detrimental with regard to grinding cracks, processing conditions have been optimized based on the factor analysis described above. Examples of the results of this optimization are shown in **Figs. 15** and **16**.

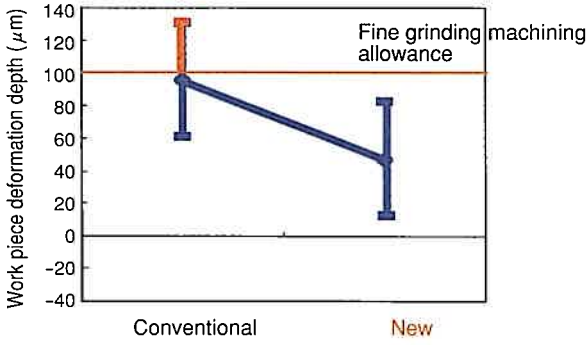

Fig. 15 Deformation Depth After Rough Grinding

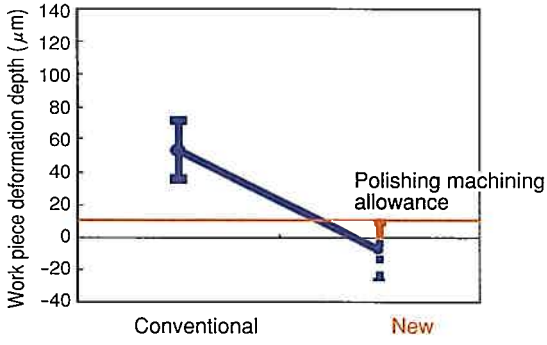

Fig. 16 Deformation Depth After Fine Grinding

When conventional conditions are applied after increasing the hardness of the raw materials, work piece deformation is generated in the rough grinding cycle (see **Fig. 15**) at or above the fine grinding machining allowance. This means that the work piece deformation cannot be removed. In contrast, process optimization has enabled the work piece deformation to be suppressed to within the fine grinding machining allowance, even allowing for variations. Moreover, although a small amount of work piece deformation may be generated in the same way in the fine grinding cycle once variations are considered (see **Fig. 16**), the amount can be suppressed to within the final polishing machining allowance and the deformation can therefore be removed completely. Thus, it is possible to mass-produce crankshafts that satisfy both product performance and environmental requirements.

4.3.2 Application to thrust surface grinding

As shown in **Fig. 17**, the thrust surfaces of conventional crankshafts do not suffer the problem of grinding cracks in non-hardened state (a). However, suppression of grinding cracks is necessary for hardened state (b), which is attained in order to increase product stiffness and the like.

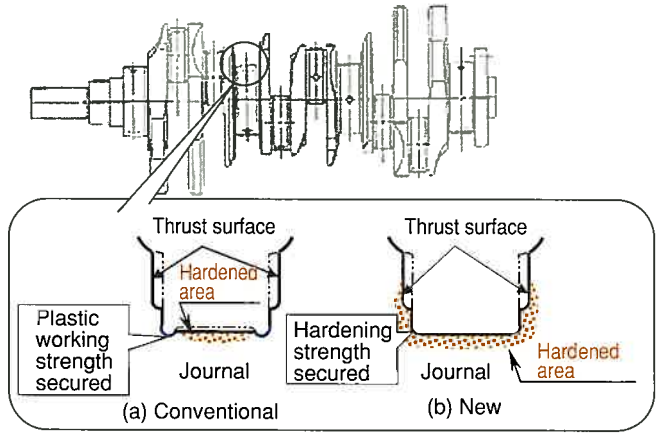

Fig. 17 Thrust Surface of Crankshaft

The crack suppression method for cylindrical grinding as described above was also tested with surface grinding. **Fig. 18** shows the changes in work piece deformation depth after rough grinding. The work piece deformation depth increased in accordance with increases in the cutting speed, but it was possible to suppress the work piece deformation depth by a substantial amount by increasing the work piece revolutions. This indicates that this method for controlling the grinding temperature is applicable to surface grinding as well as cylindrical grinding.

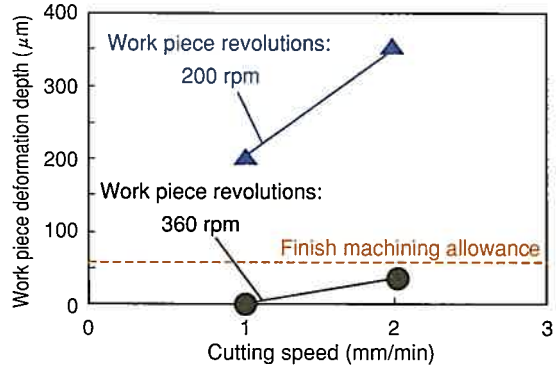

Fig. 18 Work Piece Deformation After Rough Grinding Stage of Surface Grinding

4.4 Prospect of high-efficiency grinding

One concern related to high-efficiency grinding is the increase in the grinding temperature. It was expected that the most likely ways of combating this issue would be through either the development of a highly efficient cooling system or the development of a grinding wheel with a high cutting capability. It may be possible, however, to achieve high-efficiency grinding within the scope of existing technology by applying the method to control grinding temperature. Unfortunately, this method has raised new issues, such as the worsening of processing accuracy and the reduction of grinding wheel lifetime. As a result, it is now necessary to optimize the process in conjunction with some other control or tool-based basic technology.

5. Conclusions

(1) The temperature during grinding with a high-speed cylindrical grinding machine was measured successfully, enabling the collection of data to verify quantitatively the theory that grinding cracks originate from temperature and the structure and residual stress of the material.
(2) It was determined that, in addition to the heat generated on grinding, reduction of the deformation temperature depth of the work piece is important for suppressing cracks.
(3) New data was discovered indicating that the deformation temperature depth is dependent on a factor described above as "heating time."
(4) The method of controlling grinding temperature is applicable to all forms of grinding. It has also contributed to improving marketability since it is compatible with increases in material strength and the like.
(5) Evaluations into the degree of impact of material composition indicated that this is a timely method with good potential, bearing in mind future increases in local sourcing of raw materials as overseas production expands.

Authors


M. SATO


H. MIWA


T. EGUCHI


S. YAMAMOTO

Development of a CAE System for Wear Prediction of Hot Forging Dies

Atsuo Watanabe*
Toshiyuki Suzuki*
Koukichi Nakanishi**
Toshiaki Tanaka**
Masatoshi Sawamura**
Yasuhiro Yogo**

Abstract

Hot forging is a manufacturing method that is applied to a wide variety of high-strength automotive components. The prediction of die life in hot forging is vital to satisfy demands for cost reduction by shortening production preparation times and designing longer life dies. Around 70% of die failures that occur in hot forging processes result from wear related to increases in die temperature. Therefore, a system has been developed to predict die life by using CAE at the product and hot forging process design stages to calculate die temperature and wear. This article describes the quantification of lubricant spray characteristics, which influence die temperature, and the improvement that was achieved in the wear prediction formula through the use of multivariate analysis, which were performed in order to put this prediction technology into practical use.

Keywords: *hot forging, process design, die life, die temperature, wear, CAE, lubrication, cooling, heat transmission coefficient, prediction formula*

1. Introduction

Forgings for strength parts of automobiles are produced in large quantities through hot forging. Reducing die costs by improving die life is important to achieve overall cost reduction. Conventionally, measures for improving forging die life have consisted of adjusting forging conditions and improving die materials at the production preparation stage on a trial-and-error basis. This revise-and-repeat method requires substantial amounts of manpower. For this reason, it became necessary to evaluate die life from the design stage taking mass-production capability into consideration. Although other companies are also studying methods to predict die life through the use of Computer-Aided Engineering (CAE), a practical technique has yet to appear. For this reason, the authors have developed a technology for predicting life by wear [1][2] that can be utilized in process design (**Fig. 1**), and that can be applied to all hot-forged parts.

This article describes the actions that were performed in order to put this prediction technology into practical use. These actions include the quantification of lubricant spray characteristics, which affect die temperature, and improvements to the wear prediction formula through the use of multivariate analysis.

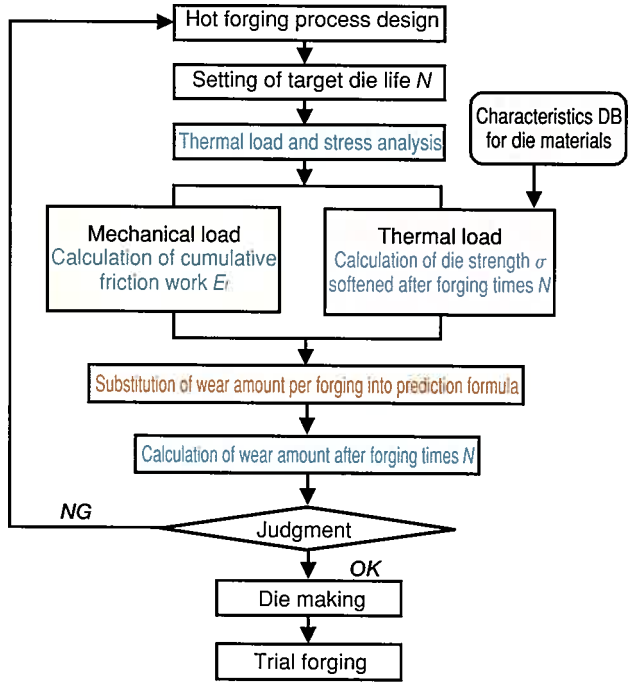

Fig. 1 Flow of Die Life Prediction

* Forging and Stamping Production Engineering Div.
** Toyota Central R&D Labs., Inc.

2. Field Investigation of Lubricant Spraying Characteristics

Fig. 2 shows an example of a hot forging process. The blank is heated to approximately 1200°C and then forged in the die. A transport device carries the forged blank to the next process, while the next blank to be forged is set in the die. While this occurs, lubricant is applied to the die to promote the release and slide of the blank from the die, to prevent seizure, and to prevent wear associated with cooling. At the production site for hot-forged parts, thousands or tens of thousands of blanks are forged with the same die. Consequently, it is often the case that service life is reached by the die becoming worn and deformed up to the point where forging tolerances can no longer be maintained.

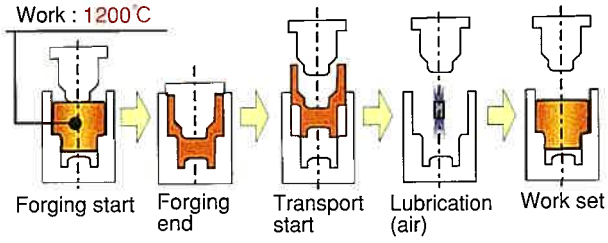

Fig. 2 One Cycle of Forging Process

Fig. 3 shows the factors that affect die wear. Previously, the accuracy in predicting mechanical loads was improved dramatically by gathering data from the production site, such as the shape of actual forgings and load measurements, and then comparing them to results obtained through CAE analysis. **Fig. 3** shows the calculation of thermal load. Here, changes in die temperature that are associated with repeated forging are calculated as a parameter λ, [3] in order to calculate the softening hardness of the die. The diagram indicates that the lubricant spraying conditions affect die wear. However, the present state of production in the field is such that lubricant spraying conditions vary by equipment or part, and that the cooling power of a die is not quantified according to differences in spraying conditions.

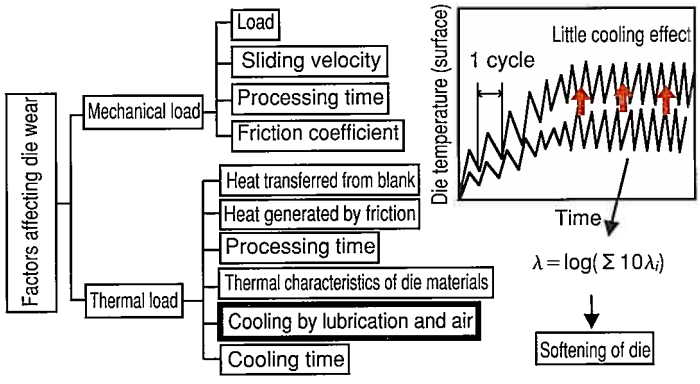

Fig. 3 Factors Affecting Die Wear

In this development, an investigation was carried out to determine the relationship between cooling power and die wear in accordance with the differences in lubricant spraying conditions. The investigation used a horizontal high-speed forging machine that produces axisymmetric rounded parts (**Fig. 4**) and a vertical forging machine that produces anomalous angular parts. On the horizontal high-speed forging machine, the lubricant is sprayed with a water flow, as shown in **Fig. 5**. During forging, lubricant is sprayed continuously without stopping and without performing an air spray. Moreover, this type of forging machine operates at high speeds of 60 to 80 cycles per minute. The vertical forging machine applies lubricant in a spray state, and an air spray is also performed after the lubricant has been applied, in order to enhance the lubrication effect. Although the forming speed of this machine during forging is 65 cycles per minute, the actual production speed is 30 cycles per minute because the forging machine stops at top dead center during lubrication and air spraying. Die cooling power was evaluated by measuring the internal die temperature at locations exhibiting severe wear (see **Fig. 6**), and then measuring the hardness and the wear amount of the dies after reaching service life. To measure the internal die temperature, a hole was drilled from the back of the die through which a thermocouple was inserted. This enabled the temperature to be measured at a position 1 mm from the die surface. Furthermore, the mechanical loads were compared by calculating the cumulative friction work (see **Fig. 1**) using CAE analysis. The cumulative friction work is expressed by equation 1.

$$E_f = \int \mu p v dt \qquad (1)$$

where μ is the friction coefficient, p is the forming surface pressure, v is the relative sliding velocity between the blank and the die, and t is the processing time.

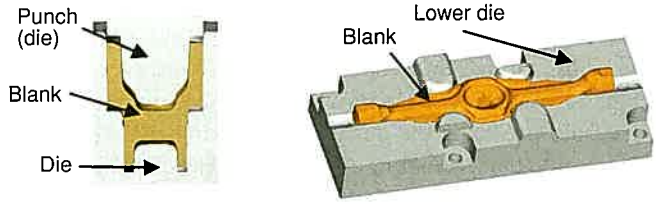

Fig. 4 Parts for Improving Die Life

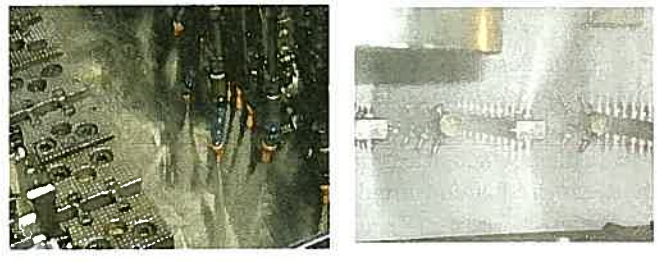

Fig. 5 Differences in Lubricant Spraying Conditions by Equipment Type

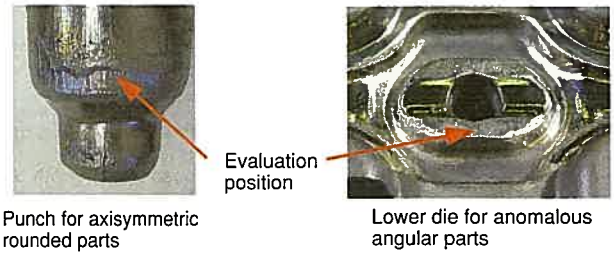

Fig. 6 Evaluation Positions of Object Dies

Fig. 7 shows the trends for the temperatures measured 1 mm from the die surface. The differences in time period widths indicate the different cycle times. Axisymmetric rounded parts exhibited variations in the state of the lubricant spray in the circumferential direction. Therefore, a comparison was made between locations sprayed with large and small amounts of lubricant. **Fig. 8** shows the hardness distribution inside the die. It was confirmed that softening occurred in the vicinity of the die surface in the location of the die used for axisymmetric rounded parts where only a small amount of lubricant was sprayed, as well as in the die for anomalous angular parts. This softening corresponded to the extent of the internal die temperature. The location of the die used for axisymmetric rounded parts where a large amount of lubricant was sprayed showed a low increase in die temperature, and it was confirmed that die softening was suppressed.

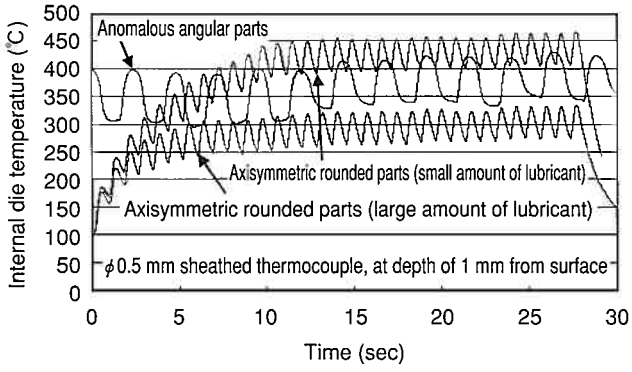

Fig. 7 Differences in Die Temperature Trends

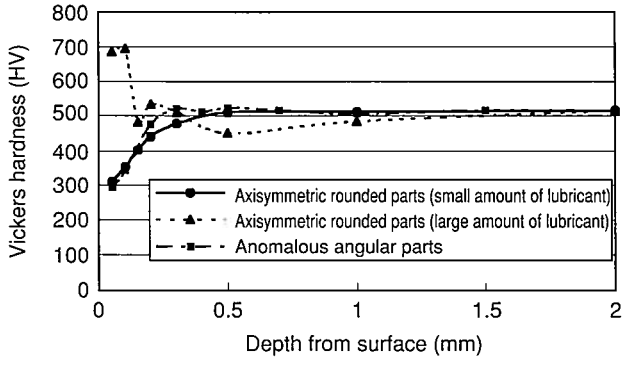

Fig. 8 Differences in Die Hardness

Fig. 9 shows the trends for die wear amount. It shows that wear advances faster in the dies for axisymmetric rounded parts than in those for anomalous angular parts. **Fig. 10** shows the results of a comparison of the cumulative friction work based on CAE analysis. The calculations were made with Coulomb friction coefficients of 0.1 and 0.3, in consideration of the changes in the friction coefficient that occur depending on the lubricant characteristics. It was confirmed the cumulative friction work in dies for anomalous angular parts is smaller, regardless of the friction coefficient. Although dies for anomalous angular parts bear a greater thermal load, it is believed that wear advances only gradually because of the small cumulative friction work. In contrast, in the case of dies for axisymmetric rounded parts, the wear in some locations was already advanced at an early stage of forging. This is believed to be due to an increase in the cumulative friction work, caused by severe blank deformation and a higher friction coefficient. This is despite the fact that the rise in the die temperature is suppressed to a certain extent by the large amount of lubricant that is sprayed.

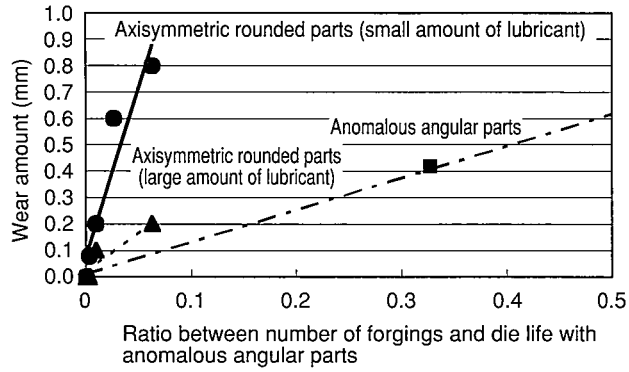

Fig. 9 Differences in Die Wear Amounts

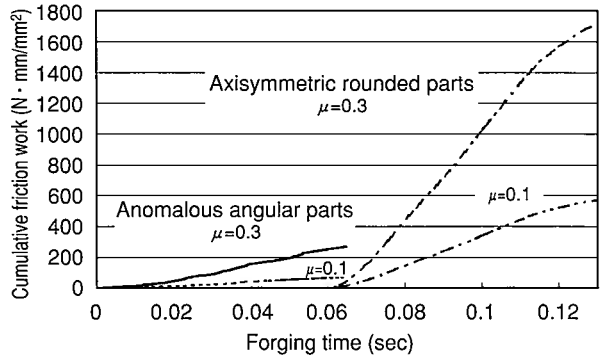

Fig. 10 Differences in Cumulative Friction Work

Based on the results described above, it is thought that the important factors for predicting the wear amount are precise predictions of the die temperature during continuous forging, as well as the prediction of mechanical loads. It is necessary, therefore, to quantify the cooling conditions of the forging die in accordance with the differences in the lubricant spraying conditions.

3. Quantifying Water Flow Cooling Conditions

Fig. 11 shows the necessary parameters for CAE analysis of the forging die cooling process. Among these parameters, however, the value for the heat transfer coefficient of the interface between the die and the coolant was unclear, since the literature contains a number of possibilities. The heat transfer coefficient is therefore expressed by equation 2.

$$hc=ql(T_w-T_o) \qquad (2)$$

where q is the heat flux, Tw is the die temperature at the interface, and To is the coolant temperature. As hc increases, it becomes more likely that the heat will be absorbed, causing the die temperature to decrease.

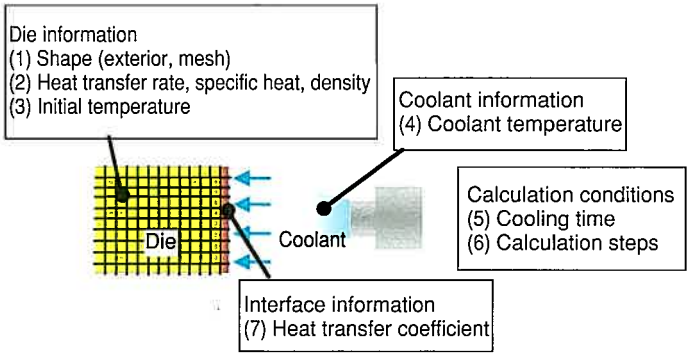

Fig. 11 Required Parameters for Analyzing Cooling Process

To quantify the heat transfer coefficient, a test device was created, which models the lubrication equipment used in mass production forging. Data was then collected in a cooling model test as shown in **Fig. 12**. Thermal conductivity and heat transfer were calculated by changing the heat transfer coefficient hc using CAE analysis. This analysis enabled the heat transfer coefficient under various cooling conditions to be rendered numerically by obtaining the temperature after 1 second of cooling at a depth of 0.5 mm from the surface, and comparing it to the actual measurement data (**Fig. 13**).

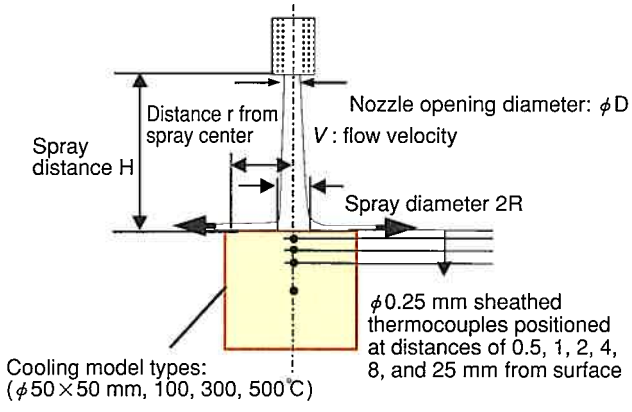

Fig. 12 Water Flow Cooling Model Test

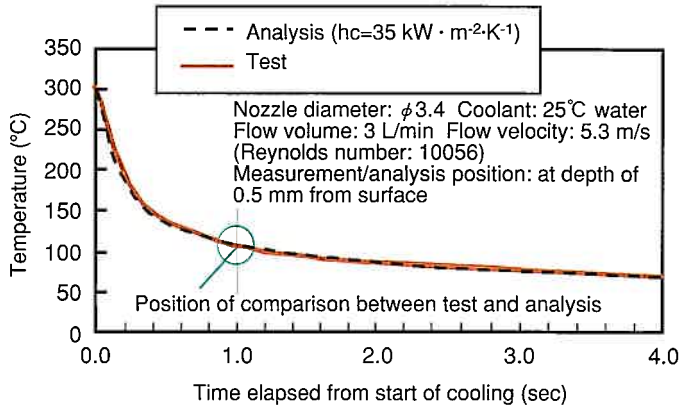

Fig. 13 Method of Identifying Heat Transfer Coefficient *hc*

Fig. 14 shows the results after ordering of the lubricant spraying conditions and the heat transfer coefficient. It was found that it is possible to simplify the heat transfer coefficient by using the Reynolds number, which represents the severity of a flow in fluid dynamics. The Reynolds number Re is expressed by equation 3.

$$Re=D \cdot V/v \qquad (3)$$

where D is the lubricant nozzle opening diameter, V is the lubricant nozzle outlet flow velocity, and v is the dynamic viscosity in which the temperature dependence of the fluid is taken into account. Other tests that were conducted by changing the die temperature, the type of lubricant, and the lubricant temperature, also indicated that it is possible to simplify the heat transfer coefficient by using the Reynolds number.

4. Quantifying Spray Cooling Conditions

As shown in **Fig. 5**, the methods for spraying lubricant in forging machines are broadly divided into two types: water flow, and spray. With the water flow type, heat is removed by the flow of the lubricant. With the spray type, however, the lubricant removes the heat by evaporation rather than flow. Therefore, the test device shown in **Fig. 15** was used to collect cooling power data based on the spray type.

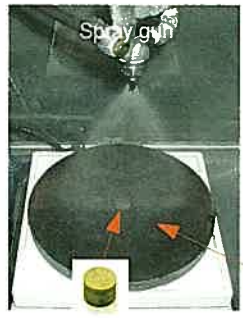

Lubricant: white lubricant
Water dilution factor (by volume): 15 times
Spray mist density ρs:
0.03, 0.1, 0.3, 0.5 cc · s-1 · cm-2
Spray pressure Ps: 0.5~1.4 kPa
Spray time: 0.5 sec
Die temperature: 150℃ to 400℃

Hot plate φ240×20 mm
(material : SKD61)

Measured die φ20×20 mm

Fig. 15 Spray Cooling Model Test

Conditions close to those in actual production were reproduced in the test. The test consisted of measuring the lubricant spraying conditions on a vertical forging machine and then modeling three conditions: spray mist density, spray pressure, and internal die temperature. Like the water flow type, the cooling power was quantified using the heat transfer coefficient *hc*, based on the changes in the internal temperature of the measured die and the results of CAE analysis.

Fig. 16 shows the effect of the spray mist density on the heat transfer coefficient. The higher the spray mist density, the greater the heat transfer coefficient becomes, and the maximum value is seen in the test die temperature range. Moreover, the heat transfer coefficient changes greatly according to the die temperature at spray mist densities below $\rho s=0.3 cc \cdot s^{-1} \cdot cm^{-2}$.

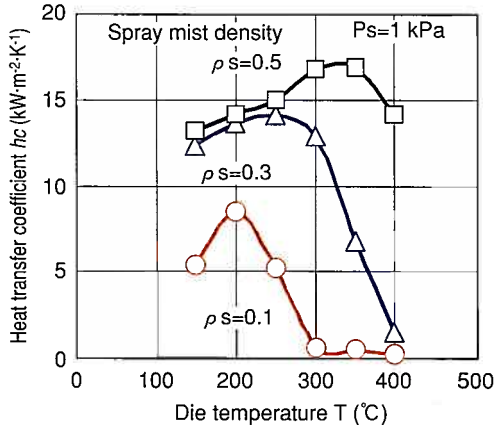

Fig. 16 Relationship Between Spray Mist Density and Heat Transfer Coefficient

Fig. 17 shows the effect of the spray pressure on the heat transfer coefficient. At a given spray mist density, the heat transfer coefficient trend increases slightly as the spray pressure rises, provided that the die temperature is below 300°C. In this way, the relationship between the spray cooling conditions and cooling power has been clearly quantified.

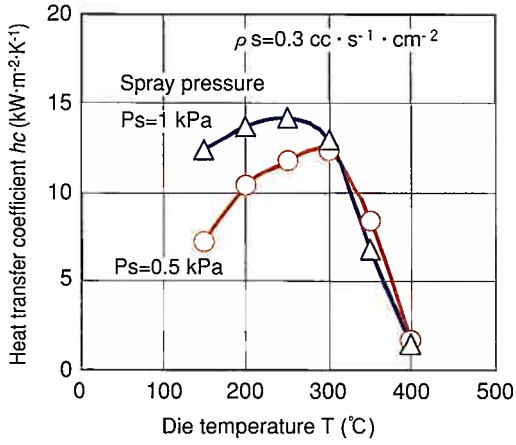

Fig. 17 Relationship Between Spray Pressure and Heat Transfer Coefficient

5. Continuous Temperature Analysis System

The database of the heat transfer coefficients created for this development was used to calculate the die temperature during continuous forging operations. However, calculation of blank deformation in thermal load and stress analysis requires an enormous amount of time to perform continuously, due to the considerable quantity of deformation analysis accompanying remeshing and remapping. For this reason, the CAE analysis system shown in **Fig. 18** was created. In this system, blank deformation analysis is performed only during the first cycle, after which only temperature analysis is performed in the subsequent repetitions. Using this analysis system has reduced calculation time by more than 50%.

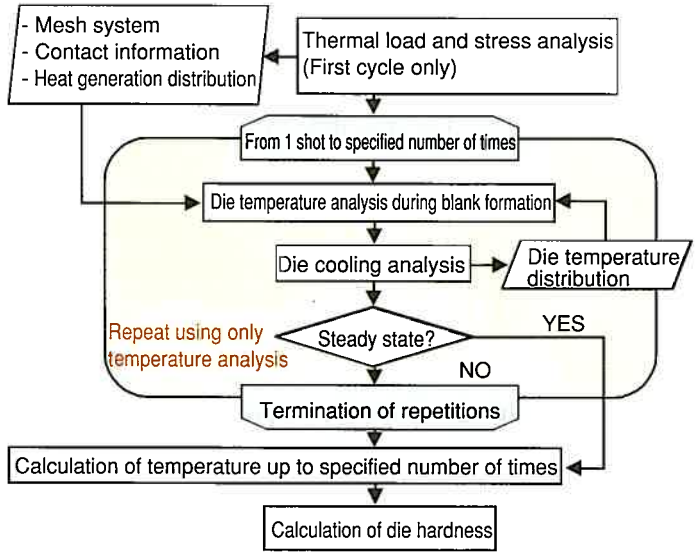

Fig. 18 Flow of Continuous Temperature Analysis System

Fig. 19 shows a comparison of actual die temperature measured at a distance of 1 mm inward of the die surface with die temperature obtained through CAE analysis. A complete match was not obtained due to a measurement response error that occurs in the actual temperature measurement. However, the trends for temperature increase are virtually the same.

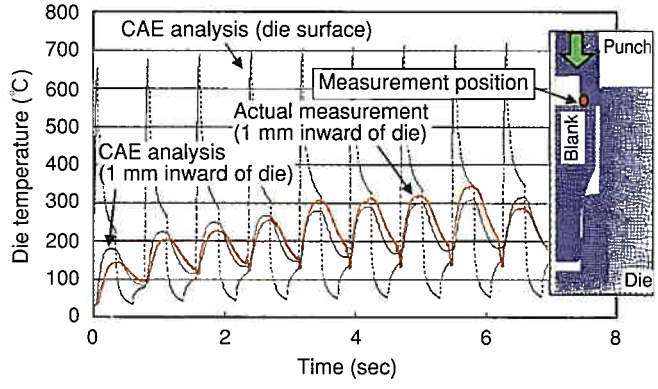

Fig. 19 Comparison of Die Temperature Trends

6. Improving Wear Prediction Formula Through Multivariate Analysis

In the die life prediction flow shown in **Fig. 1**, CAE analysis is used to calculate the mechanical and thermal loads that act on the die, which are then substituted into equation 4 in order to calculate the wear amount w per forging.

$$w=C\cdot (Ef)^{a}/(\sigma)^{b} \quad (4)$$

where Ef is the cumulative friction work (mechanical load), and σ is the strength of the softened die (thermal load). Constants C, a, and b are obtained from the actual wear amount measurement and through utilization of multivariate analysis. The wear amount for the number of forgings is calculated by integrating the wear amount w per forging. In this development, data for five parts and 36 patterns of axisymmetric rounded parts were used for the purpose of improving the accuracy of the wear prediction formula. The data differed depending on the die materials, die surface treatment, location, and forging count, even with similarly shaped parts. This necessitated the classification of die characteristics. Therefore, principal component analysis was performed using data on the actual wear amount, the cumulative friction work, and the strength of the softened die. **Fig. 20** shows the results of this analysis. Because the characteristics are classified in accordance with the die surface treatment, a wear prediction formula was created for each classification. **Fig. 21** shows the proportions of die loads for each surface treatment obtained from these friction prediction formulae. It is believed that the wear amount of a die where no surface treatment is performed is more easily affected by mechanical load than thermal load. Conversely, it is believed that the wear amount of a die after surface treatment is more easily affected by thermal load than mechanical load.

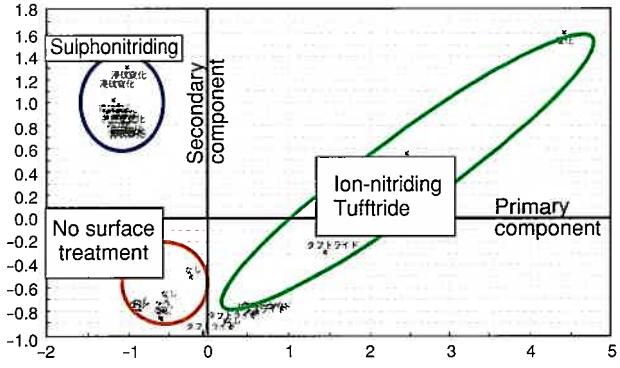

Fig. 20 Classification by Surface Treatment (Results of Principal Component Analysis)

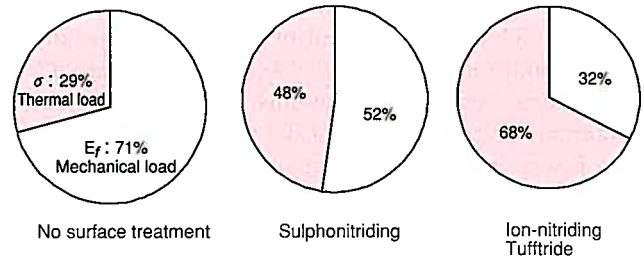

Fig. 21 Proportion of Die Load by Surface Treatment

Fig. 22 shows verification results for the created wear prediction formulae. It shows a comparison between prediction values and actual measurement values for increases in wear amount, in accordance with the number of forgings for each of the three parts. The prediction error for the wear amount at the final forging was approximately 10%.

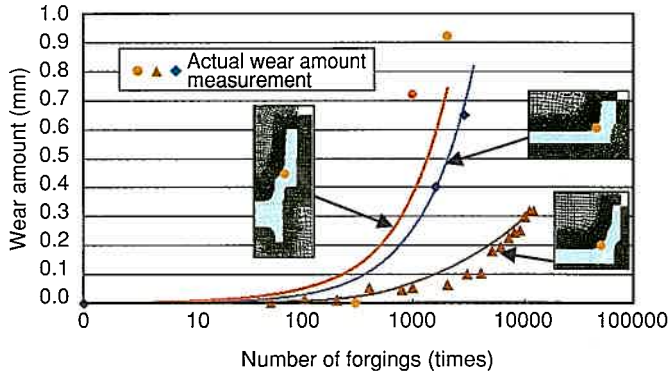

Fig. 22 Comparison Between Prediction and Actual Measurement of Wear Amount

Future intentions include further improving the prediction accuracy during forging by clarifying the mechanisms of surface treatment peeling and elimination, and then incorporating these phenomena into the prediction technology.

7. Conclusion

Lubricant spray characteristics that affect die temperature were clarified and the accuracy of wear prediction formulae were improved, in order to put die life prediction technology into practical use and improve the life of hot forging dies. In the future, it is planned to use this technology for designing dies for axisymmetric rounded parts as well as for anomalous angular parts.

This article is the result of a development project carried out jointly with the Materials Department, Advanced Metal Laboratory of Toyota Central R&D Labs., Inc. The authors wish to express their gratitude for the cooperation of all the people associated with this project.

References

(1) Suzuki et al. *Toyota Technical Review* Vol. 52 No. 2 (2003) pp. 80-85.
(2) Tanaka et al. *The Proceedings of the 52nd Japanese Joint Conference for the Technology of Plasticity* (2001) pp. 259-260.
(3) Inoue. *Iron and Steel* Vol. 66 No. 10 (1980) p. 74.

Authors


A. WATANABE


T. SUZUKI


K. NAKANISHI


T. TANAKA


M. SAWAMURA


Y. YOGO

Analysis of Solder Joint Breakdown Life in Electronic Devices Mounted in Cars

Kazuhiro Igarashi*
Kimimasa Murayama*
Takashi Nakanishi**
Qiang Yu***
Masaki Shiratori***

Abstract
The spread of automotive electronics has progressed to the stage where cars are now installed with a large amount of electronic equipment, in which electronic devices are mounted on printed circuit boards using solder. Since automotive electronic equipment is exposed to a harsh use environment and requires a high degree of reliability, evaluation of solder joint life is of the utmost importance. Analyzing solder life using the Finite Element Method (FEM) allows many design factors to be investigated in a short period of time, thereby enabling the performance of highly reliable design. However, conventional methods of solder life analysis can only predict the generation of initial cracks and are therefore unable to reproduce product function breakdown caused by actual joint fracture. As a result, use of these methods is limited to the research field. This article describes a practical method of solder breakdown life analysis that combines prediction of crack initiation and crack propagation to enable prediction of the number of cycles to total fracture of solder joints.

Keywords: *solder joint, fatigue life, crack propagation, breakdown life, FEM, simulation*

1. Introduction

1.1 Background

In recent years, the use of automotive electronics has continued to spread. Vehicles are now installed with a large amount of electronic equipment, in which electronic devices are mounted on wiring boards using solder to form electrical circuits (**Fig. 1**).

In most items of electronic equipment, the coefficients of linear thermal expansion of the electronic devices and the wiring board are different. As a result, changes in environmental temperature produce thermal stress, generating large amounts of strain in the softest solder joints. Repeated application of strain leads to the initiation of cracks that, if allowed to propagate, may eventually lead to breakdown of the joint (**Fig. 2**).

Automotive electronic equipment is exposed to a use environment that has harsher changes in temperature than household electronic goods, and must also be highly reliable from the standpoint of safety. For these reasons, evaluation of solder joint life is of the utmost importance.

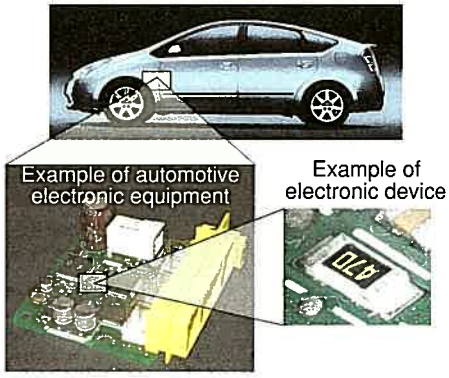

Fig. 1 Automotive Electronic Equipment and Electronic Devices

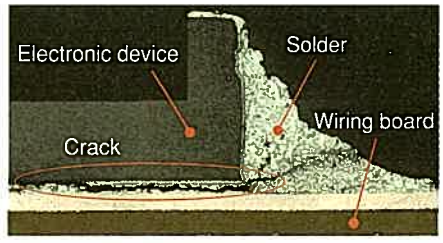

Fig. 2 Solder Joint Crack

1.2 Method of evaluating solder joints

The thermal fatigue life of solder joints is generally evaluated by thermal cycle tests. [1] The electronic unit is placed inside a tester and exposed to thermal loads by repeatedly altering the ambient temperature to low and high levels (**Fig. 3**). The unit is removed at the end of a predetermined number of thermal cycles

* Electronic Components Engineering Div.
** Electronics Engineering Div. 1
*** Yokohama National University

and subjected to function checks and cross section examinations of the solder. Adjusting the temperature conditions and the number of cycles of the test enables the unit to be assessed under the temperature ranges found in various regions around the world, and in consideration of differences in usage conditions and installation positions. Thermal cycle tests provide highly consistent results since environments close to actual usage conditions can be simulated, but overall effectiveness of these tests is hindered by the extremely long testing period and the fact that only a small amount of data can be collected.

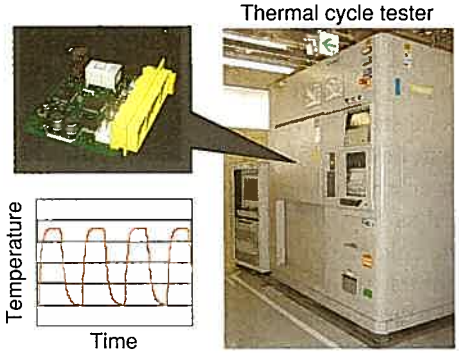

Fig. 3 Thermal Cycle Test

1.3 Solder life analysis using FEM

Analyzing solder life using the Finite Element Method (FEM) allows many design factors to be examined in a short period of time. FEM analysis permits the visualization of stress, strain and other factors affecting the solder, thereby enabling larger amounts of data to be obtained. As a result, FEM enables highly reliable design to be performed by allowing feedback to be applied to designs at the product development stage and aiding understanding of the causes and mechanisms of solder degradation.

However, conventional methods of solder life analysis can only predict the generation of initial cracks and are therefore unable to reproduce product function failures due to actual joint breakdown. As a result, use of these methods is restricted to the research field. This article describes the development of a practical method of solder life analysis that combines prediction of crack initiation with crack propagation analysis to enable prediction of the number of cycles to total breakdown of solder joints.

2. Method of Analysis [2]

2.1 Definition of crack initiation

The size of the solder crystals used in this study was between 10 μm and several tens of μm. Crack initiation was defined as the point when the initial crack length reaches 50 μm, which may be assumed to be the length of 2 to 3 crystals (**Fig. 4**). Crack initiation and propagation was analyzed based on this definition.

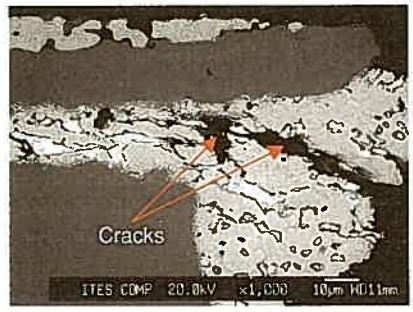

Fig. 4 SEM Image of Solder Cracks

2.2 Prediction of crack initiation

The fatigue life of solder joints correlates with the inelastic strain amplitude close to the points where strain concentrates, and can be understood in accordance with the Manson-Coffin law. Equation 1, which was calculated from the results obtained from a large number of tests, was used in this study to calculate the number of cycles to crack initiation from the inelastic strain amplitude.

$$N_f = 1000^*(\Delta \varepsilon_{in}/0.01)^{-2} \quad (1)$$

where,

N_f: number of cycles to crack initiation

$\Delta \varepsilon_{in}$: inelastic strain amplitude

Inelastic strain is calculated as the sum of the creep strain and the plastic strain. The inelastic strain amplitude in thermal cycle tests is defined as the mean change in the cumulative values of inelastic strain when the ambient temperature is switched from low to high and vice-versa, respectively (**Fig. 5**).

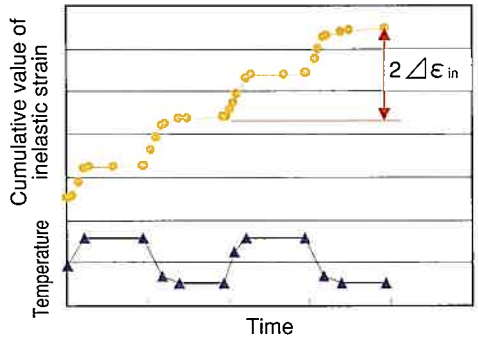

Fig. 5 Definition of Inelastic Strain Amplitude

2.3 Crack propagation and breakdown prediction

A fatigue fracture in a solder joint leads to eventual breakdown after passing through localized crack initiation and crack propagation stages. Damage is accumulated in accordance with the strain in each portion in each stage. This damage rate may be evaluated quantitatively by the law of cumulative linear damage as expressed by equation 2.

$$\eta = \sum_{i=1}^{n} \frac{N_i}{N_{fi}} \qquad (2)$$

where,

η: damage rate
Ni: number of strain cycles
Nfi: fatigue life under single load

When the damage rate becomes 1.0, the solder reaches fatigue life and a crack is initiated.

In this study, crack initiation was defined as the point when the crack length reaches 50 μm, and crack propagation was also expressed in units of 50 μm. An analysis model was used to create further models depicting cracks in the solder joint at 50 μm intervals, and the inelastic strain amplitude and fatigue life were calculated for each model. The number of cycles to crack propagation was obtained by calculating the number of cycles required for the damage rate of the tip of the crack to reach 1.0.

Figs. 6 and **7** show representative diagrams of the calculations. **Fig. 6** is a representative diagram of fatigue life calculation. The fatigue life was calculated using the mean inelastic strain amplitude of the solder joint in each 50 μm region. It was confirmed that strain decreased and fatigue life increased the larger the distance from the surface of the solder.

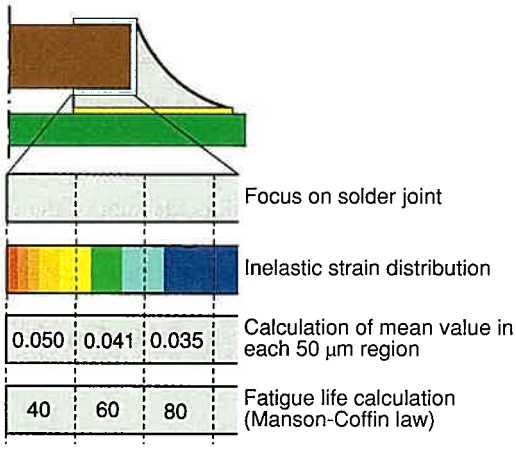

Fig. 6 Representative Diagram of Fatigue Life Calculation

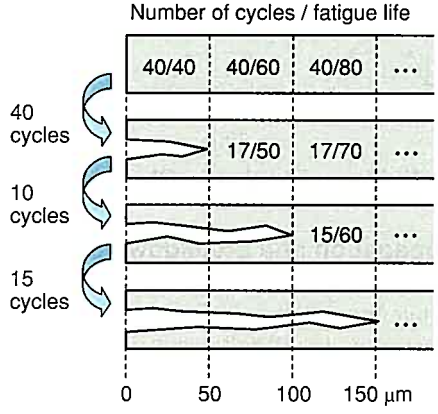

Fig. 7 Representative Diagram of Law of Cumulative Linear Damage

Fig. 7 is a representative diagram of the law of cumulative linear damage. The top line shows the initial state of the solder. The following lines show the state of crack propagation every 50 μm. The figures show the degree of damage in each 50 μm region of the solder, indicated by number of cycles/fatigue life.

The initial state shows absolutely no damage at the crack tip (the 0 to 50 μm region). This indicates that the crack is initiated when the number of strain cycles reaches 40 for a fatigue life of 40 cycles. In the subsequent 50 to 100 μm region, damage is accumulated at a rate of 40/60. In the next range, the damage rate accumulation is 40/80.

In the second step shown on the second level from the top, the crack tip reaches the 50 to 100 μm region. In the model containing a crack propagated to 50 μm, the fatigue life cycles are calculated as 50 and 70 from the tip using the same method of fatigue life calculation as shown in **Fig. 6**. Since the damage rate of the crack tip in the previous step was 40/60 and the fatigue life in the current step is 50 cycles, N_2 (the number of cycles to crack propagation) is calculated to be N_2=17, using $40/60+N_2/50=1$. Assuming the same damage accumulation in step 3, $40/80+17/70+N_3/60=1$ shows that N_3=15.

The number of cycles that the crack takes to progress 50 μm intervals can be calculated for each step by repeating this calculation. As a result, it is possible to predict crack propagation and breakdown life.

3. Conditions of Analysis

3.1 Parts under analysis

Many types of electronic devices are mounted in automotive electronic equipment. In this study, chip resistance, a large number of which are provided in such equipment, and which has a generally short life, was selected for analysis (**Fig. 8**). The electrodes at both ends of chip resistance are joined to the board using solder. The analysis model was a 1/4 symmetry analysis model with two planes of symmetry and one point of constraint located at the upper surface of the circuit board.

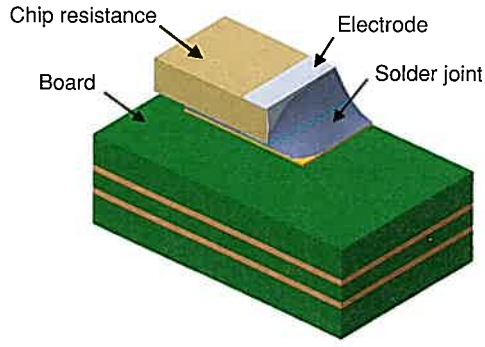

Fig. 8 Analysis Model (Chip Resistance)

3.2 Conditions

An SnPb eutectic solder was emulated as the solder material, and provided with creep properties and a yield stress that take the respective temperature dependencies into consideration. Creep properties were defined based on Norton's law (equation 3).

$$\dot{\varepsilon}_c = A\,\sigma^n \qquad (3)$$

where,

$\dot{\varepsilon}_c$: creep strain rate
σ: stress
A, n: material constant

A temperature profile that recreated a thermal cycle test was used for the temperature conditions. Analysis was performed utilizing the finite element method general-purpose ABAQUS software.

4. Analysis Results

4.1 Prediction of crack initiation

Fig. 9 shows the inelastic strain amplitude distribution for one thermal load cycle with regard to the solder joint of the chip resistance. In addition, **Table 1** shows the predicted results for crack initiation fatigue life for solder portions A, B, and C in **Fig. 9**. These results were calculated using the Manson-Coffin law after the mean inelastic strain amplitude was obtained for the 50 μm depth range in the direction of crack propagation.

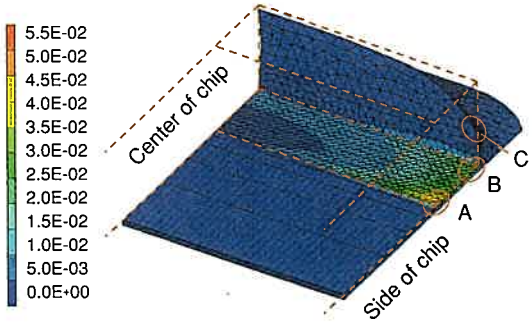

Fig. 9 Inelastic Strain Amplitude Distribution (Initial)

Table 1 Calculation Results for Number of Cycles to Crack Initiation

	A	B	C
$\Delta\varepsilon_{in}$	4.96E-02	2.53E-02	1.37E-03
N_f	41	156	53279

Fig. 9 and **Table 1** indicate that the portion in which the crack initiates is corner A, which is located in the solder layer under the electrode at the side of the chip. The data also shows that the predicted number of cycles to crack initiation is 41. The solder layer under the electrode that is exposed to the difference in thermal elasticity between the chip and the board is extremely thin. This leads to an increase in shear strain, and it is believed that crack initiation occurs in this layer first.

4.2 Direction of crack propagation

The location of crack initiation can be predicted from the location of strain concentration, but the direction of crack propagation must be predicted before crack propagation itself can be analyzed. Since, in this model, the location of crack initiation is the thin solder layer under the electrode, crack propagation can only occur within a flat plane. It is therefore possible to predict the direction of propagation by looking at the strain amplitude distribution (**Fig. 10**).

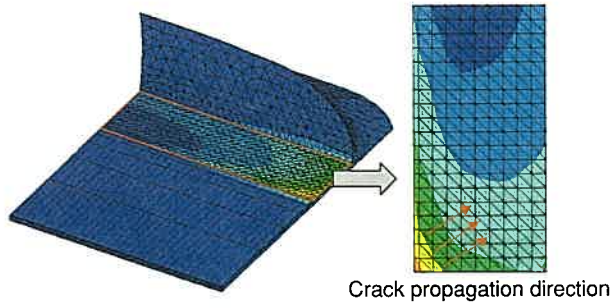

Fig. 10 Prediction of Crack Propagation Direction

However, since the crack will reach a fillet portion once a certain amount of propagation occurs, it is imperative that the direction of propagation be predicted three-dimensionally. Currently, however, three-dimensional prediction of the propagation direction is extremely difficult using only the results of analysis. Therefore, as shown in **Fig. 11**, the face of the crack propagation path was assumed based on the results of cross sectional observation of a solder portion after a thermal cycle test. The results of this test showed that crack propagation is limited to within the face, thereby allowing the direction of crack propagation to be predicted from the inelastic strain amplitude distribution.

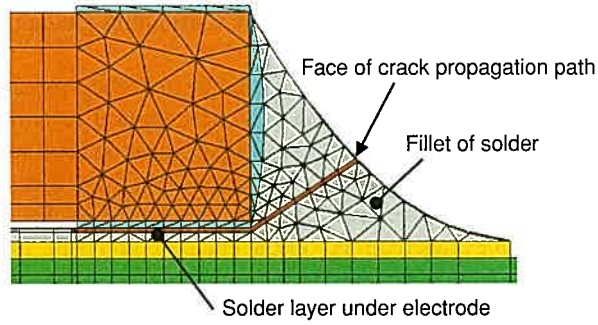

Fig. 11 Face of Crack Propagation Path

4.3 Crack propagation and prediction of breakdown life

The inelastic strain amplitude distribution was obtained by thermal stress analysis, and used to predict the direction of crack propagation. A model was then created in which a crack was propagated by 50 μm in the propagation direction, and the thermal stress analysis was performed again. This was repeated until breakdown of the solder joint was reached.

Fig. 12 shows the inelastic strain distribution of the crack propagation process. The red portion, which shows the area with the greatest inelastic strain distribution, indicates the tip of the crack. The orange, yellow and green portions close to the crack show areas where relatively large amounts of strain are generated. The strain in the regions through which the crack has already propagated (shaded in black) and the regions separated from the crack is extremely low.

Fig. 12 shows that the crack propagates simultaneously inward from the side surface of the solder layer under the electrode and toward the fillet portion. It also shows that the strain at the fillet portion is lower than the solder layer under the electrode, allowing a slower rate of crack propagation to be predicted.

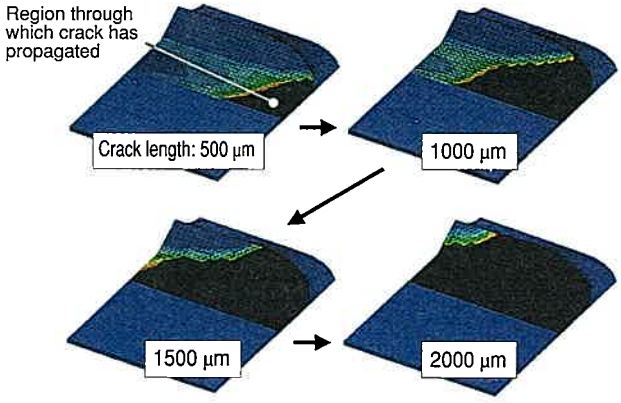

Fig. 12 Appearance of Crack Propagation

Fig. 13 shows a graph of the inelastic strain amplitude distribution for each rate of crack propagation. Each line shows a single analysis result. The graph shows that the largest strain is located in the solder at the crack tip, and that the strain becomes smaller the further away the solder is from the tip. The graph also shows that the overall strain distribution gradually reduces as the crack propagates.

Based on the inelastic strain amplitude data in each 50 μm region, the Manson-Coffin law was applied to calculate the fatigue life, and the law of cumulative linear damage was applied to calculate the number of cycles required for the damage rate of the crack tip to become 1.0. This number of cycles equals the number of cycles required for the crack to propagate 50 μm.

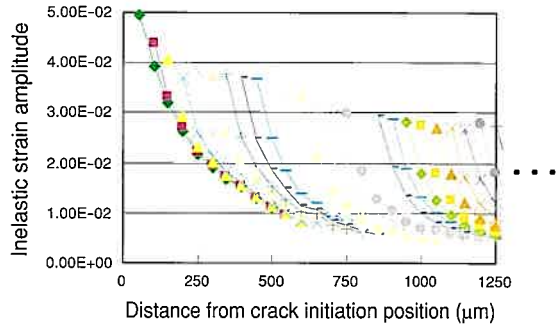

Fig. 13 Strain Distribution for Each Rate of Crack Propagation

Fig. 14 is a graph showing a comparison between prediction results and test results, after calculation of the relationship of the number of cycles of the thermal load and the crack length from crack initiation to breakdown. The test results use a sample consisting of a certain number of cycles extracted from a thermal cycle test, in which a solder crack was verified in a cross section close to the side surface and a section in the center (**Fig. 15**).

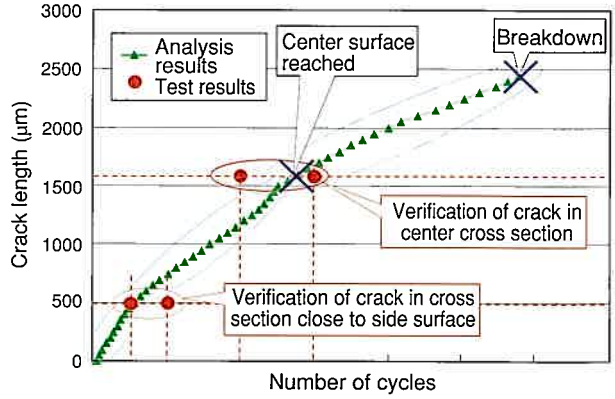

Fig. 14 Comparison of Analysis and Test Results

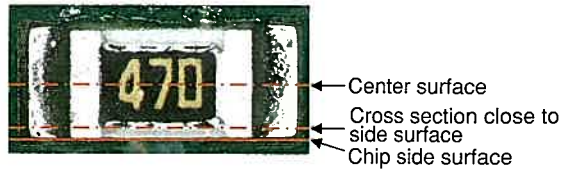

Fig. 15 Cross Section Observance Positions

When the results of the prediction for crack propagation and the test results were compared, it was found that the number of cycles required for the crack to reach the cross section close to the side surface and the chip center were virtually the same, indicating that the prediction and the test results were consistent.

The following results were also found. In the initial period when the crack was short, the rate of crack propagation was high because of the large joint length and the high amount of strain.

Subsequently, the rate of crack propagation slowed as the length of the crack grew, slowing further when the crack reached the fillet portion.

5. Solder Life Factor Analysis

5.1 Clarification of factors

Reducing the inelastic strain of the solder is necessary for improving solder life. The key factors were clarified using a technique that combined solder life analysis with a statistical method.

The factors affecting the inelastic strain amplitude of solder were specified using the relation drawing shown in **Fig. 16**. Inelastic strain amplitude is caused by thermal stress, and it can be categorized into effects that depend on physical and form-based properties. Six factors related to physical properties and four factors related to form-based properties were clarified. The six physical properties were the Young's modulus and the coefficients of linear thermal expansion of the solder, the chip part and the board. The four form-based properties were the height of the solder below the chip part, the solder length, the protrusion length of the land, and the thickness of the printing tool (**Fig. 17**).

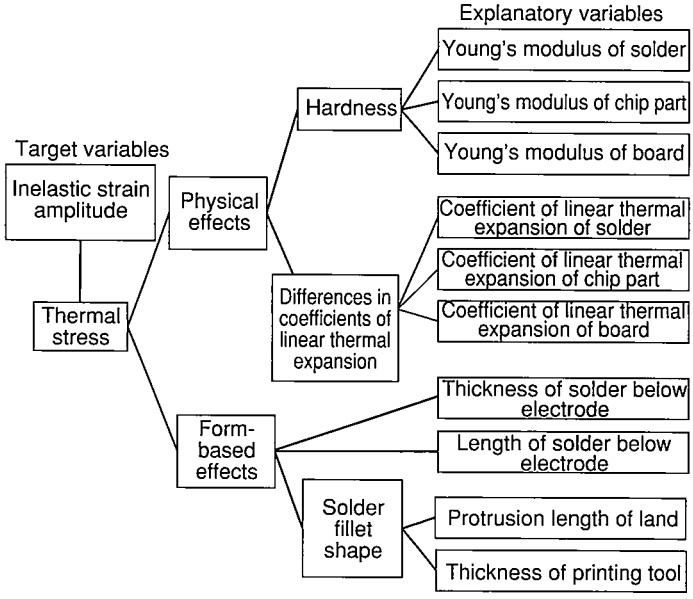

Fig. 16 Clarification of Factors

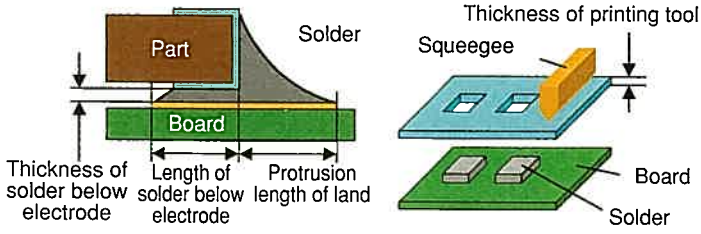

Fig. 17 Form-Based Factors

5.2 Analysis of contribution rate of factors

A simulation plan was formed in order to analyze the contribution rate of the factors by means of a screening design of experiments (DoE) utilizing the tolerances of the ten factors described in Section 5.1 as upper and lower limit values. Fig. 18 is a representative diagram of the distribution of this plan (fractional factorial resolution III). The black circles show the values of the implemented factors. Solder life analysis was performed based on this plan.

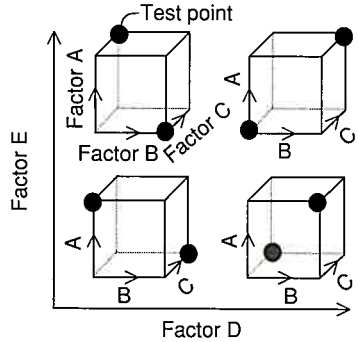

(Distribution diagram for five factors)

Fig. 18 Distribution Diagram of Test Plan

The contribution rate of the factors was calculated by performing the screening DoE with the inelastic strain amplitude obtained from solder life analysis as the parameter (**Fig. 19**). It was found that the factors with the largest contribution rate were the coefficients of linear thermal expansion of the board and the chip part, and the height of the solder below the chip part. Furthermore, a high value (0.923) was obtained for the square of the correlation coefficient, R^2.

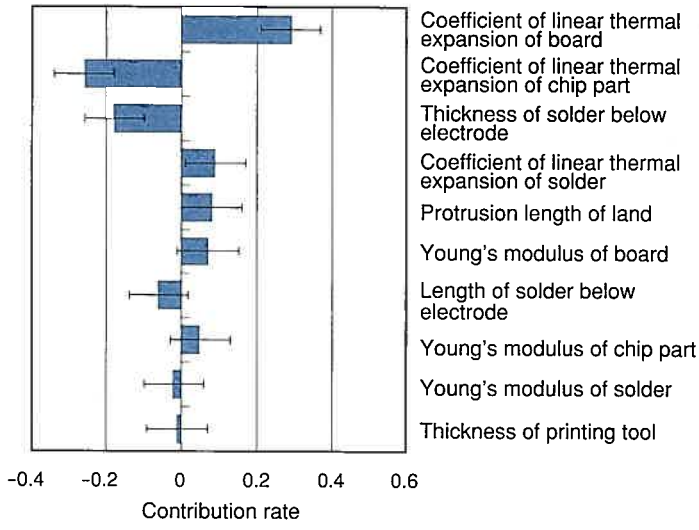

Fig. 19 Contribution Rate of Factors Affecting Solder Life

6. Conclusions

The chip resistance of an automotive electronic device was examined by focusing on the inelastic strain amplitude of the solder joint. The number of cycles required for complete breakdown of the solder joint was calculated using the Manson-Coffin law and the law of cumulative linear damage. The consistency of these calculations was then verified by comparison to test results. In addition, factor analysis of solder life enabled the factors with the greatest contribution rate to be specified.

In-house breakdown life analysis of solder joints has been performed for a large number of cases, and the consistency of the analysis with tests has been verified. As a result, this method has already been put into practical use. It is believed that applying this solder life analysis method from the development stage of an even greater number of products in the future will prove a useful way to improve reliability and shorten development times.

Finally, the authors would like to offer their sincere gratitude for the valuable cooperation of all the staff at Yokohama National University who contributed to this research.

References

(1) JSME. "JSME Mechanical Engineers' Handbook, Fundamentals, A4: Strength of Materials." *Maruzen Co., Ltd.* (1984) pp. 146-147.

(2) Y. Qiang et al. "Evaluation for Thermal Fatigue Life of Electronic Device Solder Joints Utilizing Car." *The 16th Computational Mechanics Conference of JSME* No. 03-26 (2003) pp. 699-700.

Authors


K. IGARASHI


K. MURAYAMA


T. NAKANISHI


Y. QIANG


M. SHIRATORI

The Award of the Society of Polymer Science, Japan

Dynamic Devulcanization/Dynamic Vulcanization for Recycling Rubbers and Developing Thermoplastic Elastomers

Yasuyuki Suzuki* Katsumasa Takeuchi** Mitsumasa Matsushita***
Kenzo Fukumori*** Norio Sato***

1. Outline

Rubber has a unique characteristic that makes it an indispensable automotive material, i.e., the ability to stretch well and then contract back to its original form. This characteristic is a consequence of crosslinking reactions during molding, which create a three-dimensionally interconnected network structure between the rubber molecules. As a result, rubber has no thermoplastic properties, making it a very difficult material to recycle.

The technology described in this article utilizes a twin-screw reactive extruder to set appropriate conditions for breaking crosslinking bonds (i.e., devulcanization) in order to manufacture a reclaimed rubber. The reclaimed rubber is then blended with resin to manufacture thermoplastic elastomers (TPE) by introducing new crosslinking. This technology has enabled the development of a high-grade and economic method of recycling.

2. Details of Technology

2.1 Dynamic devulcanization

In the network chains of sulfur crosslinked rubber, the bond energies of the crosslinking bonds (S-S: 270 kJ/mol, C-S: 310 kJ/mol) are comparatively lower than that of the main chains (C-C: 370 kJ/mol).

Utilizing the differences in the bond energies, a technology was developed capable of breaking selectively crosslinking points only, by the application of appropriate amounts of heat and shear stress in the twin-screw reactive extruder (**Fig. 1**).

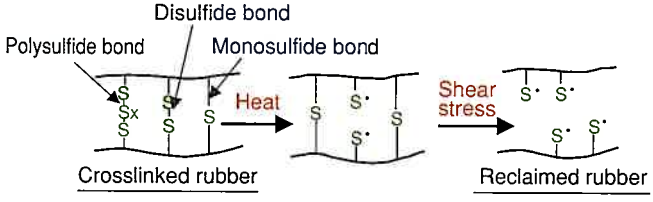

Fig. 1 Outline Diagram of Devulcanization Reaction

The resulting reclaimed rubber can be vulcanized by usual methods and it was confirmed that it has the same physical properties as new rubber.

* Material Engineering Div. 2 ** Toyoda Gosei Co., Ltd.
*** Toyota Central R & D Labs., Inc.

2.2 Dynamic vulcanization

A continuous TPE manufacturing technology was developed in order to increase added value. In more detail, after the rubber has been reclaimed, it is then dynamically vulcanized by blending with resin in the twin-screw reactive extruder (process time: 10 min or less), as shown in **Fig. 2**. Note that the peculiar odor generated on rubber reclamation has been removed by a deodorizing treatment that injects water and traps the odor in high-pressure vapor.

The TPE obtained under optimum conditions has virtually identical physical properties as commercial TPE.

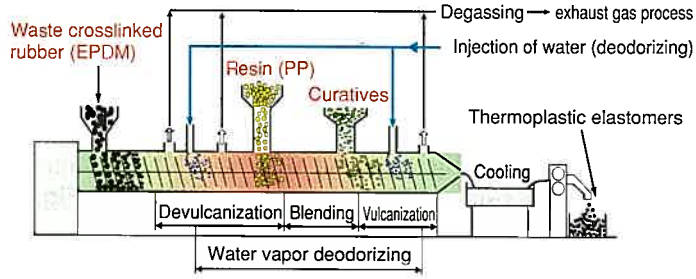

Fig. 2 TPE Manufacturing Technology Using

3. Conclusion

Rubber parts compounded by rubber reclaimed using this technology have been put into practical use since 1997 by Toyoda Gosei Co., Ltd., and are now widely applied in mass-produced vehicles. Use of TPE manufactured by this technology is scheduled to start in 2005.

This technology has been licensed to three companies within Japan and it is hoped that its application will also spread to other countries.

The development of this technology would not have been possible without the cooperation of Toyota Central R & D Labs., Inc., Toyoda Gosei Co., Ltd., as well as staff within Toyota Motor Corporation.

The Technology Award of The Society of Fiber Science and Technology, Japan

Development of PLA Fiber Board

Takashi Inoh* Takayasu Mori** Yuhei Maeda***

1. Introduction

Rapid increases in the amount of CO_2 emissions and the advancement of global warming owing to heavy consumption of fossil resources are acknowledged as problems requiring great attention. Replacing plastics derived from petroleum with plastics derived from plant sources is considered an effective means for helping combat global warming, and technology has been developed for application to automotive parts. Polylactic acid (PLA) is the only mass-produced bio-plastic that synthesizes lactic acid extracted from glucide in plants. This research focused on improving the weaknesses of PLA, namely, heat resistance, impact resistance, and hydrolysis resistance, in a board formed by combining kenaf (plant) fiber with PLA fiber, after which heat is used to melt the PLA.

2. Summary of Development

2.1 Improved heat resistance and impact resistance

The effect of combining kenaf fiber with PLA resulted in improved heat resistance (**Fig. 1**) and impact resistance (**Fig. 2**).

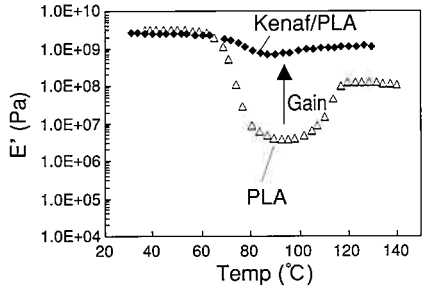

Fig. 1 Comparison of Storage Modulus

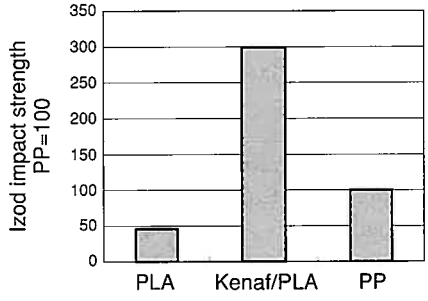

Fig. 2 Impact Resistance

2.2 Improved hydrolysis resistance

It is believed that hydrolysis of PLA is promoted by lactide remaining in polymers that acts as an acid catalyst. Therefore, a study was conducted on the amount of lactide remaining. The results are shown in **Fig. 3**. By reducing the amount of lactide, it was possible to slow down hydrolysis.

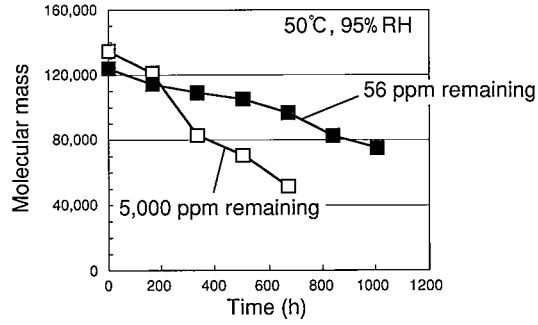

Fig. 3 Hydrolysis Property (Reduced Molecular Mass)

2.3 CO_2 gas reduction effect

Fig. 4 shows the comparison results of the amount of CO_2 gas emitted from the manufacturing stage of polypropylene and kenaf/PLA material up to thermal recycling for a part shape (spare tire cover). Energy from discarded biomass generated in the process for manufacturing raw material serves as the energy required for manufacturing PLA. The results showed that this has the potential to reduce CO_2 gas emissions by 82%.

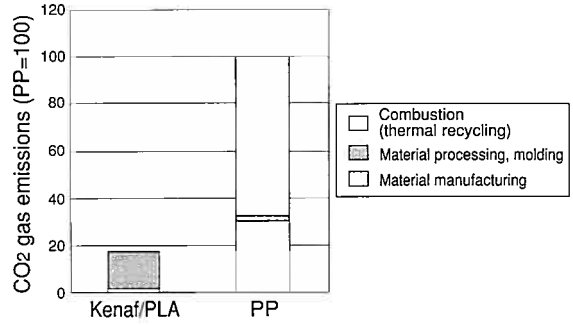

Fig. 4 Comparison of CO_2 Gas Emissions

3. Conclusion

Incorporation of the developed technology in kenaf and PLA boards has made possible the world's first mass production of a bio-plastic automotive part—a spare tire cover for the Raum model sold in 2003.

* Material Engineering Div. 2 ** Toyota Boshoku Corporation
*** Toray Industries, Inc.

The Technology and Takeda Memorial Awards of The Society of Instrument and Control Engineers

Robust Design for Torque Converter Clutch Slip Control System by means of H_∞ Control and LMI Approach

Katsumi Kono* Hiroshi Itoh*
Ryoichi Hibino** Masataka Osawa**

1. Introduction

As automatic transmission (AT) vehicles have become extensively used in the present day, technologies for improving the fuel consumption and reducing the CO2 emissions of AT vehicles are urgently required. In particular, slip control, in which the torque converter's lock-up clutch is engaged by application of slight, steady slip, has great potential as an effective technology for promoting good fuel economy, since it enables the benefits of lock-up to be attained even in the low and middle speed ranges. However, the control target, namely, the lock-up clutch, has input-output characteristics that change substantially depending on differences in running conditions. As a result, highly accurate slip control is difficult to perform.

The authors have addressed this problem through development of a controller design method that simultaneously achieves robust stability and target following characteristics. Along with this, a development method enabling controller design within a short design time has been established, thus allowing system development to be carried out quickly.

2. Overview

Fig. 1 shows the slip control system. In this system, the dynamic characteristics of the lock-up clutch and the hydraulic control device vary significantly due to factors like change in the operating conditions and deterioration of the hydraulic fluid.

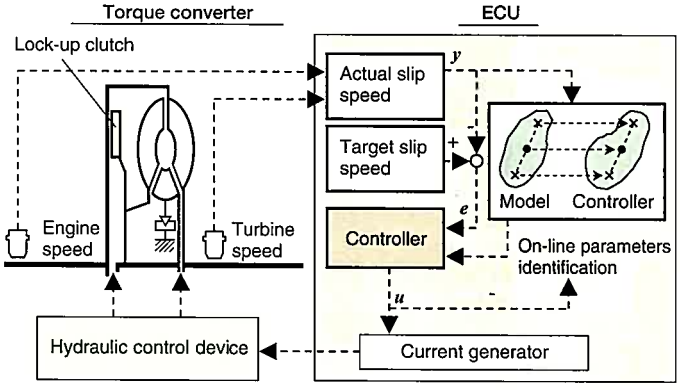

Fig. 1 Slip Control System

To perform loop shaping that focused on the peak characteristics of the complementary sensitivity function as a measure of stability with respect to the variation, H_∞ control and an LMI approach were used. As a result, a controller capable of simultaneously achieving outstandingly robust stability and target following characteristics was introduced. At the same time, simplified representation was introduced for the model and controller based on the end point characteristics of each set and interpolation thereof, and the mutually interpolated parameters were set with a dual relationship. Thus, it became possible to design the controller immediately after model identification.

Fig. 2 shows a comparison of the H_∞ controller obtained using the developed design method and the classic PID controller when operating in conditions when the hydraulic fluid has deteriorated. It is clearly apparent that the H_∞ controller shows outstanding stability. In addition, the controller design time was reduced by one-third as compared to methods in which strict modeling is performed.

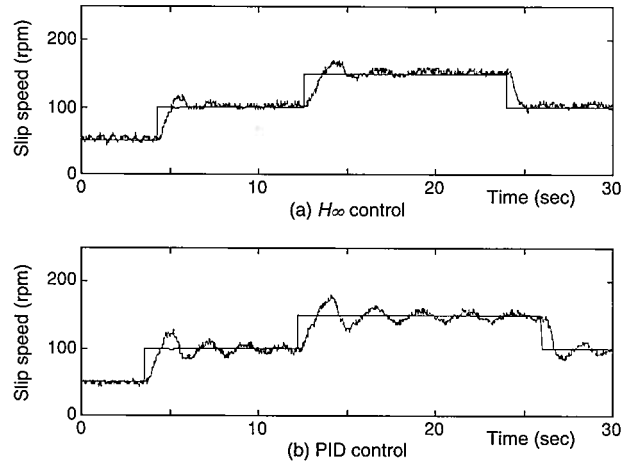

Fig. 2 Test Results when Hydraulic Fluid has Deteriorated

3. Conclusion

A new design method was introduced that allows rapid development of a system offering outstanding fuel consumption. This system is now being utilized in many different vehicle models.

* Drive Train Engineering Div. 2
** Toyota Central Research & Development Laboratories, Inc.

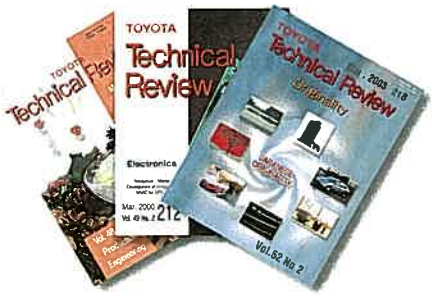

Back Number Index

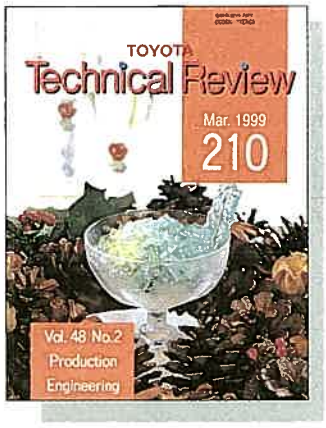

Vol. 48 No. 2
Theme: Production Engineering

Vol. 49 No. 2
Theme: Electronics

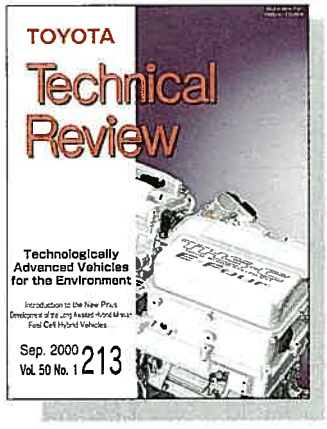

Vol. 50 No. 1
Theme: Technologically Advanced Vehicles for the Environment

Vol. 50 No. 2
Theme: Engine

Vol. 51 No. 1
Theme: Safety

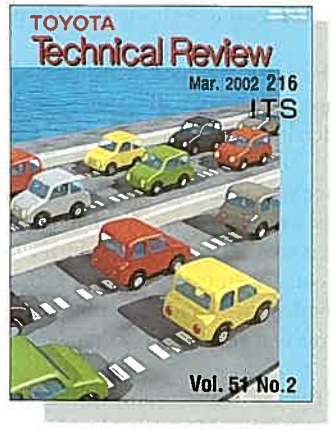

Vol. 51 No. 2
Theme: ITS

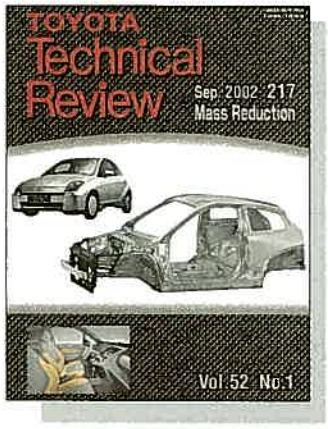

Vol. 52 No. 1
Theme: Mass Reduction

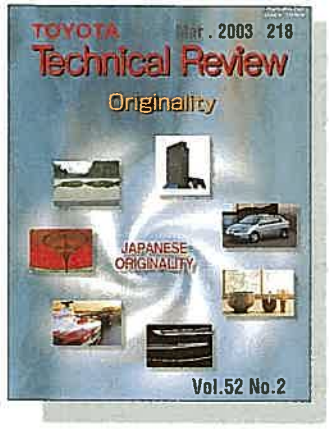

Vol. 52 No. 2
Theme: Originality

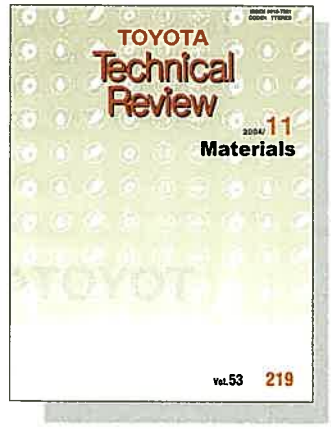

Vol. 53
Theme: Materials

¥2,940 (Tax included)

* Vol. 48 No. 1 “Recycling” and
Vol. 49 No. 1 “Design” are no longer on sale.

Distributor: Ohmsha, Ltd.
Tel: 81-3-3233-0641
http://www.ohmsha.co.jp/information/st/magazine/index.htm

As the season begins to turn, we present to you Vol. 54 No. 1 of the Toyota Technical Review.

The name Toyota is recognized all over the country and we hope the Toyota Technical Review, Toyota's only technical journal, will become similarly well known. With a view to gaining even the slightest increase in our readership, we have decided to switch back to a bi-annual publication of the Review instead of the annual publication in recent years. For this reason and others, we have included as many of the various latest technologies gaining attention at Toyota as would fit in the Review. More diagrams and color pages have been added as well, and we avoided obscure technical terms where possible so that general readers may also appreciate the content. The articles published in the Review are written by engineers and researchers at the front line of Toyota. Therefore, we believe that not only fans of Toyota, but also anyone with an interest in automotive technology will find subscribing to the Review worthwhile. With the Review, you too can become an expert on Toyota and get a window into the latest technological trends at Toyota. (Yamazaki)

"'Hybrid' will probably be this year's keyword in the automotive industry."

It was around January when I first saw that line written in a magazine article. At that time, we had just started preparations after deciding to make hybrids the topic of this Toyota Technical Review. Since then I have often seen the word "hybrid" in automotive-related magazines, making me glad that we focused on hybrids in this Review. The spotlight on the hybrid technologies and trends of carmakers has been growing brighter. I hope Toyota's only technical journal, the Toyota Technical Review, will generate further interest in Toyota's technologies among our readers.

This being my first turn as editor of the Review, I must admit that it has been an overwhelming experience. Thanks to the contributing authors and generous cooperation of others, we were able to see the smooth publication of this Review. I am deeply grateful for everyone's help. Starting this year, the Review will be published on a bi-annual basis and we intend to continue publication of the Toyota Technical Review with an emphasis on timely topics. Thank you for reading the Toyota Technical Review. (Hayashi)

TOYOTA Technical Review Vol. 54 No. 1

Publisher's Office	Technical Administration Div. TOYOTA MOTOR CORPORATION 1 Toyota-cho, Toyota, Aichi, 471-8572 Japan 81-565-28-2121 (Operator)
Publisher	Katsuhisa Yamazaki
Editor	Shima Hayashi Intellectual Property Div. TOYOTA TECHNO SERVICE CORPORATION
Printer	Sasatoku Printing Co., Ltd. Owaki 7, Sakae-cho, Toyoake, Aichi, 470-1196 Japan
Distributor	Ohmsha, Ltd. 81-3-3233-0641 (Operator) http://www.ohmsha.co.jp/
Printed	November 1, 2005

Printed on recycled paper.

ECO.

TOYOTA

TOYOTA
Technical
Review

2005/ 11
Vol. 54 No. 1 220

発売元　株式会社 オーム社
定価 2,940円(本体2,800円)
Distributor: Ohmsha, Ltd.
¥ 2,940 (Tax included)